HIGH PERFORMANCE CONTROL OF PM SYNCHRONOUS GENERATOR (PMSG) FOR WIND ENERGY CONVERSION

Teză destinată obţinerii
titlului ştiinţific de doctor inginer
la
Universitatea "Politehnica" din Timişoara
în domeniul INGINERIE ELECTRICĂ
de către

Eng. Marius FĂTU

Supervisor: Prof.dr.eng. Ion Boldea, Fellow IEEE
Reviewers: Prof.dr.eng. Frede Blaabjerg
                Prof.dr.eng. Dorin Popovici
                Prof.dr.eng. Radu Munteanu

Ziua susţinerii tezei: 29.02.2008

Seriile Teze de doctorat ale UPT sunt:

1. Automatică
2. Chimie
3. Energetică
4. Ingineria Chimică
5. Inginerie Civilă
6. Inginerie Electrică
7. Inginerie Electronică şi Telecomunicaţii
8. Inginerie Industrială
9. Inginerie Mecanică
10. Ştiinţa Calculatoarelor
11. Ştiinţa şi Ingineria Materialelor

Universitatea „Politehnica" din Timişoara a iniţiat seriile de mai sus în scopul diseminării expertizei, cunoştinţelor şi rezultatelor cercetărilor întreprinse în cadrul şcolii doctorale a universităţii. Seriile conţin, potrivit H.B.Ex.S Nr. 14 / 14.07.2006, tezele de doctorat susţinute în universitate începând cu 1 octombrie 2006.

Copyright © Editura Politehnica – Timişoara, 2008

România, 300159 Timişoara, Bd. Republicii 9,
tel. 0256 403823, fax. 0256 403221
e-mail: editura@edipol.upt.ro

PREFACE

This thesis represents an approach, based on the permanent magnet synchronous generator with two back-to-back PWM inverters, for wind applications.

Study motivation

According with International Energy Agency in the last decade wind power had one of the highest average annual growth rates among renewable sources. This situation imposes higher and higher demands regarding electric generators and their control. Now the wind turbines must remain connected during grid faults and thus implies a series of measures that should be taken in order to protect the power converters. Other technical issues are the capability of the grid inverter to work both in grid-connected mode but also in stand-alone mode and reducing harmonic pollution caused by nonlinear loads.

Small and medium wind turbines, equipped with permanent magnet synchronous generator connected to the local grid through two back-to-back PWM inverters, are becoming viable solutions for a number of reasons: four quadrant control at variable speed with ± 100% active and reactive power capabilities, high efficiency reasonable cost and high flexibility.

The motivation of the work for the present thesis is fully based on the above mentioned statement. The most of the considered solutions were subject of industrial research and development studies. The target of the thesis was to offer concrete advanced sensorless control solutions for permanent magnet synchronous generator systems for wind power applications.

Timişoara,
ianuarie 2008

Eng. Marius Fătu

Rezumat
The present thesis is dedicated to high performance control of a variable speed permanent magnet synchronous generator with two back to back PWM converters for renewable energy applications in general and for wind applications in special.
The wind power potential in many countries around the world has led to a large interest and fast development of wind turbine (WT) technology in the last decade. The integration of a high level of wind power into electrical network implies new challenges as well as new approaches in operation of the power system. According to the new requirements the wind turbines should stay connected and contribute to the grid in case of disturbances such as voltage sags, dips. The grid side inverter capability to work both in grid-connected but also in stand alone mode as well as the protection in the case of the fault event are considered to be the most challenging in terms of control strategy and the limited fault current.
The main goal of the thesis is to offer new high performance solutions in the area of control permanent magnet synchronous generator with two back to back PWM inverters for wind applications.

ACKNOWLEDGEMENTS

I wish to express my deep gratitude to my supervisor Prof. Ion Boldea. His guidance, support and encouragement made this work possible. I would like to thank also Prof. Frede Blaabjerg and Prof. Remus Teodorescu from the Institute of Energy Technology, Aalborg University, Denmark for their support and for the fruitful discussions during my researching period in Aalborg.

Many thanks to Prof. Gheorghe Daniel Andreescu from Faculty of Automation and Computers, Timisoara, Romania. His numerous inputs and fruitful discussions during my entire Ph.D. period were very helpful.

I want to thank all of those who contributed to my engineering education and also to my colleagues from Intelligent Motion Control Laboratory at Faculty of Electrical Engineering, Timisoara; Asoc. Prof. Lucian Tutelea and Assist. Prof. Cristian Lascu deserve my special gratitude.

Finally, and most of all, I want to thank my parents, to my girlfriend and to her family for their support and understanding.

This thesis is dedicated to them.

Timisoara January 18th , 2008

Marius Fatu

Outline of the thesis

The present thesis is organized in 8 chapters following the above presented objectives:

The *first* chapter presents an overview of the variable speed generators and their power converters. Detailed information is given for the actual solutions in wind turbine applications.

In the *second* chapter the simulation models developed in Simulink for analysis of the permanent magnet synchronous generator with two back to back converters and their control are illustrated and discussed. A possible sensorless control solution for PMSG connected to the grid for different wind profiles is presented.

In the *third* chapter, the behavior of a motion sensorless control PMSG system, is investigated through ample experiments under asymmetric grid voltage sags. A new estimator based on D-module filter for positive sequence of grid voltage as well as a rotor position and speed estimator without emf integration are proposed and investigated through one, two, three phase voltage sags.

In chapter *four* a new seamless (uninterrupted load current) transition, based on phase locked-loop technique, from grid-connected to stand alone and vice versa is presented. The control system detects when the grid parameters are out of their nominal range and automatically switches the control of the grid-inverter from current control to voltage control. When the grid is recovered, the stand alone voltages are synchronized with grid voltages and the control strategy automatically switches to grid-connected control mode.

The system was experimentally shown capable of supplying local load in good conditions in both operation modes.

In chapter *five,* a novel harmonic voltage compensation solution for nonlinear (diode rectifier) load operation in stand alone PMSG with bidirectional converter motion sensorless vector control is proposed. Both the case of three phases and two phase output of the load side converter, with voltage symmetrisation by negative component active cancellation, are treated. The system was experimentally shown capable of supplying local load in good conditions (with much lower negative sequence ac voltages and lower harmonics content of the latter) even if one terminal of the load- side inverter is open and the load is nonlinear (diode rectifier load).

In chapter *six* a novel hybrid motion-sensorless control system for permanent magnet synchronous motors (PMSM) using a new robust start-up method called *I-f* control, and a smooth transition to emf-based vector control is presented. This solution allows ultra low-speed sensorless control without initial rotor-position estimation, and without machine parameters identification. Digital simulations for PMSM start-up with full load torque are presented for different initial rotor-positions. The transitions from *I-f* to emf motion-sensorless vector control and back as well, at very low-speeds, are fully validated by experimental results.

In chapter *seven* the test rigs used for experimental work are illustrated as well as some software details implementation of the proposed algorithms.

In chapter *eight* the work is summarized and the conclusions, contributions and future perspectives are presented.

Objectives of the thesis

The major objectives of thesis are:

- developing simulation models for the complete system with PMSG for wind power applications, including the prime mover, electric generator, power electronics and control.
- analyze the behaviour of the permanent magnet synchronous generator under grid voltage sags an search for possible solutions to control and protect the power electronics without disconnecting the system from power grid.
- find a seamless transfer method from grid-connected to stand alone and vice versa for the system with PMSG
- find a sensorless control strategy robust an accurate in all circumstances
- develop a selective harmonic and negative sequence voltage compensation scheme under nonlinear and non symmetric load for the system in stand alone mode.
- Investigate the possibilities of the system for self-starting, and motoring regime which might be very useful when the PMSG is connected to the grid, or moving the rotor a little for inspections/repairs and for general industrial variable speed drives where slightly hesitant but full-load self-starting is allowable.

TABLE OF CONTENTS

Chapter 1

Variable speed generators

Abstract

In this chapter, an overview of the variable speed generators and their power electronics is presented. Then, the generators and power electronics concepts are detailed from the electrical point of view. Classical and new solutions are discussed based on technical aspects and market trends.

1.1 Introduction

Global warming has been attributed to the increase of the atmospheric gases concentration produced by the burn of fossil fuel [1, 2]. Due to decreasing oil and coal reserve, environmental concerns and fear of nuclear disasters, it is believed that future power generation will not be limited to the conventional power plants. Despite rapidly climbing prices for natural gas and oil, alternative energy in all its forms might be a competitive on the price front for everyday users. Alternative energy is generally defined as any power source that is not based on fossil fuels or nuclear reactions. That includes electricity generated from wind, solar, geothermal, biomass or plant matter, and hydro power. Alternative fuels also can include ethanol from corn, biodiesel made from vegetable crops and methane made from waste or other sources. Wind power is a potential candidate in non-conventional power generation family.

Wind power generation is an important alternative to mitigate this problem mainly due its smaller environmental impact and its renewable characteristic that contribute for a sustainable development [3]. Wind farms are becoming an increasingly common sight on off-shore and on-shore. Their large scale integration in the electricity system presents some planning and operational difficulties due to mainly the intermittent and difficult to

predict nature of wind which is considered at unreliable energy sources. However, the percentage of energy provided by wind is increasing due to technology and efficiency

improvements, government financial support and energy policies. Wind turbines have become more efficient and their costs have dropped about 80 percent since 1980 to about four to eight cents per kilowatt-hour today, vs. about 38 cents to 40 cents 25 years ago.

Generally speaking, there are two constructive types of electric generators:

      - Horizontal axis;
      - Vertical axis;

Respectively, there are two operating modes in generating:

- Constant Speed – Constant Frequency (CSCF) – this system always needs back to back
   inverters;
- Variable Speed – Constant Frequency (VSCF) – this system needs a speed controller to
 obtain the maximum from wind power and a converter to change Variable Frequency
(VF) into Constant Frequency (CF);
The constant speed configuration is characterized by stiff power train dynamics due to the fact that electrical generator is locked to the grid; as a result, just a small variation of the rotor shaft speed is allowed. The construction and performance of this system are very much dependent on the mechanical characteristic of the mechanical subsystems, pitch control time constant, etc. In addition, the turbulence and tower shadow induces rapidly fluctuation loads that appear as variations in the power ($P \approx v^3$). These variations are undesired for grid-connected wind turbine, since they result in mechanical stresses that decrease the lifetime of wind turbine [4, 5, 7] and decrease the power quality. Furthermore, with constant speed there is only one wind velocity that results in an optimum tip speed ratio. Therefore, the wind turbine is often operated off its optimum performance, and it generally does not extract the maximum power from the wind [5, 8].
Alternatively, variable speed configurations provide the ability to control the rotor speed. This allows the wind turbine system to operate constantly near to its optimum tip-speed ratio. The wing generation systems with variable speed wind turbine generators are connected to the network trough power electronic converters that supply a soft link between the shaft speed of the machine and the network frequency.
 The following advantages of variable-speed over constant-speed can be highlighted:

(1) The Annual Energy Production (AEP) increases because the turbine speed can be adjusted as a function of wind speed to maximize output power.
Depending on the turbine aerodynamics and wind regime, the turbine will on average collect up to 10% more annual energy [5].
(2) The mechanical stresses are reduced due to the compliance to the power train. The turbulence and wind shear can be absorbed, i.e., the energy is stored in the mechanical inertia of the turbine, creating a compliance that reduces the torque pulsations [6, 7].
(3) The output power variation is somewhat decoupled from the instantaneous condition present in the wind and mechanical systems. When a gust of the wind arrives at the turbine, the electrical system can continue delivering constant power to the network while the inertia of mechanical system absorbs the surplus energy by increasing rotor speed.
(4) Power quality can be improved by reduction the power pulsations. The reduction of the power pulsation results decreases voltage deviations from its rated value in the point of common coupling (PCC). This allows increasing the penetration of the wind power in the network [6, 7].
(5) The pitch control complexity can be reduced. This is because the pitch control time constant can be longer with variable speed [7].

(6) Acoustic noises are reduced. The acoustic noise may be an important factor when sitting new wind farms near populated areas [6, 7]. Although the main disadvantage of the variable-speed configuration are the additional cost and the complexity of power converters required to interface the generator and the grid, its use has been increased due the above mentioned advantages.

Thus, the present state-of-art of large wind turbines is including:

- **pitch control** combined with variable speed. Moreover, the variable speed concept is mainly realized using configuration "c", i.e. the doubly-fed induction generator with a rotor connected IGBT-based frequency converter. The blades can be turned out or into the wind as the power output becomes too high or too low respectively. This type of control has certain advantages like good power control (at high wind speeds the mean value of the power output is kept close to the rated power of the generator), assisted start-up and emergency stop.

  The disadvantages are technical complexity of the pitch mechanism and the higher power fluctuations at high wind speeds. Also, the instantaneous power will, because of wind gusts and the limited speed of the pitch mechanism, fluctuate around the rated mean value of the power.

- **active stall** with a two speed induction generator. At low wind speeds the blades are pitched similarly with the pitch control in order to achieve maximum efficiency. At high wind speeds the blades go into a deeper stall by being pitched into the direction opposite to that of pitch control. Thus, the turbine achieves a smoother limited power, without higher power fluctuations like in the case of pitch-controlled turbines. The active stall control has the advantage of being able to compensate variations in air density. The combination with the pitch mechanism helps in case of emergency stops and for starting-up.

1.2. GENERATORS AND TOPOLOGIES

1.2.1 Synchronous Generators

a) *Wound Field Synchronous Generator* (WFSG)

A wind generation system (WGS) equipped with wound field synchronous generator is show in Fig. 1.1. The stator winding is connected to network through a four-quadrant power converter comprised of two back-to-back PWM-VSI. The machine side converter regulates the electromagnetic torque, while the supply side converter regulates the real and reactive power delivered by the WGS to the utility. The power converter may be formed also by a diode rectifier with a boost chopper converter connected to a PWM power inverter.

Synchronous generator has some advantages because this electromagnetic machine provides its own magnetization energy.

- The efficiency of this machine is usually high, because it employs the whole stator current for the electromagnetic torque production [10].
- The main benefit of the employment of wound field synchronous generator with salient pole is that it allows the direct control of the power factor of the machine, consequently the stator current may be minimized any operation circumstances [11].
- The pole pitch of this of this generator can be smaller than that of induction machine. This could be a very important characteristic in order to obtain low speed multiple pole machines, eliminating the gear box [12].
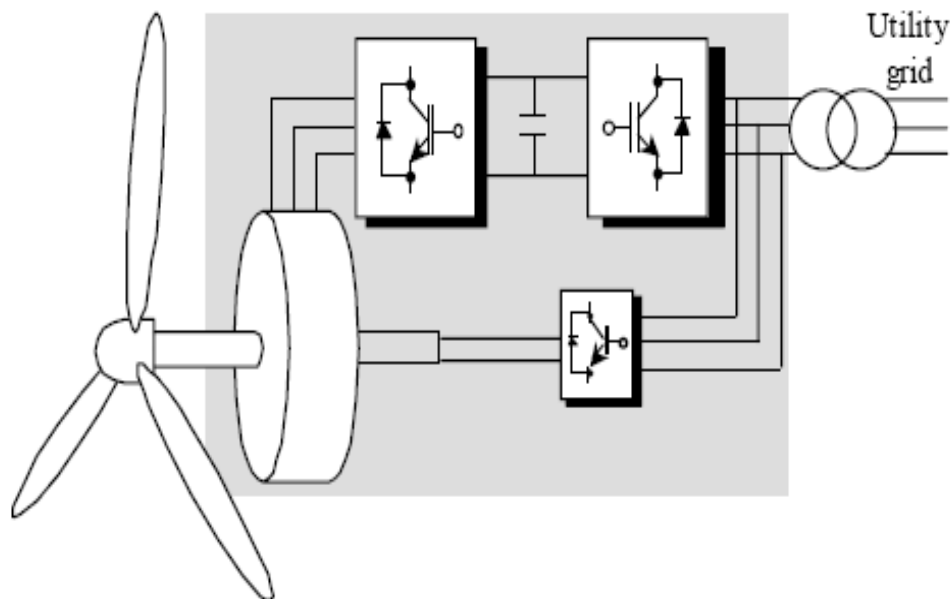
Fig.1.1 Variable Speed Field Winding Synchronous generator [9]

The existence of a winding circuit in the rotor may be a drawback as compared with permanent magnet synchronous generator. In addition, to regulate the active and reactive power generated, the converter must be sized typically 1.2 times of the WGS rated power [11, 13]. This implies very hard conditions of operation for the switching components of the converter because of the limited rate values of the voltage and current of these components. For this reason the switching frequency must be reduced and, in consequence, the power quality is also reduced [15, 16].

b) Permanent-Magnet Synchronous Generator (PMSG)

In Fig.1.2 a permanent magnet synchronous generator connected to a three phase diode rectifier followed by a boost converter is presented [15, 16]. In this configuration the boost converter regulates the electromagnetic torque. The supply-side converter maintains constant the level of the dc link voltage and controls the

input power factor. The advantage of the diode rectifier is that the energy can only flow from the generator to the DC side, however, it gives rise to current distortion and a lagging power factor [12-15,17].
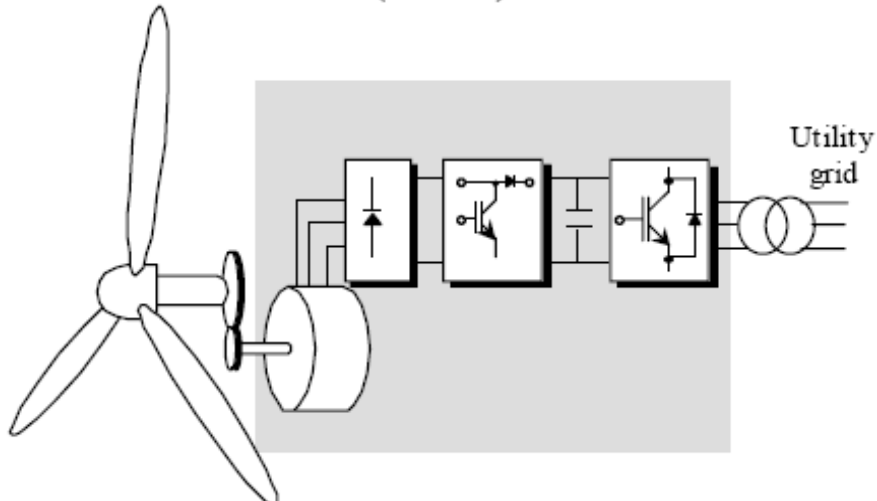
Fig.1.2 Permanent-Magnet Synchronous Generator with a Boost Chopper [9]

Other scheme is shown in Fig.1.3 where the diode rectifier and the chopper are replaced by a PWM rectifier between the generator and the grid-side inverter.
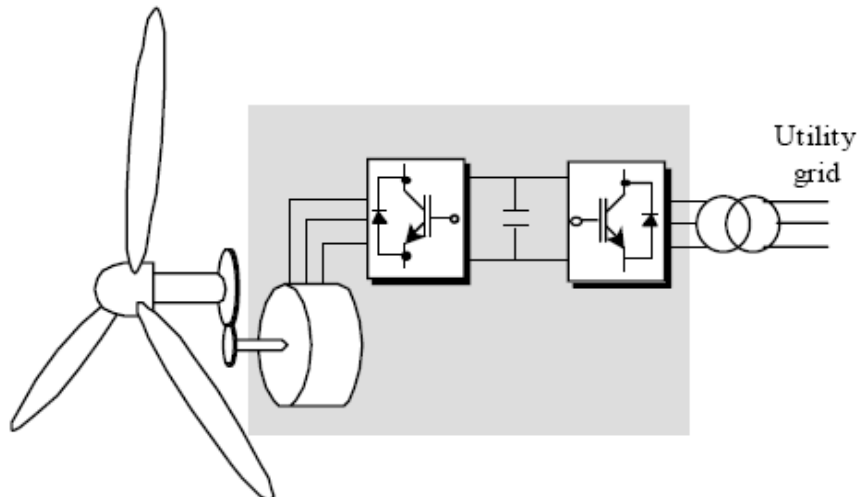
Fig.1.3 Permanent-Magnet Synchronous Generator with PWM converter [9].

To achieve full control of the grid current, the DC-link voltage must be boosted to a level higher than the amplitude of the grid line-line voltage. The power flow of the grid side converter is controlled in order to keep the DC-link voltage constant, while

the control of the generator side is set to suit the magnetization demand and the reference speed [21]. The use of a controlled rectifier allows several advantages. The PMSG current may be controlled to be sinusoidal, thus avoiding the above-mentioned problems related with the usage of a diode rectifier. The amplitude of the voltage may be controlled to match the grid voltage, independent of shaft speed. Especially, the PMSG is more isolated from the grid, making it possible to control fault currents in the PMSG, arising from external faults in the grid. The use of the inverter effectively decouples the generator from the grid [22]. This also removes the need for special starting and synchronising equipment for the PMSG. The system may operate at any power angle, without losing synchronism.

Direct-drive applications are on increase because the gearbox can be eliminated. As compared to a conventional gearbox-coupled wind-turbine generator, a direct-drive generator has reduced the overall size, has lower installation and maintenance cost, has a flexible control method and quick response to wind fluctuations, and load variation. For small wind turbine, permanent magnet synchronous machines are more popular because of their higher efficiency, high-power density, and robust rotor structure as compared to induction and synchronous machines. A number of alternative concepts have been proposed for direct drive electrical generators for use in grid-connected or stand alone wind turbines [29].

1.2.2 Induction Generators

a) *Doubly Fed Induction Generator* (DFIG)

The wind power applications the doubly-fed induction generator with two back-to-back inverters in the rotor circuit is a proved, robust and widely considered solution having in the present 47% of the world market share of wind turbine concepts and the market is growing.

The wind power generation system shown in Fig.1.4 consists of a doubly fed induction generator (DFIG), where the stator winding is directly connected to the network and the rotor winding is connected to the network through two back-to-back PWM-VSI.
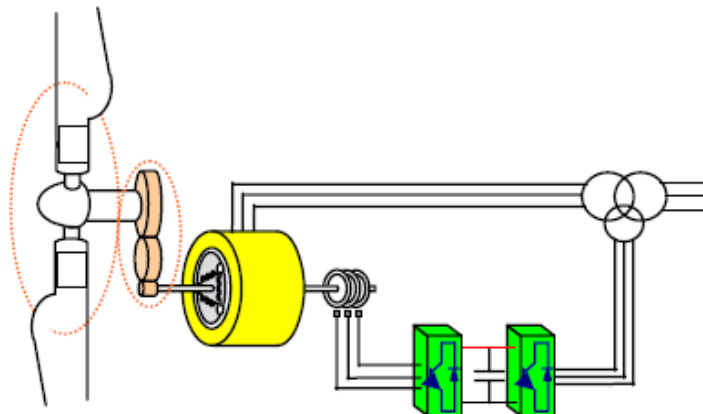

Fig.1.4 WGS with Variable Speed Doubly Fed Wound Rotor Asynchronous Generator [11]

The task of the rotor side converter is to control electromagnetic torque and to supply the reactive power to maintain the magnetization of the machine. The grid-

side inverter keeps the dc-link voltage constant and regulates the active and reactive power delivered by WGS to network [23-28].

There are some advantages and drawbacks in using DFIG in WGS as:

- The main benefit of this system is reduced cost of the inverter rating typically 25% of the total system power because the inverter only needs to control the "slip" power of the rotor [7].
- Also the first advantage implies a reduced cost of the inverter filter and EMI filters, because filters rated for 0.25 p.u. total system power, and inverter harmonics represent a smaller fraction of total system harmonics [7].
- Another advantages are the robustness and stable response of this machine facing   against external disturbance [11].
- The major drawback is that the machine must be excited by the supply system because it can't produce the magnetic energy by itself. This implies that its operation characteristics are very strongly dependent on the network characteristics (stability, grid short-circuit power...).
- This type of WGS always needs a gear box between the generator and the turbine because a multipole asynchronous machine will require a big size.
- The use of slip rings is another drawback of this system because requires periodic maintenance especially at sea shore sites.

Another DFIG configuration was introduced by Danish manufacturers Vestas and Nordic Windpower, which is the semivariable-speed turbine, in which the rotor resistance of the squirrel cage generator can be varied instantly using fast power electronics. So far, Vestas alone has succeeded in commercializing this system under the trade name OptiSlip®. A number of turbines, ranging from 600 kW to 2.75 MW, have now been equipped with this system, which allows transient rotor speed increases of up to 10% of the nominal value. In that case, the variable-speed conditions are achieved dissipating the energy within a resistor placed in the rotor, as shown in Fig.1.5. The disadvantages are the configuration still needs a reactive power compensation system, the control of active and reactive power.

The efficiency of the system decreases when the slip increases and speed control is limited to a narrow margin.
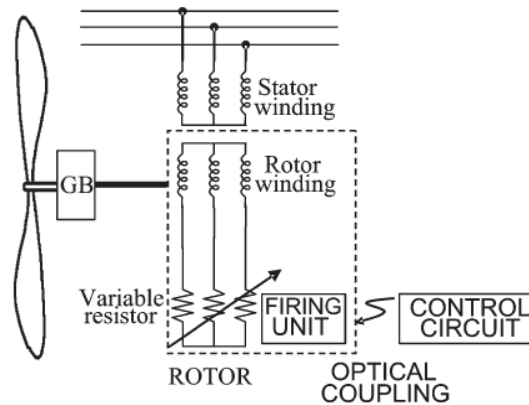
Fig.1.5 Doubly fed induction machine controlled with slip power dissipation in an internal resistor.[29]

Another configuration for a WGS using a DFIG is shown in Fig.1.6 with a dc-transmission link.
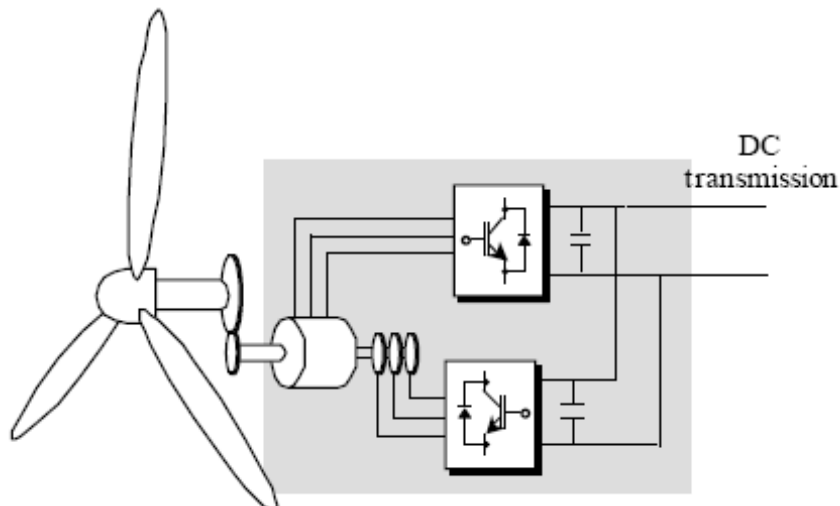
Fig.1.6 Doubly-fed Full Controlled Induction Generator [9]

This type of WGS offers the possibility to control the voltages and frequencies of the rotor and stator, consequently this system provide a higher flexibility on the control system than the conventional doubly-fed induction generator shown in Fig. 1.4. In addition, this WGS has been considered for offshore sites, which are connecting to land gateway by submarine cables [30].

In order to avoid the maintenance issues of DFIG, other electrical machine called Brushless Doubly Fed Asynchronous Generator (BDFAG) is proposed. This machine is characterized by two independent three-phase stator windings: the power winding and the control winding.

The power winding is directly connected to electric grid, so it works with constant frequency (f_p=50Hz), whereas the control winding is fed with a variable frequency through a power electronic converter (Fig 1.7).
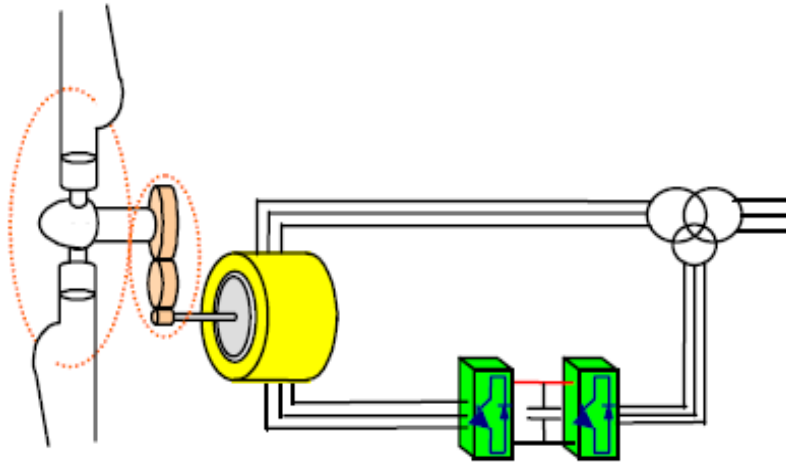
Fig.1.7 Operational scheme of a Variable Speed Generation System with BDFAG [11]

b) *Squirrel Cage Induction Generator* (**SCIG**)

A WGS equipped with squirrel cage induction generator is shown in Fig.1.8. The stator winding is connected to the grid through to back-to-back PWM VSI inverters. The stator-side converter controls the electromagnetic torque and supplies the reactive power to maintain the machine magnetized, while the supply-side converter keeps the Dc-link voltage level constant and regulates the active and reactive power delivered by the WGS to the utility grid [32-40].
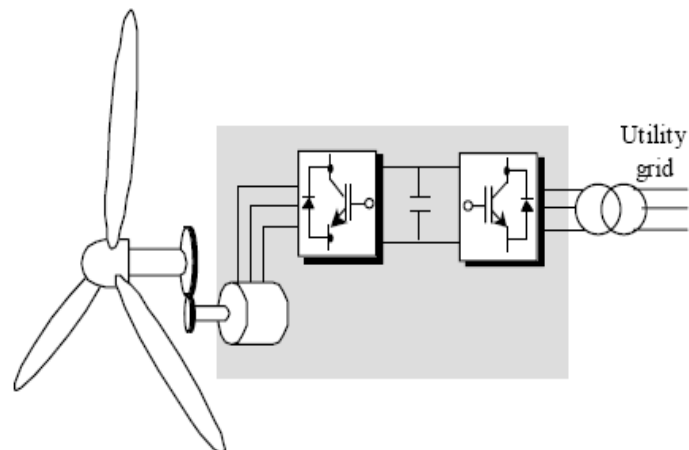
Fig.1.8 Variable Speed Squirrel Cage Induction Generator [9]

This type of WGS has some important advantages over the other to be used in micro-wind generator system such:

- Rotor mechanical simplicity, high efficiency and low maintenance requirements
- Fast transient response is possible [31].
- The inverter can be operated as a VAR/harmonic compensator when spare capacity is available [31].
- Nevertheless when using an asynchronous machine in small size WGS, the use of the gearbox can be avoided. This is because the optimal speed of wind turbines is around the 500-800 rpm range, and consequently, direct drive wind turbine generators can be reached employing an electrical machine with reasonable number of pole pairs [32].

The drawbacks of this system are:

- The stator-side converter must be oversized 30-50% with respect to rated power, in order to supply the magnetizing requirement of the machine [11].
- The full load power factor is relatively low due to the magnetizing current extracted from the grid by the stator winding. At high wind speeds the generator can produce more active power with the price of the more reactive power drawn from the grid. And the amount of the reactive power is uncontrollable because it is varying with the wind conditions.
- Complex system control (FOC) whose performance is dependent on the good knowledge of the generator parameter that varies with temperature and frequency [30].

The squirrel-cage induction generator can be used both in fixed-speed wind turbines and in full variable-speed wind turbines (with bidirectional full-load back-to-back power converter).

1.3 The power electronics

Power electronics is a rapidly developing technology. Improvements in the performances and reliability of power semiconductors with better electrical characteristics and lower prices made them available in wind applications. The IGBTs are now the main components for power electronics in wind-turbine applications. They are now mature technology turn-on components adapted to a very high power (6 kV–1.2 kA), and they are in competition with gate turn-off thyristors (GTOs) for high power applications [41].

1.3.1 Diode rectifier
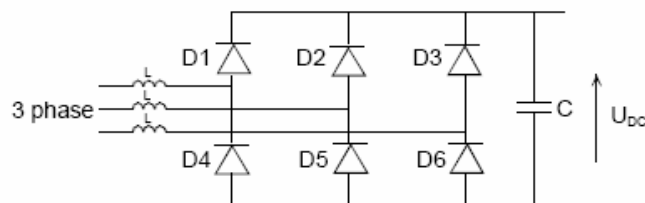
Fig.1.9 Diode rectifier

The main topology is with six diode rectifier (Fig.1.9). This configuration it is simple and allows only one quadrant, operation when no control before Dc is needed, with the price of high current harmonic content on the grid-side. One of the methods to

improve the power quality is to increase the Dc voltage level. This could be done by using boost chopper (Fig.1.10).
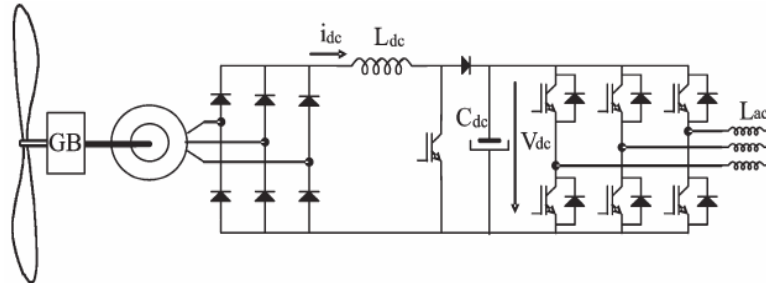
Fig.1.10 Step-up converter in the rectifier circuit and full power inverter topology used in wind-turbine applications. [29]

1.3.2 The back-to-back PWM-VSI

The back-to-back PWM-VSI is a bidirectional power converter consisting of two PWM-VSI as is shown in Fig.1.11.
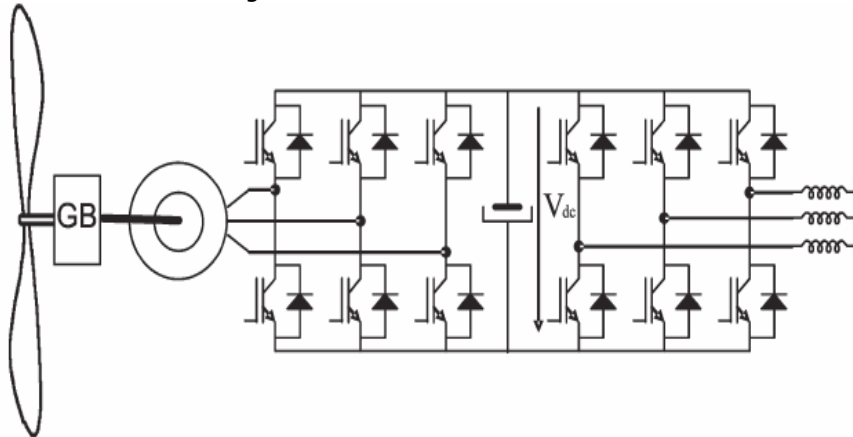
Fig.1.11 The back-to-back PWM-VSI topology [29]

One of the technical advantages of this configuration is the capacitor decoupling between grid-side inverter and machine-side inverter. This decupling offers the possibility of separate control for each inverter. The objective of the dc link is to act as energy storage, so that the captured energy from the wind is stored as a charge in the capacitors and may be instantaneously injected into the grid.
 The presence of the Dc link capacitor is considered a drawback in some papers [42] since it is heavy and bulky and reduces the overall lifetime of the system.

Another drawback is the switching losses since this configuration implies two inverters. The high switching speed to the grid may also require extra EMI-filters.

1.3.3 High-Power Medium-Voltage Converter Topologies:

In order to decrease the cost per megawatt and to increase the efficiency of the wind-energy conversion, nominal power of wind turbines has been continuously growing in the last years [43].

Trends on wind-turbine market are to increase the nominal power (some megawatts) and due to the voltage and current ratings. This makes the multilevel converter suitable for modern high-power wind-turbine applications (Fig.1.12). The increase of voltage rating allows for connection of the converter of the wind turbine directly to the wind-farm distribution network, avoiding the use of a bulky transformer [44].

The different proposed multilevel-converter topologies can be classified into the following five categories [45]:

1) multilevel configurations with diode clamps;
2) multilevel configurations with bidirectional switch interconnection;
3) multilevel configurations with flying capacitors;
4) multilevel configurations with multiple three-phase inverters;
5) multilevel configurations with cascaded single-phase H-bridge inverters.
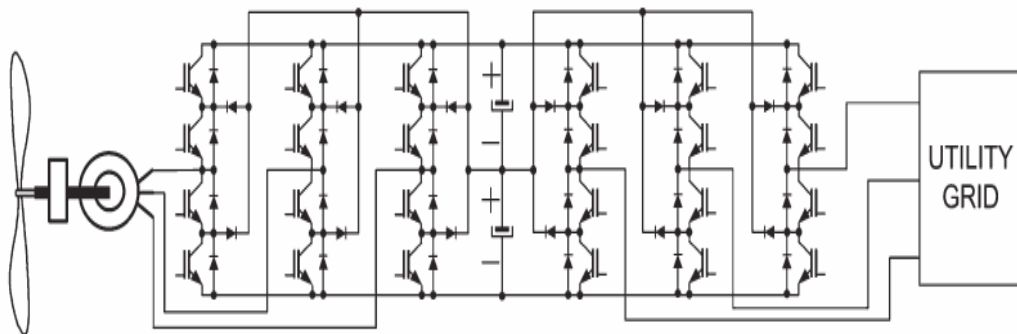
Fig.1.12 Multilevel back-to-back converter for a direct connection of a wind turbine to the utility grid.[44]

The main advantages of using multilevel converters for large electric drives include the following [45]:

a) They are suitable for large voltampere-rated and/or high voltage motor drives.
b) These multilevel converter systems have higher efficiency because the devices can be switched at minimum frequency.
c) Power factor is close to unity for multilevel inverters used as a rectifier to convert generated ac to dc.
d) No EMI problem or common-mode voltage/current problem exists.

e) No charge unbalance problem results when the converters are in either charge
   mode (rectification) or drive mode (inversion).

The most commonly reported disadvantage of the multilevel converters with split dc
link is the voltage unbalance between the capacitors that integrate it [44].

Numerous hardware and software solutions are reported: the first one needs
additional components that increase the cost of the converter and reduce its
reliability; the second one needs enough computational capacity to carry out the
modulation signals. Recent papers illustrate that the balance problem can be
formulated in terms of the model of the converter, and this   formulation permits
solving the balancing problem directly modifying the reference voltage with a
relatively low computational burden [46], [47].

Another drawback of some multilevel topologies is the necessity to obtain different
dc-voltage independent sources needed for the multilevel modulation. The use of
low-speed permanent-magnet generators that have a large number of poles allows
obtaining the dc sources from the multiple wounds of this electrical machine, as can
be seen in Fig.1.13. The continuous reduction of the cost per kilowatt of PEBBs is
making the multilevel cascaded topologies to be the most commonly used by the
industrial solutions [29].
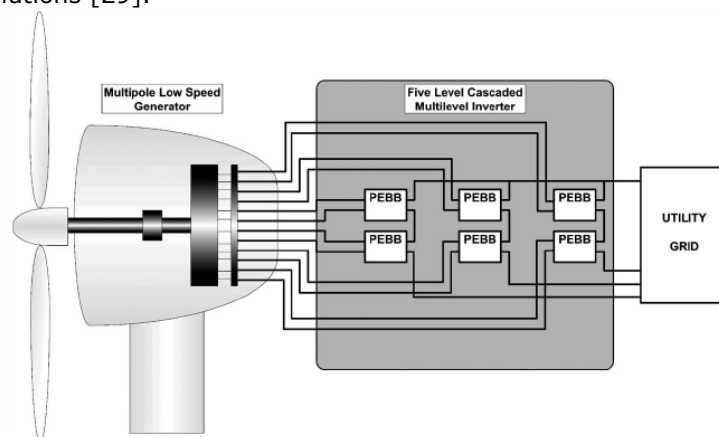
Fig.1.13 Five-level cascaded multilevel converter connected to a multipole low-speed wind-
turbine generator.[29]

In this case, the power-electronic building block (PEBB) can be composed of a
rectifier, a dc link, and an H-bridge [29].

1.4 Conclusion

In this first chapter a review of existing systems with variable speed generators is
presented. There are both, solutions being in series production and also
noncommercial solutions, but possible candidates in the future for renewable energy
generating systems.

Variable speed generators are attractive for wind turbines for a number of
reasons: it will reduce the mechanical stress in the gearbox, increase the amount of
energy captured from the wind and improve the controllability of the active and

reactive power, which becomes more and more important in respect to integrate the wind turbines into the grid. The control system may incorporate very efficient control algorithms of the dynamics of the electromagnetic torque developed by the electrical generator, the way that, the excess or default of energy coming from the wind oscillations, can be stored in the rotating mass of the turbine-generator units. This can eliminate the wind power plant short-term fluctuations and contributes to maintain the voltage quality in the network connection point.

In the small and medium wind turbine systems both the SCIG and PMSG have been used while for large size wind turbine systems both DFIG and SG are preferred. The back-to-back four-quadrant PWM-VSI converter is preferred because the PWM modulation reduces the current harmonic component in the input and output of the system. As a result, it reduces the torque pulsation on the generator and allows improving the output power quality.

Permanent magnet synchronous generators (PMSG) with two back-to-back inverters are good candidates for wind power applications for number reasons: four quadrant control at variable speed with ± 100% active and reactive power capabilities, high efficiency reasonable cost and high flexibility.

The following chapters will deal only with the vector control of PMSG.

References:

[1] Legget, J. "Global Warming", The Greenpeace Rebacort, Oxford University Press, 1990.
[2] Scheling, W. and Lichter, J. "Limited carbon storage in soil and litter of experimental forest plots under increased atmospheric CO2" Nature 411, pp. 466-469, 2001.
[3] Tolmasquim, M. T, Szklo, A S, Soares, J. B "POTENTIAL USE FOR ALTERNATIVE ENERGY SOURCES IN BRAZIL", Annual Petrobras Conference 2002, Oxford, Inglaterra.
[4] Leithead, W.E.; de la Salle, S.; Reardon, D. "Role and objectives of control for wind turbines "Generation, Transmission and Distribution, IEE Proceedings C, Volume: 138 Issue: 2, pp: 135-148, March 1991.
[5] Carlin, P.W. Laxson, A.S. and Muljadi, E.B. "The History and State of the Art of Variable-Speed Wind Turbines Technology" NREL, February 2001.
[6] Weigand, C.H., Lauw, H.K. and Marckx, D.A. "Variable-Speed Generation Subsystem Using the Doubly Fed Generator." NREL, April 1999.
[7] Muller, S. Deicke, M. De Doncker, R.W. "Doubly fed induction generator systems for wind turbines" IEEE Industry Applications Magazine, Volume: 8 Issue: 3, May-June 2002, pp: 26 –33.
[8] Muljadi, E.; Butterfield, C.P. and Handman, D. "Dual-Speed Wind Turbine Generation." NREL, June 1996.
[9] Marchez J., Pinheiro H., H. A. Gründling, J. R. Pinheiro, H. L. Hey, "A SURVEY ON VARIABLE-SPEED WIND TURBINE SYSTEM"
[10] Robert L. Ames " AC Generators. Design and Application". John Wiley, 1990.
[11] Nicolás, C.V, Lafoz, M. And Iglesias, J. "Guidelines for the Design and Control of Electrical Generator Systems for new Grid connected Wind Turbine Generator." IECON 2002.

[12] Spooner, E. and Williamson, A.C. "Direct coupled, permanent magnet generators for wind turbine applications". Electric Power Applications, IEE Proceedings, Volume: 143 , Jan. 1996, pp:1 –8.

[13] S. Morimoto, H. Nakayama, M. Sanada, Y.Takeda, "Sensorless Output Maximization Control for Variable-Speed Wind Generation System Using IPMSG", IEEE TRANSACTIONS ON INDUSTRY APPLICATIONS, VOL. 41, NO. 1,pp. 60-68, JANUARY/FEBRUARY 2005.

[14] R. Esmaili, L. Xu, D. K. Nichols, "A New Control Method of Permanent Magnet Generator for Maximum Power Tracking in Wind Turbine Application", 2005, IEEE.

[15] R. Esmaili, L. Xu, "Sensorless Control of Permanent Magnet Generator in Wind Turbine Application"

[16] Carlin, P.W. Laxson, A.S. and Muljadi, E.B. "The History and State of the Art of Variable-Speed Wind Turbines Technology" NREL, February 2001.

[17] Chen, Z.; Spooner, E. "Grid power quality with variable speed wind turbines" Energy Conversion, IEEE Transaction on power electronics, Volume: 16 Issue: 2 , June 2001, pp: 148 -154.

[18] Hansen, Helle, Blaabjerg, Ritchie, Munk-Nielsen, Bidner, Sorensen and Bak-Jensen "Conceptual survey of Generators and Power Electronics for Wind Turbines" Report R-1205 RISO National Laboratory Denmark 2001.

[19] Veganzones, Alonso, Burgos, Rodriguez Amenedo, "Transiens operation simulator for variable speed wind energy with double output induction generator", Proccd. ICEM, Vigo 1996.

[20] Hao, S.; Hunter, G.; Ramsden, V.; Patterson, D." Control system design for a 20 kW wind turbine generator with a boost converter and battery bank load ", PESC. 2001 IEEE 32nd Annual , Volume: 4 2001,pp: 2203 -2206.

[21] Hansen, L.H. Madsen, P.H.; Blaabjerg, F.; Christensen, H.C.; Lindhard, U.; Eskildsen, K. "Generators and power electronics technology for wind turbines" IECON 2001, vol.3, pp: 2000 -2005.

[22] Chen,Z.,& Spooner,E "A solid-state synchronous voltage source with low harmonic distortion", In Procedings on Opportunities and Advances in International Electric Power Generation, 1996, 158-163.

[23] R. Pena, J.C. Clare, G.M. Asher "Doubly fed induction generator using back-to-back PWM converters and its application to variable-speed wind-energy generation", IEE Proc-Electr. Power Appl. Vol. 143, No. 3, May 1996

[24] Weigand, C.H., Lauw, H.K. and Marckx, D.A."Variable-Speed Generation Subsystem Using the Doubly Fed Generator." NREL, April 1999.

[25] Eel-Hwan Kim; Sung-Bo Oh; Yong-Hyun Kim; Chang-Su Kim, "Power control of a doubly fed induction machine without rotational transducers", Proceedings. PIEMC 2000, Vol. 2 pp: 951 -955.

[26] Hofmann, W.; Okafor, F., "Optimal control of doubly-fed full controlled induction wind generator with high efficiency," IECON 2001,Volume: 2 , pp: 1213 –1218.

[27] F. M. Hughes, O. Anaya-Lara, N. Jenkins, and G. Strbac, "Control of DFIG-based wind generation for power network support," IEEE Trans.Power Syst., vol. 20, no. 4, pp. 1958–1966, Nov. 2005.

[28] S. Bhowmik, R. Spée, Johan H. R. Enslin, "Performance Optimization for Doubly Fed Wind Power Generation Systems", IEEE TRANSACTIONS ON INDUSTRY APPLICATIONS, VOL. 35, NO. 4, JULY/AUGUST 1999

[29] J. M. Carrasco, L. G. Franquelo, J. T. Bialasiewicz, E. Galván, R. C. Portillo Guisado, Ma. Ángeles Martín Prats,J. I. León, N.M.-Alfonso, "Power-Electronic Systems for the Grid Integration of Renewable Energy Sources: A Survey", IEEE TRANSACTIONS ON INDUSTRIAL ELECTRONICS, VOL. 53, NO. 4, AUGUST 2006

[30] M. G. Simões, B. K. Bose and R. J. Spiegel, "Fuzzy Logic BasedIntelligent Control of a variable Speed Cage Machine Wind Generation System," IEEE Transactions on Power Electronics, Vol. 12, Nº.1, pp. 87-95, January 1997.

[31] Clausen, Wood, Recent Advances in Small Wind Turbine Technology Wind Engineering Vol 24, no 3, 2000.

[32] Martins, C.A.; Carvalho, A.S. "Technological trends in induction motor electrical drives" Power Tech   Proceedings, 2001 IEEE Porto, vol.2.

[33] M. A. Abdel-Halim, "Solid-State Control of a Grid Connected Induction Generator", *EPCS 29, pp. 163-178, 2001.*

[34] F. Castelli Dezza, A. Di Gerlando, R. Perrini, "Performance Comparison Among Different Converters Fed by Self Excited Wind Driven Induction Generators, Electrical Machines and Drives", *Proceedings of PowerElectronics and Variable Speed Drives, 11-13 September 1995, Conference Publication No. 412, © IEE, 1995.*

[35] I. Cadirci, M. Ermis, E. Nalcaci, B. Ertan, M. Rahman, "A Solid State Direct On Line Starter for Medium Voltage Induction Motors with Minimized Current and Torque Pulsation", *IEEE Transactions on Energy Conversion,vol. 14, No.3, Sept. 1999.*

[36] R. M. Hilloowala, A. M. Sharaf, "Modelling, Simulation and Analysis of Variable Speed Constant Frequency Wind Energy Conversion Scheme Using Self-Excited Induction Generator", *IEEE 1991.*

[37] S. Wekhande and V. Agarwal, "A new variable speed constant voltage controller for self-excited induction generator," *Electr. Power Syst. Res.,*vol. 59, no. 3, pp. 157–164, 2001.

[38] C. Grantham, F. Rahman, and D. Seyoum, "A regulated self-excited induction generator for use in a remote area power supply," *Int. J. RenewableEnergy Eng.*, vol. 2, no. 1, Apr. 2000.

[39] R. C. Bansal, T. S. Bhatti, and D. P. Kothari, "Induction generator for isolated hybrid power system applications: A review," *J. Inst. Eng.*, vol.83, pp. 262–269, Mar. 2003.

[40] P. K. S. Khan and J. K. Chatterjee, "Three-phase induction generators: A discussion on performance," *Elect. Mach. Power Syst.*, vol. 27, pp.813–832, 1998.

[41] J. M. Peter, "Main future trends for power semiconductors from the state of the art to future trends," presented at the PCIM, Nürnberg, Germany, Jun. 1999, Paper R2 667-671.

[42] Kim,J.S.,& Sul,S.K. (1993). New control scheme for AC-DC-AC converter without DC link electrolytic capacitor. In IEEE power electronics specialists conference. 300-306.

[43] R. Swisher, C. R. de Azua, and J. Clendenin, "Strong winds on the horizon: Wind power comes on age," *Proc. IEEE*, vol. 89, no. 12,pp. 1757–1764, Dec. 2001.

[45] S. Bum-Seok, G. Sinha, M. D. Manjrekar, and T. A. Lipo, "Multilevel power conversion—An overview of topologies and modulations strategies," in *Proc. Int. Conf. Optimization Electr. and Electron. Equipments,OPTIM*, 1998, vol. 2, pp. AD1-1–AD-2.

[46] G. Escobar, J. Leyva-Ramos, J. M. Carrasco, E. Galvan, R. C. Portillo, M. M. Prats, and L. G. Franquelo, "Control of a three level converter used as a synchronous rectifier," in *Proc. IEEE PESC*, Aachen, Germany, 2004, pp. 3458–6464.

[47] ——, "Modeling of a three level converter used as a synchronous rectifier," in *Proc. IEEE PESC*, Aachen, Germany, 2004, pp. 4606–4611.

Chapter 2

Motion sensorless variable speed PMSG control at power grid

Abstract – In this chapter, a rather simple motion –sensorless control strategy for an optimal extraction of output power from grid connected variable speed wind energy conversion is presented. The armature current vector of the PMSG is controlled according to the generator speed in order to maximize the generated power from the wind turbine. The surface mounted PM rotor ($L_d=L_q$) with fractionary windings, low speed PMSG is controlled by the loss-minimization i_q control and the supply-side converter is controlled at unity power factor. The proposed position and speed estimators are described in detail.

2.1 Introduction

Recently, wind generation systems have been attracting great attention as clean and safety renewable power sources. In the wind generation system, the variable-speed generation system is more attractive than the fixed-speed system because of the improvement in wind energy production and the reduction of the flicker problem by the variable-speed generation [1]-[5]. In the variable-speed generation system, the wind turbine can be operated at the maximum power operating point for various wind speeds by adjusting the shaft speed optimally. In order to achieve the maximum power point tracking (MPPT) control, various control schemes has been studied. For example, a search-based or perturbation-based strategy, fuzzy logic control [4] and a wind speed estimation based algorithm [6] have been applied.

In general, permanent magnet technology provides several advantages over conventional solutions. The speed of a permanent magnet motor can be regulated without the need for gears, and very high torque can be achieved at low speeds.

Therefore generators can be smaller, higher output levels can be achieved without the need to increase the size of the generator.

Permanent magnet synchronous motors (PMSMs) are widely used in many applications as high-performance variable-speed drives. There are a few topologies of converters used for variable speed generation: with PMSG connected to three phase rectifier followed by boost converter; in other schemes PWM rectifier is placed between generator and the DC-link and PWM inverter is connected to the grid [1].

The wind energy conversion system presented in this chapter consists of a low speed, fractionary windings PMSG driven by a fixed pitch wind turbine connected through the gearbox with gear ratio 2:1, two back-to-back PWM inverters and a RL filter as is shown in Fig. 2.1. This chapter is organized as follows: section 2.2 and 2.3 presents the mathematical model of wind turbine and the PMSG, section 2.4 discusses the supply-side converter vector control. The proposed rotor position and speed estimation methods are shown in Section 2.5. In Section 2.6, the proposed sensorless control of PMSG is presented and the validity of the proposed method is confirmed through simulations in Section 2.6. The test platform and preliminary results are show in Section 2.7. The conclusions are presented in Section 2.8.
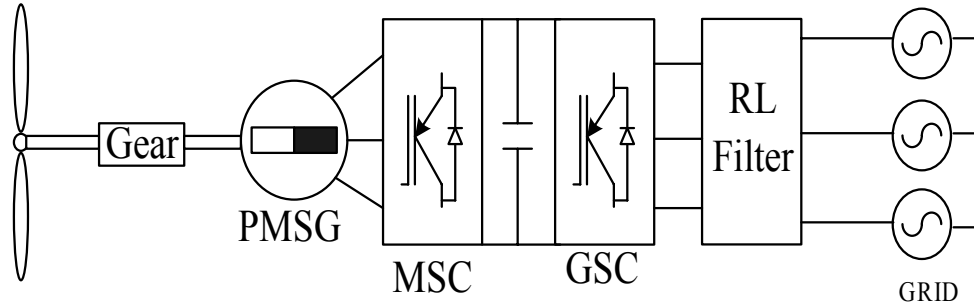
Fig.2.1 Wind energy conversion system

2.2. Mathematical model of wind turbine

A wind turbine is characterized by the non-dimensional curve of coefficient of performance C_p as a function of tip-speed ratio λ, defined as:

$$\lambda = \frac{R_t \omega}{v} \tag{2.1}$$

where R_t - radius of the wind turbine rotor (m)

ω - wind turbine rotor velocity (rps)

v - velocity of the wind (m/s)

For the wind turbine used here, C_p as a function of λ is expressed by the following equation and it is shown in Figure 2.2 It can be noticed that C_p is maximum for $\lambda=3.75$.

$$C_p = 0.0284\lambda + 0.119\lambda^2 - 0.1508\lambda^3 + 0.0679\lambda^4 - 0.0089\lambda^5 \tag{2.2}$$

The output power of the wind turbine may be calculated as:

$$P_t = \frac{1}{2} C_p(\lambda) \rho \pi R_t^2 v^3 \tag{2.3}$$

where ρ is air density (kg/m^3)

The torque developed by the wind turbine can be written as:

$$T_t = \frac{1}{2} \rho \pi R_t^3 \frac{C_p(\lambda)}{\lambda} v^2 \tag{2.4}$$
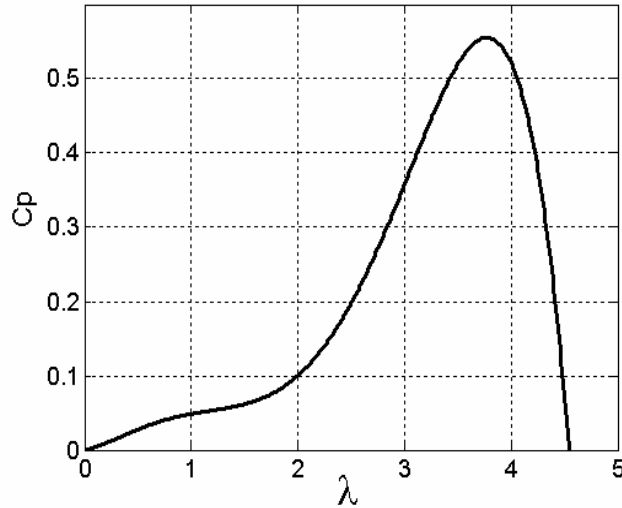
Fig.2.2 C_p versus λ characteristic

For optimum energy extraction, the speed of the turbine should be varied with the wind speed so that the optimum tip-speed ratio is maintained.

Fig.2.3 depicts the characteristics of wind turbine for different wind velocities for the simulated wind turbine.
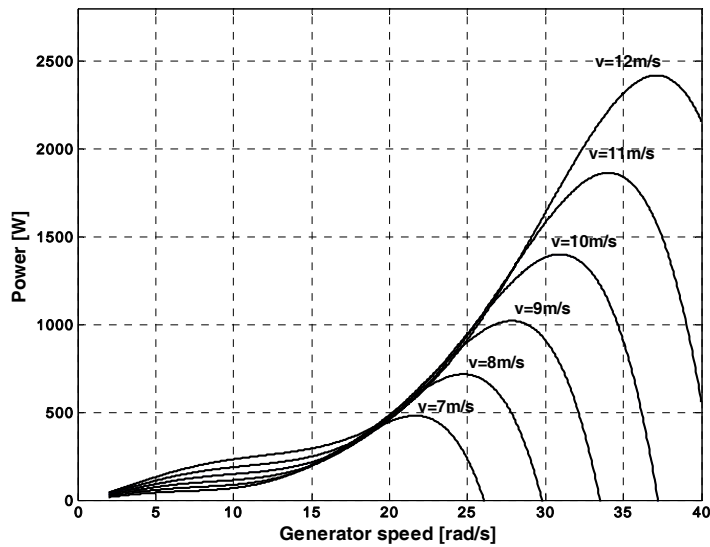

Fig.2.3 Power versus speed characteristics for various wind speeds

2.3. Permanent magnet synchronous generator

The generator is factionary windings, equipped with surface mounted permanent magnets ($L_d=L_q$). Here, since the direction of energy is defined on the basis of an electric motor, all variables are defined as generator variables when negative torque is applied to a permanent magnet synchronous motor (PMSM) is applied. Thus, it is modeled by the following voltage equations in the rotor reference frame (Park's transformation in dq axes)[7]:

$$V_{ds} = R_s i_{ds} + \frac{d\lambda_{ds}}{dt} - \omega_r \lambda_{qs} \tag{2.5}$$

$$V_{qs} = R_s i_{qs} + \frac{d\lambda_{qs}}{dt} + \omega_r \lambda_{ds} \tag{2.6}$$

$$\lambda_{ds} = \Psi_{PM} + L_s i_{ds}, \ \lambda_{qs} = L_s i_{qs} \tag{2.7}$$

where $V_{dqs}, i_{dqs}, \lambda_{dqs}$, are d, q axis voltages, currents and flux linkages respectively.

The electrical angular velocity ω_r, is calculated by:

$$T_e - T_t = \frac{J}{p} \frac{d\omega_r}{dt} \tag{2.8}$$

where J is the combined moment of inertia of generator and the turbine, p is the number of pole pairs, T_t is the mechanical torque of the turbine and T_e the electromagnetic torque, given by:

$$T_e = \frac{3}{2} p \left(\lambda_{ds} i_{qs} - \lambda_{qs} i_{ds} \right) \tag{2.9}$$

For generating $i_{qs}<0$, $V_{ds}>0$ and $V_{qs}>0$.

2.4. Control of supply-side PWM converter

The task of the grid-side converter (GSC) is to keep dc-link voltage constant. A vector-control approach is used, with reference frame orientated along the supply voltage vector position, enabling independent control of the active and reactive power flowing between grid and supply-side converter [9]. The PWM converter is current controlled, with the direct axis current used to regulate Dc-link voltage, meanwhile the quadrature current component used to regulate the power factor.

  The voltage balance for line inductor for three-phase system without a neutral connection (Fig.4) can be written as [10]:

$$\begin{bmatrix} V_{sa}^* \\ V_{sb}^* \\ V_{sc}^* \end{bmatrix} - \begin{bmatrix} V_A \\ V_B \\ V_C \end{bmatrix} = R_f \begin{bmatrix} i_a \\ i_b \\ i_c \end{bmatrix} + L_f \frac{d}{dt} \begin{bmatrix} i_a \\ i_b \\ i_c \end{bmatrix} \tag{2.10}$$

where L_f, R_f are the filter parameters, i_a, i_b, i_c are the phase currents and V_{sa}^*, V_{sb}^*, V_{sc}^* the phase voltages that should be produced by the grid inverter. The

inductor has to be carefully designed because low inductance will result in a high current ripple. A high value of inductance will give a low ripple, but simultaneously will reduce the operation range of the converter.[10]

Those voltages can be calculated using Dc. link voltage and duty cycles as:

$$\begin{bmatrix} V_{sa}^{*} \\ V_{sb}^{*} \\ V_{sc}^{*} \end{bmatrix} = \frac{V_{dc}}{3} \begin{bmatrix} 2 & -1 & -1 \\ -1 & 2 & -1 \\ -1 & -1 & 2 \end{bmatrix} \begin{bmatrix} d_a \\ d_b \\ d_c \end{bmatrix} \tag{2.11}$$

Using complex vector notation, the model for the plant in stationary reference frame is transformed to synchronous reference frame by substituting the "s" operator with "$s\text{-}j\omega_{grid}$" [10]:

$$V_{d1}^{*} - V_d = R_f i_d + L_f \frac{di_d}{dt} - \omega L_f i_q \tag{2.12}$$

$$V_{q1}^{*} - V_q = R_f i_q + L_f \frac{di_q}{dt} + \omega L_f i_d \tag{2.13}$$

The dc voltage controller is a proportional-integral (PI) unit which receives as input the reference V_{dc}^{*} and the measured dc voltage V_{dc}, and output the reference current, I_d^{*}, in synchronous frame.

$$I_d^{*} = (k_{p\_Vdc} + \frac{k_{i\_Vdc}}{s})(V_{dc}^{*} - V_{dc}) \tag{2.14}$$

Controller gains are constant, k_{p_Vdc} = 10 and k_{i_Vdc} = 50, tuned for slow dynamic response, which is desirable in order to avoid interference between the current and voltage controllers. The dc. voltage reference is constant, $V_{dc}^{*} = 700V$.

The current controller is a feedback controller which provides pole zero-cancellation for the R-L plant with decoupling of cross-coupling and feed-forward voltage compensation [10].

$$\underline{V}_{dq}^{*} = (k_p + \frac{k_i}{s})(\underline{I}^{*} - \underline{I}) + j\omega_{grid}L_f\underline{I} + \underline{V}_{dq} \tag{2.15}$$

where $\underline{I} = I_d + jI_q$ is filter current and $\underline{V}_{dq} = V_d + jV_q$ measured grid voltage vector respectively.

A block diagram of the current control loop in synchronous reference frame including the controller (2.15), grid inverter and R_f-L_f plant (2.12, 2.13) is shown in Fig.2.4. The grid-side inverter was modeled as a pure delay of two sample periods.
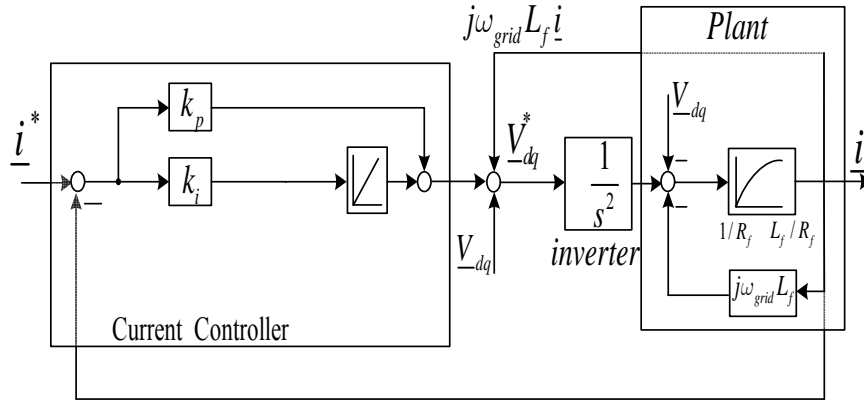
Fig.2.4 Block diagram of the grid current controller

The reference for the current controller is $\underline{I}^* = I_d^* + jI_q^*$. The active reference current,

I_d^* , is the output of the voltage controller while the reactive current, I_q^* , is set to

zero in order to achieve unity power factor. The filter current is measured and then
transformed in synchronous reference frame.

The transfer function of current control loop is:

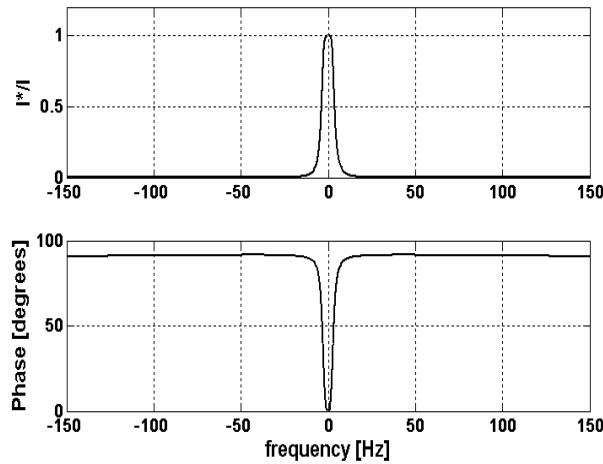$$H_{crt}(s) = \frac{k_p s + k_i}{s^4 L_f + s^3 R_f + k_p s + k_i} \qquad (2.16)$$

Fig.2.5 Frequency response of the current control loop in synchronous reference frame

The frequency response of the current control loop is shown in Fig.2.5 and it was obtained for $k_p=10$ respectively $k_i=2500$.

A PLL observer is used to estimate the phase of the grid voltage vector $\underline{V}_{grid}$ in order to maintain the synchronism of the line inverter voltages. In essence the angle estimation error, $\Delta\theta=\theta_{grid}-\theta$ can be obtained from the imaginary component of the product $Im(\underline{V}_{grid},\underline{V}_1{}^{\#})$ where $\underline{V}_1{}^{\#}$ is unity vector.

$$\underline{V}_{grid} = Ve^{j\theta_{grid}} = V_\beta + jV_\beta, \qquad \underline{V}_1 = e^{j\theta} \tag{2.17}$$

$$\Delta\theta \cong \sin\Delta\theta = Im(\underline{V}_{grid} \cdot \underline{V}_1^{\#})/V = (V_\beta \cos\theta - V_\alpha \sin\theta)/V \tag{2.18}$$

where the superscript $^{\#}$ refers to the vector conjugate operator, θ_{grid} is the grid voltage angle, θ is the inverter voltage angle that is the estimation of θ_{grid} and V is the *rms* value of the grid voltage.

In PLL from Fig. 2.5b, the PI controller output is the inverter frequency ω, which is integrated to obtain the inverter angle θ.

$$\omega_{grid} = (k_p + k_i/s)(V_\beta \cos\theta - V_\alpha \sin\theta)/V \, , \ \theta = \int \omega_{grid} dt \, , \tag{2.19}$$

where $k_p = 7$ and $k_i = 1000$ are the PI controller gains.

The control scheme of the grid-side converter is shown in Fig.2.6.

Fig.2.6 Grid-side inverter control

2.5. Machine side converter control

The configuration of the proposed motion-sensorless control system for PMSG is depicted in Fig.7.The machine- side converter is speed controlled along q-axis. The reference $i^*_{q\_gen}$ (see Fig.7) is obtained from speed control loop as output of PI controller, which has as input the error between the reference speed, ω^*_r, and estimated rotor speed, $\hat{\omega}_r$.

$$i^*_{q\_gen} = (k_{p\_crt} + k_{i\_crt}/s)(\omega^*_r - \hat{\omega}_r) \ k_{p\_crt} = 25 \tag{2.20}$$

where $k_{p\_crt} = 25$, $k_{i\_crt} = 20000$ are the PI gains.

The speed reference is given by:

$$\omega^*_r = \frac{\lambda_{opt} \cdot v_{wind}}{R_t} \tag{2.21}$$

where v_{wind} is the measured wind speed.

In order to avoid power fluctuations caused by wind gusts a first order low pass filter with transfer function $\frac{1}{0.25s+1}$ is used.

The commanded magnetizing current, $i^*_{d\_gen}$ in Fig.2.7, is set to zero to operate at max. torque/ current (typical for surface PM rotors).

The current controllers are implemented in rotor reference frame and produce the reference voltage vector, $\underline{V}_{gen} = V^*_{d\_gen} + jV^*_{q\_gen}$:

$$V^*_{d\_gen} = (k_{p\_crt} + k_{i\_crt}/s)(i^*_{d\_gen} - i_{d\_gen}) + \hat{\omega}_r i_{q\_gen} L_s \tag{2.22}$$

$$V^*_q = (k_{p\_crt} + k_{i\_crt}/s)(i^*_{q\_gen} - i_{q\_gen}) - \hat{\omega}_r(i_{d\_gen} L_s + \lambda_{PM}) \tag{2.23}$$
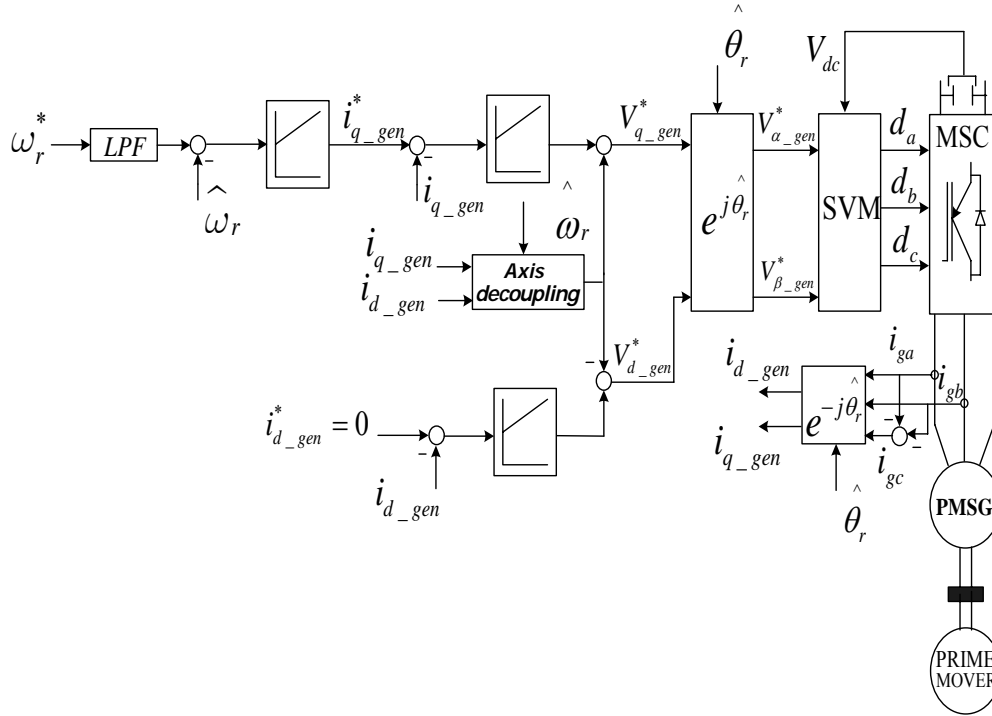
Fig.2.7 Motion sensorless of PMSG

The proposed motion sensorless control algorithm is depicted in Fig.2.8. The stator flux estimator $\underline{\lambda}_s$, based on voltage model in stator reference frame, employs an integrator in close loop with a PI controller to compensate the dc-offset.
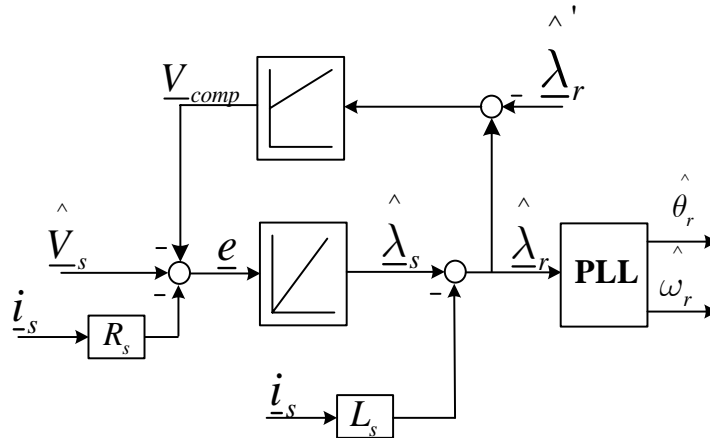

Fig.2.8 Proposed estimation algorithm

The stator flux vector is obtained using the integrator with the corrections from the PI controller to integrate the emf vector $\underline{e}$:

$$\dot{\hat{\underline{\lambda}}}_S = \underline{e} = \int (\hat{\underline{V}}_S - \underline{i}_s R_s - \underline{V}_{comp})dt \qquad (2.24)$$

The stator vector voltage $\underline{V}_s$ is reconstructed from the duty cycles d_a, d_b, d_c of the voltage source-inverter and the measured dc-link voltage V_{dc}:

$$\hat{\underline{V}}_S = V_\alpha + jV_\beta = V_{dc}(2d_a - d_b - d_c)/3 + jV_{dc}(d_b - d_c)/\sqrt{3} \qquad (2.25)$$

The estimated rotor flux $\hat{\underline{\lambda}}_r$ is obtain using $\hat{\underline{\lambda}}_s$ and the measured stator current $\underline{i}_s$:

$$\hat{\underline{\lambda}}_r = \hat{\underline{\lambda}}_s - L_s \underline{i}_s \qquad (2.26)$$

A phase-locked loop (PLL) state-observer (Fig.2.9) extracts the phase of $\hat{\underline{\lambda}}_r$ vector to estimate the rotor position $\hat{\theta}_r$ and speed $\hat{\omega}_r$. The PLL error $\Delta\theta = \theta_r - \hat{\theta}_r$ is obtained from the imaginary part of the vector product $Im(\hat{\underline{\lambda}}_r, \underline{\lambda}_1)$ where:

$$\hat{\underline{\lambda}} = \lambda e^{\cdot} = \hat{\lambda} + j\hat{\lambda} ; \quad \underline{\lambda} = e^{\cdot} = \cos\hat{\theta} - j\sin\hat{\theta} \qquad (2.27)$$

$$\Delta\theta \cong \sin\Delta\theta = Im(\hat{\underline{\lambda}}_r, \underline{\lambda}_1) = \hat{\lambda}_{r\beta}\cos\hat{\theta}_r - \hat{\lambda}_{r\alpha}\sin\hat{\theta}_r \qquad (2.28)$$

In PLL from Fig. 2.9, the PI controller output is the PMSG speed $\hat{\omega}_r$, which is integrated to obtain the rotor position $\hat{\theta}_r$.

$$\hat{\omega}_r = (k_p + k_i/s)\left(\hat{\lambda}_{r\alpha}\cos\hat{\theta}_r - \hat{\lambda}_{r\beta}\sin\hat{\theta}_r\right)/\lambda_{PM} , \quad \hat{\theta}_r = \int \hat{\omega}_r \, dt , \qquad (2.29)$$
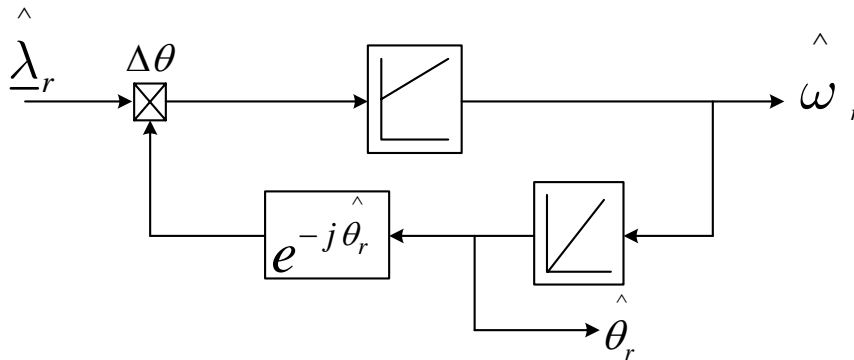

Fig. 2.9 PLL observer for speed and position

The PI controller gains are selected as $k_{p\_PLL} = 20$, $k_{i\_PLL} = 10000$.

The correction term $\underline{V}_{comp}$ is the output of the PI controller which has as input the

error between the estimated rotor flux $\hat{\underline{\lambda}}_r$, obtained from the voltage model and the

rotor flux $\hat{\underline{\lambda}}_r^{'}$ calculated as:

$$\hat{\underline{\lambda}}_r^{'} = \lambda_{r\alpha}^{'} + j\lambda_{r\beta}^{'} = \lambda_{PM}(\cos\hat{\theta}_r + j\sin\hat{\theta}_r) \qquad (2.30)$$

$$\underline{V}_{comp} = V_{\alpha comp} + jV_{\beta comp} = (k_{p\_comp} + \frac{k_{i\_comp}}{s})(\hat{\underline{\lambda}}_r - \hat{\underline{\lambda}}_r^{'}) \qquad (2.31)$$

The PI controller gains are selected as $k_{p\_comp} = 40$, $k_{i\_comp} = 800$.

2.6. Simulation results

The proposed control algorithm was implemented in Matlab/Simulink with the simulation step equal with 100µs.
The PMSG parameters are illustrated in Table I, respectively the R-L filter and wind turbine parameters in Table II, III.

Table I
PMSG parameters

Stator resistance per phase R_s	2.6 Ω
Inductance L_s	0.04 H
Number of pole pairs p	34
Rotor permanent–magnet flux (λ_{PM})	0.2 s·rad^{-1}
Inertia coefficient J	2 kg·m^2

Table II
R-L filter parameters

L_f	0.00125 H
R_f	0.33 Ω

Table III

Air density ρ	1.225 (kg/m^3)
Radius of the wind turbine R_t	1.2 (m)
Gear ratio	2:1

As initial conditions the dc-link voltage across the capacitor is 700 V. The performances of the proposed wind energy conversion system have been investigated under two different wind profiles. The first (Fig.2.10) presents a medium wind speed ramp variation. It can be noticed the tip-speed is maintained at λ_{opt} for steady state.
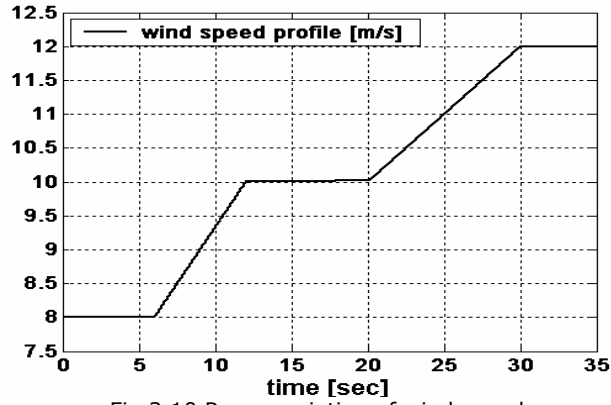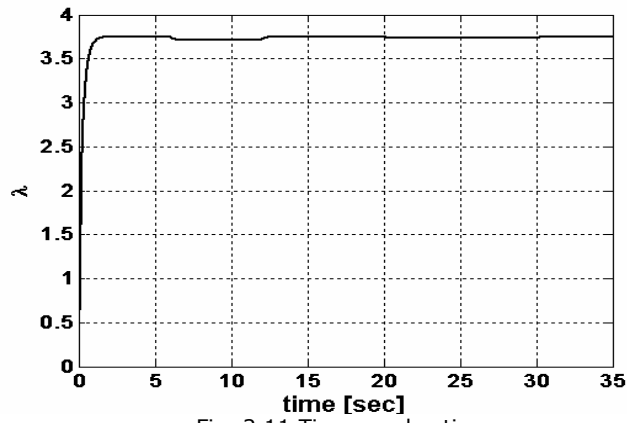
Fig.2.10 Ramp variation of wind speed
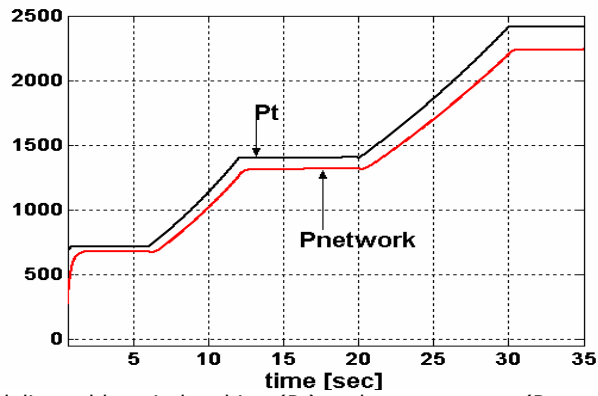

Fig. 2.11 Tip- speed-ratio

Fig. 2.12 Power delivered by wind turbine (Pt) and output power (Pnetwork) for wind speed ramp variation
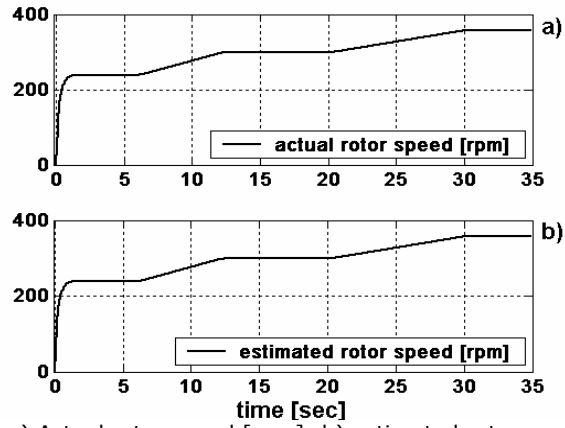
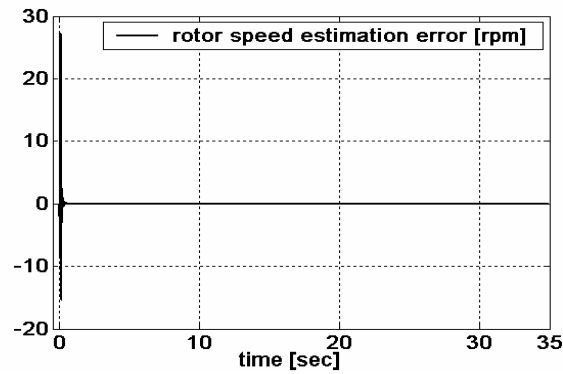Fig. 2.13 a) Actual rotor speed [rpm]; b) estimated rotor speed [rpm]
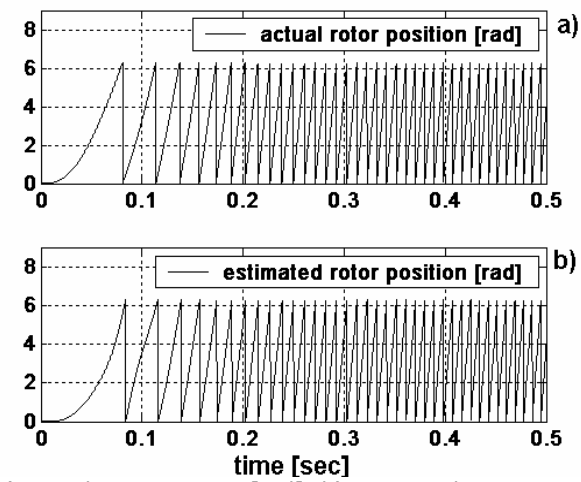

Fig. 2.14 Rotor speed estimation error [rpm]

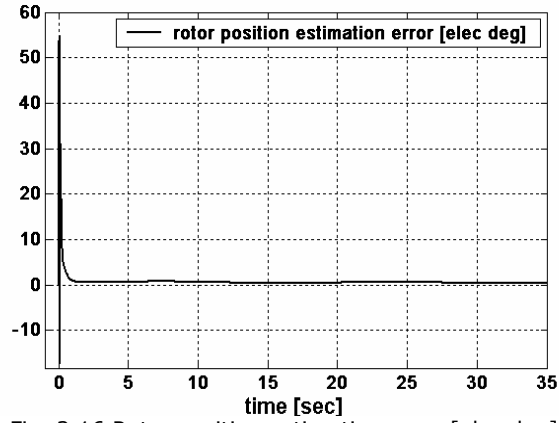Fig. 2.15 a) Actual rotor position [rad]; b) Estimated rotor position [rad]

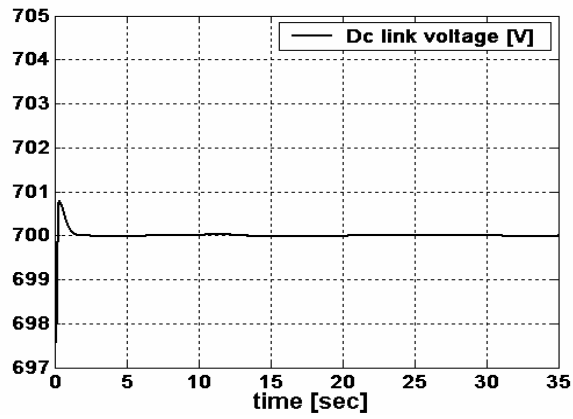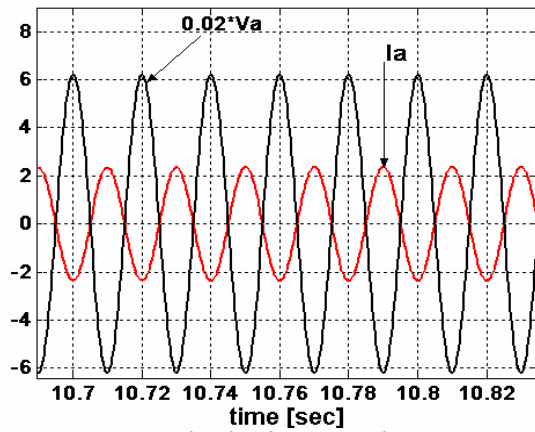Fig. 2.16 Rotor position estimation error [elec deg]

Fig. 2.17 Dc-link voltage [V]

Fig. 2.18 Grid-side phase A and its current

The power extracted by the wind turbine (P_t) and output power delivered in the network ($P_{network}$) are show in fig.2.12. The actual and estimated rotor speed are depicted in Fig.2.13 a, b, respectively the error between those in Fig.2.14. During entire simulation period there is a very close agreement between the estimated and the actual rotor speed, showing a good tracking performance and good estimation results (Fig.2014). The actual and estimated rotor position and the estimation error are shown in Fig.2.15a,b respectively Fig.2.16. The dc-link voltage (Fig.2.17) is kept constant for any wind speed variation. The grid A-phase and its anti-phase current are illustrated in Fig.2.17.
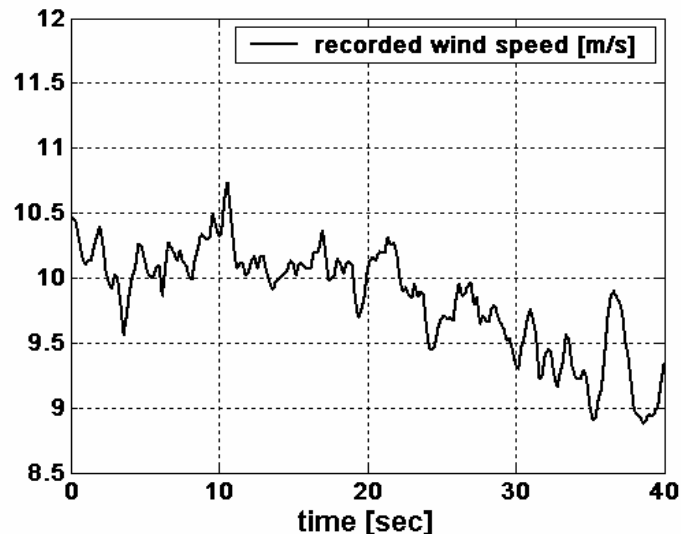

Fig.2.19 Typical wind speed [m/s]

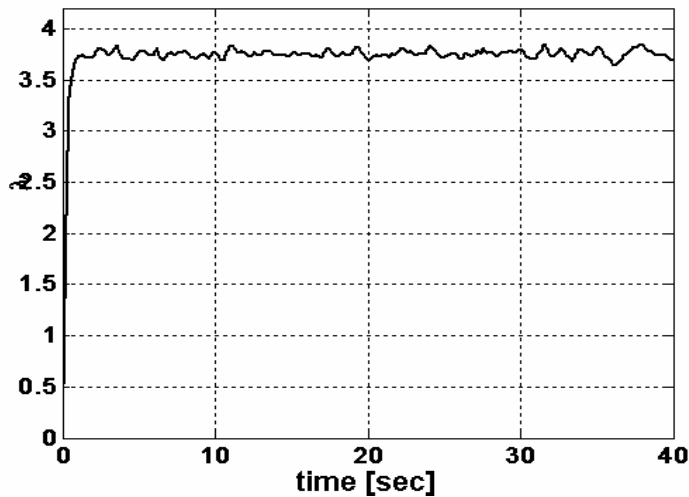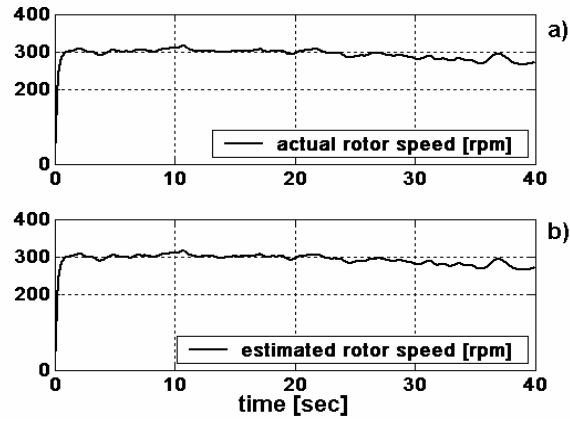Fig.2.20 Tip-speed ratio

Fig.2.21 a) Actual rotor speed [rpm]; b) estimated rotor speed [rpm]
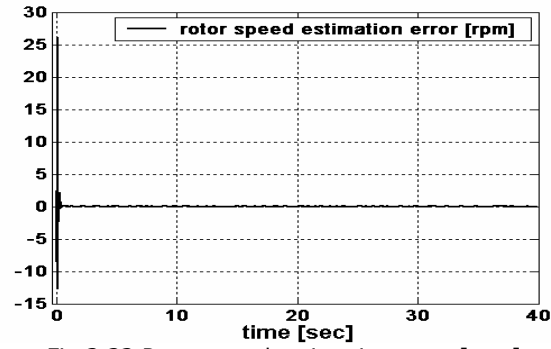

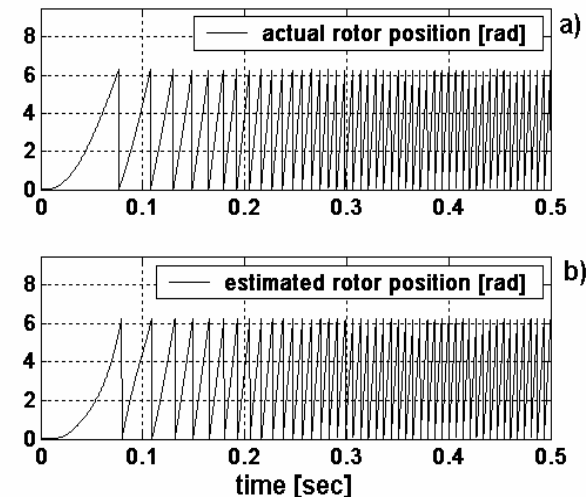Fig.2.22 Rotor speed estimation error [rpm]

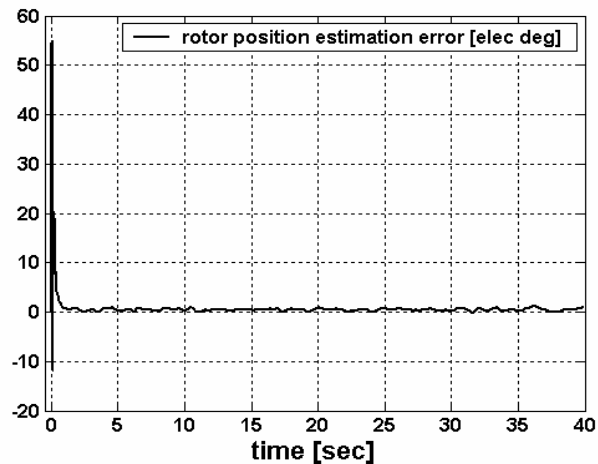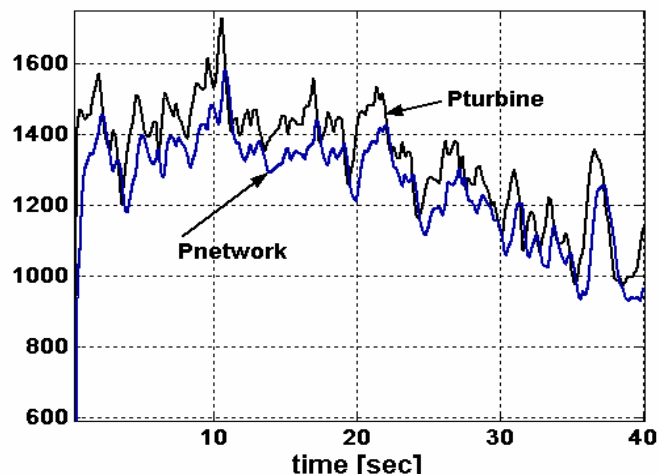Fig.2.23 a) Actual rotor position [rad]; b) estimated rotor position [rad]

Fig.2.24 Rotor position estimation error [elec deg]

Fig.2.25 Power delivered by wind turbine (Pt) and output power ($P_{network}$) for typical wind speed variation

Other simulations were performed for a real wind measured data (Fig.2.19). Again the tip-speed is maintained at $λ_{opt}$ (Fig.2.20). The estimated and actual rotor speed respectively actual and estimated rotor position and the error between them are shown in Fig. 2.21-24. A good tracking performance of speed/ position observer used for motion-sensorless control of PMSG is notable. The power extracted by turbine (P_t) and output power delivered in the network, ($P_{network}$) are illustrated in Fig.2.25.

The cancellations of Dc-offset, the errors of flux –initial positions and variation of machine parameters are investigated.

The DC signal is applied to integrator input $e_{dc} = 0.1\ V$. In Fig. 2.26 shows the estimated rotor flux in two case scenarios; first (Fig.2.26a) represent the estimated rotor flux obtained from ideal integrator without DC offset cancellation. In the second case
(Fig.2.26b) illustrates the estimated rotor with compensation loop and proves the DC- drift cancellation.
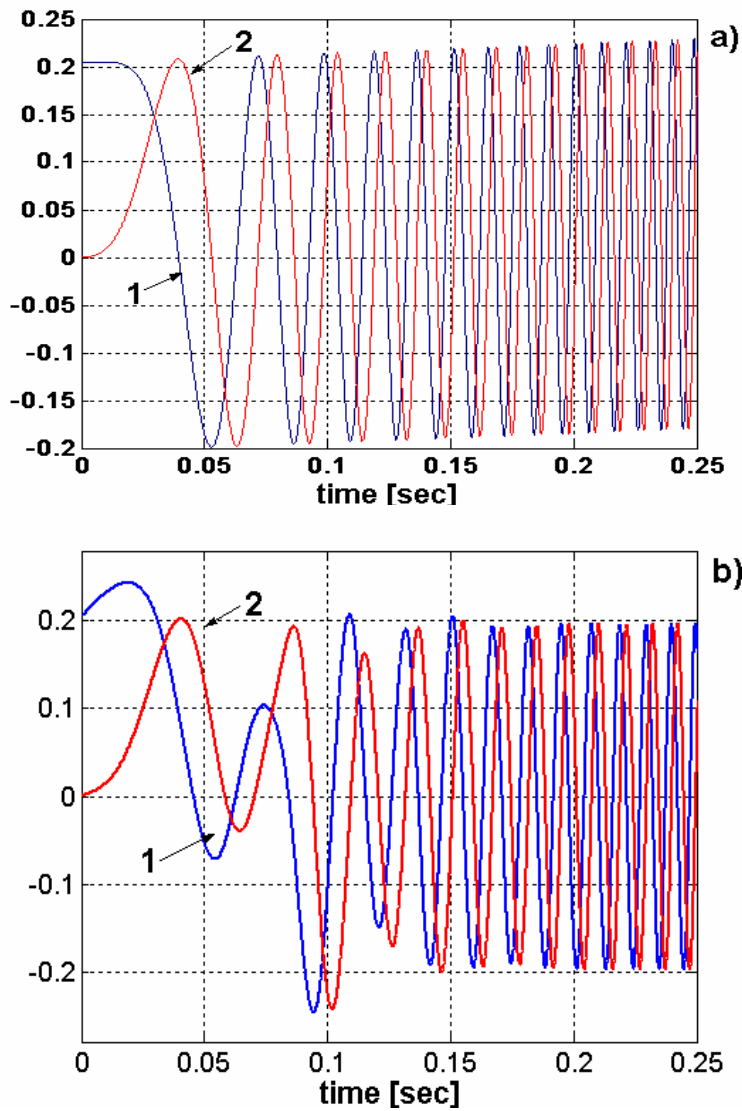

Fig. 2.26 Drift cancellation (1- $\hat{\lambda}_{pm\alpha}$, 2- $\hat{\lambda}_{pm\beta}$); a)ideal integrator ; b) integrator with loop compensation

Fig.2.27 proves the error cancellation of flux-initial position of $\hat{\lambda}_r$ versus ideal integrator.
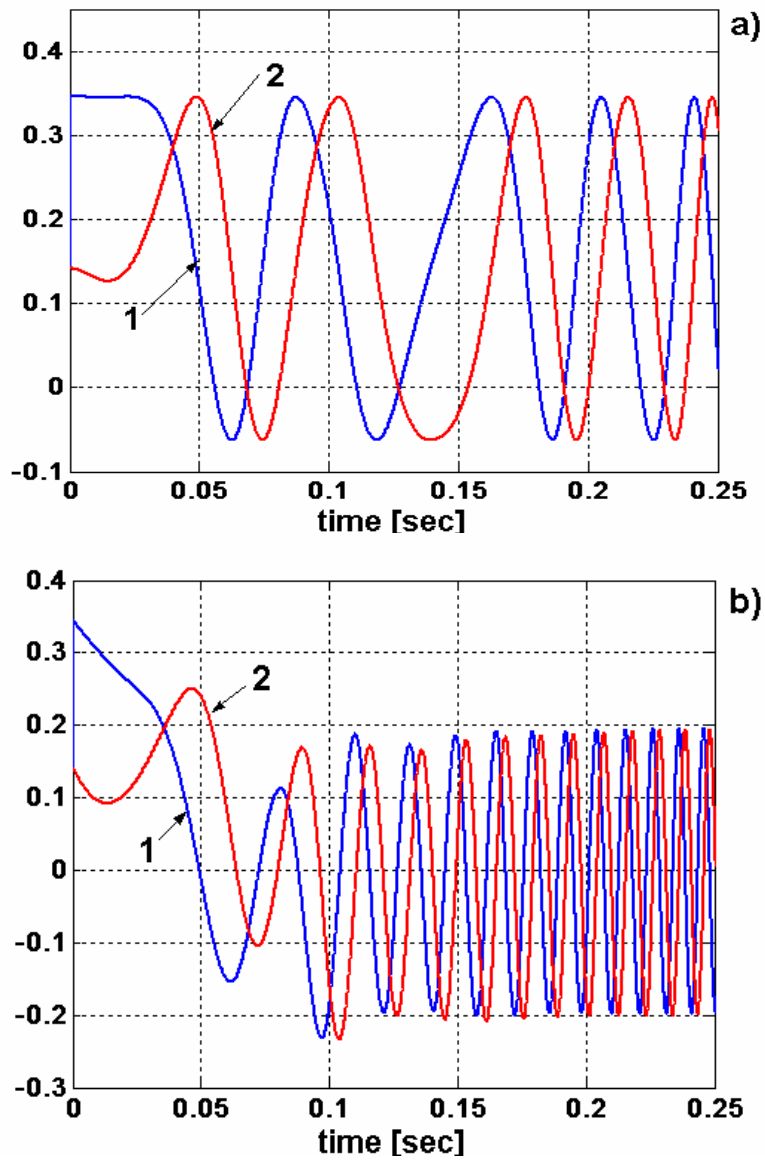

Fig. 2.27 Rotor flux initial position error cancellation (1- $\hat{\lambda}_{pm\alpha}$, 2- $\hat{\lambda}_{pm\beta}$) ;a) ideal integrator; b) integrator with compensation loop
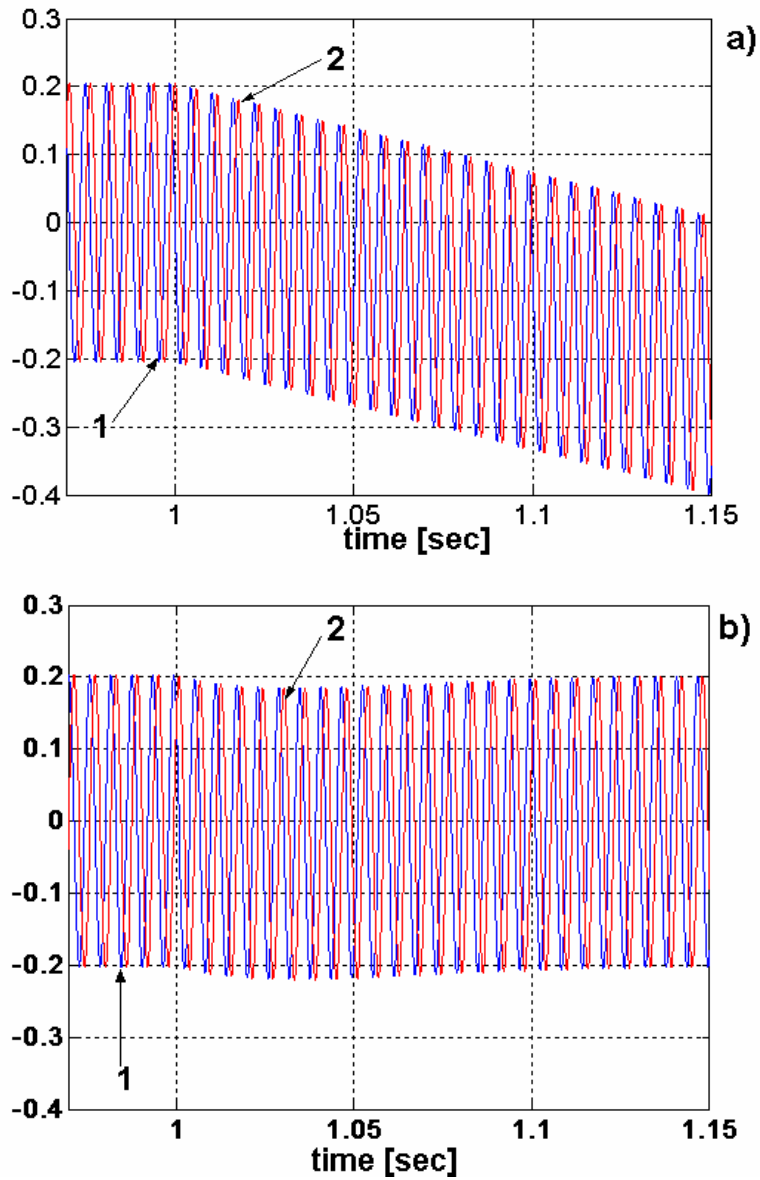
Fig. 2.28 Estimated rotor flux (1- $\hat{\lambda}_{pm\alpha}$, 2- $\hat{\lambda}_{pm\beta}$) for R_s step change a) ideal integrator; b) integrator with compensation loop

An ideal step change from 2.6Ω to 3.9Ω in rotor resistance was simulated at time *t=1s* in Fig. 2.28. It can be noticed that the estimated rotor flux obtained with an

ideal integrator (Fig. 2.28a) goes into saturation while with compensation loop it's kept constant after a short transient period.

2.7. The test platform and preliminary results

The electrical block-diagram of the test platform is shown in Fig. 2.30. For driving the WECS a 10kW/1500 rpm induction motor is used. The motor was supplied from a S_N=25 kVA ABB ACS600 bidirectional inverter. The GSC and MSC in Fig. 2.30 are two VLT 5004, S_N=4.2kVA (Danfoss Drives) inverters. The control and acquisition unit is DS 1103, Dspace GmbH.

Fig. 2.30   Test platform

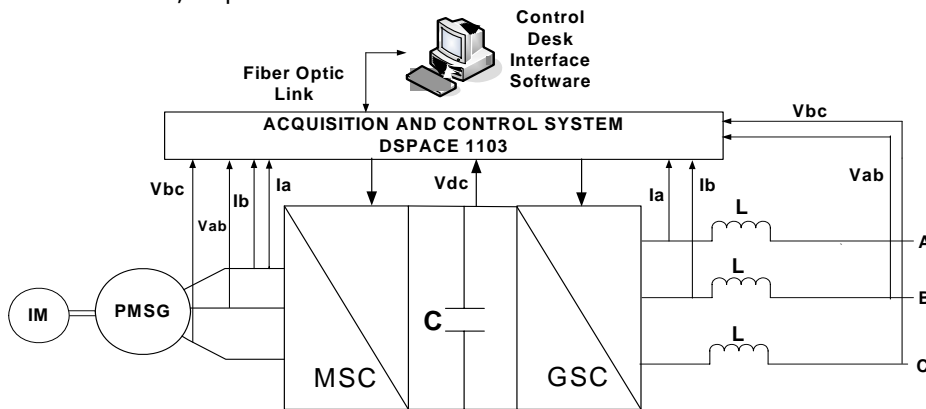For testing the control of the grid-side converter, some experiments have been already carried out. In Fig. 2.31, a few step changes of DC link voltage from 600V to 630V are shown. The reference DC voltage ($V_{dc}*$) and measured DC voltage (V_{dc}) in Fig. 2.31 show fairly good response.
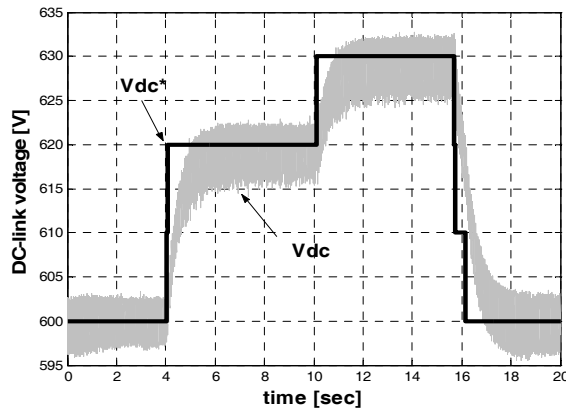

Fig. 2.31 Reference Dc voltage($V_{dc}*$) and measured DC voltage (V_{dc}) for step changes from 600V to 630V

2.8. Conclusion

A variable-speed wind generation system using and low speed, fractionary windings PMSG has been discussed in this paper. A strategy for an optimal extraction of power is presented. The PMSG is driven by the sensorless control strategy and, thus, the mechanical sensors such as rotor speed sensor and position sensor can be eliminated. Simulations confirm that the proposed method gives a good tracking performance for different wind speeds and robust cancellation of the DC-offset, error in flux initial-position and machine parameter variations.

References:

[1] M.Fatu, I.Boldea, C.Lascu, L.Tutelea, G.D.Andreescu, „Motion sensorless variable speed PMSG control at power grid", Proceedings of OPTIM 2006, Braşov, Romania.

[2] D.S.Zinger, E.Muljadi, "Annualized wind energy improvement using variable speed", IEEE Ind. Appl. vol. 33, no. 6, pp. 1444-1447, Nov/Dec. 1997.

[3] P. Bauer, S.W.H. de Hann, C.R. Meyl and J.T.G. Pierik, "Evaluation of electrical systems for offshore windfarms." In Conf. Rec. IEEE-IAS Annu. Meeting. 2000, pp. 1416-1423.

[4] M.G.Simoes, B.K. Bose "Design and performance evaluation of a fuzzy-logic-based variable-speed wind generation system" IEEE Trans. Ind. Appl. vol. 33, no. 4, pp. 956-965, Jul/Aug. 1997.

[5] J. Marques, H.Pinheiro, H.A.Grundling, J.R. Pinheiro, H.L.Hey "A survey on variable-speed wind turbine system"

[6] S.Bhowmik, R.Spee, J.H.R.Enslin, "Performance optimization for doubly fed wind power generation systems", "IEEE Trans. Ind. Appl. vol.35, no.4, pp. p49-958, Jul/Aug. 1999.

[7] D.C. Aliprantis, S.A. Papathanassiou, M.P. Papadopoulus, A.G. Kladas, "Modelling and control of variable-speed wind turbine equipped with permanent synchronous generator", ICEM 2000 28-30 August 2000 Espoo, Finland .

[8] R. Pena, J.C. Clare, G.M. Asher "Doubly fed induction generator using back-to-back PWM converters and its application to variable-speed wind-energy generation", IEE Proc-Electr. Power Appl. Vol. 143, No. 3, May 1996.

[9] M. P. Kazmierkowski, L.Malesani, "Current control techniques for three-phase voltage-source PWM converters: a survey " IEEE Trans. Indust. Electron. 45 691-703, 1998.

[10] F.Briz del Blanco, M.W.Degner, R.D. Lorenz, "Dynamic Analysis of Current Regulators for AC Motors Using Complex Vectors", IEEE TRANS.IND. APPL., VOL. 35, NO. 6, 1999.

Chapter 3

Voltage Sags Ride-Through of Motion Sensorless Controlled PMSG for Wind Turbines

Abstract **–**This chapter describes a variable-speed motion-sensorless permanent magnet synchronous generator (PMSG) control system for wind energy generation. The proposed system contains a PMSG connected to the grid by a back-to-back PWM inverter with bidirectional power flow, a line filter, and a transformer. The control system employs PI current controllers with cross-coupling decoupling for inverters, an active power controller, and a DC link voltage controller. The PMSG rotor speed without using emf integration, and the line voltage frequency are estimated by two PLL based observers. A D-module filter is used to robustly estimate the grid voltage positive-sequence for control in the case of asymmetric voltages. The chapter investigates the ride-through performance of this system during *asymmetric* power grid voltage sags. Design details for various parts of the control system are presented, together with experimental results for single-, two-, and three-phase voltage source sags. Smooth transition through asymmetric voltage sags is demonstrated by all experiments.

3.1 Introduction

Nowadays, fossil fuel is the main energy supplier of the worldwide economy, but the recognition of it as being a major cause of environmental problems makes the mankind to look for alternative resources in power generation. Moreover, the day-by-day increasing demand for energy can create problems for the power distributors, like grid instability and even outages. The necessity of producing more energy combined with the interest in clean technologies yields in an increased development of power distribution systems using renewable energy [1].

Among the renewable energy sources, hydropower and wind energy have the largest utilization nowadays. In countries with hydropower potential, small hydro turbines are used at the distribution level to sustain the utility network in dispersed or remote locations. The wind power potential in many countries around the world has led to a large interest and fast development of wind turbine (WT) technology in the last decade [2] (see Fig.3.1).

A study from European Wind Energy Association [4] estimates that wind is capable of delivering 12% from the electricity consumption by 2020 and in excess of 20% by 2030. According with International Energy Agency in the last decade wind power had one of the highest average annual growth rates among renewable sources [5]. On the same time the wind turbines become in the last decade bigger and bigger and currently single units up to 5 MW are commercially available. Europe seems to lead at this moment the penetration of the wind power into the electrical network, Denmark
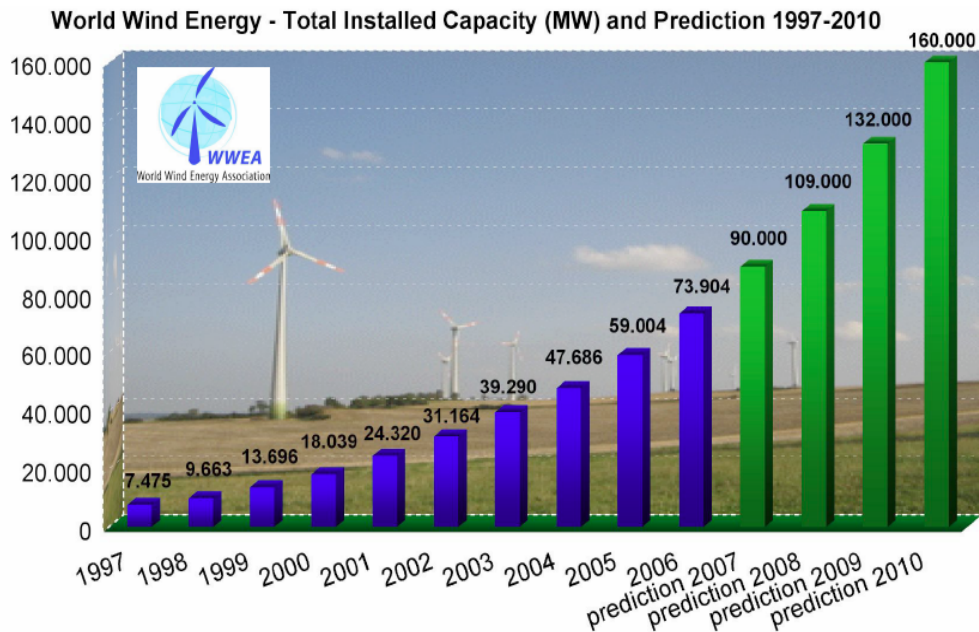
Fig.3.1 Installed capacity worldwide from 1997-2006 and prediction [3]

northern Germany having the highest level of penetration. In 2006 more than 20% from the total electricity consumption in Denmark was provided by the wind power. Spain and Ireland as well as Great Britain will install more wind power in the near future. The future development of wind power is also expected in Canada, Australia and Japan.

However, in order to achieve objectives as continuity and security of the supply a high level of wind power into electrical network implies new challenges as well as new approaches in operation of the power system. Therefore some countries have issued dedicated grid codes for connecting the wind turbines/farms to the electrical network addressed to transmission and/or distributed system. In most of the cases, e.g. Denmark, Germany, Ireland these requirements have focus on power controllability, power quality, and fault ride-through capability. Moreover, some grid codes require grid support during network disturbances e.g. Germany and Spain. Denmark has the most demanding requirements regarding the controllability of the produced power.

Wind farms connected at the transmission level shall act as a conventional power plant providing a wide range of controlling the output power based on Transmission Network Operators demands and also participation in primary and secondary control. The power quality requirements are very demanding in respect with flicker emission as well as the harmonic compatibility levels for voltages especially at Distribution System level comparing with relevant standards. All existing grid codes require fault ride- through capabilities for wind turbines. Voltage profiles are given specifying the depth of the voltage dip and the clearance time as well.

To enable large-scale application of wind energy **without** compromising power system stability, the turbines should stay connected and contribute to the grid in case of a disturbance such **as** a voltage dip, sags. They should similar to conventional power plants supply active and reactive power **for** frequency and voltage recovery, immediately after the fault has been cleared [6].

A number f papers have been published to investigate the dynamic behaviour and protection of DFIG under faults [7, 8]. They demonstrated that over-current and over speed phenomenon of DFIG under voltage sags. A traditional scheme to protect rotor side circuit under voltage sags was to short circuit the rotor circuit the rotor windings with a so called " thyristor crowbar" [9]. The thyristor crowbar is enabled when the rotor current exceeds a certain limit. The crowbar is connected until to the rotor windings until the stator is disconnected from the grid. The crowbar is made of anti-parallel thyristors or diode bridge with thyristor but this method is not suitable for the new grid codes. An active crowbar is full controlled switch utilizing IGBTs [10]. The generator is not tripped any more as the active crowbar can be disabled regaining the control. However high current oscillations occur when the active crowbar is disabled. In [11] the idea was to limit the high rotor current via a set of thyristors controlled by pass resistors. Other protection scheme was proposed in [12]. Here the power rating of the converters have been designed for higher current rating to handle the over-current   of the rotor circuit and to remain connected to the grid without any crowbar action.

The generators are connected to the grid through a voltage source converter (VSCs). Benefits of using VSCs are sinusoidal currents, high current bandwidth, controllable   reactive power to regulate power factor or bus voltage level and minimize resonances between the grid and the converter.

A major drawback when using grid-connected VSCs is their sensitiveness to grid disturbances. This is especially true for variable speed wind turbines, which are often located in rural areas and connected to the grid by long overhead lines, easily subject to faults. Short-duration grid disturbances often result in forced stoppage of the turbine, thus in production losses. In the wide range of power quality disturbances, the interest focuses on voltage dips, which can severely affect the performance of the VSC. A voltage dip is a drop in voltage with duration between one half-cycle and one minute [12], which is in most cases caused by a short-circuit fault. A complete classification of voltage dips has been carried out by Bollen [13].

Most faults result in dips characterized not only by a positive-sequence voltage component, but also by negative- and zero-sequence voltage components. Thus, a controller capable of handling steps in both positive and negative sequence components is needed.

In those conditions the VSCs must ensure fast adaptation to faulty conditions improving the fault tolerance of the wind generation system and avoiding the post fault collapse of the power system because the generators are lost.

Low pass, band stop and notch filters can detect positive and negative sequence in synchronous frame but their response is too slow. An effective detection method for its both steady state and transient performance is delay signal cancellation. The proposed method implies delaying the signal by one fourth of period at the fundamental frequency (5 ms), which constitutes its inherent time delay. Positive and negative sequence components thus obtained are then transformed into the *dqp* and the *dqn*-frame, respectively [14].

When utility frequency is not constant, the usage of phase-locked-loop (PLL) close loop adaptive methods, are indeed the most representative especially implemented in synchronous reference frame [15]. In case the utility voltage is distorted with high-order harmonics, the SRF-PLL can still operate satisfactorily if its bandwidth is reduced in order to reject and cancel out the effect of these harmonics on the output. But under voltage unbalance however, the bandwidth reduction is not an acceptable solution since the overall dynamic performance of the PLL system would become unacceptably deficient [16]. This drawback can be overcome by using a PLL based on the decoupled double synchronous reference frame (DSRF-PLL) [17] or other additional improvements in order to provide a clean synchronization signal [18, 19].

In the DSRF-PLL, a decoupling network permits a proper isolation of the positive- and negative-sequence components. An alternative technique for frequency-adaptive positive sequence detection is presented in [20]. Such technique uses a single-phase enhanced phase-locked loop (EPLL) for each phase of the three-phase system allowing fundamental frequency adaptation. The phase voltages and its respective 90-degree shifted versions detected by the EPLL are used by the ISC method in order to detect the positive-sequence voltages of the three-phase system. Finally, a fourth single phase EPLL is applied to the output of the ISC method to estimate the phase-angle of the positive-sequence voltage.

Another method of synchronization employs the recursive weighted least-squares estimation (WLSE) algorithm [21]. The WLSE-based synchronization method of [21] rejects the impact of negative-sequence and accommodates variations in the frequency. In addition to the threshold and change detection problems, this method exhibits two other shortcomings as: 1) long transient time intervals in detecting frequency changes and 2) the computational problems associated with the LS methods. Moreover, the frequency-varying WLSE-based method is sensitive to noise and distortions [21].

An advanced variable speed permanent magnet synchronous generator (PMSG) connected to the power grid via two back-to-back voltage source PWM inverters with bidirectional power flow, as shown in Fig. 3.2, is typical for distributed generation systems of the future.
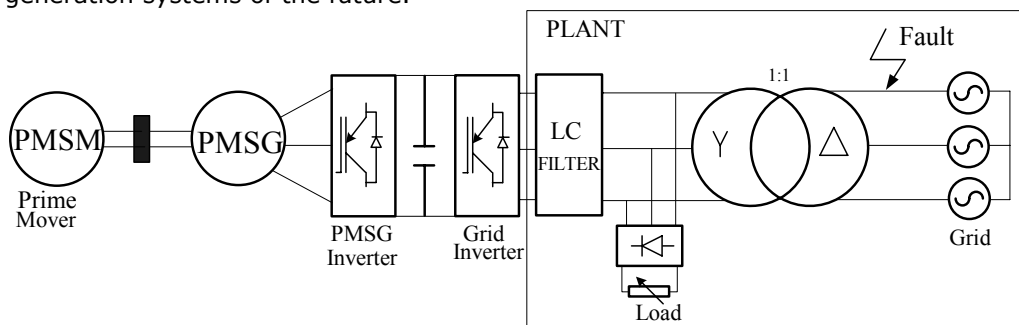

Fig.3.2 Distributed generation system

3.2 WIND TURBINE EMULATOR

The wind turbine mechanical shaft is emulated using a 14.7Nm-3000rpm PMSM driven by a commercial inverter operated in open loop torque control mode. The aerodynamic model of the wind turbine is characterized by a non-dimensional curve that introduces the performance coefficient C_p as a function of blade tip-speed ratio λ defined as:

$$\lambda = R_t \omega / v \tag{3.1}$$

where R_t is the radius of wind turbine rotor (m), ω is the wind turbine rotor velocity (rad/s), and v is the wind velocity (m/s).

For the wind turbine used here, C_p as a function of λ is expressed by the following equation and it is shown in Fig. 3.3.

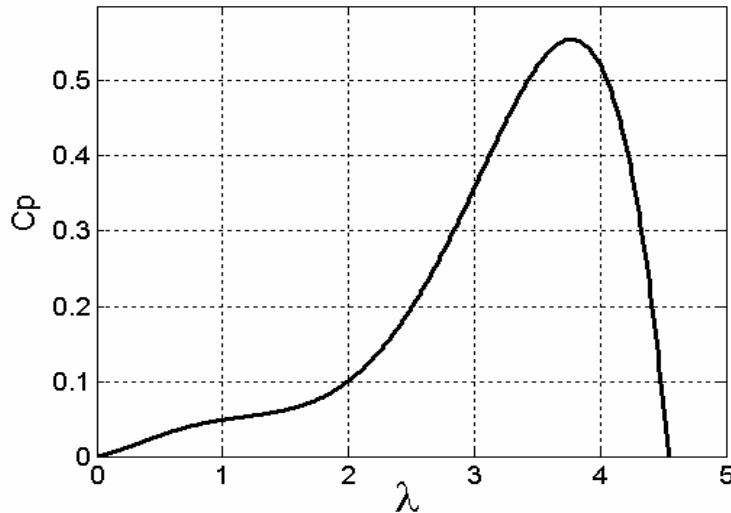$$C_p = 0.0284\lambda + 0.119\lambda^2 - 0.1508\lambda^3 + 0.0679\lambda^4 - 0.0089\lambda^5 \tag{3.2}$$

Fig.3.3 C_p versus λ characteristic of the wind turbine

The output power of the wind turbine is calculated as:

$$P_t = 0.5 C_p(\lambda)\rho\pi R_t^2 v^3 \tag{3.3}$$

where $\rho = 1.225$ kg/m^3 is the air density and $R_t = 1.2$ m. The torque developed by the wind turbine is:

$$T = 0.5\rho\pi R \frac{C(\lambda)}{\lambda} v \tag{3.4}$$

Equation (3.4) is implemented in the PMSM prime mover drive that emulates the wind turbine in the actual experiments.

3.3 PMSG MODEL

The space-vector model of PMSG, equipped with interior permanent magnets, in rotor reference frame (Park's transformation in *dq* axes) [22] is:

$$-\underline{V}_s = \underline{i}_s R_s + \frac{d\underline{\Psi}_s}{dt} + j\omega_r \underline{\Psi}_s \tag{3.5}$$

$$\underline{\Psi}_s = \Psi_d + j\Psi_q = \lambda_{PM} + L_d i_d + jL_q i_q \tag{3.6}$$

where $\underline{V}_s = V_d + jV_q$, $\underline{i}_s = i_d + ji_q$, and $\underline{\Psi}_s$ are the stator voltage, current and flux vectors, respectively, *Rs* is the stator phase resistance, L_d and L_q are the *dq* inductances, λ_{PM} is the PM flux, ω_r is the rotor speed.

3.4 GRID-SIDE INVERTER / FILTER / TRANSFORMER / GRID MODELING

In a typical situation, the distributed generation system is connected through a transformer to local grid. The plant considered in this application, shown in Fig. 3.4, contains the *LC* filter attached to the line-side power inverter, a nonlinear resistive load and the secondary side of the line transformer.

  The circuit shown in Fig. 3.4 uses the following quantities to describe its behavior. The inverter output phase voltages and phase currents are represented by the vectors $\underline{V}_i = [V_{ai} \ V_{bi} \ V_{ci}]$ and $\underline{i}_i = [i_{ai} \ i_{bi} \ i_{ci}]$, respectively. The transformer secondary windings are Y-connected and its phase voltage and current vectors are represented by $\underline{V}_t = [V_{ta} \ V_{tb} \ V_{tc}]$ and $\underline{i}_t = [i_{ta} \ i_{tb} \ i_{tc}]$, respectively. The transformer primary windings are Δ-connected and its line-to-line voltages are represented by $\underline{V}_p = [V_{AB} \ V_{BC} \ V_{CA}]$ and phase voltages by $\underline{V}_{grid} = [V_A \ V_B \ V_C]$.
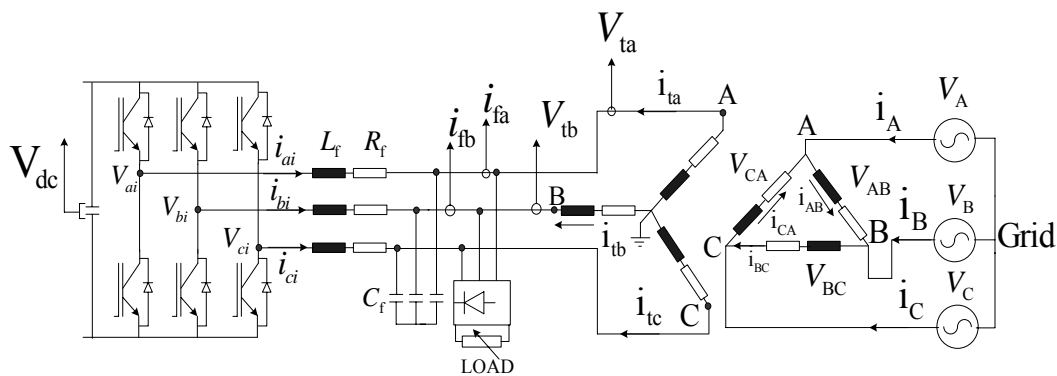

Fig.3.4 Configuration of the grid-side inverter connected through delta-wye transformer to local grid

During the experiments the grid was emulated by a programmable ac three-phase voltage source that cannot receive power, and for this reason the transformer with ac voltage sources are considered as disturbance. Therefore, the single phase

equivalent circuit is presented in Fig. 3.5. The transfer function between the current i_f and the inverter voltage V_i is:

$$H_p(s) = \frac{i_f(s)}{V_i(s)} = \frac{1}{(sL_f + R_f) \cdot (sR_{Load}C_f + 1) + R_{Load}}$$

(3.7)

The filter parameters are: L_f = 0.01 H, R_f = 0.4 Ω, C_f = 0.7 µF, and the resistive load R_{Load} that was set to 80Ω.
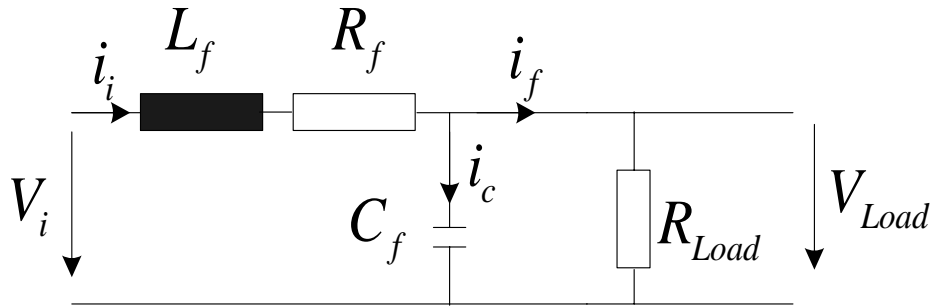

Fig.3.5 Single phase model of the plant

3.5 POSITIVE-SEQUENCE ESTIMATION IN STATIONARY REFERENCE FRAME BY D-MODULE FILTER

The grid voltage-vector position is estimated by means of a PLL observer which has as input the positive voltage sequence obtained from a band-pass filter using D-module filter, as shown in Fig. 3.6a. Vector (two-input/output) filters in D-module, shown in Fig. 3.6 [23], are a class of filters that can separate the positive and negative-sequence frequencies of signals, which is crucial to solve the problem here. In this application, a 2nd order scalar filter with the following transfer function was considered:

$$F(s) = \frac{b_2 s^2 + b_1 s + b_0}{s^2 + a_1 s + a_0}$$

(3.8)

The D-module filter design is based on the following property: if the parameters of the single input-output filter $F(s)$ are designed as low-pass filter (LPF) with an appropriate bandwidth, then the associated vector (two input/output) filter in D-module, $\underline{F}(\underline{D}(s, \omega_c))$ will be a band-pass filter (BPF) with the central frequency ω_c and the same bandwidth.

Define a 2x2 matrix $D(s, \omega_c)$ using a real shift-signal ω_c and the differential operator "s" as [25]:

$$D(s, \omega) = \begin{bmatrix} s & -\omega \\ \omega & s \end{bmatrix} = sI + \omega J$$

(3.9)

where I is identity matrix and J is a skew-symmetric matrix such as:

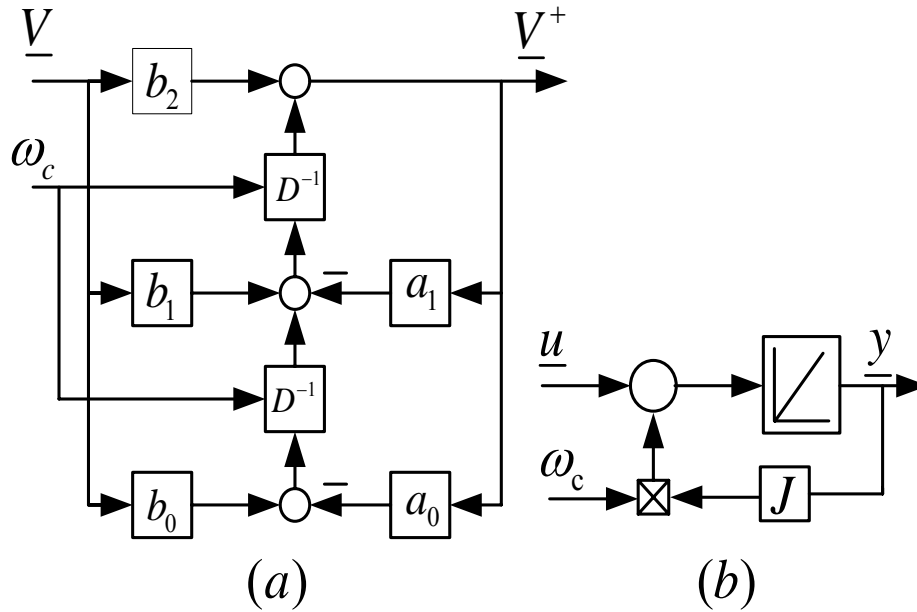$$J = \begin{bmatrix} 0 & -1 \\ 1 & 0 \end{bmatrix} \tag{3.10}$$

Fig. 3.6 a) 2nd order vector BPF $F(D(s,\omega_c))$ with filter in D-module, b) Realization of inverse D-1(s,ω_c) module

The matrix $D(s,\omega)$ and a $2X2$ matrix $diag(s \pm j\omega)$ are similar where j indicates the imaginary part of a complex number [24].

The module filter has the following filtering property [24]:

Let two components of $2X1$ real input $\boldsymbol{u}$ and output $\boldsymbol{y}$ of the module filter be u_α, u_β and y_α, y_β respectively. We can write:

$$\begin{bmatrix} y_\alpha + jy_\beta \\ y_\alpha - jy_\beta \end{bmatrix} = \begin{bmatrix} F(s+j\omega)(u_\alpha + ju_\beta) \\ F(s-j\omega)(u_\alpha - ju_\beta) \end{bmatrix} \tag{3.11}$$

The relation (11) indicates input/output relations of positive and negative phase components in the two –phase signals, respectively that the module filter has different frequency characteristics for the two components, and the filtering characteristics for positive and negative phase components can be dynamically changed by the scalar shift signal ω which can be positive or negative [24].

For this application the focus was mainly on detection of the positive sequence component from grid voltages and the shift signal was selected as $\omega_c = 100\pi$ rad/s. The relation (11) now becomes:

$$V_\alpha^+ + jV_\beta^+ = F(s + j\omega_c)(V_\alpha + V_\beta) \qquad (3.12)$$

where $\underline{V}^+ = V_\alpha^+ + jV_\beta^+$ is the positive sequence voltage vector and $\underline{V} = V_\alpha + jV_\beta$ is the grid voltage vector.

It is known that the filter in the D-module is very robust to distortion of sinusoidal input signals, i.e., it produces almost pure sinusoidal output even for distorted input [24].

The BPF with D-module filter $F(D(s,\omega_c))$, shown in Fig. 3.6a, employs the inverse $\underline{D}^{-1}(s,\omega_c)$ module function with the realization shown in Fig. 3.6b. In the application in Fig. 3.7, $F(s)$ is selected as a 2nd-order LPF with $b_2 = b_1 = 0$ and $b_0 = a_0$. The cut-off frequency is chosen $\omega_0 = 20$ rad/s and the damping factor $\xi = 0.7$. The corresponding BPF parameters are:

$a_0 = \omega_0^2$, $a_1 = 2 \cdot \xi \cdot \omega_0$, with $\omega_c = 2\pi \cdot 50$ rad/s.

Fig. 3.7 shows the response of the proposed calculation method for two phases unbalanced voltage sag. The faulty-phases in the transformer secondary are shown in Fig. 3.7a. The estimated positive and negative sequence phase voltages in the natural *abc* reference frame are depicted in Fig. 3.7b and Fig. 3.7c, respectively. In this case the estimation starts at $t = 1.5$ s, at the same time as the fault occurs, and stops at $t = 1.7$ s, in order to show the estimator transient response. In the real application the estimator works continuously in the background, in order to avoid the startup transients. The plots from Fig. 6 confirm the good behavior of the proposed estimator. The tracking performance of estimated positive and negative-sequence is accurate and smooth.
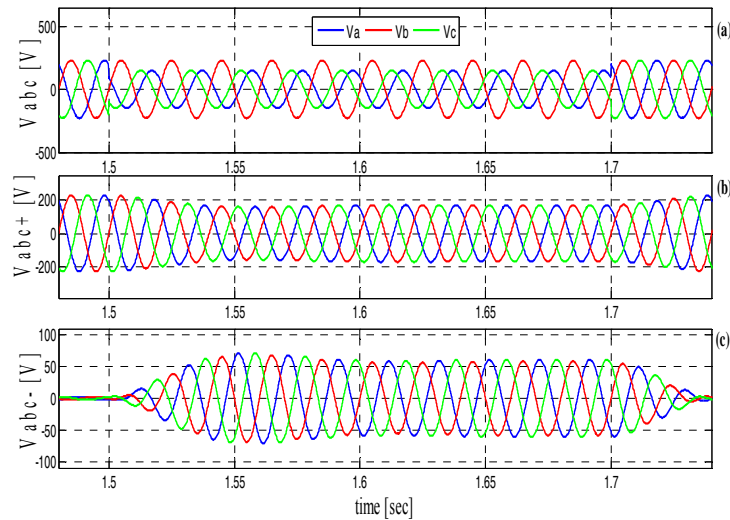

Fig.3.7 a) Two-phase voltage sag in the primary of the transformer, b) Positive-sequence estimation for unbalanced voltage sag, c) Negative-sequence estimation for unbalanced voltage sag

A PLL observer is used to estimate the phase of the positive-sequence grid-voltage vector $\underline{V}^+$, in order to maintain the synchronism of the line inverter voltages. In essence, the angle estimation error $\Delta\theta = \theta_{grid} - \theta$ is obtained from the imaginary component $Im(\underline{V}^+ \cdot \underline{V}_1^\#)$, where $\underline{V}_1$ is a unity vector.

$$\underline{V}^+ = V^+ e^{j\theta_{grid}} = V_\alpha^+ + jV_\beta^+, \qquad \underline{V}_1 = e^{j\theta}, \tag{3.13}$$

$$\Delta\theta \cong sin\,\Delta\theta = Im(\underline{V}^+ \cdot \underline{V}_1^\#)\,/\,V^+ = \left(V_\beta^+ cos\,\theta - V_\alpha^+ sin\,\theta\right)/\,V^+, \tag{3.14}$$

where the superscript $^\#$ refers to the vector conjugate operator, θ_{grid} is the grid voltage angle, and θ is the inverter voltage angle that is the estimation of θ_{grid}.

In PLL from Fig. 3.8b, the PI controller output is the inverter frequency ω, which is integrated to obtain the inverter angle θ.

$$\omega = (k_p + k_i\,/\,s)\left(V_\beta^+ cos\,\theta - V_\alpha^+ sin\,\theta\right)/\,V^+, \; \theta = \int \omega dt, \tag{3.15}$$

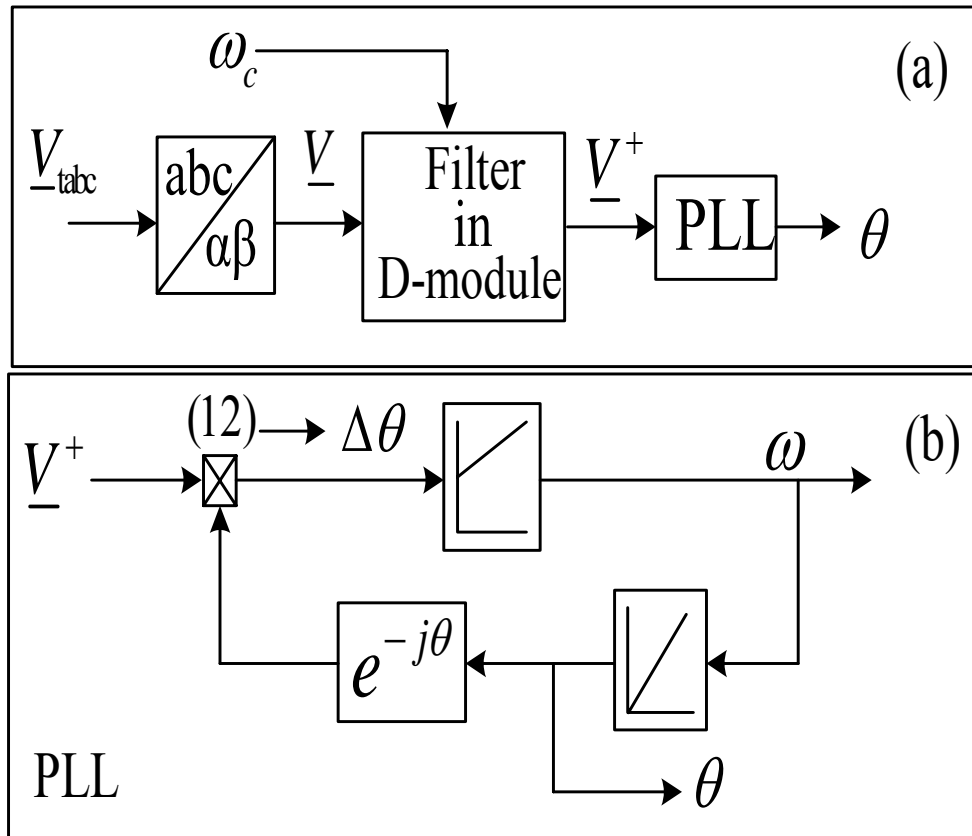where $k_p = 7$ and $k_i = 1000$ are the PI controller gains.

Fig.3.8 a) Extraction of grid voltage positive-sequence, b) PLL observer structure

3.6 GRID-SIDE INVERTER CONTROL SYSTEM DESIGN

The control strategy applied to the grid-side converter consists mainly of two cascaded loops. Usually, there is a fast internal current loop, which regulates the grid current, and an external voltage loop, which controls the dc-link voltage [25]–[28].

In some works, the control of grid-side controller is based on a dc-link voltage loop cascaded with an inner power loop instead of a current loop. In this way, the current injected into the utility network is indirectly controlled [29]. Moreover, control strategies employing an outer power loop and an inner current loop are also reported [30].
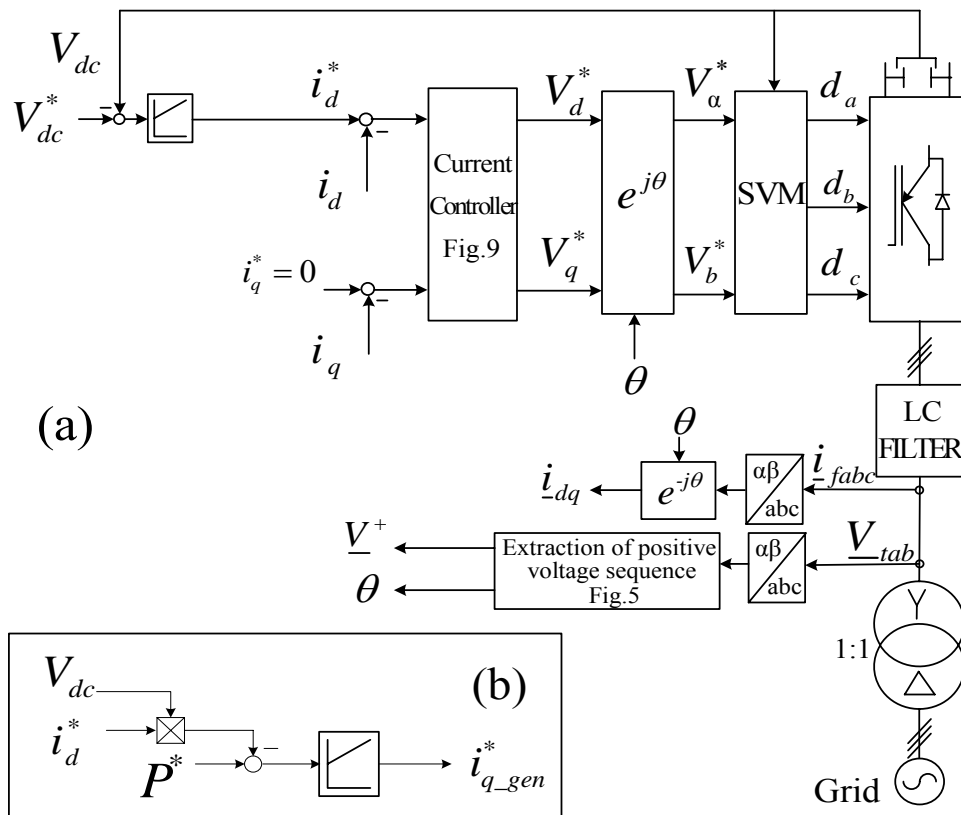
Fig. 3.9 a) Grid-side inverter control, b) Active power control loop

The grid-side inverter is current controlled, with the direct axis aligned to grid-voltage vector, enabling independent control of the active and reactive power.

The control scheme shown in Fig. 3.9a utilizes current control loops for i_d and i_q. The i_d^* demand is derived from the PI regulator of the DC-link voltage V_{dc} (3.14). Meanwhile the i_q^* reference is set to zero in order to achieve unity power factor.

The DC-link controller produces the reference d-axis current:

$$i_d^* = (K_{p\_Vdc} + K_{i\_Vdc} / s)(V_{dc}^* - V_{dc})$$ (3.16)

The PI controller gains are selected as $K_{p\text{-}Vdc}$ = 0.02 and $K_{i\text{-}Vdc}$ = 0.1 for slow dynamic response, to avoid interference between the current and voltage controllers.

The current control scheme is implemented in synchronous reference frame. The *dq* control structure is normally associated with proportional–integral (PI) controllers since they have a satisfactory behavior when regulating dc variables. Since the controlled current has to be in phase with the grid voltage, the phase angle used by the *αβ   dq* transformation module has to be extracted from the grid voltages. As a solution, filtering of the grid voltages and using arctangent function to extract the phase angle can be a possibility [31]–[33]. In addition, the phase-locked loop (PLL) technique [34]–[38] became a state of the art in extracting the phase angle of the grid voltages in the case of distributed generation systems. In order to improve the performance of PI controller cross-coupling decoupling between the *q* and *d* axes and voltage feedforward are usually used [26, 39].

The cross- coupling decoupling synchronous frame PI current regulator approximately moved the plant pole to the location of the controller zero through the use of decoupling. The dual to this methodology is to move the controller zero to the location of the plant pole by modifying the controller structure. The modified form of the synchronous frame PI current regulator which achieves this desired pole zero cancellation is shown in Fig**.** 3.10. This form of the synchronous frame PI current regulator is called the complex vector synchronous frame PI current regulator [40].

The fundamental $\underline{i}_{dq}$ current controller is a complex-coefficient controller with cross-coupling decoupling and with line voltage feedforward compensation [40]:

$$\underline{V}_{dq}^* = (k_p + (k_i + j\omega_c k_p)\frac{1}{s})(\underline{i}_f^* - \underline{i}_f) + \underline{V}_{dq}^+$$ (3.17)

where k_p = 5, k_i = 15000 are the PI controller gains.

The reference current vector for the current controller is $\underline{i}_f^* = i_d^* + ji_q^*$, $\underline{i}_f = i_d + ji_q$ is the grid current vector, and $\underline{V}_{dq}^+ = V_d^+ + jV_q^+$ is the positive-sequence line voltage vector. The block diagram of the current controller and the plant (Fig. 3.5), in fundamental reference frame, is presented in Fig. 3.10.
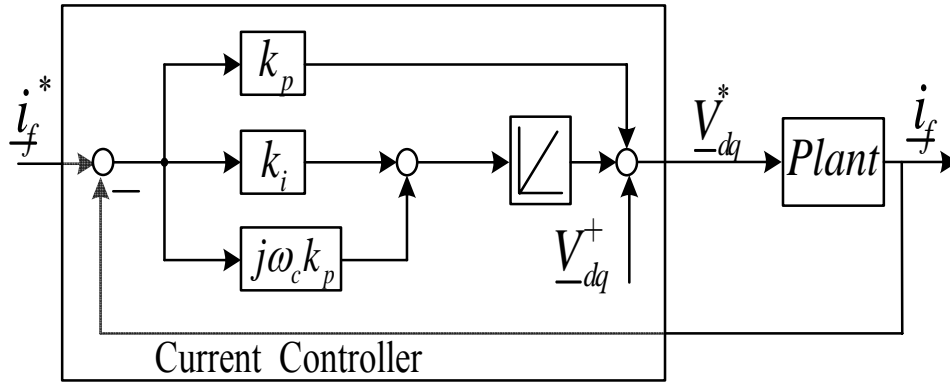
Fig. 3.10 Block diagram of the current loop of the grid-side inverter

Assuming an ideal inverter, with the grid voltage as disturbance, the transfer function of current control loop in stationary reference frame is:

$$H_{crt}(s) = \frac{i_f}{i_f^*} = \frac{k_p s + k_i + j\omega_c k_p}{s^3 k_3 + s^2 k_2 + s k_1 + k_i + j\omega_c k_p} \qquad (3.18)$$

where $k_3 = L_f R_{Load} C_f$, $k_2 = L_f + R_f R_{Load} C_f$, $k_1 = R_{Load} + R_f + k_p$

The frequency response of H_{crt} in stationary reference frame for positive-sequence is shown in Fig. 3.11, on linear scales. The response around 50 Hz is quite good. This is important for smooth transition through voltage sags.
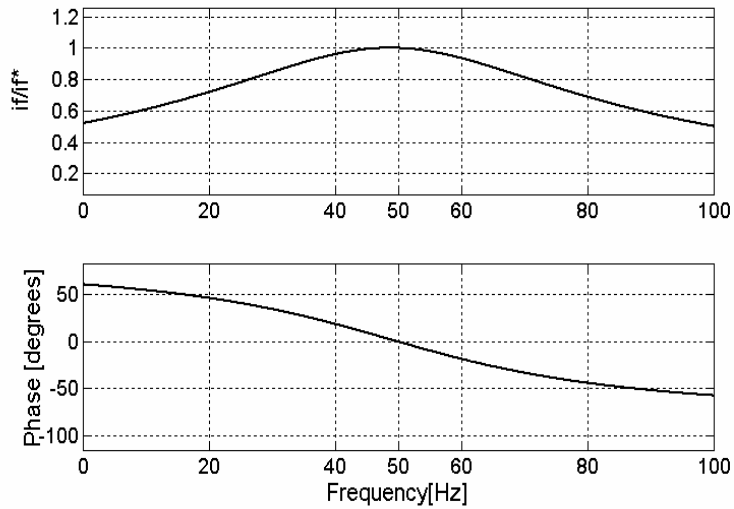
Fig. 3.11 Frequency response of the grid-side inverter current controller

3.7 MOTION-SENSORLESS CONTROL OF PMSG

The configuration of the proposed motion-sensorless PMSG control system is depicted in Fig. 3.12a. The PMSG inverter is power controlled along the q-axis. The reference $i_{q\_gen}^*$ (see Fig. 3.9b) is obtained from the power-control loop as output of a PI controller, which has as input the error between the demanded active power P^* and the active power delivered in the network $V_{dc}i_d^*$.

$$i_{q\_gen}^* = (k_{p\_pow} + k_{i\_pow}/s)(P^* - V_{dc}i_d^*)$$ (3.19)

where $k_{p\_pow} = 0.002$ and $k_{i\_pow} = 0.1$ are the PI gains.

The commanded magnetizing current, i_d^* in Fig. 3.12a, is set to zero to operate at max. torque/ current (typical for surface PM rotors, but acceptable also for small saliency inset PM rotors).

The current controllers are implemented in rotor reference frame, and produce the reference voltage vector, $\underline{V}^* = V_d^* + jV_q^*$:

(a)
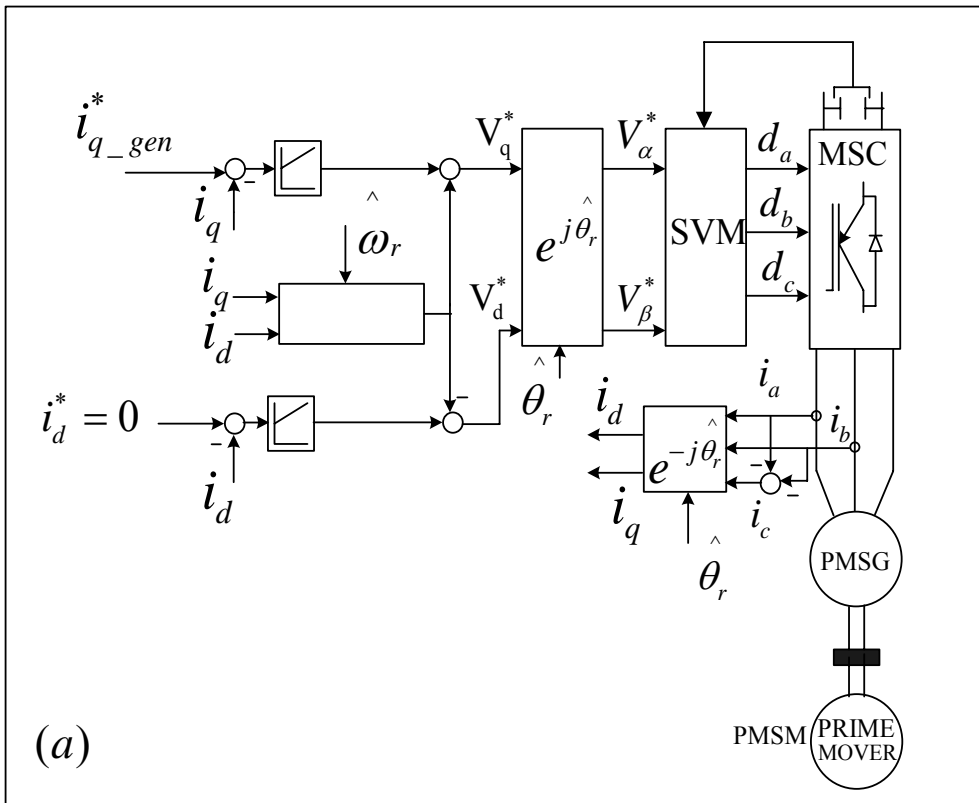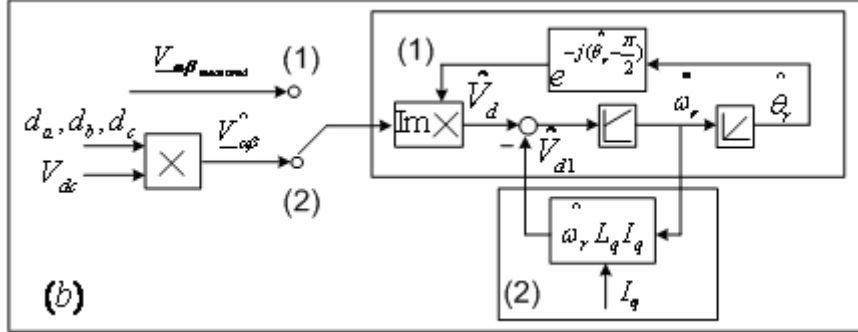
Fig. 3.12 Motion-sensorless control of PMSG: a) current controllers, b) Rotor speed and position estimator

The current controllers are implemented in rotor reference frame, and produce the reference voltage vector $\underline{V}^* = V_d^* + jV_q^*$:

$$V_d^* = (k_{pcrt} + k_{icrt} / s)(i_d^* - i_d) + \hat{\omega}_r i_q L_q ,$$ (3.20)

$$V_q^* = (k_{pcrt} + k_{icrt} / s)(i_{q\_gen}^* - i_q) - \hat{\omega}_r(i_d L_d + \lambda_{PM}) ,$$ (3.21)

Where $k_{pcrt}=25$ and $k_{icrt}=25000$ are the PI controllers gains.

The proposed rotor position $\hat{\theta_r}$ and speed $\hat{\omega_r}$ estimator is depicted in Fig.3.12b. There are two operation regimes [41].

a) The 1st operation regime is for PMSG at startup and low speed, no loading ($\underline{i}_s = 0$). From (3.5)-(3.6), θ_r is obtained from the position angle of the stator voltage vector θ_v :

$$\underline{V}_s = -j\omega_r \lambda_{PM}, \quad V_d = 0, \quad \theta_v = \theta_r - \pi / 2 .$$ (3.22)

A PLL state observer extracts the rotor position and speed estimations from the measured stator voltage vector $\underline{V}_{\alpha\beta}$. The PLL error $\Delta\theta = \theta_r - \hat{\theta_r}$ is obtained from the imaginary part of the vector product in (3.23), where V_s is the stator voltage vector amplitude. Finally $\Delta\theta$ is given by (3.22). The PLL goal is to lead $\Delta\theta$ to zero, i.e., equivalent to lead V_d to zero (3.22).

$$\Delta\theta \cdot V_s \approx Im[\underline{V}_{\alpha\beta}e^{-j(\hat{\theta}r-\pi / 2)}], \quad \Delta\theta = \theta_r - \hat{\theta}_r ,$$ (3.23)

$$\Delta\theta \cdot V_s \approx V_\alpha \cos \hat{\theta}_r + V_\beta \sin \hat{\theta}_r = \hat{V}_d .$$ (3.24)

Note that the initial position is not needed, and the estimation is robust to PMSG parameter variations, i.e., the position error is independent of them. The PI controller gains are selected as $k_{p\_est}=0.5$ and $k_{i\_est}=100$. This estimation is used only to prepare the initial rotor speed/ position used in the next regime.

b) The 2nd operation regime is for PMSG with load, imposing the condition that $i_d = 0$. From (3.5)-(3.6) the d axis stator voltage estimated component $\hat{V_{d1}}$ is

$$\hat{V}_{d1} = \hat{\omega}_r L_q i_q .$$ (3.25)

Now, a correction is used in PLL, based on the two expressions of V_d: $\hat{V_d}$ (3.24) and $\hat{V_{d1}}$ (3.25), that implements an internal minor control loop shown at the bottom side of the Fig. 3.12b. This is equivalent to a model reference adaptive system

(MRAS), with the reference $V_d\hat{}$ (3.24), and the adaptive model $V_{d1}\hat{}$ (3.25). The MRAS goal is to lead the V_d error to zero using a PI controller:

$$\hat{\omega}_r = (k_{p\_est} + k_{i\_est} / s)\left(\hat{V}_d - \hat{V}_{d1}\right) \tag{3.26}$$

The stator vector voltage $\underline{V}_{\alpha\beta}$ can be reconstructed from the duty cycles d_a, d_b, d_c of the PMSG voltage source-inverter and the measured Dc-link voltage V_{dc}:

$$\underline{V}_{\alpha\beta} = V_{dc}(2d_a - d_b - d_c)/3 + jV_{dc}(d_b - d_c)/\sqrt{3} \tag{3.27}$$

The new estimator is robust to PMSG parameters variation, depending only on L_q (3.25). This estimator is really suitable for PMSG sensorless control in wind turbines applications.

3.8 TEST PLATFORM AND EXPERIMENTAL RESULTS

The electrical-block diagram of the experimental test platform is shown in Fig. 3.13. The test setup consists in a 12 Nm PMSG connected to the grid by two back-to-back Danfoss VLT 5005 voltage source inverters, and mechanically driven by a PMSM prime mover with SIMOVERT MASTERDRIVE.

The grid is here replaced by a programmable three phase ac power source (California Instruments 5005), capable to create voltage faults. Since the ac power source cannot receive power, a resistive local load has been connected to the system.
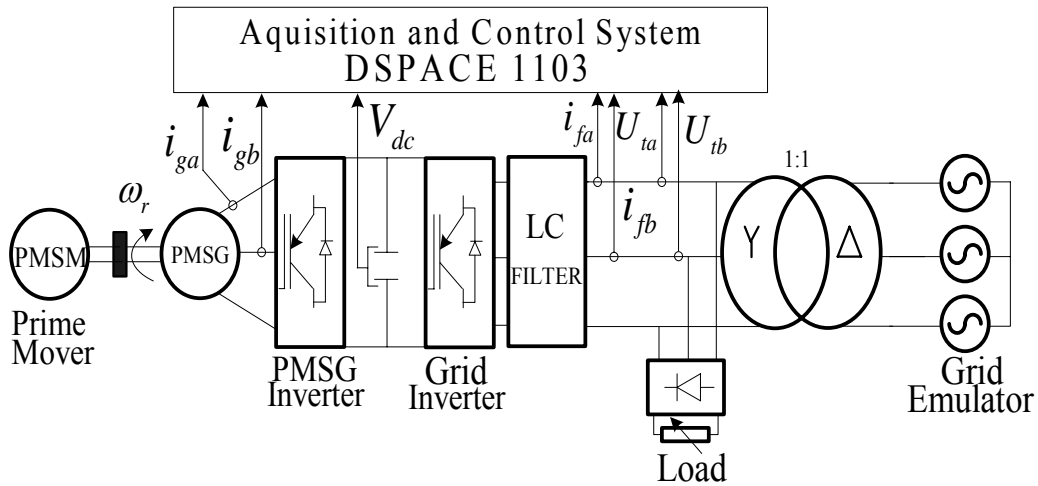
Fig.3.13 Experimental test platform

The control structure is implemented in a DSpace 1103 system. The sampling and switching frequency is set to 9 kHz.

The PMSG parameters are presented in Table I.

Table I
PMSG Parameters

Number of pole pairs (p)	3
Rated power	2.2 kW
Rated speed	1750 rpm
Rated frequency	87.5 Hz
Rated torque	12 Nm
Rated phase to phase voltage	380 V(rms)
Rated phase current	4.1 A(rms)
Stator resistance per phase (R_s)	3.3 Ω
d-axis inductance (L_d)	41.59 mH
q-axis inductance (L_q)	57.06 mH
Rotor permanent–magnet flux λ_{PM})	0.4832 V s rad-1
Inertia of the rotating system (J)	10.07_*10^{-3} kgm^2
Viscous friction coefficient (B)	20.44_*10^{-4} Nms/rad

3.9 Experimental results

The performance of the proposed control system has been investigated in three cases of grid faults: single-phase, two-phase, respectively three-phase symmetrical voltage sags.

A) Single-Phase Voltage Sag

The ac power source was programmed to perform single-phase voltage sag from $230V_{RMS}$ to $120V_{RMS}$, from 5.2s – 5.7s in the primary side of the transformer. The voltages in the secondary side of the transformer are shown in Fig. 3.14. The faulty phase and its current are presented in Fig. 3.15. The Dc-link voltage reference was set to 600V (Fig. 3.16) and during the transient the voltage controller is capable to maintain the reference value within 6% variation. The estimated and measured rotor speeds are shown in Fig. 3.17a, and the error between those two in Fig. 3.17b. It can be noticed that during the transient the speed observer shows fairly good response. The PMSG phase A current is presented in Fig. 3.18a, and the reference and measured q-axis current in Fig. 3.18b. There are no significant transients during the fault. However, the grid currents during the fault exhibit quite large transients as expected and visible in Fig. 3.19.
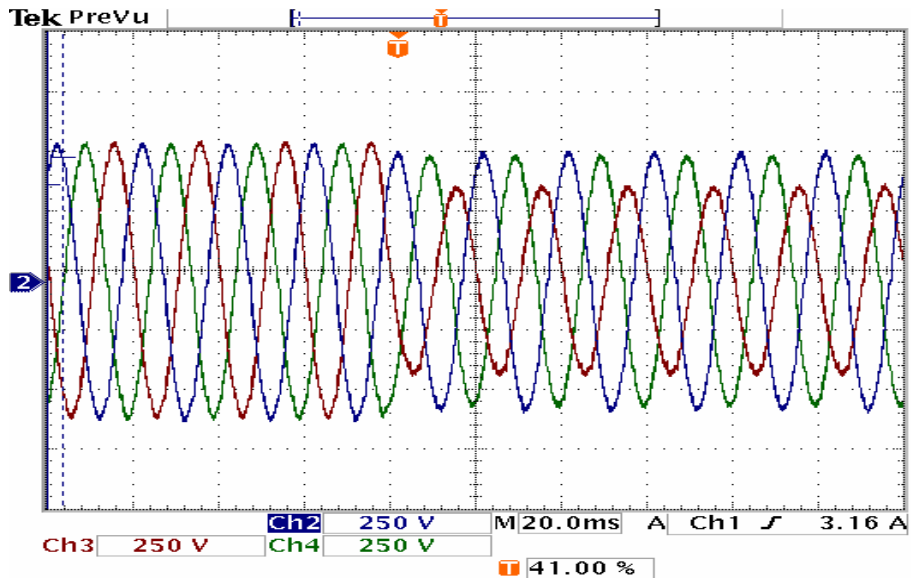
Fig. 3.14 Grid voltages after transformer with single-phase voltage sag (250V/div)
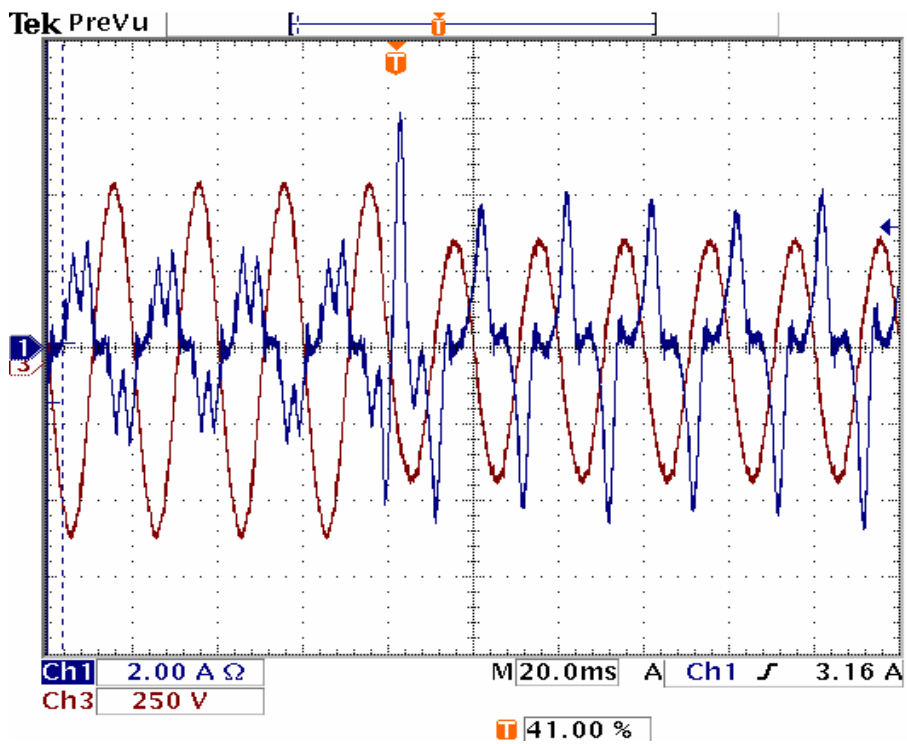

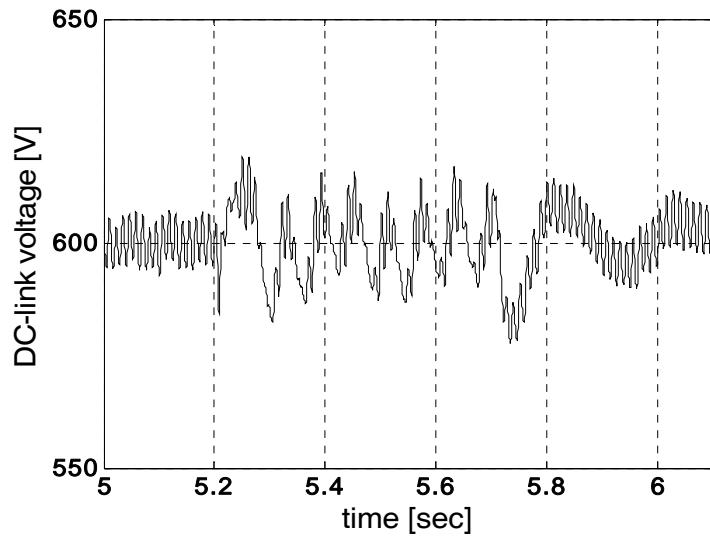Fig. 3.15 Grid-side phase voltage and current (250V/div,5A/div)

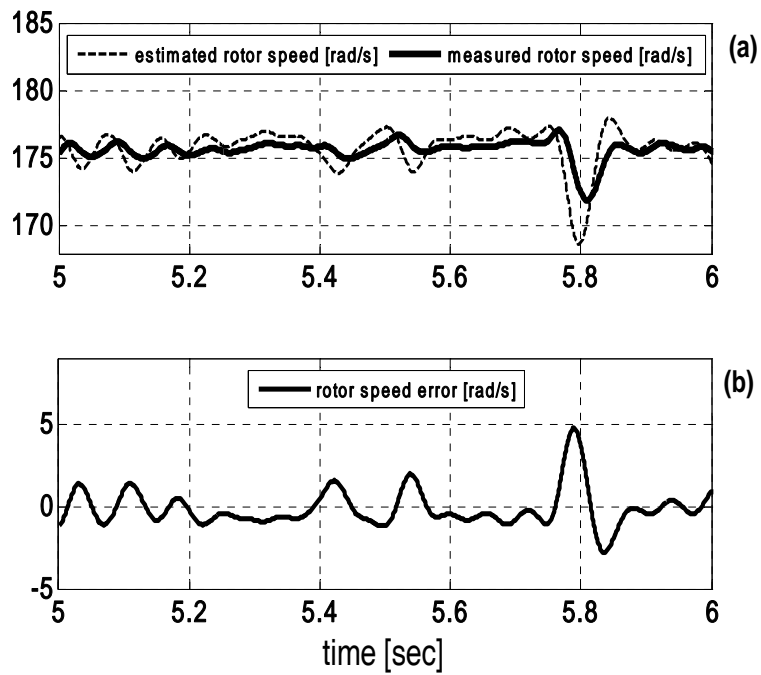Fig. 3.16 Dc-link voltage during single-phase voltage sag

Fig. 3.17 a) Estimated and measured rotor speed, b) Rotor speed error [rad/s]
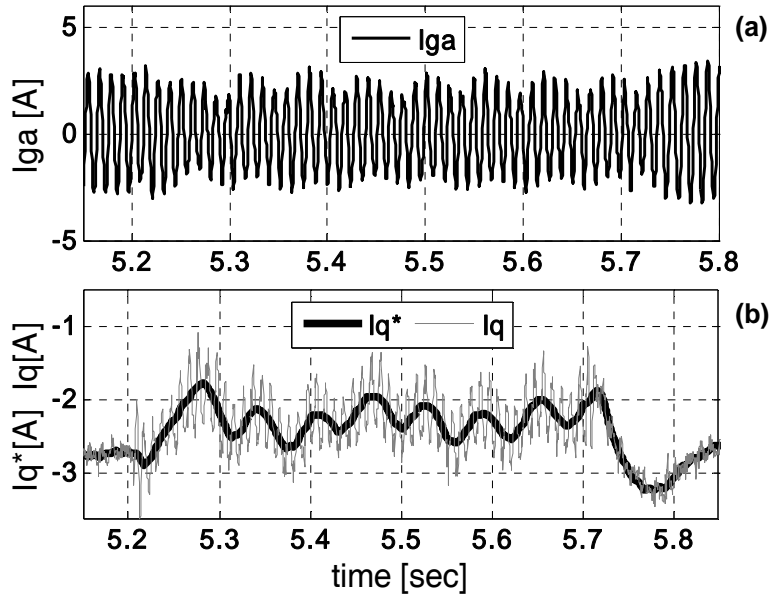
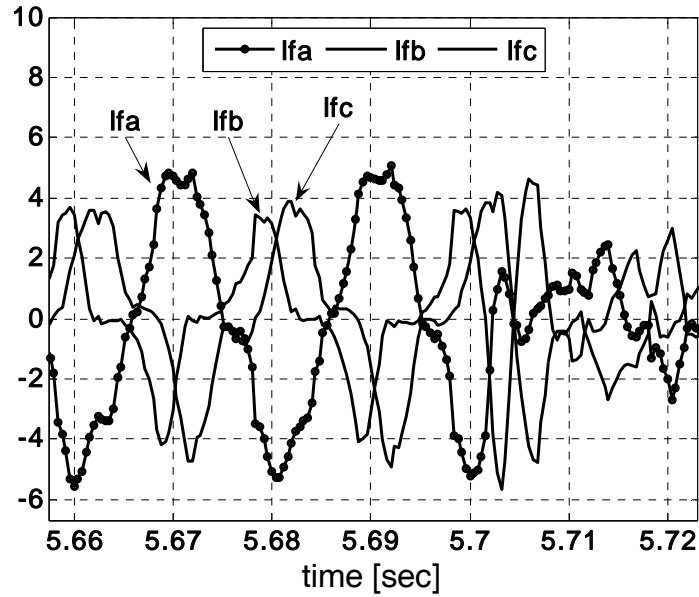Fig. 3.18 a) PMSG phase current, b) PMSG q-axis reference and measured current

Fig.3.19 Grid currents during the fault

B) Two-Phase Voltage Sag

The ac programmable source was then set to perform two-phase voltage sag from $230V_{RMS}$ to $110V_{RMS}$, from 9.4s – 9.9s in the primary side of transformer. The voltage waveforms in the secondary side of transformer in this situation are illustrated in Fig.3.20. One of the faulty phases and its current are shown in Fig. 3.21. It may be noticed that at the end of the fault the system recovers rapidly in one cycle. The DC-link voltage (Fig. 3.22) is maintained at 600V during the transients. The estimated and measured rotor speed and the estimation error are shown in Fig. 3.23. A close agreement between estimated and actual rotor position is evident certifying a good tracking performance and good estimation results. The PMSG phase A current, respectively the reference and measured PMSG q-axis current are illustrated in Fig. 3.24. The PMSG currents show only small transients during the fault.

The grid currents, shown in Fig. 3.25, present at fault starting transients as large twice their steady-state condition but quickly recover (without any transient) after the fault clearance.
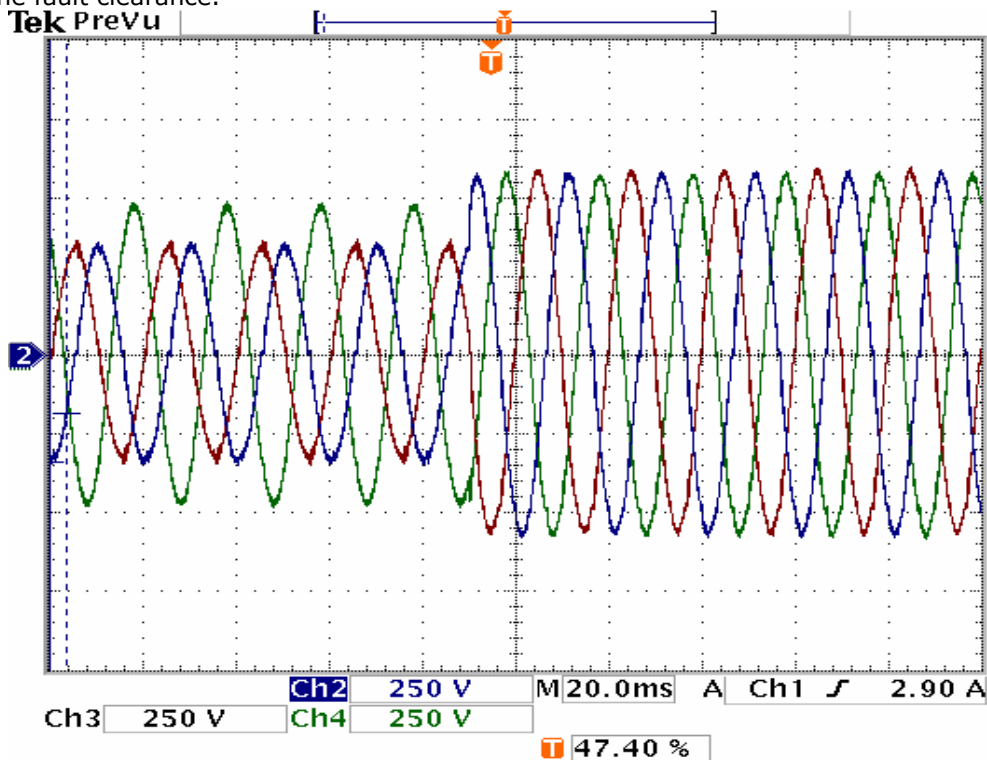

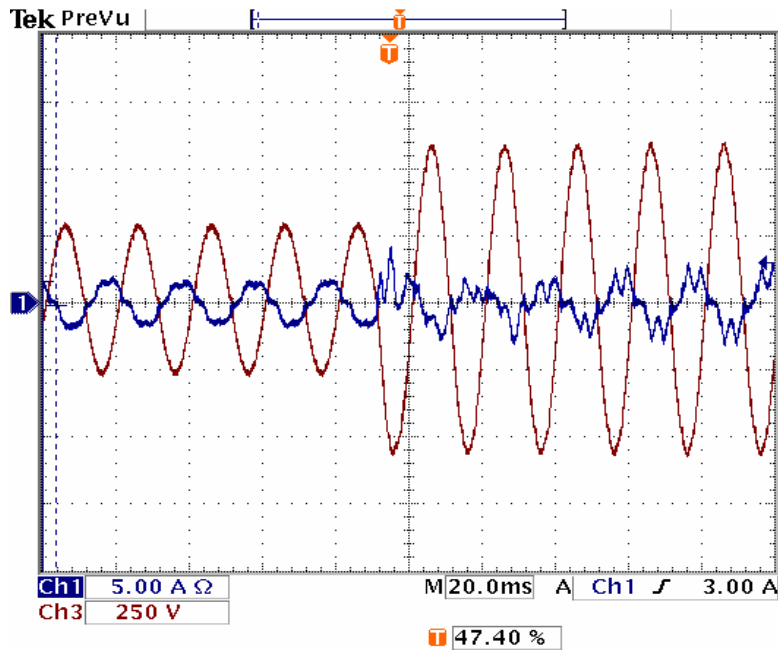Fig.3.20 Grid voltages after transformer (250V/div) with two-phase voltage sag

Fig. 3.21 Grid-side phase voltage and current (250V/div,5A/div)
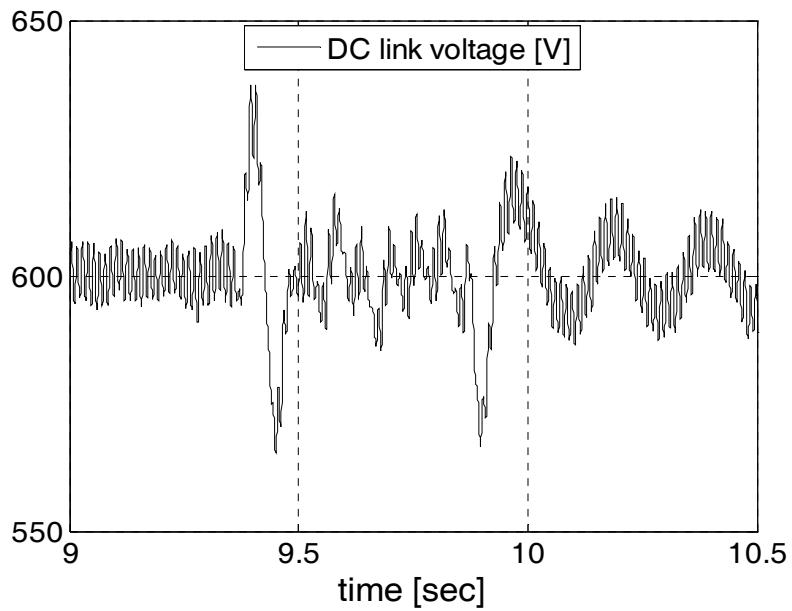

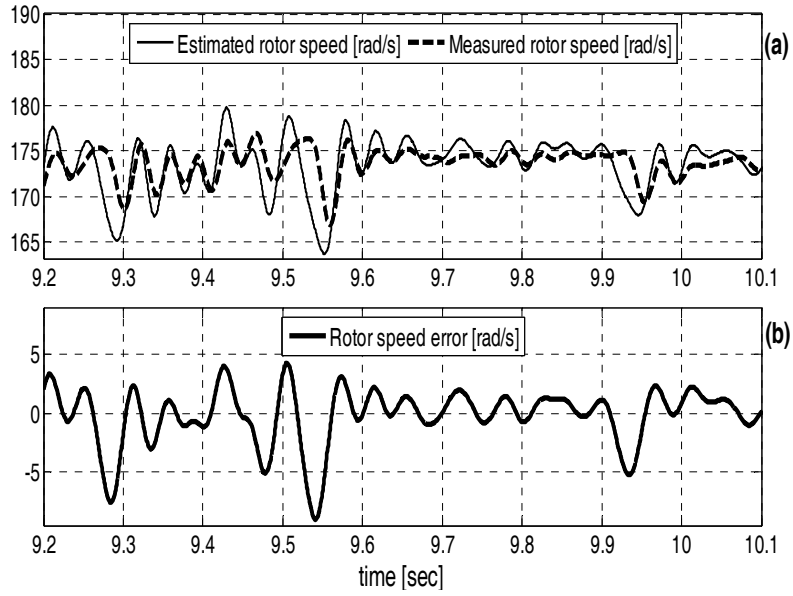Fig. 3.22 Dc-link voltage during two-phase voltage sag

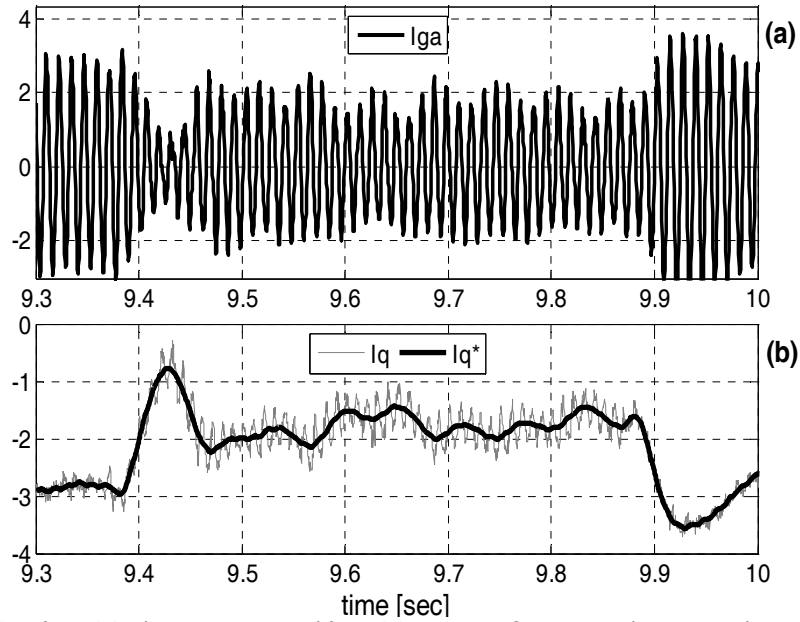Fig. 3.23 a) Estimated and measured rotor speed, b) Rotor speed error [rad/s]

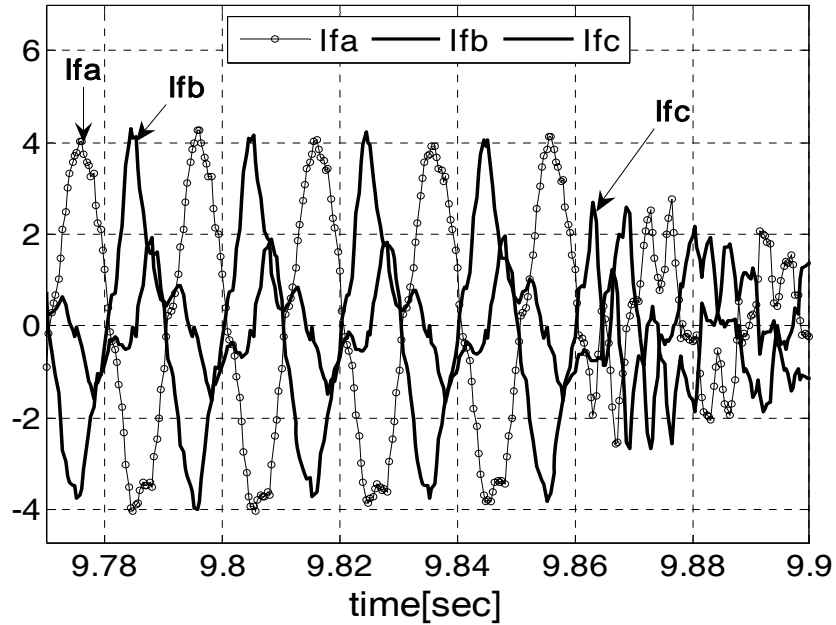Fig. 3.24 a) PMSG phase A current, b) PMSG q-axis reference and measured current

Fig. 3.25 Grid phase currents during the fault

B) Three-Phase Voltage Sag

Another type of grid fault is the three-phase voltage sag situation. In this case all three phases register the same magnitude of voltage drops. The voltage waveforms and one phase current are illustrated in Fig. 3.26. The magnitude of all three voltages drops from $230V_{RMS}$ to $110V_{RMS}$ from 6.5s – 7s, but no phase jump is registered, and the system recovers rapidly in one cycle. The Dc-link voltage shown in Fig. 3.27 is kept almost constant at 600V during the fault. The estimated and measured rotor speed and the error between them are shown in Fig. 3.28. A good tracking performance of speed/ position observer used for motion-sensorless control of PMSG is notable. The phase currents of PMSG and q-axis reference, and measured currents are illustrated in Fig. 3.29.
Again, there are no notable transients during the fault. The grid currents depicted in Fig. 3.30 during and after the fault clearance, show reasonable spikes.
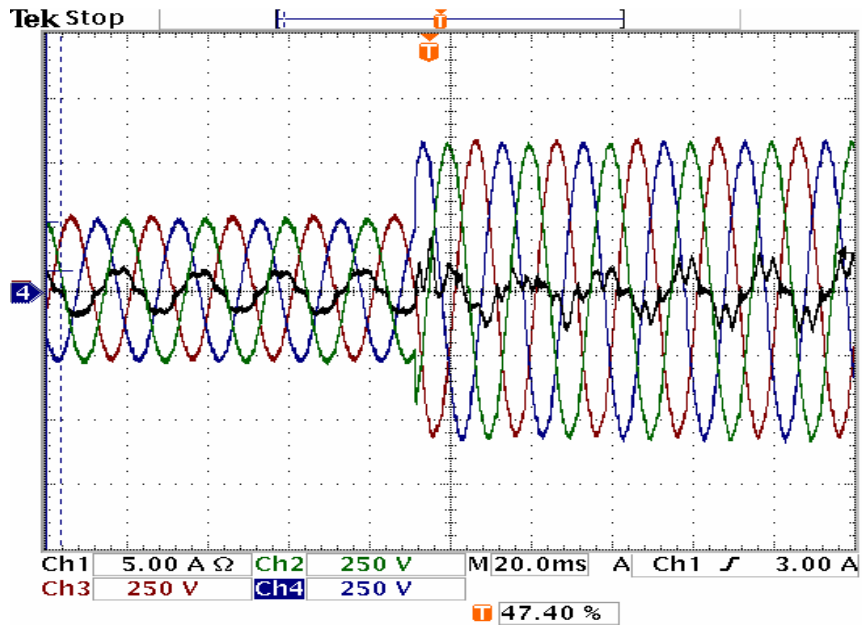
Fig. 3.26 Grid voltages after transformer and phase current (250V/div, 3A/div)
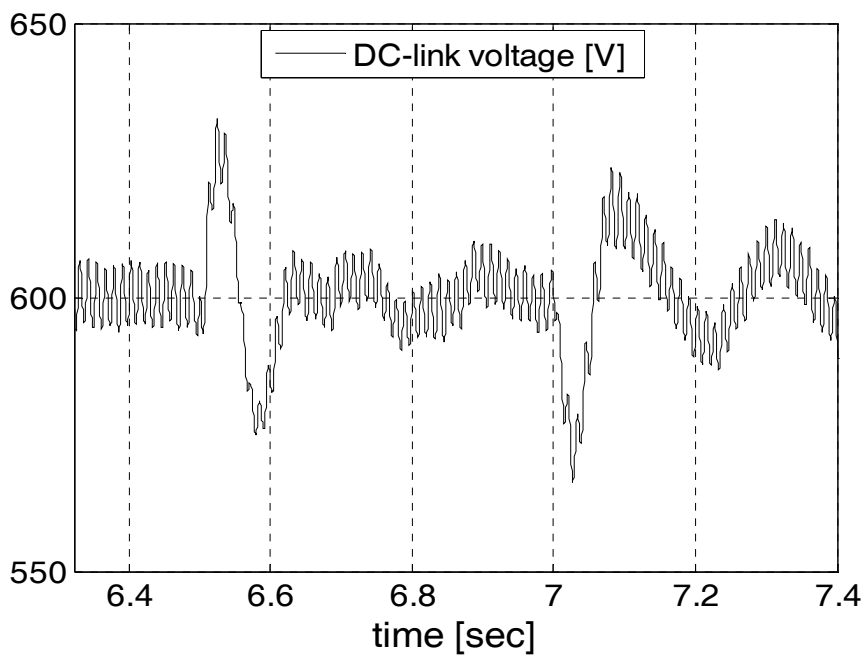

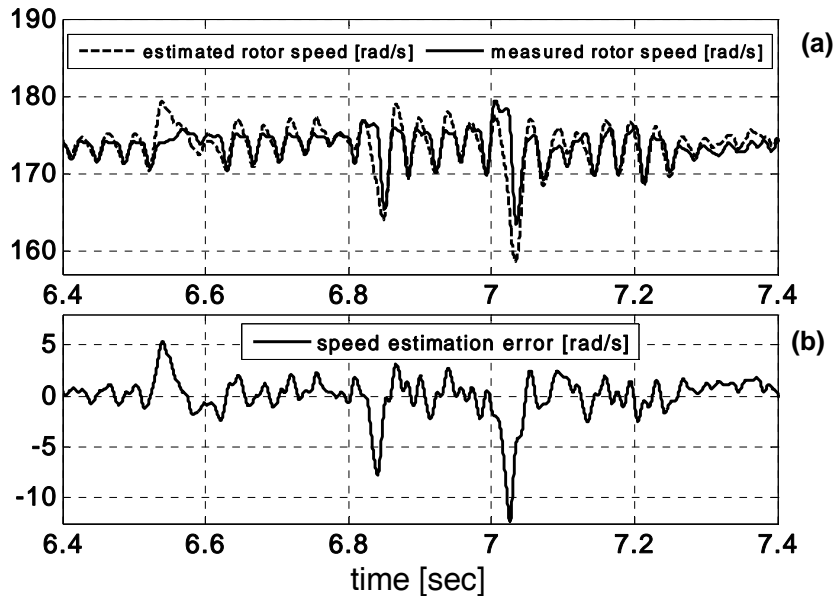Fig. 3.27 Dc-link voltage during three-phase voltage sags

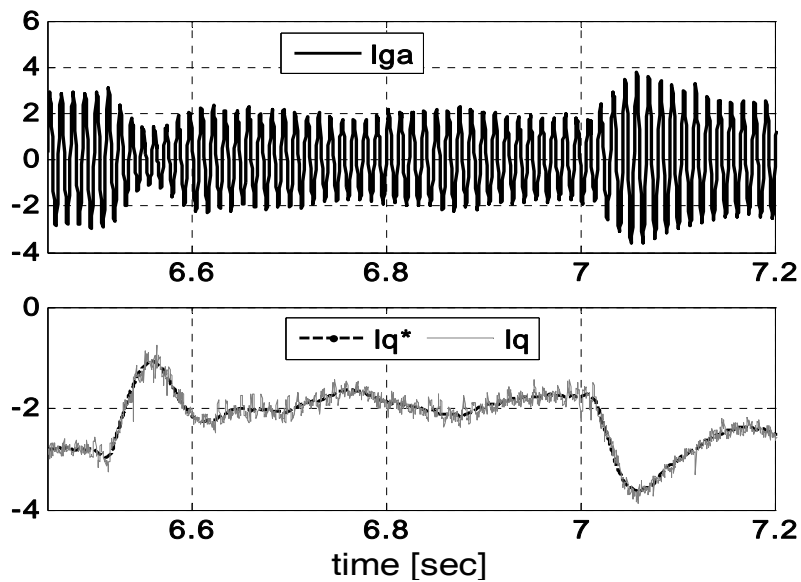Fig. 3.28 a) Estimated and measured rotor speed, b) Rotor speed error [rad/s]

Fig. 3.29 a) PMSG phase A current, b) PMSG q-axis reference and measured current
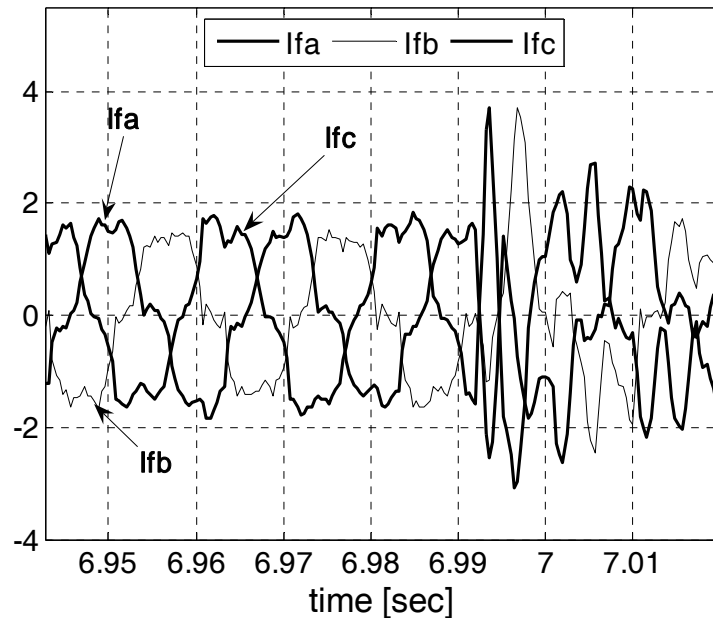
Fig.29. Grid phase currents during the fault

3.10 CONCLUSION

  The chapter aimed at documenting through analysis, design and experimental tests, the smooth ride-through of asymmetric voltage sags of a motion-sensorless controlled PMSG for wind power generation. The presentation focuses on the following key attributes of the proposed control system:
▪ Band-pass filter based on D-module filter to extract the positive-sequence voltages of the power grid.
▪ Positive-sequence voltage vector control of the grid-side inverter during asymmetric voltage sags.
▪ Smooth and fast transition through asymmetric voltage transients has been demonstrated through tests, both on the grid-side source and the generator side, with small DC-link transients.
▪ A comprehensive control system which includes: an active power controller, current controllers with cross-coupling decoupling, and a Dc voltage controller, is put in place.
▪ Good PMSG rotor position and speed estimation without using emf. integration, during one-, two- and three-phase voltage sags has been demonstrated.

References:

[1] R. Lawrence, "The new guy on the block", Ind. Appl. Mag., vol. 11, no. 1, pp. 54–59, Jan./Feb. 2005.

[2] EWEA Oct. 2005, Online Documentation:http://www

[3] EWEA Press Release: New world

[4] EWEA Large scale integration of wind energy in European Power supply; December 2005

[5] Variability of wind power and other renewables. Management options and strategies. IEA.www.iea.org

[6] F.Iov, A.D. Hansen, P. Sørensen, N.A Cutululis "Mapping of grid faults and grid codes", Risø-R-   167

[7] Xie Bing, B. Fox, D. Flynn, " Study of fault ride-through for DFIG based wind turbines", Electric Utility Deregulation, Restructuring and Power Technologies, 2004. (DRPT 2004). Proceedings of the 2004 IEEE International Conference on Volume 1, 5-8 April 2004 Page(s):411 - 416 Vol.1

[8] T. Sun, Z. Chen, and F. Blaabjerg, "Transient Analysis of Grid-Connected Wind Turbines with DFIG after an External Short-Circuit Fault," *Nordic Wind Power Conference*, March 2004.

[9] T.Sun, Z.Chen, and F.Blaabjerg, "Voltage recovery of grid connected wind turbines with DFIG after a short circuit fault " 35th Annual Power Electronics Specialists Conference, Aschen, Germany, 1991-199, 2004.

[10] J. Niiramen "Voltage dips ride through of a doubly fed generator equipped with an crowbar", Nordic Wind Power Conference, 1-2 March, Chalmers, 2004.

[11] J. Morren, S.W. de Han, " Ride through of wind turbines with doubly fed induction generator During a voltage dip" , IEEE Trans. On Energy Conversion, vol.20, pp. 435-441, June 2005.

[12] R. Pena, J. C. Clare, and G. M. Asher, "Doubly fed induction generator using back-to-back PWM converters and its application to variable speed wind-energy generation," Proc. Inst. Elect. Eng.,, vol. 143, no. 3, pp. 231–241, May 1996.

[13] M. H. J. Bollen, Understanding Power Quality Problems: Voltage Sags and Interruptions. New   York: IEEE Press, 1999.

[14] G. Saccomando and J. Svensson, "Transient operation of grid-connected voltage source converter under unbalanced voltage conditions," in *Proc.IAS*, Chicago, IL, 2001, vol. 4, pp. 2419–2424.

[15] V. Kaura and V. Blasco, "Operation of a phase locked loop system under distorted utility conditions," *IEEE Trans. Ind. Applicat.*, vol.33, pp. 58-63, Jan./Feb. 1997.

[16] S. Chung, "A phase tracking system for three phase utility interface inverters," *IEEE Trans. Power Electron.*, vol. 15, pp. 431-438, May 2000.

[17] P. Rodríguez, J. Pou, J. Bergas, I. Candela, R. Burgos, and D.Boroyevich, "Double synchronous reference frame PLL for power converters," *in Proc. IEEE Power Electron. Spec. Conf. PESC'05*, 2005, pp. 1415-1421.

[18] A. V. Timbus, M. Liserre, F. Blaabjerg, R. Teodorescu, and P. Rodriguez, "PLL algorithm for power generation systems robust to grid faults," in *Proc. IEEE PESC*, 2006, pp. 1360–1366.

[19] M. C. Benhabib and S. Saadate, "A new robust experimentally validated phase-looked loop for power electronic control," *EPE J.*, vol. 15, no. 3, pp. 36–48, Aug. 2005.

[20] M. Karimi-Ghartemani and M.R. Iravani, "A method for synchronization of power electronic converters in polluted and variable-frequency environments," *IEEE Trans. Power Systems*, vol.   19, Aug. 2004, pp. 1263–1270.

[21] H.-S. Song and K. Nam, "Instantaneous phase-angle estimation algorithm under unbalanced voltage-sag conditions," in *Proc. Inst. Elect.Eng. Generation, Transmission, and Distribution*, vol.147, 2000, pp.409–415.

[22] I. Boldea, *"Variable Speed Generators",* CRC Press Florida, Taylor&Francis Group, 2006.

[23] S. Shinnaka, "New "Mirror-phase vector control" for sensorless drive of IPM synchronous motor,"in *Proc. IEEE Int. Electric Machines and Drives Conf. IEEE-IEMDC'03*, Madison, WI, USA, June 2003, vol. 3, pp. 1875–1881.

[24] S. Shinnaka, "A new characteristics-variable two-input/output filter in D-module – Designs, realizations, and equivalences," *IEEE Trans. Ind. Appl.,* vol. 38, no. 5, Sept./Oct. 2002, pp. 1290– 1296.

[25] I. Agirman and V. Blasko, "A novel control method of a VSC without ac line voltage sensors," *IEEE Trans. Ind. Appl.*, vol. 39, no. 2, pp. 519–524, Mar./Apr. 2003.

[26] R. Teodorescu and F. Blaabjerg, "Flexible control of small wind turbines with grid failure detection operating in stand-alone or grid-connected mode," *IEEE Trans. Power Electron.*, vol. 19, no. 5, pp. 1323–1332, Sep. 2004.

[27] S.-H. Song, S.-I. Kang, and N.-K. Hahm, "Implementation and control of grid connected ac–dc–ac power converter for variable speed wind energy conversion system," in *Proc. IEEE APEC*, 2003, vol. 1, pp. 154–158.

[28] H. Zhu, B. Arnet, L. Haines, E. Shaffer, and J.-S. Lai, "Grid synchronization control without ac voltage sensors," in *Proc. IEEE APEC*, 2003, vol. 1, pp. 172–178.

[29] D. Candusso, L. Valero, and A. Walter, "Modelling, control and simulation of a fuel cell based power supply system with energy management," in *Proc. IEEE IECON*, 2002, vol. 2, pp. 1294–1299.

[30] M. Kazmierkowski, R. Krishnan, and F. Blaabjerg, *Control in PowerElectronics—Selected Problems*. New York: Academic, 2002.

[31] J. Svensson, "Synchronisation methods for grid-connected voltage source converters," *Proc. Inst. Electr. Eng.—Gener. Transm. Distrib.*, vol. 148, no. 3, pp. 229–235, May 2001.

[32] H. Kim, S.-J. Lee, and S.-K. Sul, "Reference wave generator in dynamic voltage restorers by use of PQR power theory," in *Proc. IEEE APEC*, 2004, vol. 3, pp. 1452–1457.

[33] S.-J. Lee, H. Kim, S.-K. Sul, and F. Blaabjerg, "A novel control algorithm for static series compensators by use of PQR instantaneous power theory," *IEEE Trans. Power Electron.*, vol. 19, no. 3, pp. 814–827,May 2004.

[34] F. M. Gardner, *Phase Lock Techniques*. New York: Wiley, 1979.

[35] G. C. Hsieh and J. C. Hung, "Phase-locked loop techniques—A survey," *IEEE Trans. Ind. Electron.*, vol. 43, no. 6, pp. 609–615, Dec. 1996.

[36] S.-K. Chung, "A phase tracking system for three phase utility interface inverters," *IEEE Trans. Power Electron.*, vol. 15, no. 3, pp. 431–438, May 2000.

[37] A. V. Timbus, M. Liserre, R. Teodorescu, and F. Blaabjerg, "Synchronization methods for three phase distributed power generation systems. An overview and evaluation," in *Proc. IEEE PESC*, 2005, pp. 2474–2481.

[38] L. N. Arruda, S. M. Silva, and B. Filho, "PLL structures for utility connected systems," in *Proc. IEEE-IAS Annu. Meeting*, 2001, vol. 4, pp. 2655–2660.

[39] E. Twining and D. G. Holmes, "Grid current regulation of a three-phase voltage source inverter with an LCL input filter," *IEEE Trans. Power Electron.*, vol. 18, no. 3, pp. 888–895, May 2003.

[40] F. Briz del Blanco, M.W. Degner, and R.D. Lorenz, "Dynamic analysis of current regulators for ac motors using complex vectors"*, IEEE Trans. Ind. Appl.*, vol. 35, no. 6, Nov./Dec. 1999, pp.1424–1432

[41] M.Fatu, C.Lascu, G.-D. Andreescu, F. Blaabjerg, R.Teodorescu, I. Boldea ," Voltage Sags Ride-Through of Motion Sensorless Controlled PMSG for Wind Turbines", Record of IAS -2007, New Orleans, USA.

Chapter 4

Motion sensorless bidirectional PWM converter control with seamless switching from power grid to stand alone and back

***Abstract** –* This chapter presents concepts and tests results on a flexible sensorless control strategy for a PMSG driven by a small wind turbine with back-to-back power converters capable to function in both stand alone and grid connection mode. A new automatic seamless transfer method, based on phase-locked-loop technique, from grid connected to stand alone and vice versa in the event of a fault on grid is proposed. Tests results show the proposed method works properly

4.1   Introduction

As a result of technological advances in small scale energy generation, deregulation of the energy sector and governmental commitments to increase the production of electrical energy from renewable sources, the number of Distributed Generation (DG) sources directly connected to the distribution grid is increasing and therefore the role played by the distribution network is changing from passive to active. This change is going to be even more drastic as the presence of coordinated DG further increases and micro-grids can be formed [1]. This poses a series of technical challenges which need to be addressed in order to guarantee an effective integration of DG into the existing network. Among these technical issues, the grid side inverter capability to work both in grid-connected but also in stand-alone mode as well as the   protection in the case of the fault event are considered to be the most challenging in terms of control strategy and the limited fault current.

In the case of sensitive and mission-critical industrial loads, maintaining a continuous, uninterrupted AC power is of utmost importance. Most of the utility-interactive inverters for distributed energy systems reported in the literature [2, 3, 4] have the capability to operate in both grid-tied and off-grid modes, but they do not address the issue of a seamless transition between the two modes. Recent advances in DSPs enable implementation of complex algorithms to control the utility-interactive system such that the load is unaffected by the transition from one mode to the other.

Small wind turbines in range of tens KW, with two back-to-back voltage source converters, are becoming a viable solution in supplying remote communities. The trend is that they should be capable to work in parallel with other generators such as photovoltaic and diesel generators in so called hybrid generator systems.

An advanced variable speed permanent magnet synchronous generator (PMSG) connected to the power grid via two-voltage source PWM, with bidirectional power as shown in Fig. 4.1 is typical for the distributed generation system of the future.
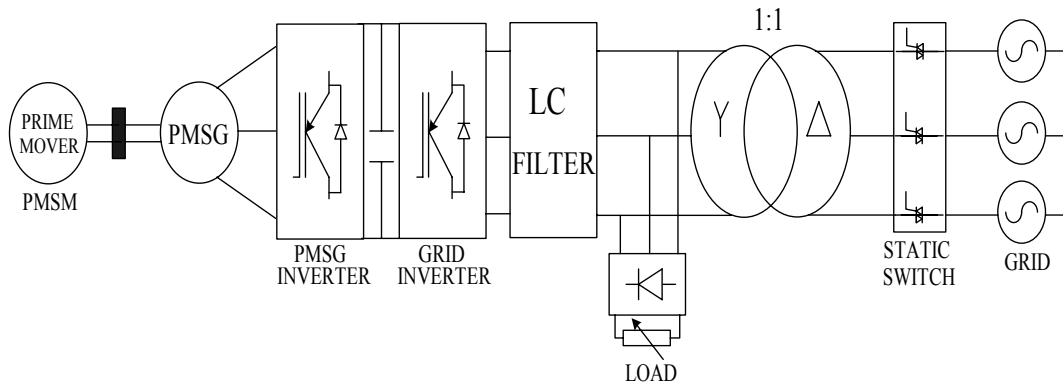
Fig. 4.1 The general system

The phase-locked loop (PLL) technique is used in grid-connected converters, mainly for grid synchronization [5], [6]. Two seamless transfer methods from grid-connected to stand-alone and vice versa for critical loads with a zero load current stage, are described is described in [7, 8, 9].

The algorithms match the magnitude and phase of the inverter voltage and the grid voltage at the time of disconnecting or reconnecting to the grid to minimize any sudden voltage change across the load but important inrush current spikes are recorded during transition from stand alone to grid connected mode in [7] because the PLL regulator is not fast enough in order to limit the rise current below the permit limit during the recovery moment.

In this chapter a novel, seamless (without load current interruption), PLL-method for automatic switching of a load from grid, when the grid is disconnected and back to the grid when the latter is restored is presented.

4.2 Wind turbine emulator

The wind turbine mechanical shaft is emulated using a 14.7Nm-3000rpm permanent magnet synchronous motor driven by a commercial inverter operated in open loop torque control mode.

The aerodynamic model of the wind turbine is characterized by a non-dimensional curve (Fig. 4.2) that introduces the performance coefficient C_p as a function of blade tip-speed ratio λ defined as:

$$\lambda = \frac{R_t \omega}{v} \tag{4.1}$$

where R_t is the radius of wind turbine rotor (m), ω is the wind turbine rotor velocity (rad/s), and v is the wind velocity (m/s).
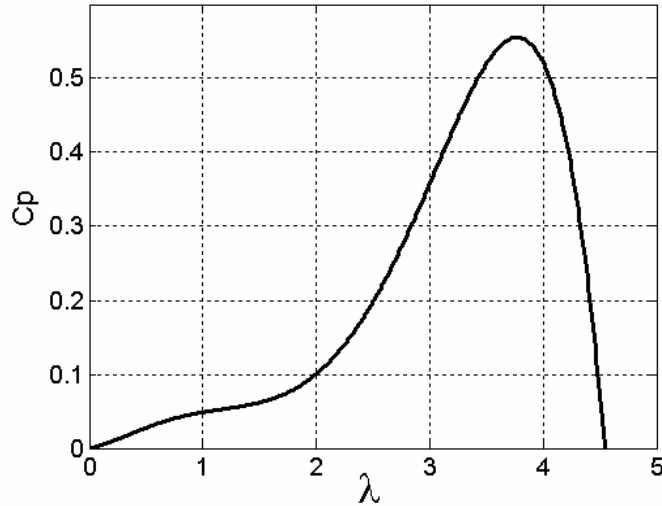
Fig. 4.2 C_p versus λ characteristic of the wind turbine

For the wind turbine used here, C_p as a function of λ is expressed by the following equation and it is shown in Fig. 4.2.

$$C_p = 0.0284\lambda + 0.119\lambda^2 - 0.1508\lambda^3 + 0.0679\lambda^4 - 0.0089\lambda^5 \qquad (4.2)$$

The output power of the wind turbine is calculated as:

$$P_t = 0.5C_p(\lambda)\rho\pi R_t^2 v^3 , \qquad (4.3)$$

where ρ = 1.225 kg/m^3 is the air density and R_t = 1.2 m.
   The torque developed by the wind turbine is

$$T_t = 0.5\rho\pi R_t^3 \frac{C_p(\lambda)}{\lambda} v^2 . \qquad (4.4)$$

Equation (4.4) is implemented in the PMSM prime mover drive that emulates the wind turbine in the actual experiments.

4.3   PMSG MODEL

The space-vector model of PMSG, equipped with interior permanent magnets, in rotor reference frame (Park's transformation in *dq* axes) [10] is:

$$-\underline{V}_s = \underline{i}_s R_s + \frac{d\underline{\Psi}_s}{dt} + j\omega_r \underline{\Psi}_s , \qquad (4.5)$$

$$\underline{\Psi}_s = \Psi_d + j\Psi_q = \lambda_{PM} + L_d i_d + jL_q i_q , \qquad (4.6)$$

where $\underline{V}_s = V_d + jV_q$, $\underline{i}_s = i_d + ji_q$, and $\underline{\Psi}_s$ are the stator voltage, current and flux vectors, respectively, R_s is the stator phase resistance, L_d and L_q are the *dq* inductances, λ_{PM} is the PM flux, ω_r is the rotor speed.

4.4 GRID-SIDE INVERTER / FILTER / TRANSFORMER / GRID MODELING

In a typical situation, the distributed generation system is connected through a transformer to local grid. The plant considered in this application, shown in Fig. 4.2, contains the *LC* filter attached to the line-side power inverter, a nonlinear resistive load and the secondary side of the line transformer.

The circuit shown in Fig. 4.2 uses the following quantities to describe its behavior. $\underline{V}_i = [V_{ai}\ V_{bi}\ V_{ci}]$ and $\underline{i}_i = [i_{ai}\ i_{bi}\ i_{ci}]$, respectively. The transformer secondary windings are Y-connected and its phase voltage and current vectors are represented by $\underline{V}_t = [V_{ta}\ V_{tb}\ V_{tc}]$ and $\underline{i}_t = [i_{ta}\ i_{tb}\ i_{tc}]$, respectively. The transformer primary windings are Δ-connected and its line-to-line voltages are represented by $\underline{V}_p = [V_{AB}\ V_{BC}\ V_{CA}]$ and phase voltages by $\underline{V}_{grid} = [V_A\ V_B\ V_C]$.
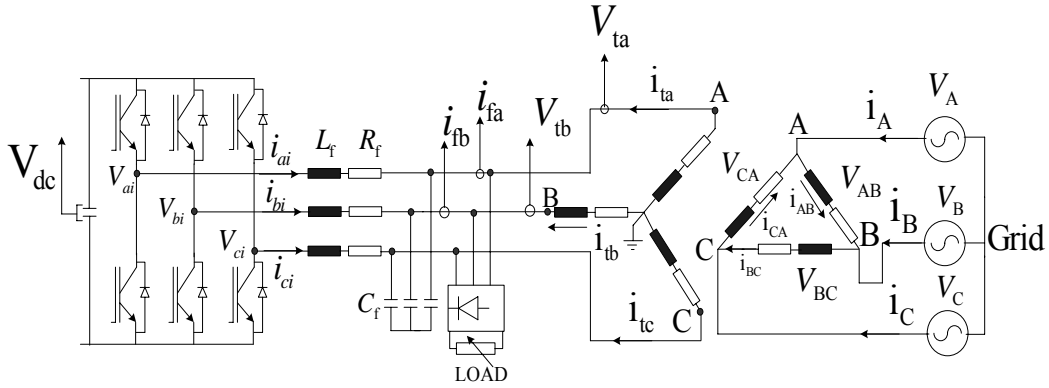
Fig. 4.2. Configuration of the grid-side inverter connected through delta-wye transformer to local grid

Based on Fig. 4.2, the voltage relation between the two sides of the transformer with 1:1 "turns ratio" can be expressed as:

$$\begin{bmatrix} V_{ta} \\ V_{tb} \\ V_{tc} \end{bmatrix} = \frac{1}{\sqrt{3}} \begin{bmatrix} V_{AB} \\ V_{BC} \\ V_{CA} \end{bmatrix} \tag{4.7}$$

$$\begin{bmatrix} V_{AB} \\ V_{BC} \\ V_{CA} \end{bmatrix} = \begin{bmatrix} 1 & -1 & 0 \\ 0 & 1 & -1 \\ -1 & 0 & 1 \end{bmatrix} \cdot \begin{bmatrix} V_A \\ V_B \\ V_C \end{bmatrix} \tag{4.8}$$

The relation of the currents flowing through the filter and load is given by:

$$i_i = i_c + i_f \tag{4.9}$$

Considering grid voltage and the transformer as perturbation the transfer function between the current i_f and inverter voltage V_i is:

$$H_p(s) = \frac{i_f(s)}{V_i(s)} = \frac{1}{(sL_f + R_f) \cdot (sR_{Load}C_f + 1) + R_{Load}} \tag{4.10}$$

The filter parameters are: L_f = 0.01 H, R_f = 0.4 Ω, C_f = 0.7 μF, and the resistive load R_{Load} that was set to 80Ω.

The equivalent single phase representation of circuit from Fig. 4.2 is shown in Fig.4.3.
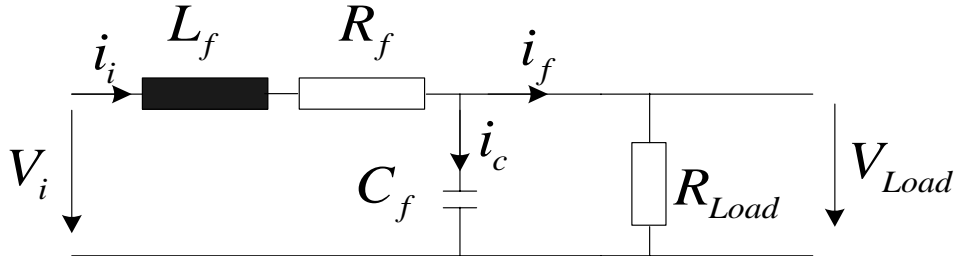

Fig. 4.3 Single phase representation of the plant

4.5 Supply side inverter control in grid connected mode

In grid-connected mode, the supply-side inverter is current controlled with direct axis aligned to supply voltage vector, enabling independent control of the active and reactive power. The control scheme thus utilizes current control loops for i_d and i_q, with the i_d demand being derived from the DC-link voltage error through a standard PI regulator:

$$I_d^* = \left(K_{p\_Vdc} + \frac{K_{i\_Vdc}}{s} \right) \cdot \left(V_{dc}^* - V_{dc} \right) \tag{4.11}$$

The design of Dc-link voltage controller may carried out in continuous domain, knowing the value of the Dc-link capacitor (C=470µF), and assuming that the inner current i_d is ideal . The transfer function of the plant (Fig.4.4) is:

$$H_{Dc-link}(s) = \frac{V_{dc}(s)}{i_d(s)} = \frac{1}{sC} \tag{4.12}$$

The frequency response of $H_{Dc-link}(s)$ on linear scales is represented in Fig.4.5. The response was obtained for $K_{p\_Vdc} = 0.02$, and $K_{i\_Vdc} = 0.2$.
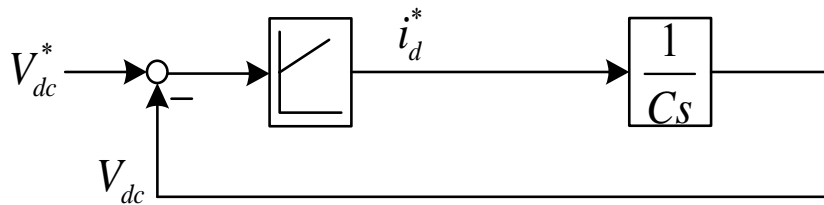

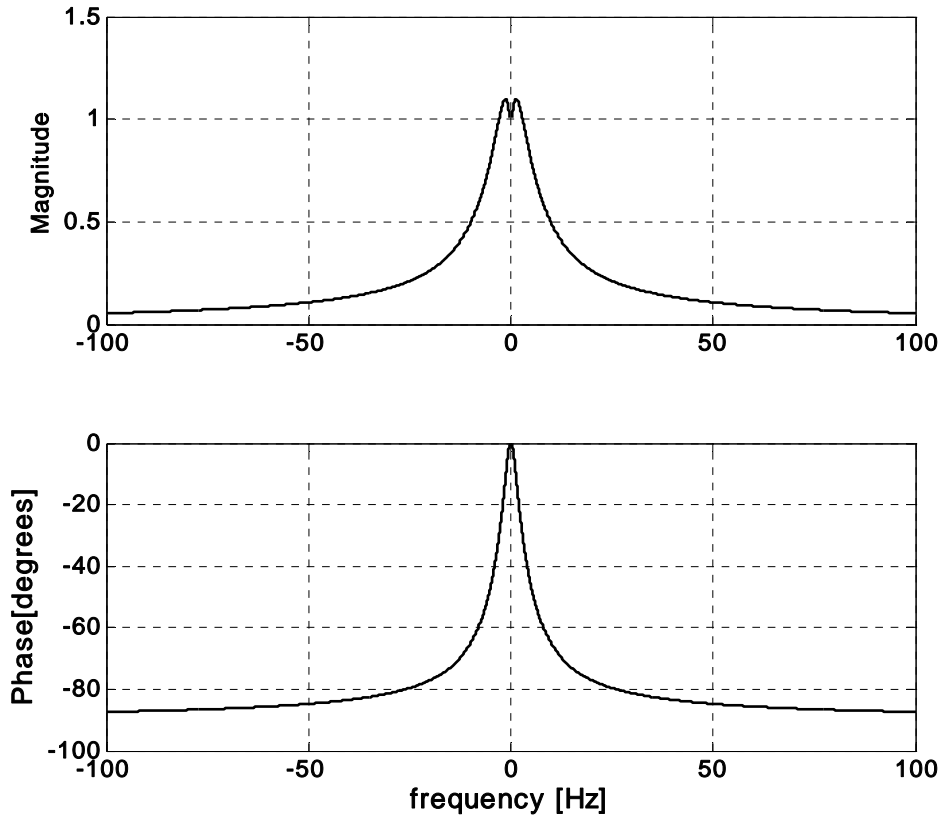Fig. 4.4 Dc-link voltage control loop

Fig.4.5 Frequency response of Dc-link controller

The current regulator is implemented in synchronous reference frame with cross-coupling decoupling and with line voltage feedforward compensation, which provide pole-zero cancellation for the plant. The output of the controller is the reference voltage vector for the space vector modulation block (SVM) $\underline{v} = V_d^* + jV_q^*$:

$$V_d^* = (k_{pcrt} + \frac{k_{icrt}}{s})e_{id} - \omega_{grid}i_qL + V_d \tag{4.13}$$

$$V_q^* = (k_{pcrt} + \frac{k_{icrt}}{s})e_{iq} + \omega_{grid}i_dL \tag{4.14}$$

where k_{pcrt} and k_{icrt} are PI controllers gains and e_{id} and e_{iq} are the current errors respectively.
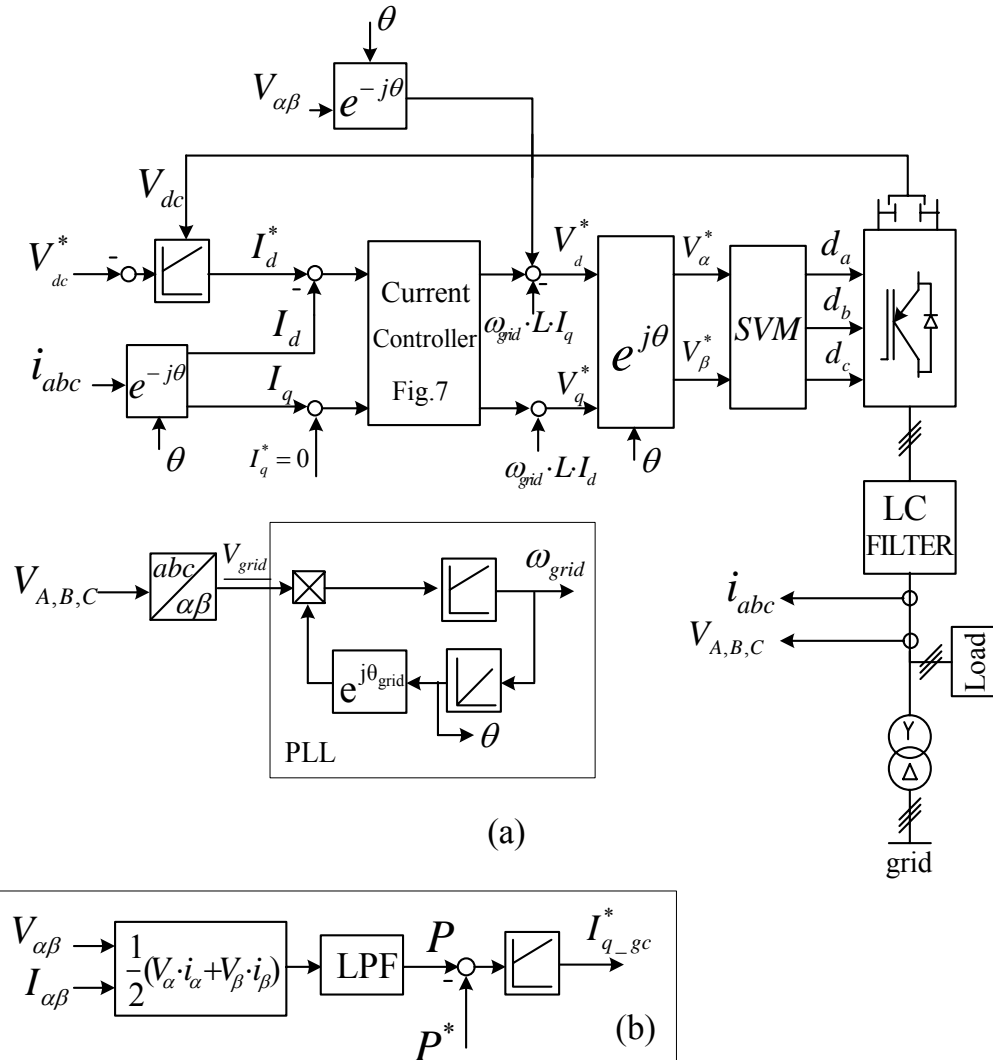
Fig.4.6 a) Supply-side inverter control in grid connected mode; b) Active power control loop

The reference current vector for the current controller is $\underline{i_f^*} = i_d^* + ji_q^*$, $\underline{i_f} = i_d + ji_q$ is the grid current vector, and $\underline{V_{dq}} = V_d + jV_q$ is the line voltage vector. The block diagram of the current controller and the plant (Fig. 4.3), in synchronous reference frame, is presented in Fig. 4.7. Using complex vector notation, the model for the plant in stationary reference frame is transformed to synchronous reference frame by substituting the "s" operator with "$s - j\omega_{sa}$" [11].
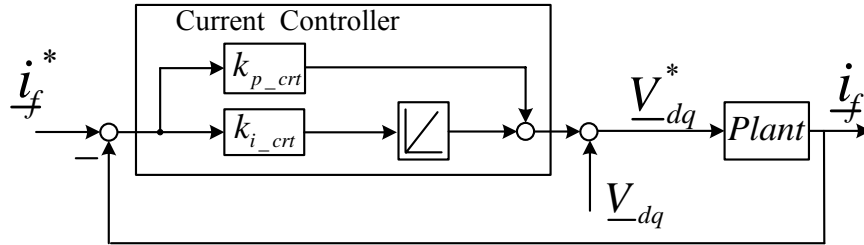
Fig.4.7 Block diagram of current loop controller of the grid-side inverter

Assuming an ideal inverter, with the grid voltage as disturbance, the transfer function of current control loop in synchronous reference frame is:

$$H_{crt}(s) = \frac{i_f}{i_f^*} = \frac{k_{p-crt}s + k_{i-crt}}{s^3 k_3 + s^2 k_2 + s k_1 + k_{i\_crt}} \tag{4.15}$$

where $k_3 = L_f R_{Load} C_f$, $k_2 = L_f + R_f R_{Load} C_f$, $k_1 = R_{Load} + R_f + k_{p\_crt}$
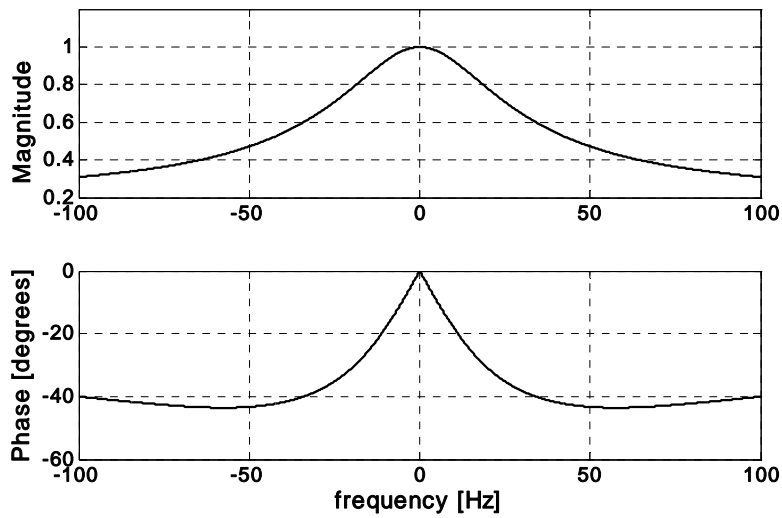

Fig. 4.8 Frequency response of the grid-side current controller

Frequency response of $H_{crt}(s)$ in synchronous reference is shown in Fig.4.8 on linear scales and was obtained for $k_{p\_crt} = 20, k_{i\_crt} = 10000$.

An observer using phase look-loop (PLL) technique is used to achieve the synchronism with the grid. The phase estimation error $\Delta\theta = \theta_{grid} - \theta$, θ_{grid} -grid

phase angle θ-inverter phase angle, can be obtained from imaginary part $Im(\underline{V_{grid}}, \underline{V_1^{\#}})$ where $\underline{V_1}$ is unity vector.

$$\underline{V_{grid}} = V_{grid} \cdot e^{j\theta_{grid}} = V_\alpha + jV_\beta, \quad \underline{V_1} = e^{j\theta} = \cos\theta + j\sin\theta \qquad (4.16)$$

$$\Delta\theta \cong \sin\Delta\theta = Im(\underline{V_{grid}}, \underline{V_1^{\#}}) / V_{grid} = (V_\beta \cdot \cos\theta - V_\alpha \cdot \sin\theta) / V_{grid} \qquad (4.17)$$

where the superscript " # " refers to the vector conjugate operator.
The reference $I^*_{q\text{-}gc\_}$ for machine-side converter is obtained as output of a PI controller which utilizes the error between the demanded active power and the active power delivered by PMSG as it can be seen also in Fig. 4.6b:

$$I^*_{q-gc} = \left(K_{p\_P} + \frac{K_{i\_P}}{s} \right) \cdot \left(P^* - P \right) \qquad (4.18)$$

where $K_{p\text{-}P}=0.005$ and $K_{i\text{-}P}=0.08$ are controller gains.
A low pass filter with time constant t=0.02s was employed to reduce the oscillations from the measured active power injected into the grid due to nonlinear currents generated by the load.

4.6 Supply side inverter control for stand-alone mode

In stand-alone mode, the voltages are controlled in terms of amplitude and frequency. Two standard PI controllers, implemented in synchronously rotating coordinates, in order to keep the voltage V_d at designated level ($v^*_d = 220\sqrt{2}$) and V_q to zero, are used (Fig.4.9).The Dc-link voltage and current limiter controllers will decrease the reference voltage only when the dc voltage is below a designated level or the load current amplitude exceeds a certain level:

$$V_{DC\text{-}limit} = (k_{p\_DC\_limit} + \frac{k_{i\_DC\_limit}}{s})(V^*_{dc} - V_{dc}) \qquad (4.19)$$

$$V_{Irms} = (k_{p\_Irms} + \frac{k_{i\_Irms}}{s})(I^*_{rms} - I_{rms}) \qquad (4.20)$$

where $k_{p\text{-}Dc\text{-}limit}=0.2$, $k_{i\text{-}Dc\text{-}limit}=4$ are Dc-link controller gains respectively $k_{p\text{-}Irms}=5$, $k_{i\text{-}Irms}=500$ are controller gains for current limiter regulator. So, finally the reference for d-axis voltage can be calculated as:

$$V^*_{d\_ref} = V^*_d - V_{DC\_limit} - V_{Irms} \qquad (4.21)$$

In stand-alone operation voltage harmonics direct reduction (by converter inverter control) seems preferable for power quality (in contrast to current harmonics external reduction by active power filter current hysteresis [12,], dead-beat [13], and linear equivalent-PI control with selective harmonic compensation [14]). In our case, two proportional resonant controllers in fundamental reference frame rotating at frequency ω_e are used to generate harmonic voltages with the same magnitude but opposite phase to load harmonic voltages. Since coordinate rotation provides a frequency shift by $-\omega_e$ in fundamental reference frame, harmonicsorders k=6n±1 become k=6n.

The controller is implemented as superposition of individual controllers, each designed for two pairs k=6n, n=1, 2 of positive and negative sequence harmonics (in Fig.4.3 only the 6th and 12th harmonic voltages are closed loop cancelled). The harmonic controller is similar to that in [15]:

$$H_{PR} = \sum_{n=1}^{2} 2 \frac{K_{pk}s^2 + K_{ik}s}{s^2 + (k\omega_e)^2} \, , \text{ k=6n} \tag{4.22}$$
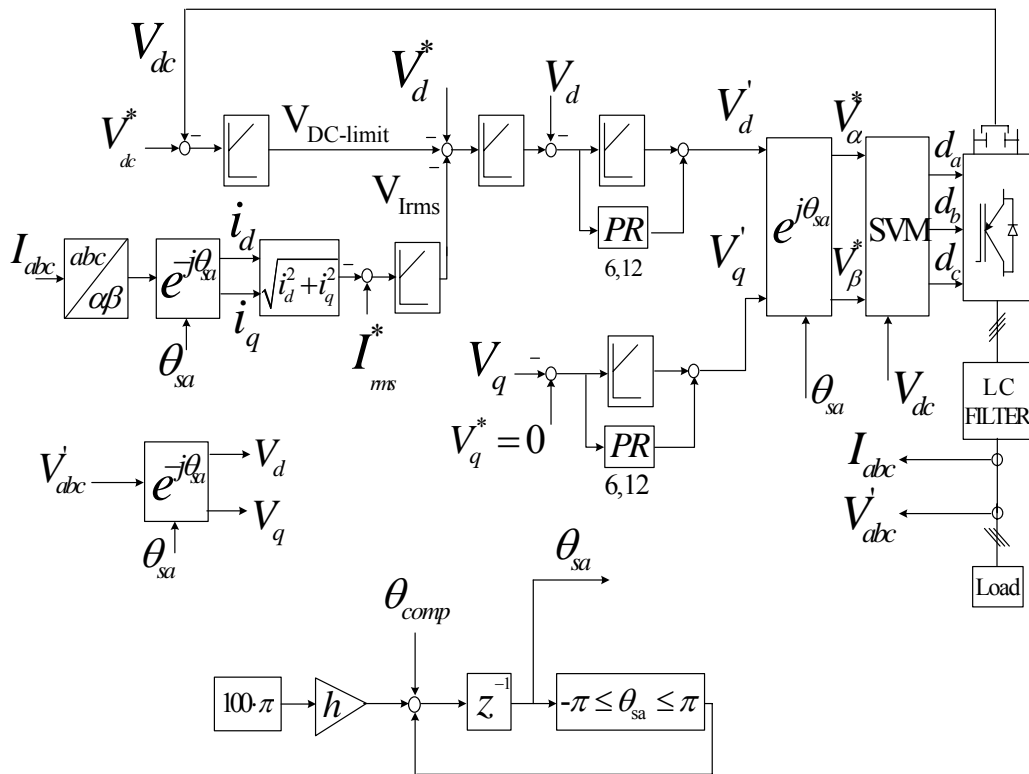

Fig.4.9 Supply-side inverter for stand-alone mode

4.7 Proposed switching strategy from stand alone to grid mode

Initially the grid converter is running in stand-alone mode. When grid is recovered (grid voltages suddenly occur), a PLL observer whose output will generate the grid frequency and phase processes the grid phase voltages (Fig. 4.10a). If the amplitude of the voltages and frequency are within the limits defined by standards, a synchronizing signal will be generated, in order to match the supply-side inverter

output phase of voltages, still in stand-alone operation, with the phase of grid voltages.

The error $\Delta\theta = \theta_{grid} - \theta_{sa}$ can be approximated, considering small arguments, with (Fig.4.10b):

$$\Delta\theta = \theta_{grid} - \theta_{sa} \cong sin\left(\theta_{grid} - \theta_{sa}\right) \tag{4.23}$$

A PI regulator (Fig. 4.10), it's used to compensate between those two:

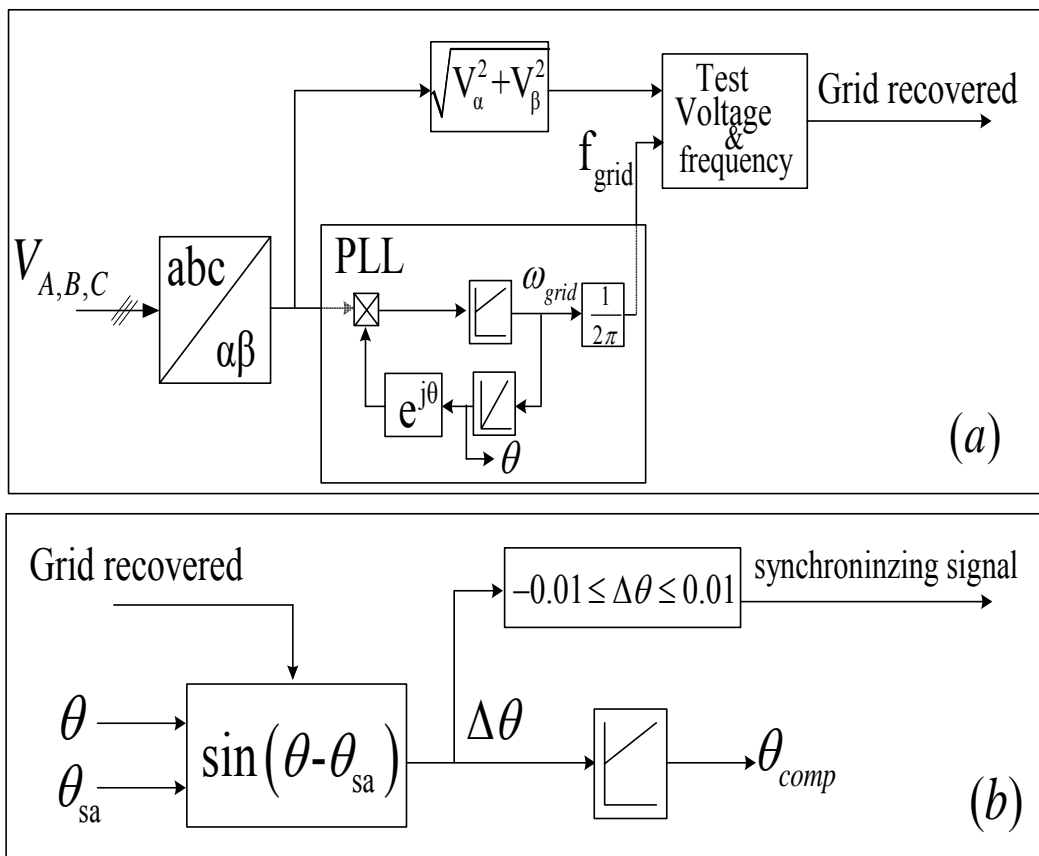$$\theta_{comp} = (k_{p\_comp} + \frac{k_{i\_comp}}{s})\Delta\theta \tag{4.24}$$

Fig.4.10 Transfer algorithm from stand alone to grid connected

In order to achieve a smooth synchronization a relatively slow dynamic was imposed to the PI regulator.

The gains of the controller were chosen as: $k_{p\_comp} = 1, k_{i\_comp} = 10$ The implementation of the proposed strategy is illustrated in Fig.4.11.
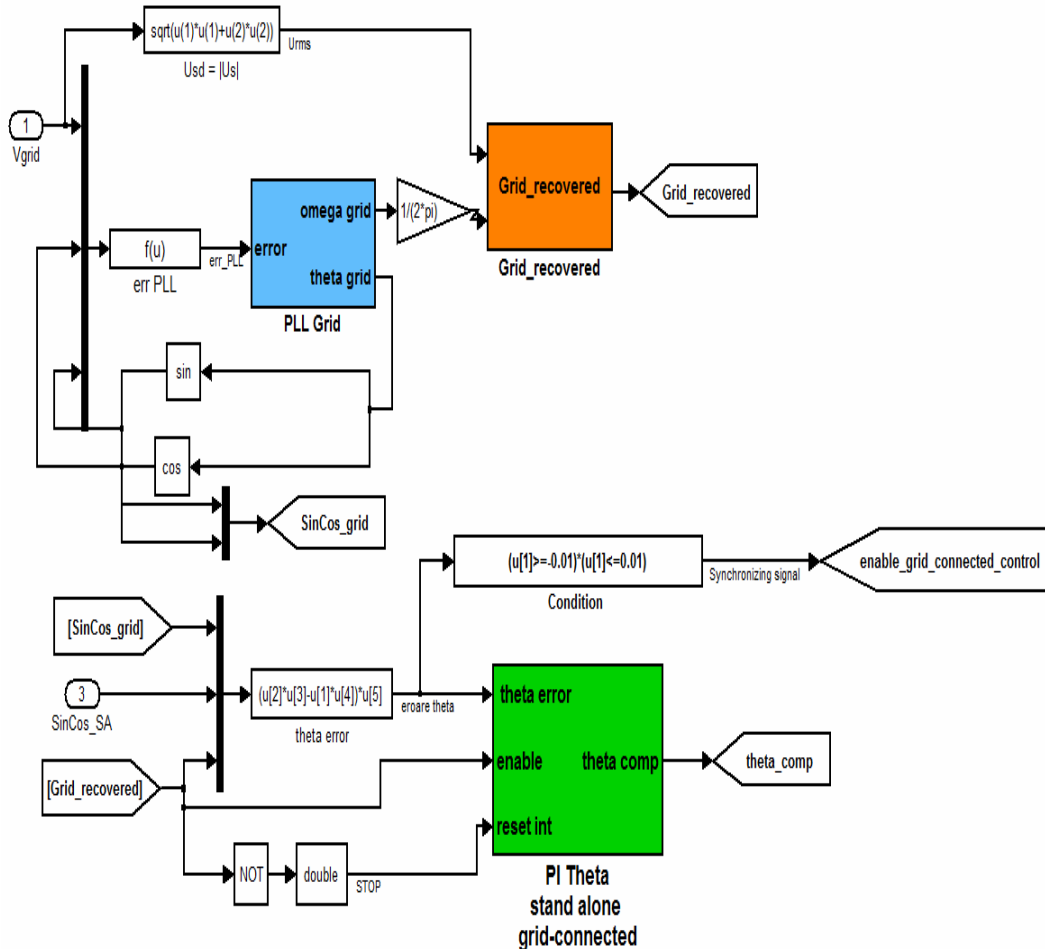
Fig. 4.11 Matlab/Simulink implementation of the proposed transition strategy
from stand-alone to grid connected

When the error is between -0.01 and 0.01 radians, the voltages are considered to be synchronized and the control of the supply-side inverter will be switched from stand-alone to grid-connected control mode. The online estimation of phase angle of stand-alone voltages (Fig.4.12) will remain on even after the system is running in grid- connected mode, in order to avoid load current interruption during future switching from power grid to stand-alone.
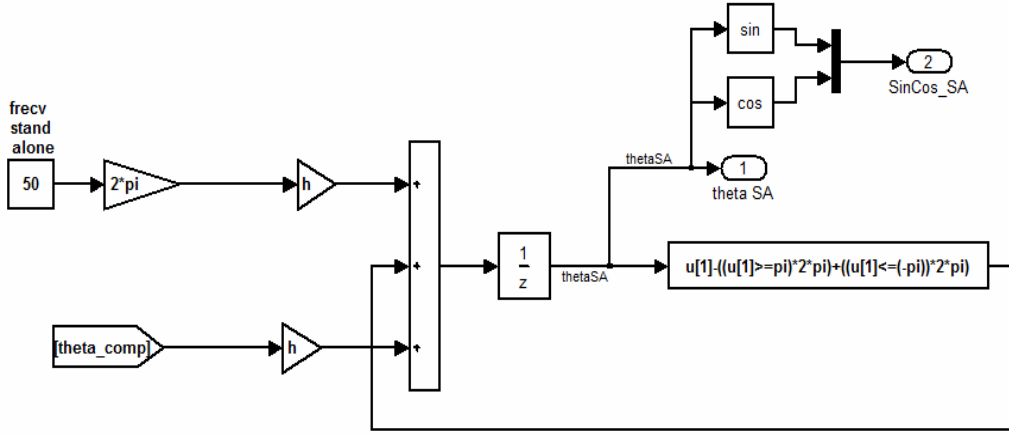
Stand alone angle calculation

Fig. 4.12 Stand alone angle computation

4.8. Transition from grid-connected to stand alone mode

Assume the grid inverter is operating in current controlled mode and that the future stand-alone load is connected to the grid in parallel. So the stand-alone load remains connected all the time at the supply-side converter output terminals. A fault event is simulated by opening the static switch S (Fig. 4.1). In this case, because we still have current control of supply-side converter (corresponding still to grid connection), there is an increase in load voltage level, and when this exceeds a certain threshold or the frequency is out of range of 49.5-50.5 Hz (see Fig.4.12), the system switches automatically to stand-alone mode (Fig. 4.13).
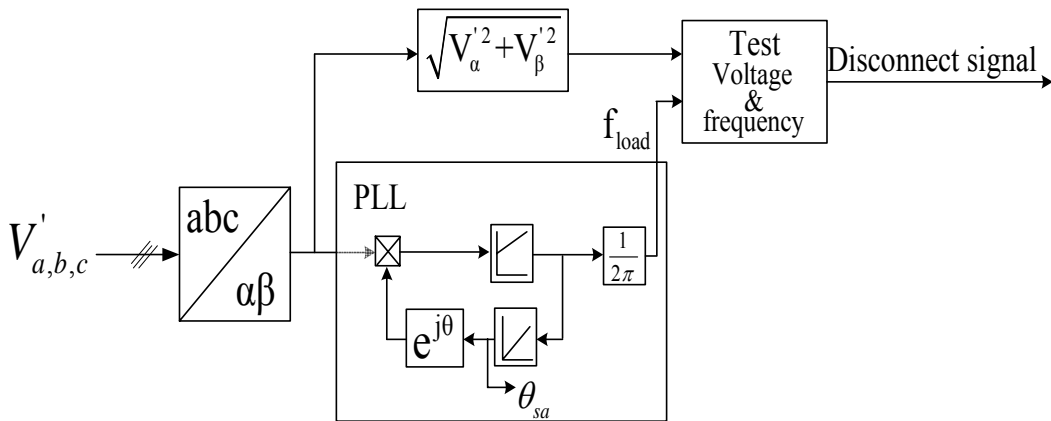
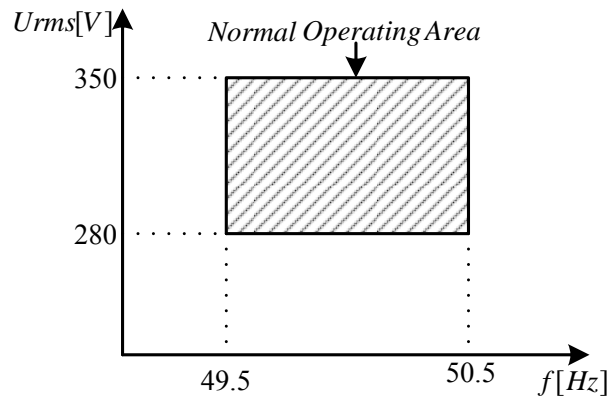Fig.4.13 Transfer algorithm from grid connected to stand alone

Fig.4.14 Design voltages and frequencies

Because the initial value of the phase angle for stand-alone voltages coincides with the last value of the grid phase angle, the transition is smooth without current interruption or current major spikes. The Matlab/Simulink implementation of the algorithm is shown in Fig.4.15
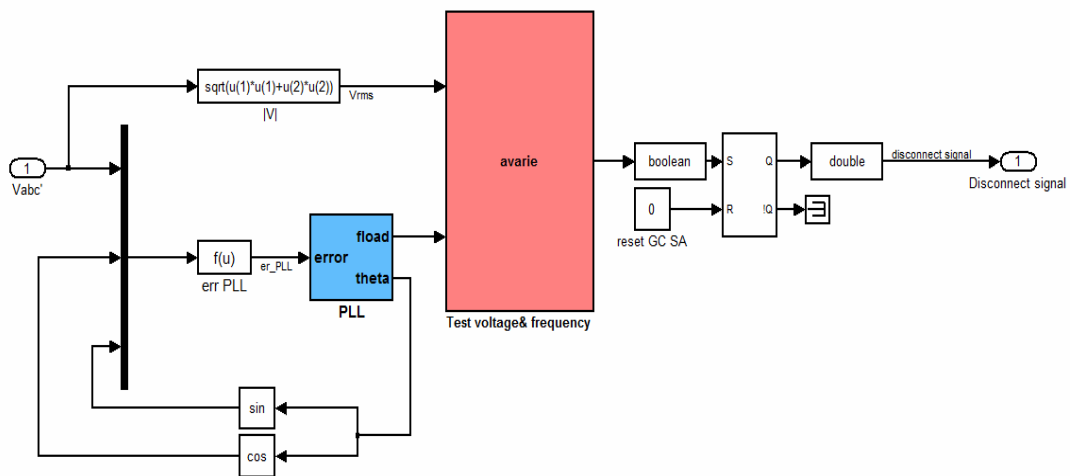

Fig.15 Matlab/Simulink implementation

4.9. Motion- sensorless vector control of machine- side converter

The configuration of the proposed motion-sensorless control system is depicted in Fig.4.16a.The machine-side converter (MSC) is power controlled along q-axis when the system works in grid-connected mode (see the reference $I^{*}_{q\text{-}gc}$ in Fig.4.6b), and

voltage controlled when is in stand alone mode. In this case the reference q-axis current is obtained from a PI regulator which has as input the error between the reference and measured Dc-link voltage:

$$i_q^* = \left(k_{pV_{DC}} + \frac{k_{iV_{DC}}}{s} \right) e_{V_{DC}} \tag{4.25}$$

where $k_{pV_{DC}}$ and $k_{iV_{DC}}$ are PI regulator gains and $e_{V_{DC}}$ is the Dc-link voltage error. The controller gains are chosen as $k_{p\_pow} = 0.03$ and $k_{i\_pow} = 1.1$.

The current regulators are implemented in synchronous reference frame and produce the reference voltage vector $\underline{v}^* = V_d^* + jV_q^*$:

$$V_d^* = (k_{pcrt} + \frac{k_{icrt}}{s})e_{id} + \hat{\omega}_r\, i_q L_s \tag{4.26}$$

$$V_q^* = (k_{pcrt} + \frac{k_{icrt}}{s})e_{iq} - \hat{\omega}_r(i_d L_s + \lambda_{PM}) \tag{4.27}$$

where k_{pcrt} and k_{icrt} are PI controllers gains and e_{id} and e_{iq} are the current errors respectively. The gains of current controllers are $k_{pcrt} = 25.0$ and $k_{icrt} = 25000$.
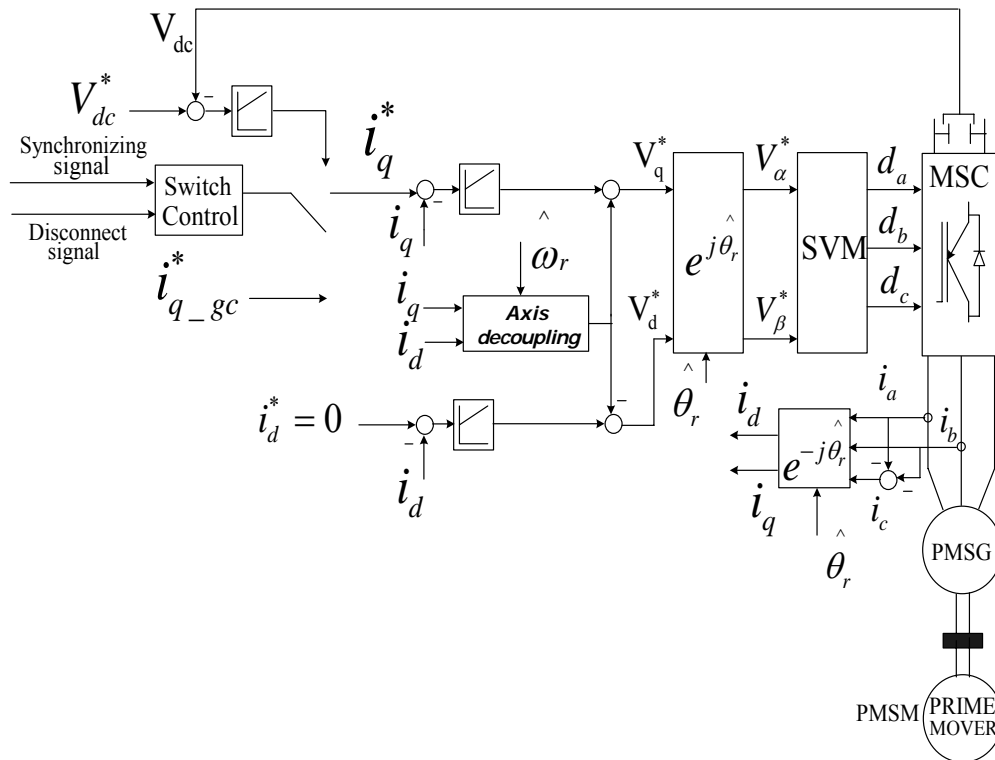

Fig. 4.16 Motion sensorless control of PMSG

The motion sensorless control algorithm was described in the previous chapter.

4.10. Test platform and experimental results

The electrical block-diagram of the test platform is shown in Fig. 4.17. The testing setup consists in a PMSG of 12 Nm rated torque driven by a Siemens SIMOVERT MASTERDRIVE, and the two inverters are Danfoss VLT 5005. The PMSG data are given in the Table 1:
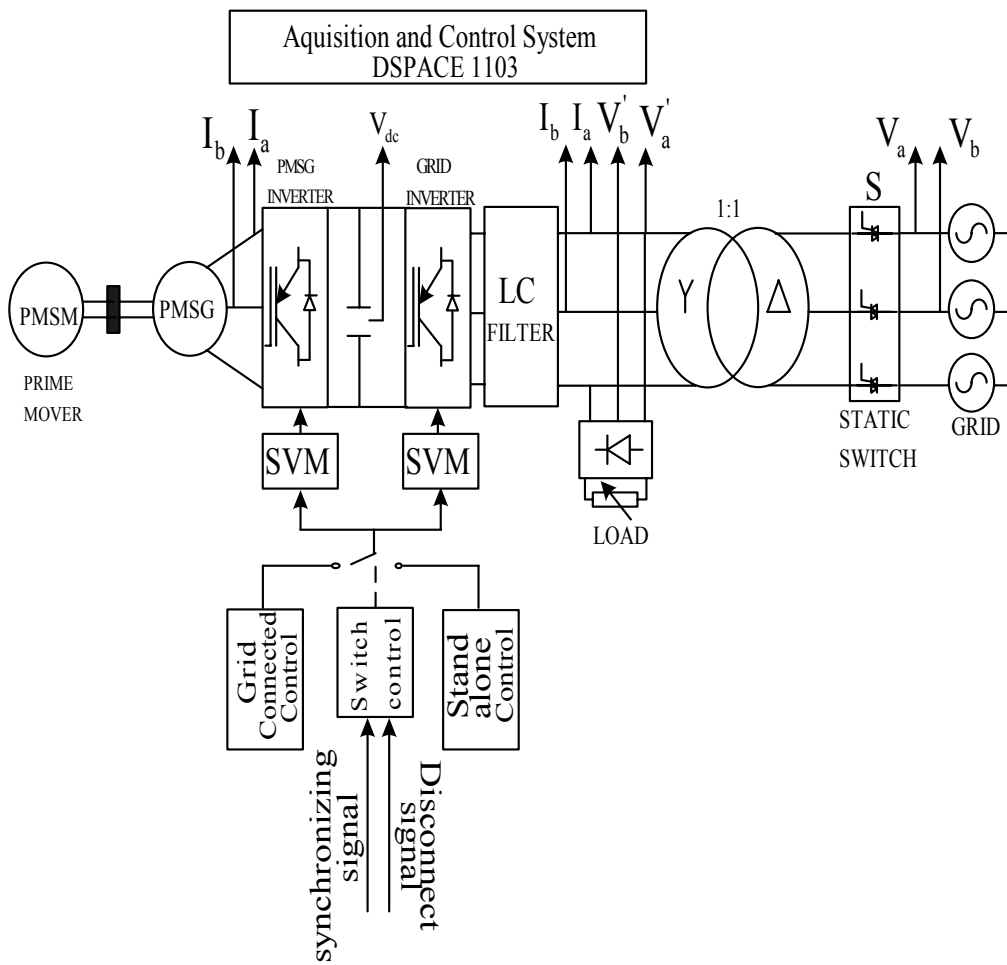
Fig. 4.17 Test Platform

Table I

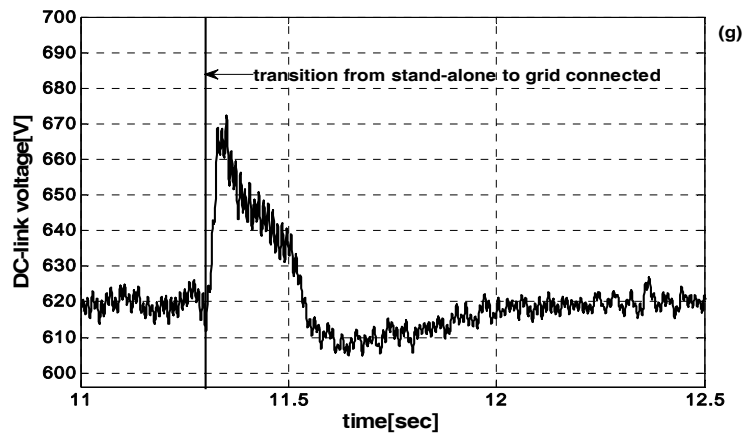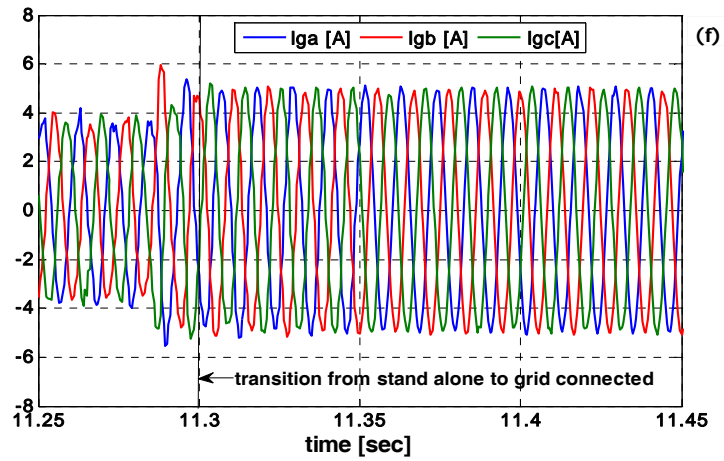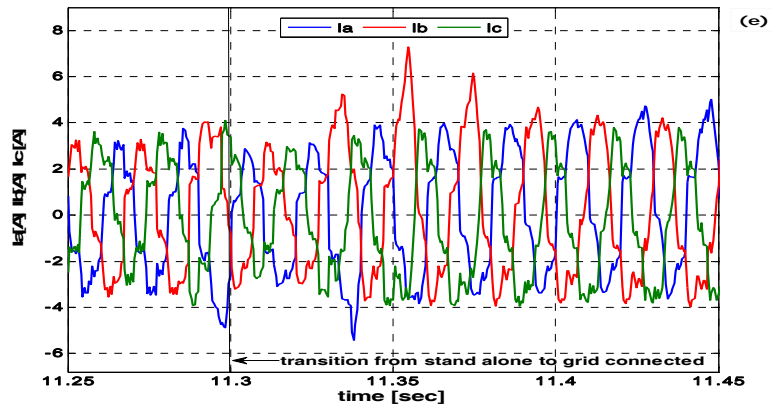| PMSG parameters	
Number of pole pairs (p)	3
Rated power	2.2 kW
Rated speed	1750 rpm
Rated frequency	87.5 Hz
Rated torque	12 Nm
Rated phase to phase voltage	380 V(rms)
Rated phase current	4.1 A(rms)
Stator resistance per phase (Rs)	3.3 Ω
d-axis inductance (Ld)	41.59 mH
q-axis inductance (Lq)	57.06 mH
Rotor permanent–magnet flux λ_{PM})	0.4832 V s rad-1
Inertia of the rotating system (J)	10.07_10-3 kgm^2
Viscous friction coefficient (Bm)	20.44_10-4Nms/rad

Comprehensive tests have been run after careful implementation and calibration of hardware and software.

a) Transition from stand alone to grid connected

First, the system is tested in stand-alone mode. At time t=10.8s the grid is connected through switch S and subsequently rendered as recovered. A synchronization signal (Fig. 4.8a) is automatically initiated in order to mach the phases between load voltages and grid voltages. When the error $\Delta\theta$ is between 0.01 ≤Δθ ≤ 0.01(Fig. 4.20a), the system switches from stand-alone control to grid connected control at t=11.3s (Fig 4.20b). Stand alone angle is synchronized with grid angle (Fig. 4.20d) and it can be noticed that there are no spikes in load voltage during this process or in the transition moment (Fig. 4.20c), but there are some reasonable transients in the load current (Fig.4.8e). The PMSG currents are shown in Fig. 4.20f without any significant transients when then system is switching from one control strategy to the other.The Dc-link voltage level was set to 620V (Fig. 4.8d) and during transition the voltage controller is capable to maintain the reference value with 8% variation. The estimated and measured rotor speed respectively the speed error is shown in Fig. 4.8 e,f. It can be noticed that during the transition the speed observer shows fairly good response.

(e)

transition from stand alone to grid connected

(f)

transition from stand alone to grid connected
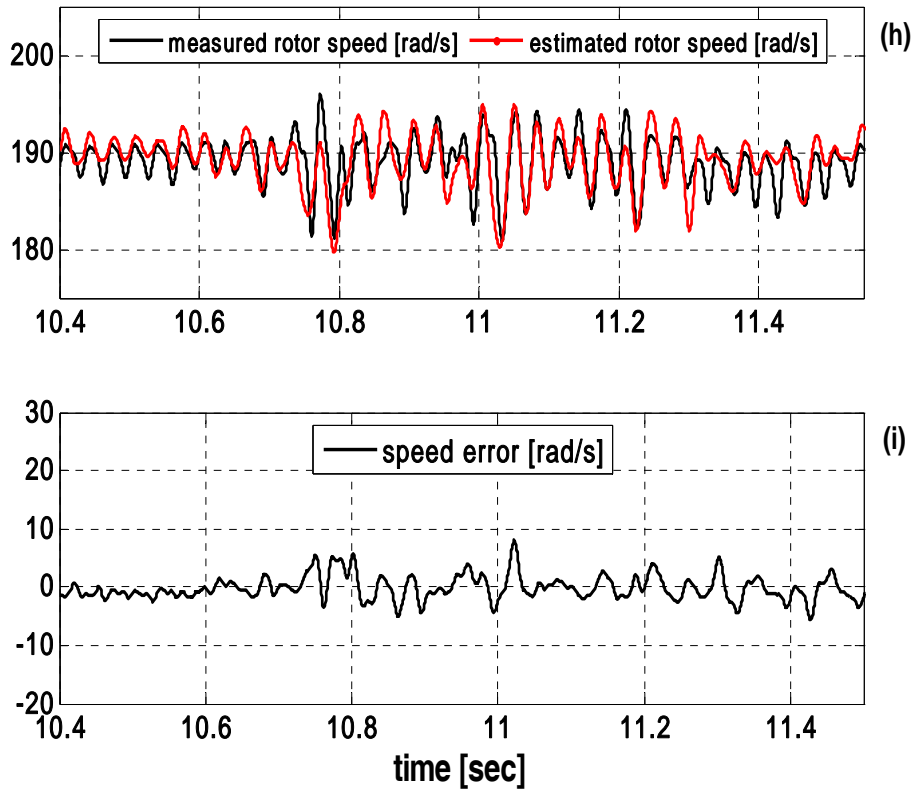
(g)
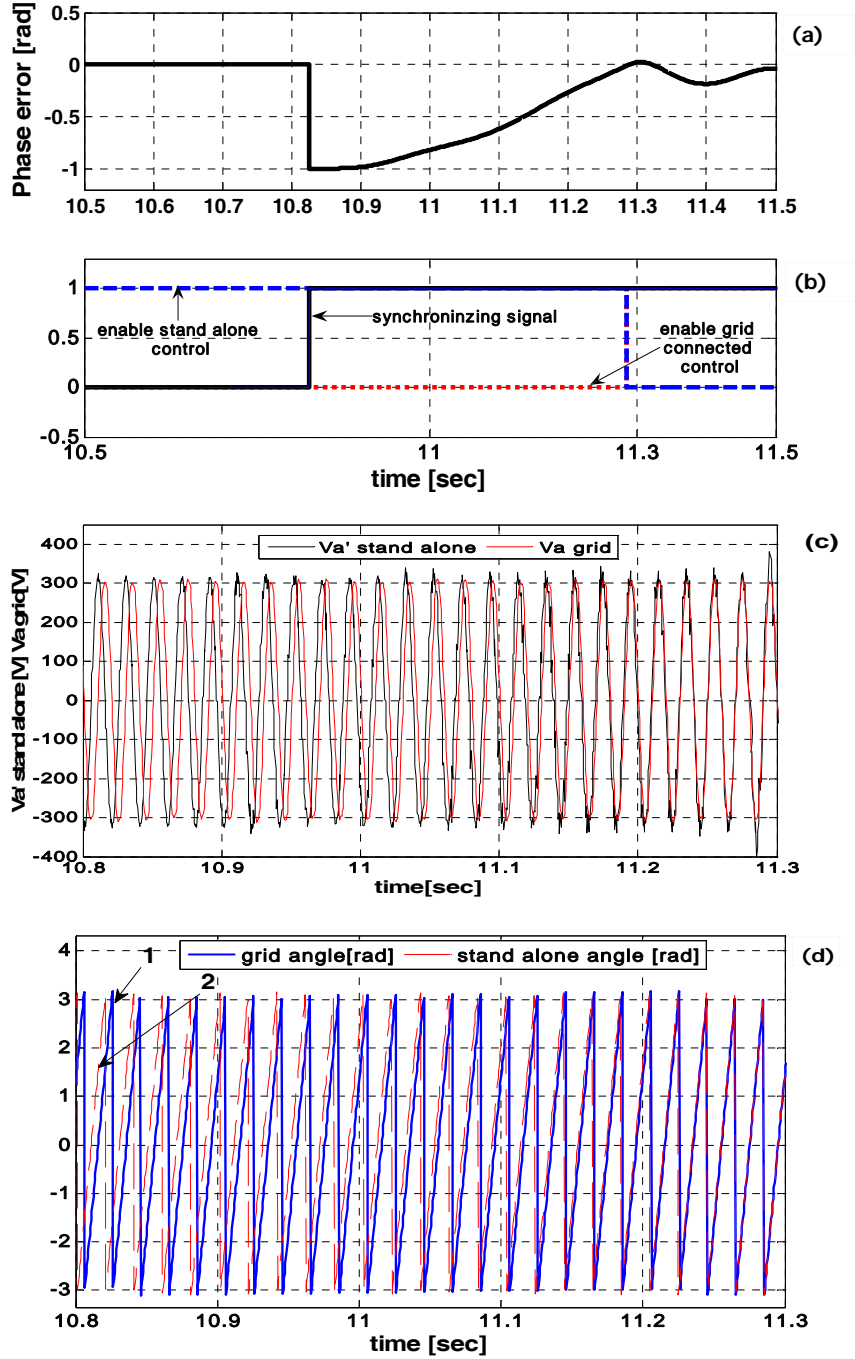
transition from stand-alone to grid connected

Fig. 4.20 Measured stand alone grid connected transition
a) Phase error
b) Synchronizing signal
c) Load voltages
d) (1)-Grid angle, (2)-stand-alone angle
e) Load currents
f) PMSG currents
g) Dc-link voltage
h) Estimated, measured rotor speed
i) Speed error

For stand-alone the phase voltage and its current waveforms, together with the voltage harmonic spectrum, without harmonic compensation, are presented in Fig.4.21 Using proportional resonant regulators for 6th and 12th harmonic voltage compensation, the ac voltage waveform is notably improved as it is seen in Fig. 4.22.
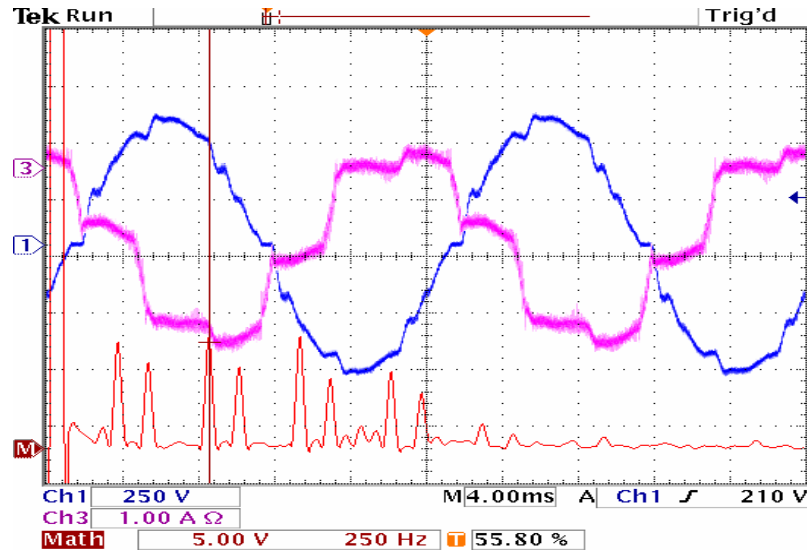
Fig. 4.21 Measured current and voltage waveform for diode rectifier load without synchronous voltage compensation
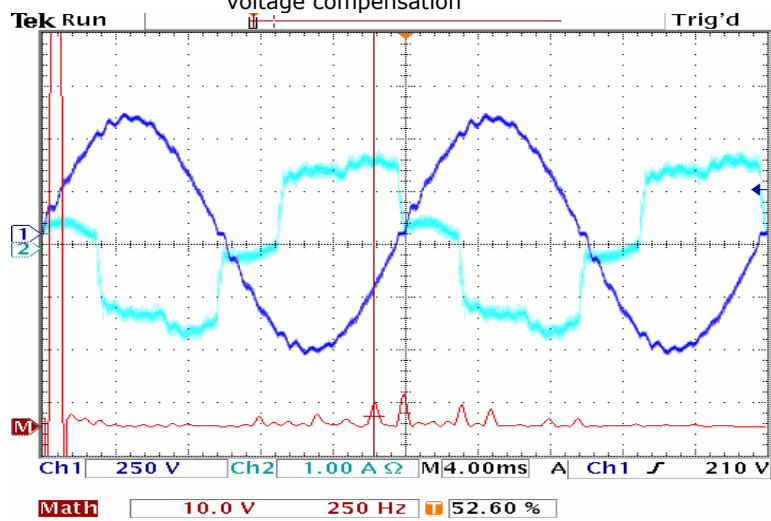

Fig.4.22 Measured current and voltage waveform for diode rectifier load without synchronous voltage compensation
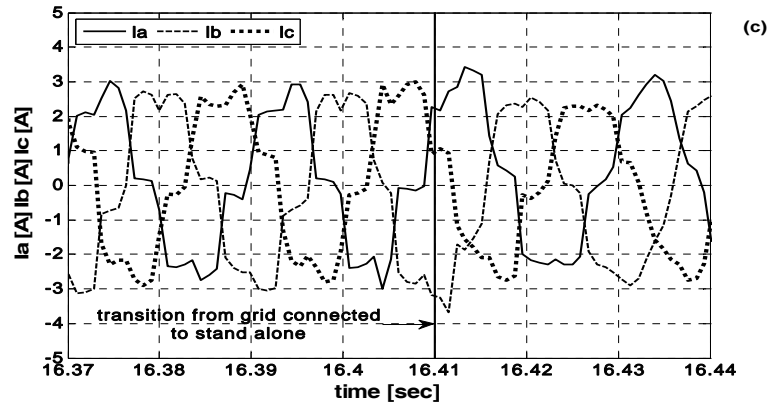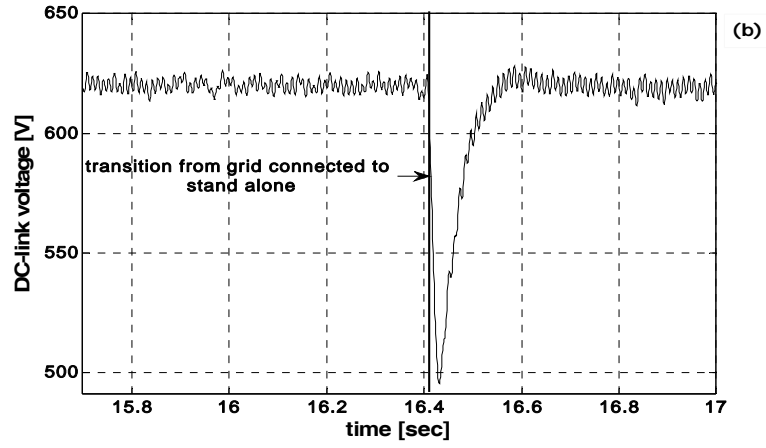
b) Transition from grid connected to stand alone

Subsequently a fault event is simulated by opening the static switch S at time t=15.8 s (Fig. 4.11a). When the monitoring system detects an increase in load voltage level or in frequency (Fig. 4.9a), it switches from grid connected to stand-alone mode.

The Dc-link voltage level was set to 620V (Fig. 4.11b)and during transition the voltage controller is capable to maintain the reference value with 15% variation Fig. 4.11c,d shows the load currents and PMSG currents, which both do not show any inrush spikes during entire transition period, indicating a smooth transition. It may be noticed that there are no important transients or generator current interruption during transition from grid connected to stand-alone mode. The estimated and actual rotor speed as well as the rotor speed error for steady state at 180 rad/s is depicted in Fig. 4.11e,f showing good tracking performance of position/speed observer used for motion- sensorless control of PMSG.
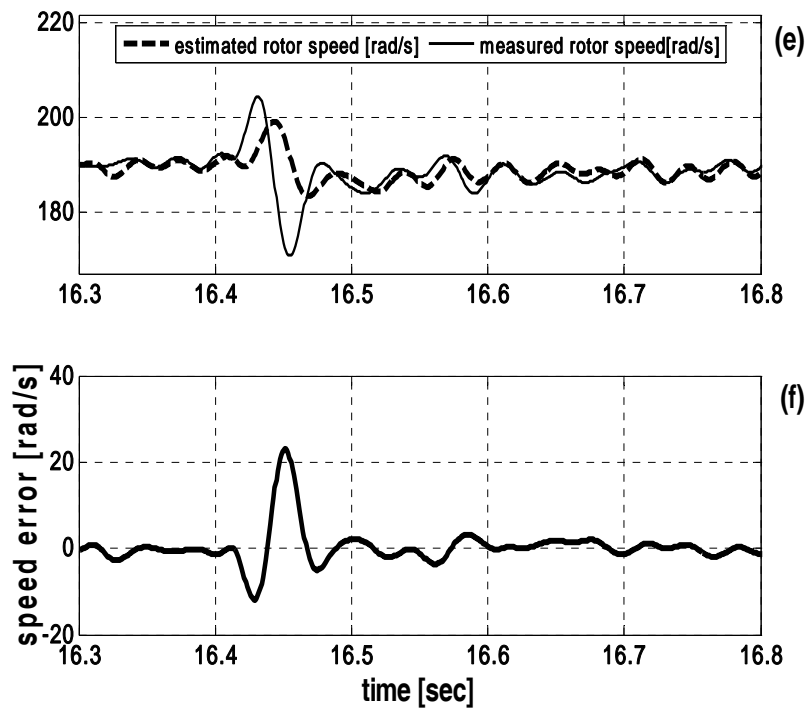
(b)

transition from grid connected to
stand alone

(c)

transition from grid connected
to stand alone

(d)

Iga

Igc

Igb

transition from grid connected
to stand alone
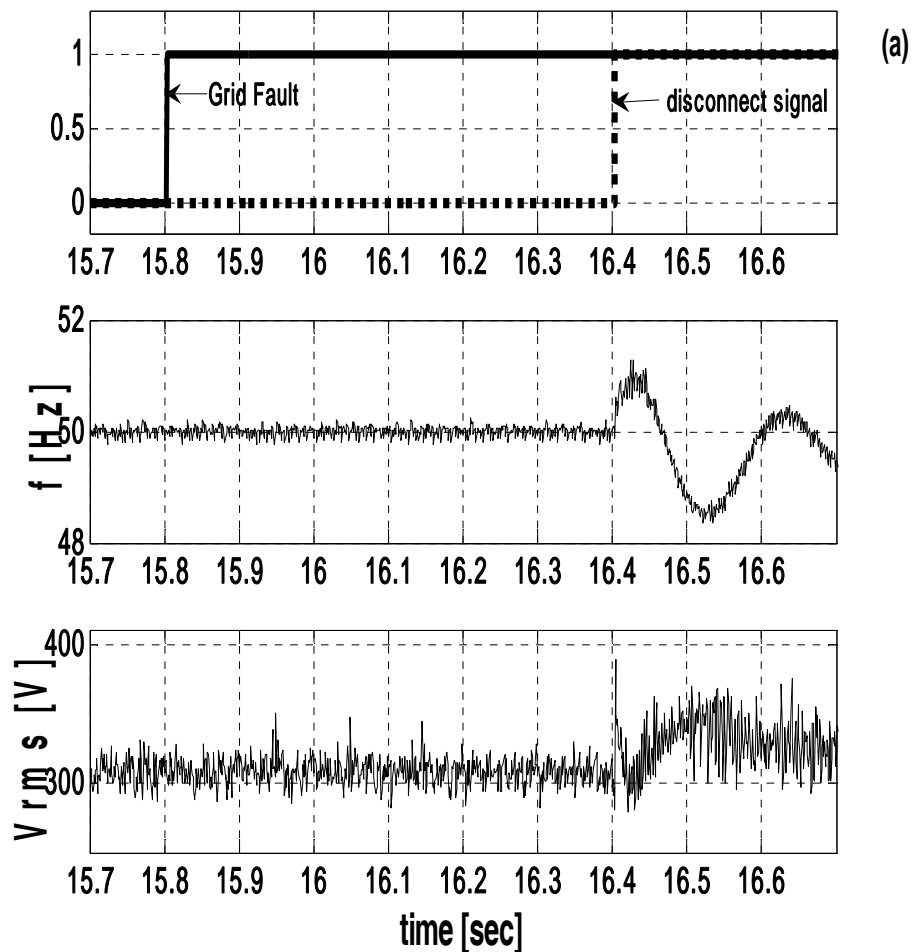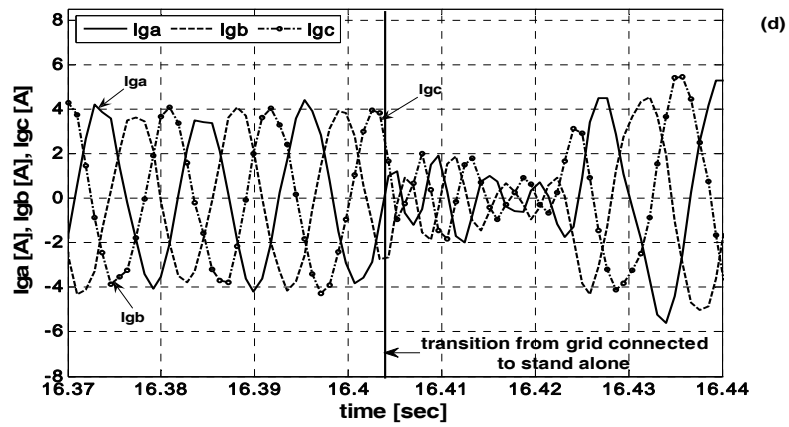
Fig.4.23 Measured stand-alone grid-connected transition
a) Disconnect signal, Urms, f_{grid}
b) Dc-link voltage
c) Grid currents
d) PMSG currents
e) Estimated and measured rotor speed
f) speed error

4.11. Discussion and Conclusion

A new, seamless (uninterrupted load current) transfer method from grid –connected to stand alone and vice versa was proposed for a motion sensorless PMSG wind energy system. Voltage harmonic compensation in stand alone mode is also provided. The system was experimentally shown capable of supplying local load in good conditions in both operation modes.

References:

[1] Lasseter, R.H.: Microgrids. Power Engineering Society Winter Meeting, vol.1, pp. 305-308, Jan. 2002.

[2] A.Cocconi, S.cuk and R.D.Middlebrook, "High-Frequency Isolated 4kW Photovoltaic Inverter for Utility Interface", Power Conversion International, May 1984, pp. 26-48.

[3] H. Watanabe, T.Shimizu and G.Kimura, " A Novel Utility Interactive Photovoltaic Inverter With Generation Control Circuit", Proc.24 th Annual Conference of the IEEE Industrial Electronics Society (IECON) 1998, pp. 721-5.

[4] N. Kikuchi, S.Shigeeda, H.Watanabe, T.Ohnishi and F.Harashima, " Single Phase Amplitude Modulation Inverter for Utility Interaction Photovoltaic System", Proc.25th Annual Conference of the IEEE Industrial Electronics Society (IECON) 1999. pp 385-9.

[5] G.-C. Hsich and J. Hung, "Phase-locked loop techniques—A survey,"*IEEE Trans. Ind. Electron.*, vol. 43, pp. 609–615, Dec.1996.

[6] S.-K. Chung, "Phase-locked loop for grid-connected three-phase power conversion systems," *Proc. Inst. Elect. Eng.*, vol. 147, no. 3, pp. 213–219, May 2000.

[7] R.Teodorescu, F. Blaabjerg, "Flexible control of small wind turbines with grid failure detection operating in stand-alone and grid-connected mode", IEEE Trans. Power Electron. vol. 19, no.5, Sept. 2004.

[8] R. Tirumala and N. Mohan, "Seamless transfer of grid-connected PWM inverters between utility-interactive and stand-alone modes," in *Proc. APEC'02 Conf.*, vol. 2, 2002, pp. 1081–1086.

[9] Z. Yao, Z. Wang, L. Xiao, Y. Yang, " A novel control strategy for grid-interactive inverter in grid-connected and stand-alone modes",

[10] I. Boldea, *"Variable Speed Generators",* CRC Press Florida, Taylor&Francis Group, 2006.

[11] F.Briz del Blanco, M.W.Degner, R.D. Lorenz, "Dynamic Analysis of Current Regulators for AC Motors Using Complex Vectors", IEEE TRANS.IND. APPL., VOL. 35, NO. 6, 1999.

[12] S. Buso, L. Malesani, P. Mattavelli, "Comparison of current control techniques for active filters applications", IEEE Trans. Industrial Electronics, vol. 45, no. 5, Oct. 1998, pp. 722-729.

[13] S. Buso, S. Fasolo, L. Malesani, P. Mattavelli, "A Dead-Beat Adaptive Hysteresis Current Control", IEEE   Trans. Industry Applications, vol. 36, no. 4, July/Aug. 2000, pp. 1174-1180.

[14] X. Yuan, W. Merk, H. Stemmler, J. Allmeling, "Stationary-frame generalized integrators for current control of active power filters with zero steady-state error for current harmonics of concern under unbalanced and distorted operating conditions" IEEE Tran. Ind. App., vol. 38, no. 2, Mar. /Apr. 2002, pp. 523-532.

[15]C.Lascu, L.Asiminoaei, I.Boldea, F.Blaabjerg, "High performance current controller for selective harmonic compensation in active power filters", OPTIM 2006.

[16] M. Fatu , L. Tutelea, R.Teodorescu, F. Blaabjerg, I. Boldea "Motion sensorless bidirectional PWM converter control with seamless switching from power grid to stand alone and back ",PESC'07, Orlando, Florida, USA, June 2007

Chapter 5

Novel motion sensorless control of stand alone permanent magnet synchronous generator (PMSG): harmonics and negative sequence voltage compensation under nonlinear load

Abstract

The present chapter introduces a novel harmonics voltage compensation solution for nonlinear (diode rectifier) load operation in stand alone PMSG with bidirectional converter motion sensorless vector control. Both the case of three phases and two phase output of the load side converter, with voltage symmetrisation by inversed component active cancellation, are treated. The latter is called unbalanced load handling. The main solutions for motion sensorless vector control of the two back-to-back PWM converters with loops to compensate output voltage harmonics and its negative sequence for diode rectifier load are introduced, implemented and validated through experimental results on 2.2 Kw PMSG systems.

5.1 Introduction

In most of the countries worldwide, there are remote communities, which are not served by the main electrical grids and may never be connected to them because of economical reasons. Diesel generators are mainly used to serve them. The potential for wind energy connected to small or isolated grids is likewise enormous, but until recently power production from wind energy, fed into small and isolated grids, have been economically unattractive due to inefficiency and technical problems with the necessary diesel generation back up system. Normally when a diesel engine operates at less than 30% of its load capacity, the diesel engine will have a bad fuel economy and will be choking thus reducing the efficiency of the engine and causing its deterioration[1].

Recently, technical developments have solved these problems, and with these developments it is now possible to operate wind-diesel system up to 100% wind penetration. With this development, remote areas and island are offered the opportunity to utilize wind energy in combination with diesel generated power (see Fig.5.1) for their power production. Such a viable wind/diesel (WD) stand-alone system will be able to operate with an estimated 50% to 80% fuel saving compared to power supply from diesel generation alone [1].

One major advantage of a wind energy based stand-alone power system is that it reduces diesel fuel consumption. In general induction generator is widely used in small renewable power plants because it offers several advantages over conventional synchronous generator: reduced unit cost, ruggedness, brushless (in squirrel cage construction), absence of separate DC source, ease of maintenance, self-protection against severe overloads and short circuits. Major disadvantage of an induction generator is that it requires reactive power for its operation. In case of

grid-connected system induction generator can get the reactive power from grid/capacitor banks, whereas in case of isolated/autonomous system reactive

power can only be supplied by capacitor banks/synchronous generator. Permanent magnet synchronous generators (PMSGs) connected to the grid by inverters are widely used in variable-speed wind generators for their high performances.
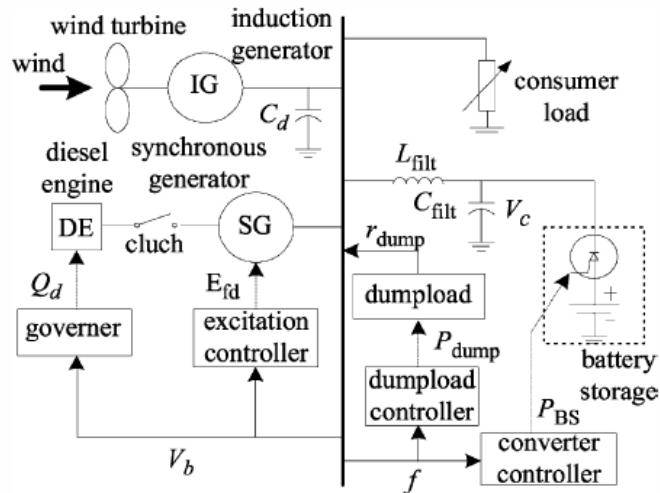

Fig. 5.1 Schematic of a generalized wind diesel system with induction generator

The main reasons rely on their optimal characteristics, which are, for example, higher efficiency and higher generated power-weight ratio than induction generators. PMSGs are also convenient, with respect to the losses, because they have a loss-free rotor, and the power losses are mainly related to the stator windings and the stator core. The ratio of the copper and iron power losses is a key issue in determining the maximum efficiency point as function of the mechanical torque that is connected to the generator shaft.

However, such stand-alone power systems are characterized by low inertia and poor reactive power support and therefore face wide voltage and frequency variations due to changes in load demand. The integration of wind turbines in such systems provokes additional power quality problems in the form of frequency and voltage fluctuations, due to rapidly changing nature of the wind [2−4].
The existing method used to solve these problems involves installation of batteries. The batteries are however constrained by their load cycles. There are some environmental concerns related to battery storage due to toxic gas generation during battery charge/discharge operation. The disposal of hazardous materials presents some disposal problems. On the other hand, the technical improvements in superconducting magnetic energy storage (SMES) and a better knowledge of dealing with cryogenic systems have made the SMES units to penetrate the market very fast [5−8]. The dynamic performance of an SMES system is far superior to other storage technologies. The shorter response time is the leading advantage and at the same time, system operation and life time are not influenced by the number of duty cycles or the depth of discharge as is the case for classical batteries. The estimated life of a typical SMES system is about 30 years. With the on going fast evolution in

power electronics and SMES technology the estimated cost within 10 years is expected to be almost 25% of present cost. SMES systems are compact, self-contained and highly mobile. They contain no hazardous chemicals, produce no flammable gases and can be kept at remote locations.
Another configuration for a hybrid wind generation for stand alone systems is depicted in Fig.5.2 [8].
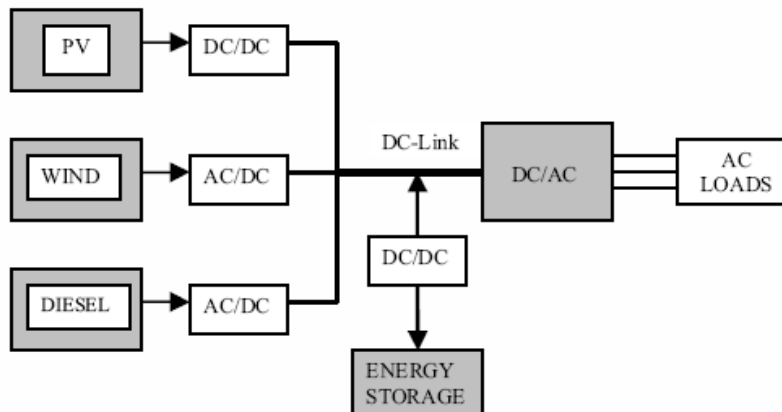

Fig.5.2 Hybrid energy system

Each generating component of the hybrid system has its raw power converted through rectifiers and DC converters to a standardized Dc-link voltage. The DC power is then inverted to supply the AC local grid.
Each of the generators can be controlled for maximum efficiency when possible, or to follow the load in the absence of energy storage or in the case of the storage being full.
The PMSG with diode rectifier dc load [10-12] or with bidirectional full power converter control for wind energy conversion has been recently proposed due to its high efficiency and lack of excitation circuit, both for power grid and stand alone applications with ac output constant voltage and frequency control [13,14].
   One of the main challenges is to reduce harmonic pollution caused by nonlinear loads which may cause additional losses and heating in the electrical equipment, failures of the sensitive equipments, resonances and interference with electronic equipment, premature ageing. Active filters are applicable to compensate current-based distortions such as current harmonics and also voltage based distortion such as voltage harmonics voltage flickers, voltage sags and voltage unbalanced. Most of these approach the control by means of filter current control implemented in various reference frames: stationary, fundamental, or harmonic frame. The stationary reference frame current control includes: hysteresis control [15, 16], dead-beat control [17], and linear equivalent-PI control with selective harmonic compensation [18].
Nonlinear (diode rectifier dc load, for example) balanced and unbalanced (one load side inverter phase terminal open) load performance, with 6, 12,17,19,23 output ac voltage harmonic compensation, with bidirectional converter, and motion sensorless control, has not yet been demonstrated with experimental results [14].
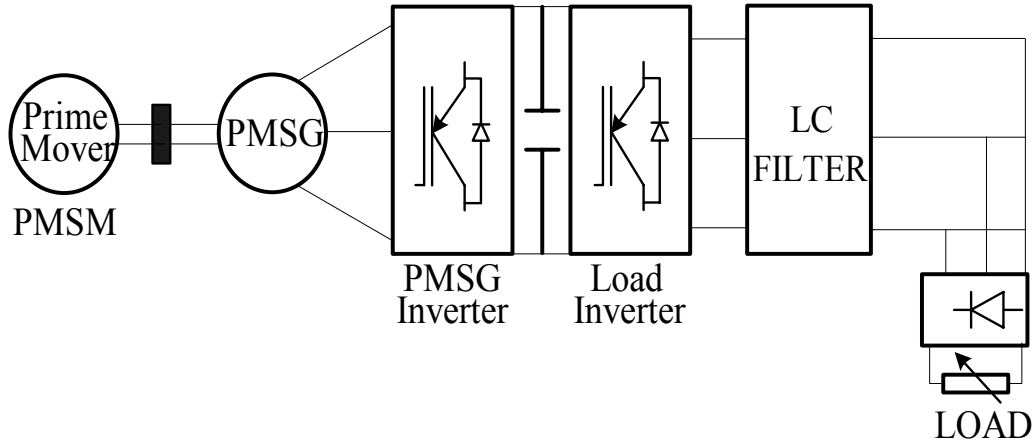
Fig.5.3 Stand alone wind energy conversion system

5.2. PMSG model

The space-vector model of PMSG, equipped with interior permanent magnets, in rotor reference frame (Park's transformation in dq axes) is [15]:

$$i_s R_s - \underline{V}_s = -\frac{d\underline{\Psi}_s}{dt} - j\omega\underline{\Psi}_s \tag{5.1}$$

$$\underline{\Psi}_s = \Psi_d + j\Psi_q \tag{5.2}$$

$$\Psi_d = \lambda_{PM} + L_d i_d \tag{5.3}$$

$$\Psi_q = L_q i_q \tag{5.4}$$

$$\underline{V}_s = V_d + jV_q \tag{5.5}$$

$$\underline{i}_s = i_d + ji_q \tag{5.6}$$

where: $\underline{V}_s$, $\underline{i}_s$ and $\underline{\Psi}_s$ are the stator voltage, current and flux vector, respectively; R_s is the stator phase resistance; L_d and L_q are the dq inductances; λ_{PM} is the PM flux; p is the pair pole number. Table II shows PMSG specifications.
A typical stand alone wind energy conversion system connected to a local load without any storage equipment is depicted in Fig.5.3. The considered plant in this application is the LC filter attached to the load-side inverter and a nonlinear load (three-phase diode rectifier).
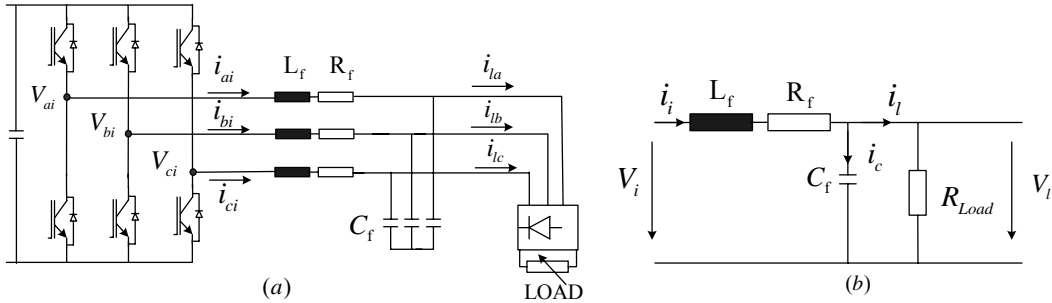
Fig. 5.4 (a) Configuration of the load-side inverter connected to the local load
(b) Single phase representation of the plant

Based on Fig.4, the relation for the currents flowing through the filter is given by:

$$i_i = i_C + i_l \qquad (5.7)$$

while the voltages can be described as:

$$V_i = (R_f + sL_f)i_C + V_C \qquad (5.8)$$

$$V_C = \frac{1}{sC_f}i_C \qquad (5.9)$$

$$V_l = i_l R_{load} \qquad (5.10)$$

Finally the transfer function between the load voltage and the inverter voltage is:

$$G_{plant}(s) = \frac{V_l(s)}{V_i(s)} = \frac{R_{load}}{s^2 R_{load}C_f L_f + s(R_{load}R_f C_f + L_f) + R_{load} + R_f} \qquad (5.11)$$

The load and LC filter parameters are listed in Table II. below:

TABLE II
LC filter parameters

R_{load}	50 Ω
R_f	0.4 Ω
L_f	0.01 H
C_f	4.2 μF

5.3. Proposed Voltage harmonics and inversed component compensation scheme

 In stand alone mode the voltages are controlled in terms of amplitude and frequency. The voltage control is divided in two distinct parts: fundamental voltage control and harmonic voltage control. In the first case the d-axis respectively q-axis voltage controllers are standard PI controllers, receive as inputs the reference

$V_d^* = 220\sqrt{2}$ voltage respectively $V_q^* = 0$. The dc link voltage and current controllers lower the reference voltage for the main voltage controller when the dc link voltage is below a designated level; respectively the load current exceeds a certain level [16].

$$V_{DC\text{-}limit} = (k_{p\_DC\_limit} + \frac{k_{i\_DC\_limit}}{s})(V_{dc}^* - V_{dc}) \qquad (5.12)$$

$$V_{Irms} = (k_{p\_Irms} + \frac{k_{i\_Irms}}{s})(I_{rms}^* - I_{rms}) \qquad (5.13)$$

where $k_{p\text{-}Dc\text{-}limit}=0.2$, $k_{i\text{-}Dc}limit=4$ are Dc-link controller gains respectively $k_{p\text{-}Irms}=5$, $k_{i\text{-}Irms}=500$ are controller gains for current limiter regulator. So, finally the reference for d-axis voltage can be calculated as:

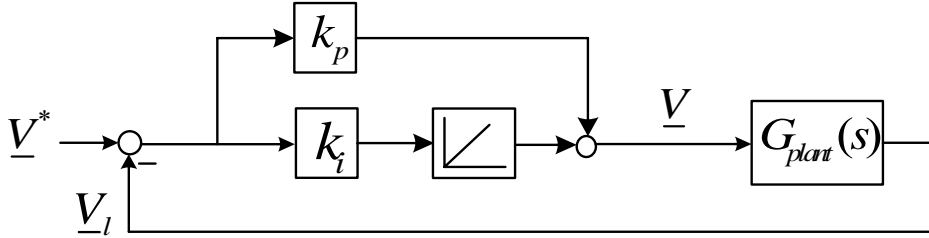$$V_{dref}^* = V_d^* - V_{DC\_limit} - V_{Irms} \qquad (5.14)$$

Fig.5.5 Fundamental voltage control loop in synchronous reference frame

The fundamental voltage controller (Fig.5.5) is a feedback controller which provides pole-zero cancellation for the plant. The reference voltage vector for the fundamental voltage controller is $\underline{V}^* = V_{dref}^* + jV_q^*$. The PI voltage controller transfer $G_{PI}(s)$ is defined as:

$$G_{PI}(s) = k_p + \frac{k_i}{s} \qquad (5.15)$$

Using complex vector notation, the model for the plant in stationary reference frame is transformed to synchronous reference frame by substituting the "s" operator with "$s\text{-}j\omega_{sa}$" [20]. Considering an ideal inverter $\underline{V}=\underline{V}^*$ the close loop transfer function for the voltage control in synchronous reference frame can be written as:

$$H(s) = \frac{G_{PI}(s) \cdot G_{plant}(s)}{1 + G_{PI}(s) \cdot G_{plant}(s)} \qquad (5.16)$$

The frequency response of $H(s)$ in synchronous frame is represented in Fig. 5.6 on linear scales. The response is obtained for $k_p=0.1$ and $k_i=10.$
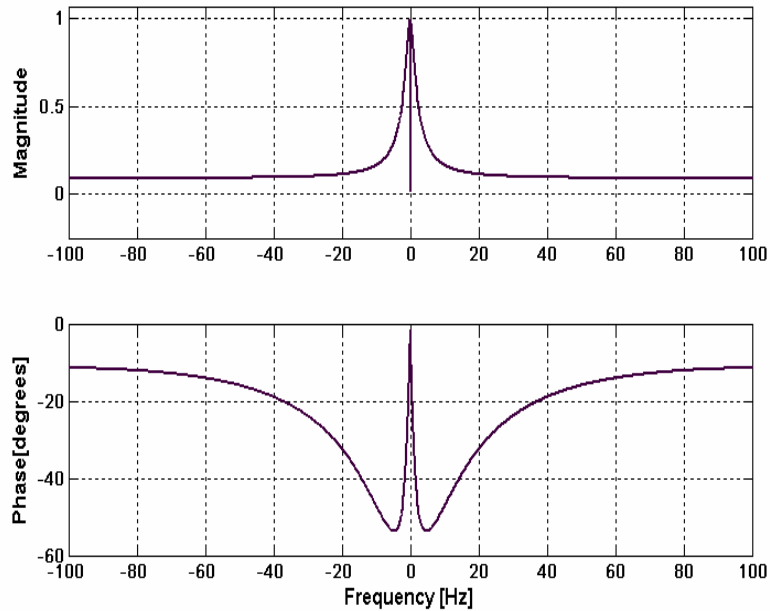
Fig.5.6 Frequency response of fundamental voltage controller in synchronous frame

The nonlinear load in this application (three-phase diode rectifier) generates nonsinusoidal currents with harmonic spectrum containing sidebands of multiple of the six of the fundamental frequency (Fig. 5.13). Same harmonics are contained also in the waveform of the load voltages.

In a second case the harmonic voltage control uses the line voltage measurements to detect the harmonic voltage to be compensated. The filter acts as a harmonic voltage source, injecting into the load voltages harmonic voltages with the same amplitude and opposite phase to the load voltages. The control structure for the load side inverter is shown in Fig. 5.7. Since coordinate rotation provides a frequency shift by $-\omega_{sa}$, in fundamental frame, harmonics orders $k=6n\pm1$ become $k=6n$. The harmonic voltage controller, is realized as superposition of individuals controllers, each design for a specific pair of harmonics ($k=6, 12, 17, 19, 23$) of positive and negative sequence. The harmonic compensator is proportional resonant type (PR) defined as [21]:

$$G_{PR_k}(s) = 2\frac{K_{pk}s^2 + K_{ik}s}{s^2 + (k\omega_{sa})^2}$$

(5.17)

Due to intense computational effort needed to implement the proposed harmonic compensation algorithm and the sample frequency set during the experiments at 9 KHz, the implementation of the PR controller tuned on 18th harmonic had not the expected results. So in order to compensate above 12th order PR resonant controllers, implemented in stationary reference frame, have been used for each of the odd 17th, 19th, 23th [12].
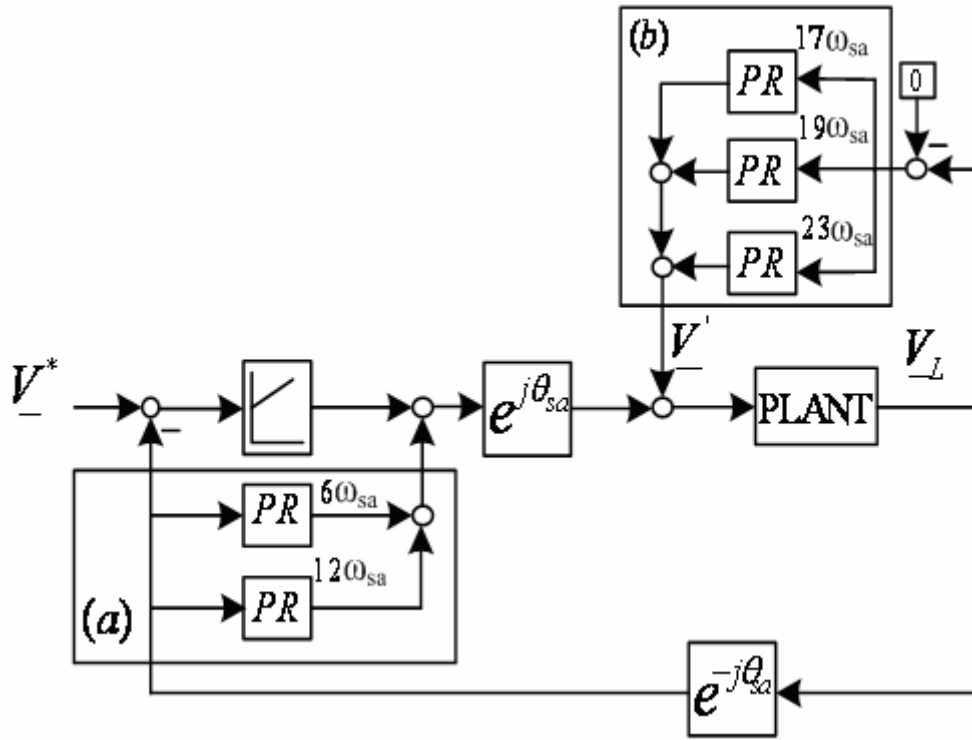
Fig.5.7 Harmonic voltage compensator structure implemented in:
a) synchronous reference frame
b) stationary reference frame

The voltage control loop, in harmonic frame, is design for dc quantities since the harmonic voltage of interest are dc in their own rotating frame. Assuming an ideal inverter the transfer function of harmonic voltage loop in synchronous reference frame is:

$$G_1(s) = \frac{V_L}{\underline{V}^*} = \frac{G_{plant}(s) \cdot G_{PI}(s) \cdot \left(\sum_{k=6,12} G_{PR_k}(s) \right)}{1 + G_{plant}(s) \cdot G_{PI}(s) \cdot \left(\sum_{k=6,12} G_{PR_k}(s) \right)} \tag{5.18}$$

This transfer function provides unity gain for the frequency $k\omega_{sa}$ $(k=6, 12)$. The frequency response of the $G(s)$ in harmonic reference frame is shown in Fig.5.8a for both positive and negative frequencies, on linear scales. The response was obtained for $k_{p6}=0.00046$, $k_{i6}=0.5$, $k_{p12}=0.0003$, $k_{i12}=0.9$.
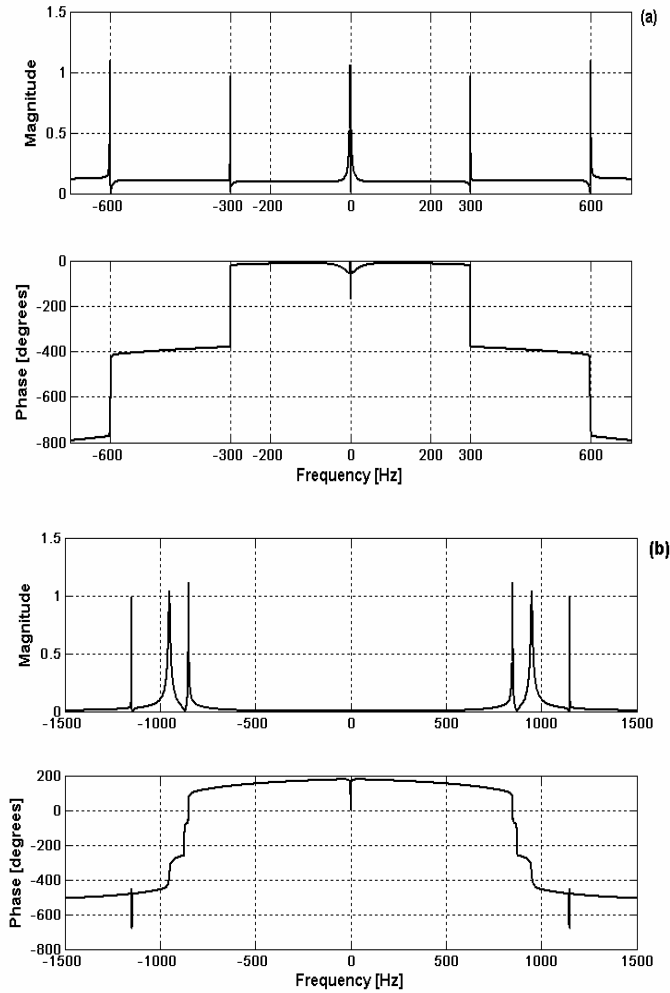
Fig.5.8 (a) Frequency response of voltage harmonic controller for 6th and 12th
(b) Frequency response of voltage harmonic controller for 17th, 19th,23th

The transfer function of harmonic voltage loop in stationary reference frame is:

$$G_2(s) = \frac{V'}{V_L} = \frac{G_{plant}(s) \cdot (\sum_{k=17,19,23} G_{PR_k}(s))}{1 + G_{plant}(s) \cdot (\sum_{k=17,19,23} G_{PR_k}(s))} \tag{5.19}$$

This transfer function provides unity gain for the frequency $k\omega_{sa}$ ($k=17, 19, 23$), and zero gain for the dc signals, i.e. it guarantees complete rejection of the fundamental frequency (which is dc quantity in its own frame). The frequency

response of $G_2(s)$ in stationary frame is represented in Fig. 5.8b for both positive and negative frequencies, on linear scales. The PR parameters are: $k_{p17}=0.002$, $k_{i17}=0.06$, $k_{p19}=0.008$, $k_{i19}=0.005$, $k_{p23}=0.00019$, $k_{i23}=0.0005$;
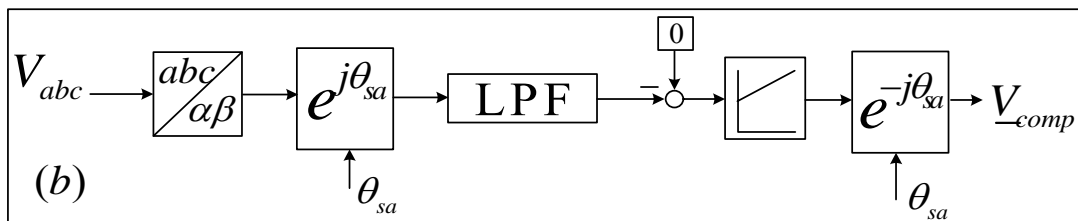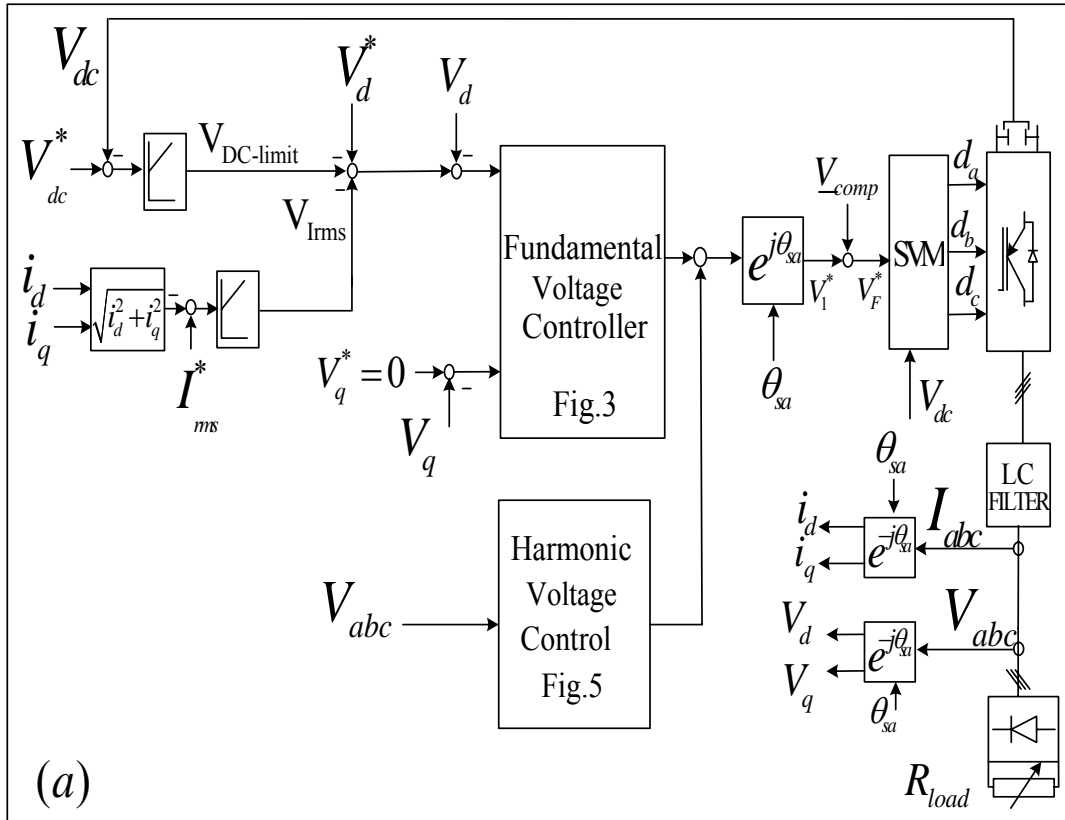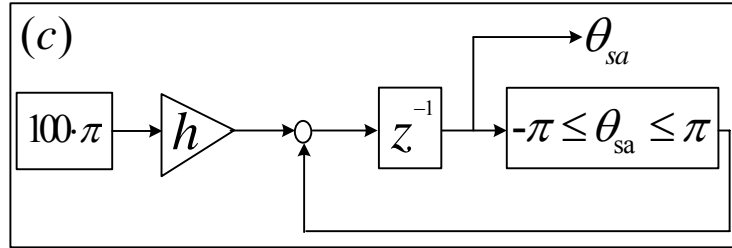
Fig.5.9 Load side inverter control
(a) Load side inverter control
(b) Negative sequence compensation
(c) Stand–alone angle computation

When an unbalanced ac load is connected (or an output terminal of the load side inverter is open), in order to keep the voltage symmetry[22]-necessary for remaining ac load- the negative sequence voltage is compensated. We can write the magnitude of the fundamental voltage as a sum of its sub harmonics:

$$V_L = V_{50} \cdot e^{j \cdot \theta sa} + V_{-50} \cdot e^{-j \cdot \theta sa} + V_{250} \cdot e^{j \cdot 5 \cdot \theta sa} + \ldots\ldots \quad (5.20)$$

The voltages are additionally rotated with inversed angle, so eq. (5.20) becomes:

$$V_L = V_{50} \cdot e^{j \cdot \theta sa} \cdot e^{j \cdot \theta sa} + V_{-50} \cdot e^{-j \cdot \theta sa} \cdot e^{j\theta sa} + V_{250} \cdot e^{-j \cdot 5 \cdot \theta sa} \cdot e^{j \cdot \theta sa} + \ldots\ldots \quad (5.21)$$

After this coordinate transformation the negative sequence is compensated in dc quantities. In order to eliminate the second order harmonic a second order low pas filter (LPF) with cut-off frequency at 50 Hz is used. A PI regulator used to compensate the error. The controller gains were selected as: $k_{p\_comp}=0.2$, $k_{i\_comp}=5$. The output of the controller is translated in stationary coordinates and added to the total reference voltage vector and is realized by a Space Vector Modulation (SVM) unit.

5.4. Proposed motion sensorless vector control with state observers for stand alone

The configuration of the general proposed motion sensorless control system is depicted in Fig.5.10. The machine side converter is voltage controlled along the q-axis. We determine the reference i_q^* by a PI controller which uses the deviation between reference dc link and measured dc link voltage.

$$i_q^* = \left(k_{pV_{DC}} + \frac{k_{iV_{DC}}}{s} \right) e_{V_{DC}} \quad (5.22)$$

where $k_{pV_{DC}}$ and $k_{iV_{DC}}$ are PI regulator gains and $e_{V_{DC}}$ is the Dc-link voltage error. The PI gains have been chosen, $k_{pVdc} = 0.02$ and $k_{iVdc} = 0.5$,for slow dynamic response in order to avoid interface between the current and voltage controllers.
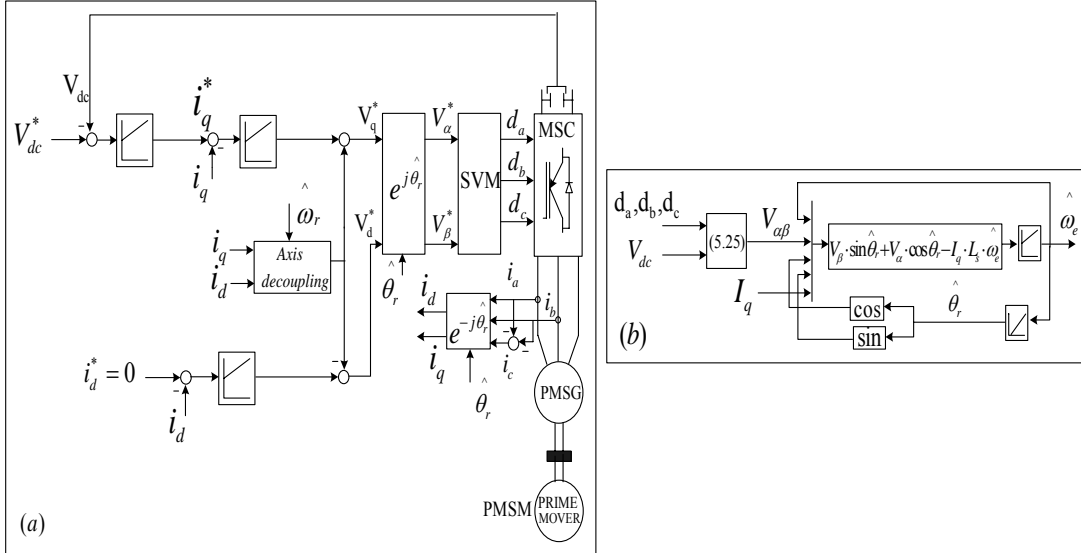
Fig.10 Sensorless control of PMSG [13]
a) General scheme
b) The position and speed observer

The current regulators are implemented in synchronous reference frame and produce the reference voltage vector $\underline{V}^* = V_d^* + jV_q^*$:

$$V_d^* = (k_{pcrt} + \frac{k_{icrt}}{s})e_{id} + \overset{\wedge}{\omega}_r \, i_q L_s \qquad (5.23)$$

$$V_q^* = (k_{pcrt} + \frac{k_{icrt}}{s})e_{iq} - \overset{\wedge}{\omega}_r (i_d L_s + \lambda_{PM}) \qquad (5.24)$$

where k_{pcrt} and k_{icrt} are PI controllers gains and e_{id} and e_{iq} are the current errors respectively. The gains of current controllers are $k_{pcrt} = 25.0$ and $k_{icrt} = 25000$.

The rotor position and speed estimator used is the same as it was presented in chapter 3.

5.5 Test platform and experimental results

The electrical block-diagram of the test platform is shown in Fig. 5.11. The testing setup consists in a PMSG of 12 Nm rated torque driven by a Siemens SIMOVERT MASTERDRIVE operated in open loop torque control mode and the two inverters are Danfoss VLT 5005.The nonlinear load considered in the experiments is a three-phase diode rectifier with a variable resistance. The control structure was implemented in a Dspace DS1103 hardware platform. The sampling and switching frequency are set to 9 kHz In all cases the total harmonic distortion (THD) of the

voltage is measured with a three-phase Voltech PM3000 power meter. The PMSG parameters are presented in Table II.

Table II

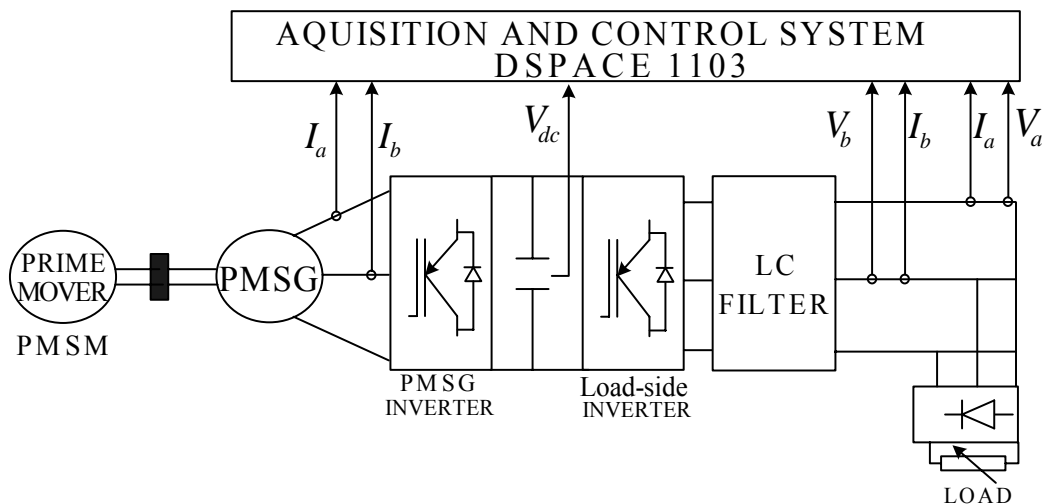| PMSG parameters	
Number of pole pairs (p)	3
Rated power	2.2 kW
Rated speed	1750 rpm
Rated frequency	87.5 Hz
Rated torque	12 Nm
Rated phase to phase voltage	380 V(rms)
Rated phase current	4.1 A(rms)
Stator resistance per phase (Rs)	3.3 Ω

Fig. 5.11 Test platform

The voltage harmonic content was studied for different diode rectifier dc variable load . The phase voltage and its current waveform together with the voltage harmonic spectrum are presented in Fig. 5.12. **without** harmonic compensation. Using proportional resonant regulators for harmonic voltage compensation the ac voltage waveform is improved as it is seen in Fig.5.13. The first peak of the spectrum harmonic, which is out of range, is the fundamental voltage magnitude. The harmonic spectrum in logarithmic scale is represented in both situations in Fig.5.14,15. Using the inverter control in order to compensate the voltage harmonics we can eliminate the first voltage harmonics (of the order 6,12,17,19,23) despite the fact that they still exist in current (Fig. 5.16) The THD factor for the uncompensated harmonic voltages is 1.338% and with harmonic compensation was reduced to 0.719%.
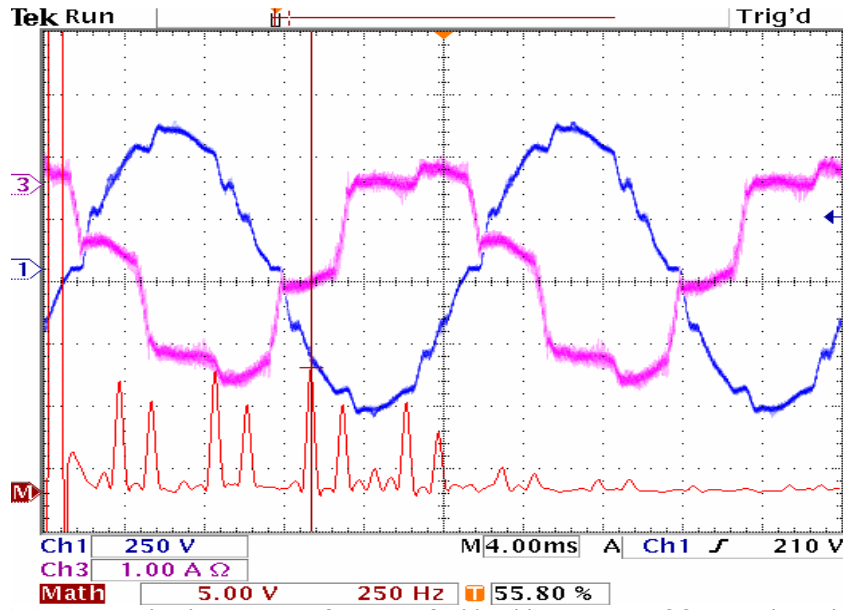
Fig.5.12 Current and voltage waves for a rectified load harmonics **without** voltage harmonic compensation
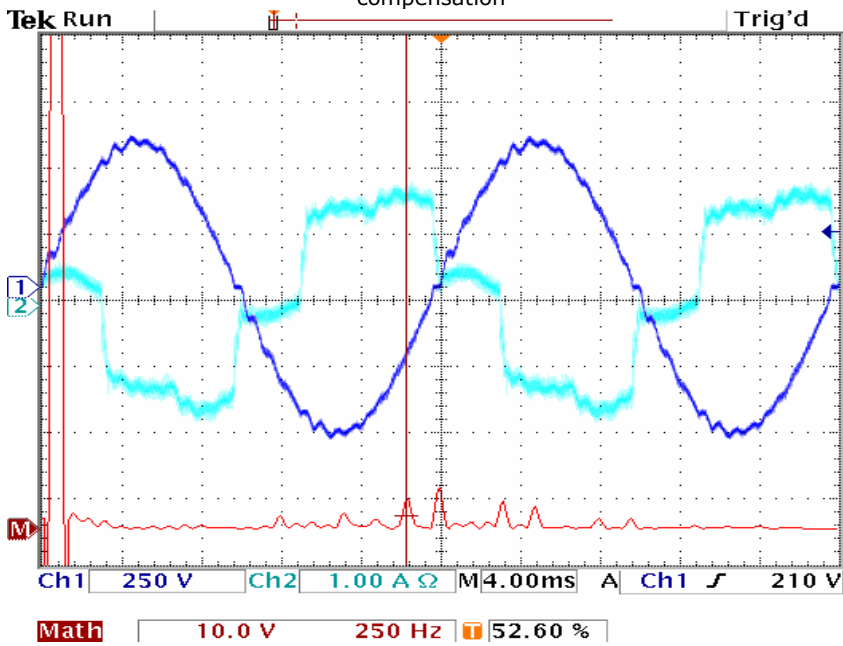

Fig. 5.13 Current and voltage waves for a rectified load **with** voltage harmonic compensation

The voltage harmonic spectrum **without and with** harmonic compensation obtained from power analyzer are depicted in Table III respectively in Table IV.

Table III Voltage harmonic spectrum without harmonic compensation

Voltage Harmonics (VH)	Channel 1	Channel 2	Channel 3
VH 1	229.9	229.6	229.9
VH 5	1.2060	1.0163	1.4500
VH 7	387.7 m	788.9 m	431.2 m
VH 11	1.4914	1.8461	1.6053
VH 13	1.1270	1.1379	986.2 m
VH 17	7.284	7.360	7.360
VH 19	5.776	4.633	4.690
VH 23	6.081	5.445	6.533

Table IV Voltage harmonic spectrum with harmonic compensation

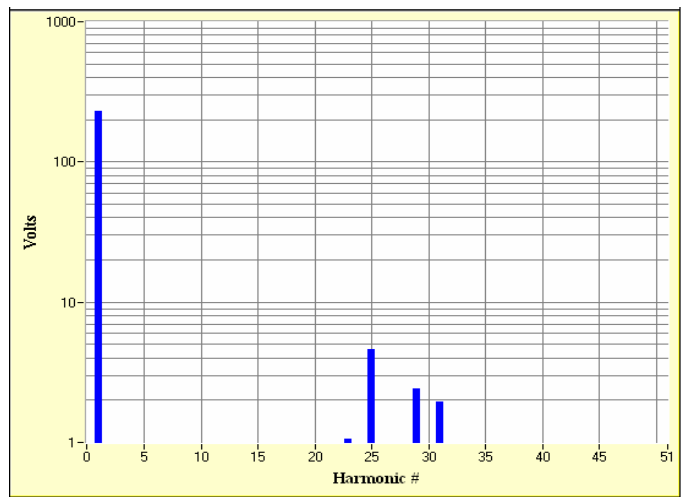| Voltage Harmonics (VH)	Channel 1	Channel 2	Channel 3
VH 1	231.3	230.1	230.2
VH 5	637.8 m	416.9 m	855.8 m
VH 7	638.1 m	264.6 m	606.3 m
VH 11	580.8 m	821.3 m	276.7 m
VH 13	1.0726	372.3 m	289.9 m
VH 17	232.9 m	394.1 m	173.48m
VH 19	970.5 m	553.1 m	454.3 m
VH 23	801.0 m	553.1 m	583.7 m

Fig. 5.14 Voltage harmonic spectrum **without** voltage harmonic compensation
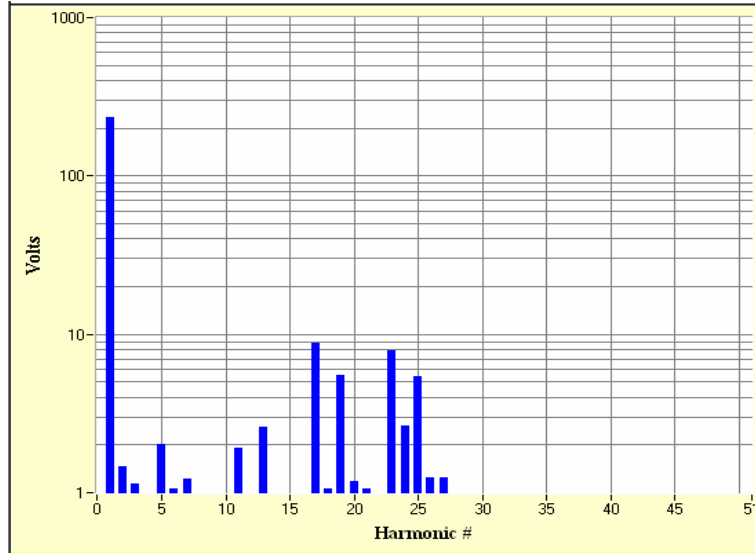
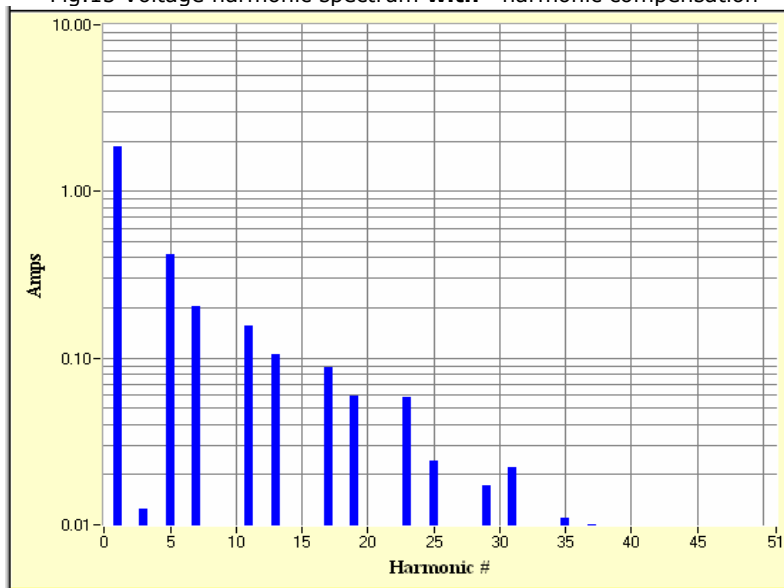Fig.15 Voltage harmonic spectrum **with**   harmonic compensation

Fig.5.16 Ac source (load inverter output) current harmonics for balanced diode rectifier load – test results

The behavior of the system is investigated for the case when one load side inverter terminal is open (t=16.5s) and when the terminal is reconnected (t= 33.2s). The generator speed is kept constant at 192 rad/s. The DC link voltage level is kept at 640V.
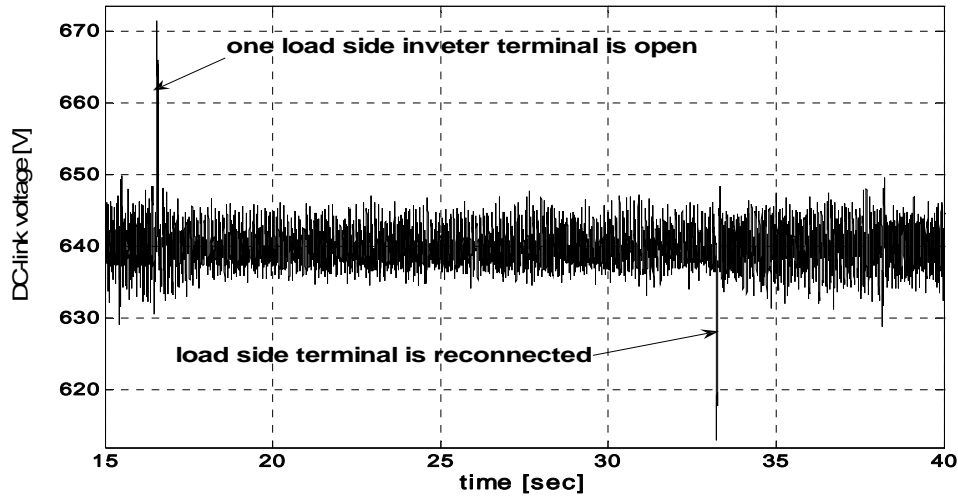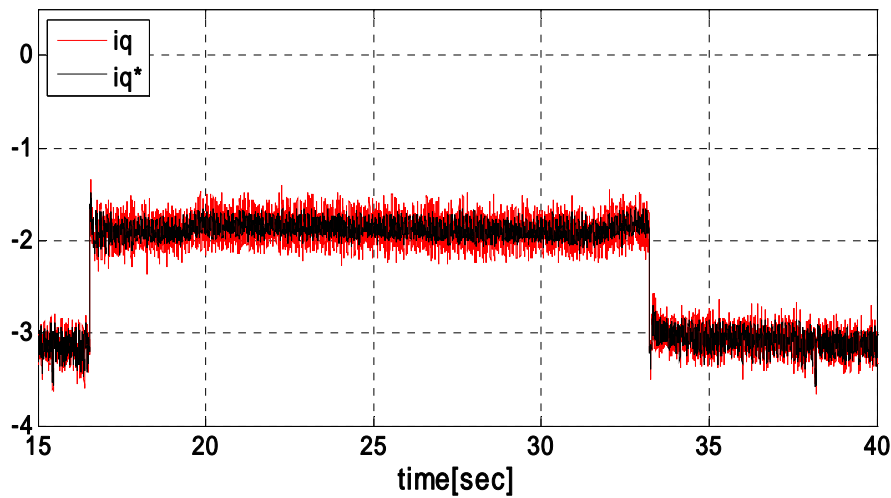
Fig.17 DC-link voltage

Fig.5.18 Reference and measured machine side Iq current

When the fault occurs a small increase (cca. 5%) is recorded in the DC link voltage level (Fig. 5.17) but no spikes in PMSG currents (Fig. 5.19b). In order to maintain the designated level the DC voltage controller reduces the reference for i_q current controller (Fig. 5.18). When the fault is cleared (t=32.5s) it can be noticed that the systems recovers quickly without major spikes in Dc-link voltage and PMSG currents (Fig.5.17, 5.18). The estimated and actual rotor speed are depicted in Fig.5.20, showing a good tracking performance of the position/speed observer used for motion sensorless control of PMSG.
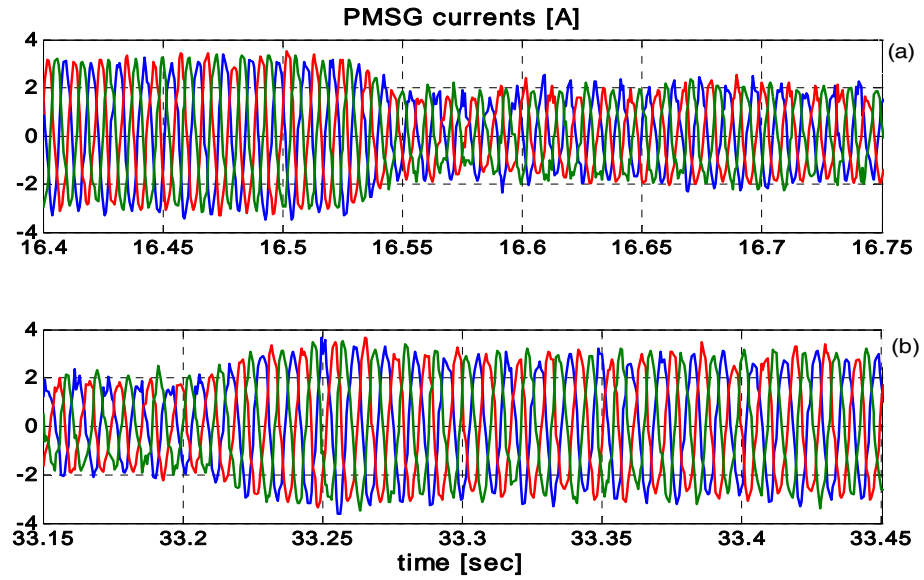
PMSG currents [A]

Fig.5.19 PMSG currents
a)   one load side inverter terminal is open
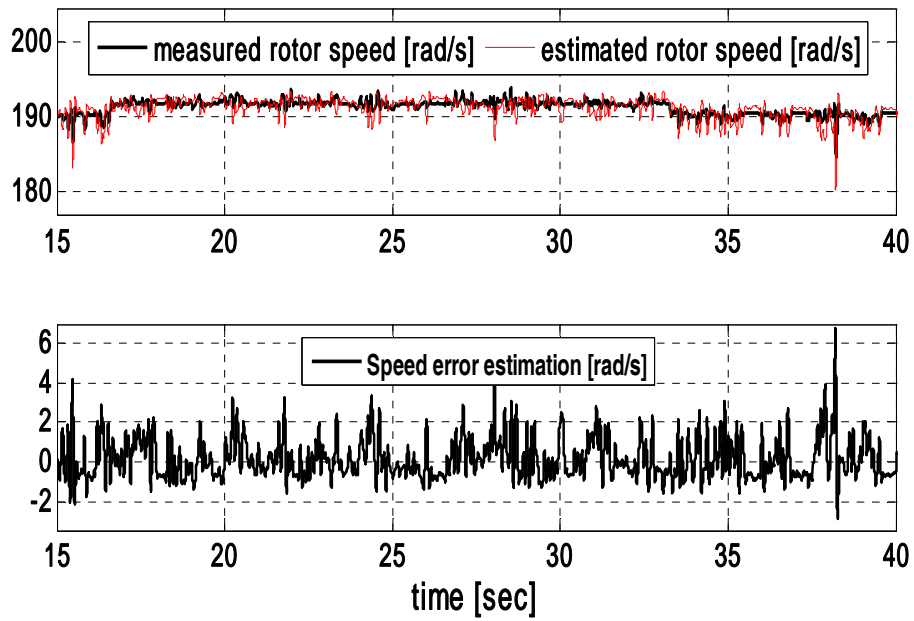b)   one load side inverter terminal is reconnected

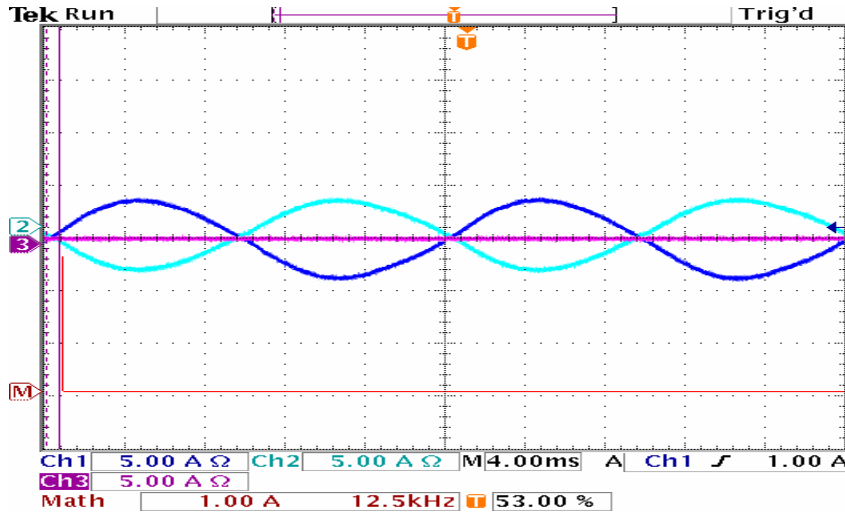Fig. 5.20 Measured and estimated rotor speed [rad/s]

Fig. 5.21 Ac source (load inverter output) current unbalanced diode rectifier load-test results

When one load side inverter terminal is open (Fig. 5.21), nonsymmetrical voltages with notable harmonics occur for same diode rectifier loads (Fig. 5.15). The parameters of the supply-side voltages when the negative voltage sequence is not compensated are depicted in Table V.

The asymmetry can be calculated as [22]:

$$d = \frac{Max(V_a, V_b, V_c) - Min(V_a, V_b, V_c)}{\dfrac{V_a + V_b + V_c}{3}} = 0.0608 \tag{5.25}$$

Table V

	Channel 1	Channel 2	Channel 3
Watts(RMS)	412.3	426.6	61.70 m
Watts(Fund.)	412.2	426.5	60.26 m
Volts(RMS)	**223.6**	**228.8**	**237.6**
Volts(Fund.)	223.6	228.8	237.7
Amps(RMS)	2.175	2.178	5.509 m
Amps(Fund.)	2.174	2.177	566.8 u
Power Factor	0.848	0.856	0.047
Cos Phi(Phase)	-0.848	0.856	-0.447
Amps(Peak)	3.082	-3.092	15.671m
Volts(Peak)	317.8	323.4	331.0

When the negative sequence voltage is compensated the voltage asymmetry was reduced from 6.08% (Fig. 5.21) to 0.608% and its harmonics content was reduced (Fig. 5.22).

The parameters of the supply-side voltages with the negative voltage sequence compensation are depicted in Table VI.

Table VI.

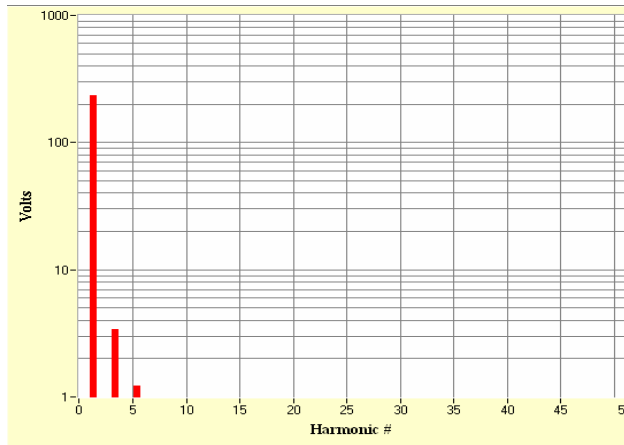|	Channel 1	Channel 2	Channel 3
Watts(RMS)	248.4	246.1	52.84 m
Watts(Fund.)	248.3	246.0	51.01 m
Volts(RMS)	**230.2**	**229.9**	**231.3**
Volts(Fund.)	230.2	229.9	231.2
Amps(RMS)	1.2425	1.2428	5.760 m
Amps(Fund.)	1.2422	1.2424	485.0 u
Power Factor	0.868	0.861	0.040
Cos Phi(Phase)	-0.868	0.861	-0.455
Amps(Peak)	326.8	327.0	-325.1
Volts(Peak)	-1.7741	-1.7719	-16.438m

Fig. 5.21 Voltage harmonic content for unbalanced rectifier load **without** negative sequence compensation
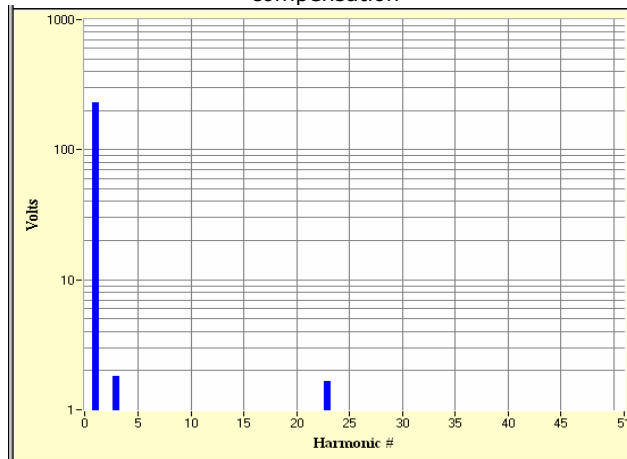

Fig. 5.22 Voltage harmonic content for unbalanced load **with** negative sequence compensation

5.6 Discussion and Conclusion

A voltage control scheme with selective harmonic compensation for a stand alone wind generation PMSG system has been proposed. The system was experimentally shown capable of supplying   local   load in good conditions (with much lower negative sequence ac voltages and lower harmonics content of the latter) even if one terminal of the load- side inverter is open and the load is nonlinear (diode rectifier load).

References:

[1] www.danvest.com

[2] P.D. Ladakakos, M.G. Ioannides, Wind Eng. 23 (6) (1999) 353 –364.

[3] I. Nojima, I. Takano, Y. Sawada, The 27th Annual Conference of Industrial Electronics Society, 2001, IECON' 01, vol. 2, 29 Nov– (2001) pp. 1303–1308.

[4] H. Sharma, S. Islam, C.V. Nayar, T. Pryor, IEEE Power Engineering Winter Meeting 2000, vol. 1, 23–
27 Jan (2000) pp. 499–504.

[5] S. Hutardo, G. Gostales, A. de Lara, N. Moreno, J.M. Carrasco, E. Galvan,J.A. Sanchez, L.G. Franquelo, A new power stabilization control system based on making use of mechanical inertia of a variable-speed wind turbine for stand-alone wind-diesel applications, in: IECON 02 Industrial Electronics Society 28th Annual conference, vol. 4, 5–8 November, 2002, pp. 3326– 3331.

[6] K.C. Seong, H.J. Kim, S.W. Kim, J.W. Cho, Y.K. Kwon, K.S. Ryu, I.K. Yu, S.Y. Hahn, Cryogenics 42   (2002) 351–355.

[7] T. Sels, C. Dragu, T.Van. Craenenbroeck, R. Belmans, New energy storage devices for an improved load managing on distribution level, in: IEEE Porto Power Tech Conference Proceedings, vol. 4, 2001, pp. 1–6.

[8] A. Abu-Siada,W.W.I. Keerthipala,W.B. Lawrance, Application of a superconducting magnetic energy storage unit to improve the stability performance of power systems, in: IEEE Canadian Conference on Electrical and Computer Engineering, 2002.

[9] Stott, P.A; Mueller, M.A; Colli, V. Delli; Marignetti, F.; Di Stefano, R., "DC Link Voltage Stabilisation in Hybrid Renewable Diesel Systems", Clean Electrical Power,ICCEP '07. International Conference, 21-23 May 2007 Page(s):20 – 25.

[10] O.Ojo, J.Cox, "Investigation into the performance characteristics of an interior permanent magnet generator including saturation effects", Conf. Rec. IEEE-IAS Annu. Meting 1996, pp.533-540

[11] B.S.Borowy,Z.M.Salameh, "Dynamic response of a stand alone- wind energy conversion system with battery energy storage to a wind gust ", IEEE-Trans. Ec -12, 1, 1997, pp. 73-78

[12] D.C. Aliprantis, S.A. Papathanassiou, M.P. Papadopoulus, A.G. Kladas, "Modelling and Control of variable-speed wind turbine equipped with permanent synchronous generator", ICEM 2000, 28-30 August 2000 Espoo, Finland

[13] R.Teodorescu, F. Blaabjerg, "Flexible control of small wind turbines with grid failure detection operating in stand-alone and grid-connected mode", IEEE Trans. Power Electron. vol. 19, no.5, Sept. 2004.

[14] M.Fatu, L.Tutelea, I. Boldea, R.Teodorescu "Novel motion sensorless control of stand alone PMSG: harmonics and negative component sequence voltage compensation under nonlinear load", *Record of EPE*-2007, Aalborg, Denmark.

[15] S. Buso, L. Malesani, P. Mattavelli, "Comparison of current control techniques for active filters applications", IEEE Trans. Ind. Electronics, vol. 45, no. 5, Oct. 1998, pp. 722-729.

[16]   S. Buso, S. Fasolo, L. Malesani, P. Mattavelli, "A Dead-Beat Adaptive Hysteresis Current Control", IEEE Trans. Ind.Applications, vol. 36, no. 4, July/Aug. 2000, pp. 1174-1180.

[17] X. Yuan, W. Merk, H. Stemmler, J. Allmeling, "Stationary-frame generalized integrators for current control of active power filters with zero steady-state error for current harmonics of concern under unbalanced and distorted operating conditions" IEEE Tran. Ind. App., vol. 38, no. 2, Mar./Apr. 2002, pp. 523-532.

[18] L. Malesani, P. Mattavelli, S. Buso, "Robust dead-beat current control for PWM rectifiers and active filters", IEEE Trans. Ind. Applications, vol. 35, no. 3, May/June 1999, pp. 613-620.

[19] I. Boldea, "Variable speed generators" ,book   CRC Press, Florida, Taylor&Francis Group, New York, 2006

[20] F.Briz del Blanco, M.W.Degner, R.D. Lorenz, "Dynamic Analysis of Current Regulators for AC Motors Using Complex Vectors", IEEE TRANS.IND. APPL., VOL. 35, NO. 6, 1999.

[21] C.Lascu, L.Asiminoaei, I.Boldea, F.Blaabjerg, "High performance current controller for selective harmonic compensation in active power filters" ,Record of OPTIM 2006, Brasov 21-23 May, 2006

[22] A.Robert, J.Marquet, "Assesing Voltage quality with relation to Harmonics, Flicker and Unbalanced", WG 36.05 Paper 36- 203, CIGRE '92

Chapter 6

I-F Starting Method with Smooth Transition to EMF Based Motion-Sensorless Vector Control of PM Synchronous Motor/Generator

Abstract

This chapter proposes a novel hybrid motion-sensorless control system for permanent magnet synchronous motors (PMSM) using a new robust start-up method called *I-f* control, and a smooth transition to emf-based vector control. The *I-f* method is based on separate control of i_d, i_q currents with the reference currents $i_d{}^* = 0$ and $i_q{}^*$ constant, and the reference frequency having ramp variation. This solution allows ultra low-speed sensorless control without initial rotor-position estimation, and without machine parameters identification. A first-order lag compensator is employed to ensure a smooth transition from *I-f* to emf sensorless vector control when the frequency reaches a certain level, and back. The PMSM rotor position and speed are extracted by using a PLL state-observer from the estimated rotor-flux, which is based on an equivalent integrator in close-loop with a PI speed-adaptive compensator to eliminate dc-offset and phase-delay. Digital simulations for PMSM start-up with full load torque are presented for different initial rotor-positions. The transitions from *I-f* to emf motion-sensorless vector control and back as well, at very low-speeds, are fully validated by experimental results. This method is suitable for both surface and interior PMSMs, but the paper refers directly only to surface PMSM. Other field of application might be in wind generators safe (faster) self starting when connected to the grid, or moving the rotor a little for inspections/repairs and for general industrial variable speed drives where slightly hesitant but full-load self-starting is allowable.

6.1   Introduction

Recently, PMSM drives have received an increased interest for industrial applications due to their higher torque per unit volume easy maintenance, high power factor and better efficiency comparing with induction motors.

Drives of PMSMs require the absolute rotor position information to exactly control the motor torque, and the position information has been provided by a resolver or an encoder. The resolution of initial position is 180 divided by number of Hall-effect detectors if the Hall-effect detector's signal conditioning has a binary output, i.e., is configured as a Hall-effect switch. For classical implementations using three Hall-effect switches, the error due to the limited angular resolution degrades starting torque. Additional resolution can be gained using an analog output Hall-effect sensor, at the expense of an additional A/D converter for each sensor.

A critical aspect to modern drive applications is reliability. A key factor affecting the reliability of motor drives is the position sensor. The additional wiring and connections to sensors degrades reliability. A simple, low-cost approach to obtain a useful initial position without requiring a position sensor involves using dc current excitation to physically align the rotor to an initial position.

The elimination of the position sensor reduces the drive cost and improves the reliability.

The sensorless control methods for PMSMs can be divided in three main categories: methods using fundamental voltage or current models, suitable for middle to high-speed range [1-7]; techniques based on state observers [8], [9] and extended Kalman filters (EKF) [10]–[14]; and methods using high-frequency signal injection for standstill and low speeds [15-10]. A combination between these two methods is presented in [11].

Position estimation based on back-EMF techniques estimates the flux and velocity from the voltage and current, which is especially sensitive to the stator resistance at low speed range. The actual voltage information on the machine terminal can hardly be detected because of the small back-EMF of the machine and the system noise produced by the nonlinear characteristics of the switching devices. The back-EMF methods have good position estimation in middle and high speed but it fails in the low speed region. The magnitude of back-EMF voltage is proportional to the rotor speed, thus at standstill it is impossible to estimate the initial position. Therefore starting from unknown rotor position may be accompanied by a temporary reverse rotation or may cause a starting failure.

The EKF is one of the most widely used for tracking and estimation for nonlinear systems due to its simplicity, optimality, trackability and robustness for low to high speed range but still fails to identify initial position.

In the last decade, several solutions have been proposed to estimate the PMSM initial rotor position. Two basic methods are pulse signal injection [15-19], and sinusoidal carrier signal injection [20-30]. The pulse signal injection methods are often based on estimating of minimum inductance location using a calculated obtained during some form of iterative square wave voltage injection to arbitrary axes such as that in [16-21]. Such methods can be applied to both surface [16]–[18], [21] and interior PMSMs [20], [21]. Magnetic axis without polarity was estimated via a method named "INFORM" (Indirect Flux detection by On-line Reactance Measurement) and the polarity was detected by finding minimum inductance on the estimated magnetic axis [19]. In these methods, initial position estimation accuracy can be affected by additional spatial harmonics such as saturation of the stator teeth.

Injection of a high-frequency, rotating [20]–[23], [28] and/or pulsating [24]–[28] excitation has also been widely used to estimate initial rotor position using either voltage [20]–[24], [27], [28] or current injection [25], [26].

For polarity-dependent-axis, the magnetic saturation was modeled as a function of current by a 2nd-order Taylor series [26]. The magnet polarity was determined from the second harmonic of the injected frequency [26]–[28].

  I-f open loop control has been proposed for RSM in [31] for wide speed range, with superior results than *V/f* control.

This chapter presents a new safe, robust sensorless start-up method called "*I-f* control" for PMSM without initial rotor-position detection, with very good performance at low speeds. Smooth transition to emf-based motion-sensorless vector-control method and vice-versa is achieved by employing a first-order lag compensator and is demonstrated with fully experimental results [32].

6.2   PMSM MODEL

The space-vector model of PMSM equipped with interior permanent magnets, in rotor reference frame (Park's rotator operator for transformation in *dq* axes) [32] is:

$$\underline{V}_s = \underline{i}_s R_s + \frac{d\underline{\Psi}_s}{dt} + j\omega_r \underline{\Psi}_s \, , \tag{6.1}$$

$$\underline{\Psi}_s = \Psi_d + j\Psi_q = \lambda_{PM} + L_d i_d + jL_q i_q \, , \tag{6.2}$$

where $\underline{V}_s = V_d + jV_q$, $\underline{i}_s = i_d + ji_q$, and $\underline{\Psi}_s$ are the stator voltage, current and flux vectors, respectively, R_s is the stator phase resistance, L_d and L_q are the *dq* inductances, λ_{PM} is the PM flux, and ω_r is the rotor speed.
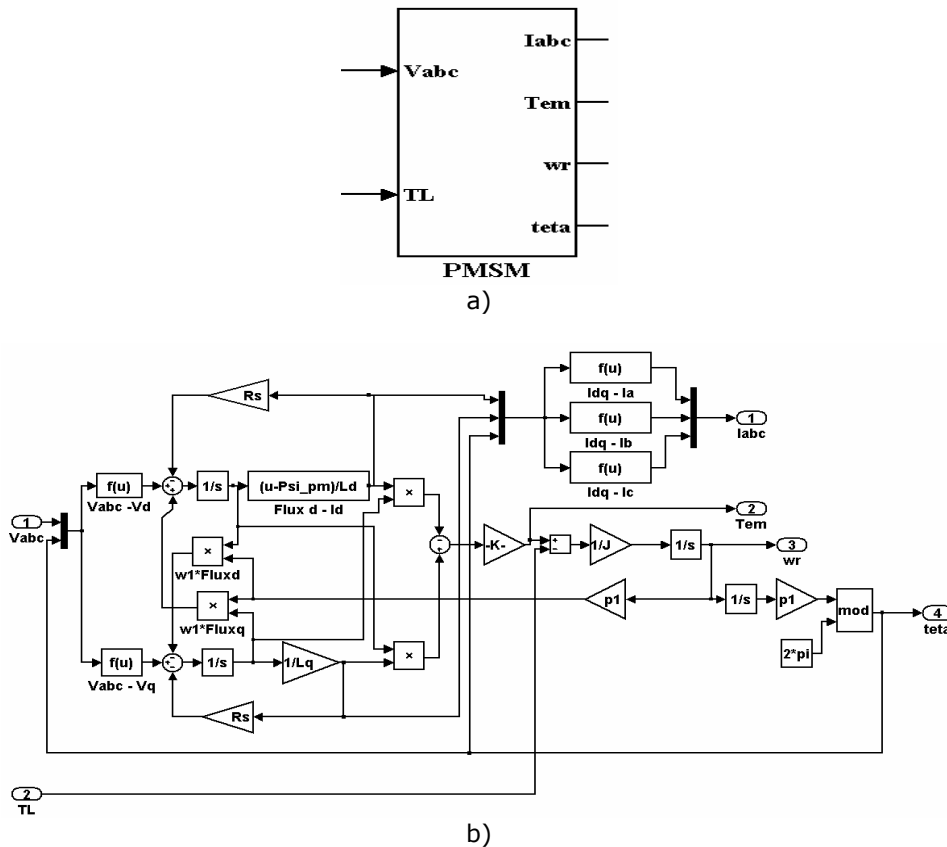

a)

b)

Fig. 6.1 The model of PMSM: a) mask of the model, b) implementation of equations

6.3 I-F CONTROL METHOD

I-f control method consists in ramping the stator current frequency while i_q^* and i_d^* references are maintaining constant. During the experiments, the frequency time- variation form is chosen as:

$$f^* = k_f t^2 \qquad\qquad (6.3)$$

where k_f is a positive constant ($k_f = 1$, in our case).

The frequency is used to calculate a reference angle (Fig.6.2) θ_{crt}, which is the feedforward position-angle corresponding to an imposed synchronous reference frame:

$$\theta_{crt} = \int 2\pi f^* dt \qquad\qquad (6.4)$$
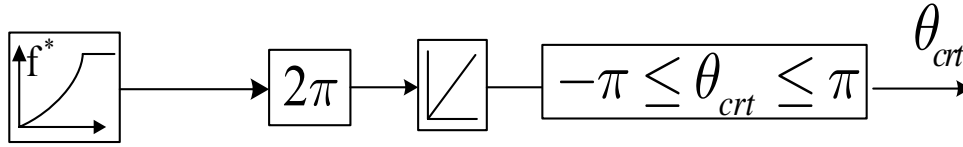
Fig. 6.2 Reference angle calculation during *I-f* starting

Two PI current controllers, implemented in synchronous reference frame, are used to "reproduce" i_{dq}^* currents in motor by a current vector control system.

6.4 MOTION-SENSORLESS CONTROL OF PMSM

The configuration of the proposed motion-sensorless vector control system for PMSM is illustrated in Fig. 6.3a. The PMSM is current vector controlled. The reference current i_q^* is set according to reference frequency variation. To avoid large speed transients during experiments, a small value (0.3A) is imposed until the frequency exceeds 10 Hz for start-up with no load. The commanded magnetizing current i_d^* is set to zero to operate at max. torque/ current (typical for surface PM rotors, but acceptable also for small saliency inset PM rotors).

The current controllers are implemented in rotor reference frame, and give the reference voltage vector $\underline{V}^* = V_d^* + jV_q^*$:

$$V_d^* = (k_{pcrt} + k_{icrt}/s)(i_d^* - i_d) - \hat{\omega}_r i_q L_q \qquad\qquad (6.5)$$

$$V_q^* = (k_{pcrt} + k_{icrt}/s)(i_{q\_gen}^* - i_q) + \hat{\omega}_r(i_d L_d + \lambda_{PM}) \qquad\qquad (6.6)$$

where k_{pcrt} = 15 and k_{icrt} = 20 are the PI controller gains.

The axis decoupling terms in (6.5), (6.6) are introduced only when the control strategy runs in emf motion-sensorless control mode.

Fig. 5.3b shows the rotor position $\hat{\theta}_r$ and speed $\hat{\omega}_r$ estimator that includes the following main components. The stator flux estimator $\hat{\underline{\lambda}}_s$, based on the voltage model in stator reference frame, employs an equivalent integrator (I+API) in close-loop, with a speed-adaptive PI controller to compensate the dc-offset and phase-delay [17]. The target is to find a structure with same frequency behavior as an ideal integrator.

The transfer function of I+API is:

$$\underline{H}(s) = \frac{\hat{\underline{\lambda}}}{\underline{e}} = \frac{s}{s^2 + k_p s + k_i} \tag{6.7}$$

The denominator canonical form is:

$$\Delta(s) = s^2 + k_p s + k_i = s^2 + 2\xi\omega_0 s + \omega_0^2 \tag{6.8}$$

where ω_0 is the corner frequency and ξ is the damping factor.

The expressions for the speed adaptive PI gains are [33]:

$$k_p = 2\frac{\xi}{d}\hat{\omega}; \; k_i = \frac{\hat{\omega}^2}{d^2}; \; \omega_0 = \frac{\hat{\omega}}{d}; \tag{6.9}$$

where $\hat{\omega}$ is the module of estimated speed; $d=12$, $\xi=0.15$ and k_p and k_i have minimum values, e.g., 1 and 10, respectively.

Now, in the frequency domain, $\underline{H}(j\omega)$ from (6.7) becomes:

$$\underline{H} = He^{j\phi}, \tag{6.10}$$

where H is the magnitude and Φ is the phase of $\underline{H}$.

$$H = \frac{d^2\omega}{\sqrt{(d^2\omega^2 - \hat{\omega}^2)^2 + (2\xi d\hat{\omega}\omega)^2}}, \tag{6.11}$$

and

$$\phi = -\frac{\pi}{2} + atan\frac{2\xi d\hat{\omega}\omega}{d^2\omega^2 - \hat{\omega}^2}. \tag{6.12}$$

When $\hat{\omega} = \omega$, the expressions (6.11), (6.12) become:

$$H = \frac{1}{\omega}a; \qquad a = \frac{d^2}{\sqrt{(d^2-1)^2 + (2\xi d)^2}};$$

$$\phi = -\frac{\pi}{2} + \phi_1; \quad \phi_1 = atan\frac{2\xi d}{d^2 - 1}. \tag{6.13}$$

Note 1. Using the speed adaptive expressions for k_p and k_i (6.9), the magnitude correction a and the phase correction Φ_1 have constant values. Therefore, an ideal integrator $\underline{H}^{\wedge}$ in the frequency domain is obtained [33]:

$$\hat{\underline{H}} = \frac{1}{a}e^{-j\phi_1}\underline{H} = \frac{1}{\omega}e^{-j\frac{\pi}{2}} \qquad (6.14)$$

The stator flux vector $\hat{\underline{\lambda}}_s$ is obtained using the adaptive integrator (6.7), (6.9) with the corrections (6.14) to integrate the emf vector $\underline{e}$:

$$\hat{\underline{\lambda}}_s = \underline{e} = \int (\underline{V}_s - \underline{i}_s R_s)dt . \qquad (6.15)$$

The stator vector voltage $\underline{V}_s$ is reconstructed from the duty cycles d_a, d_b, d_c of the voltage source-inverter and the measured dc-link voltage V_{dc}:

$$\underline{V}_s = V_\alpha + jV_\beta = V_{dc}(2d_a - d_b - d_c)/3 + jV_{dc}(d_b - d_c)/\sqrt{3} \qquad 6.16)$$

The estimated rotor flux $\hat{\underline{\lambda}}_r$ is obtain using $\hat{\underline{\lambda}}_s$ and the measured stator current $\underline{i}_s$:

$$\hat{\underline{\lambda}}_r = \hat{\underline{\lambda}}_s - L_s \underline{i}_s . \qquad 6.17)$$

A phase-locked loop (PLL) state-observer (Fig. 6.3c) extracts the phase of $\hat{\underline{\lambda}}_r$ vector to estimate the rotor position $\hat{\theta}_r$ and speed $\hat{\omega}_r$. The PLL error $\Delta\theta = \theta_r - \hat{\theta}_r$ is obtained from the imaginary part of the vector product $Im(\hat{\underline{\lambda}}_r, \underline{\lambda}_1)$ where:

$$\hat{\underline{\lambda}}_r = \lambda_r e^{j\theta_r} = \hat{\lambda}_{r\alpha} + j\hat{\lambda}_{r\beta}; \quad \underline{\lambda}_1 = e^{-j\hat{\theta}_r} = \cos\hat{\theta}_r - j\sin\hat{\theta}_r \qquad (6.18)$$

$$\Delta\theta \cong \sin\Delta\theta = Im(\hat{\underline{\lambda}}_r, \underline{\lambda}_1) = \hat{\lambda}_{r\beta}\cos\hat{\theta}_r - \hat{\lambda}_{r\alpha}\sin\hat{\theta}_r \qquad (6.19)$$

In practice, to simplify (6.9), the PI controller gains, that are speed adaptive, are chosen as:

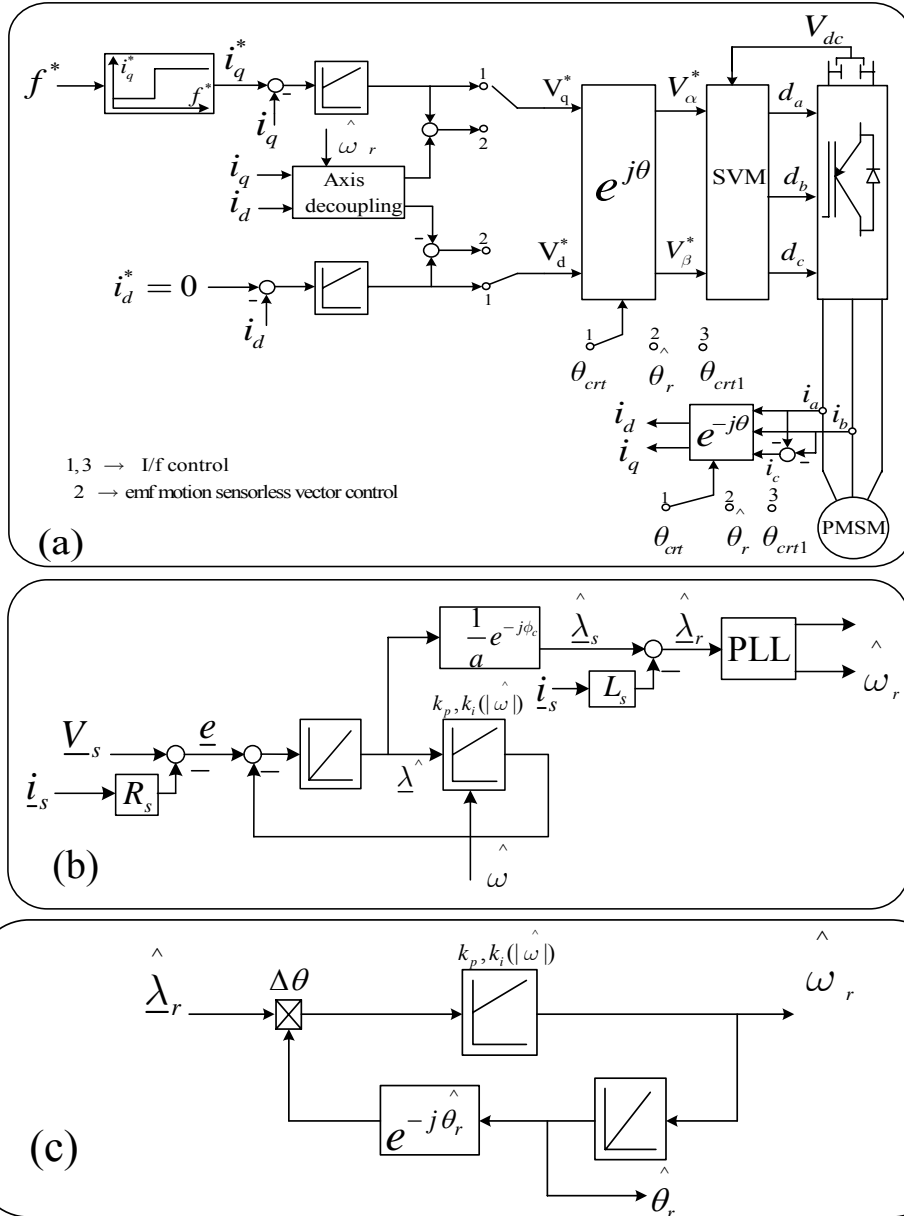$$k_p = 5 + 2|\hat{\omega}|, \quad k_i = 1 + 0.5|\hat{\omega}| \qquad (6.20)$$

Fig. 6.3 Motion-sensorless control of PMSM: a) current controllers, b) rotor speed and position estimator, c) PLL state-observer structure

6.5 TRANSITION STRATEGIES

A. Transition from I-F Control to EMF Sensorless Control

The system uses *I-f* control for start-up and low speeds. When the reference frequency exceeds a certain level (f_{min}), the transition to emf motion-sensorless vector control is automatically initiated (Fig. 6.4a). In order to achieve a smooth transition, a first-order lag compensator is used having zero input, and the error $\theta_{crt} - \hat{\theta}_r$ set as initial condition. The time constant $T_c = 0.04s$ is chosen. Therefore, the angle θ, used for Park rotator operator, goes smoothly from θ_{crt} to $\hat{\theta}_r$.

$$\theta_{comp1} = \frac{1}{1 + sT_c}(\theta_{crt} - \hat{\theta}_r), \quad \theta_{comp1}(0) = \theta_{crt} - \hat{\theta}_r \tag{6.21}$$

$$\theta = \hat{\theta}_r + \theta_{comp1} \tag{6.22}$$

When the reference frequency reaches f_{max}, the control strategy switches to the emf motion-sensorless vector control ($\theta = \hat{\theta}_r$) and the first order delay (1→2) is disabled (θ_{comp1}=0) (Fig. 5a).
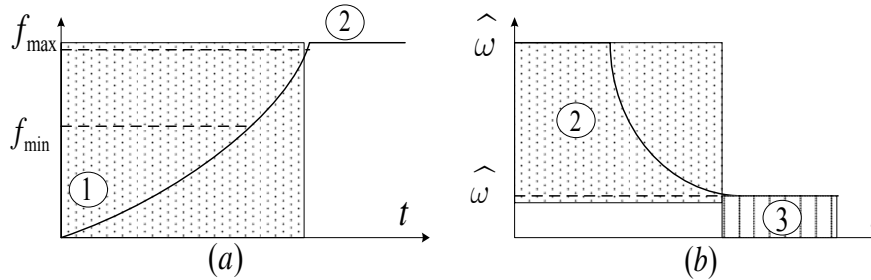
Fig. 6.4 Control strategy: 1) *I-f* control; 2) emf motion-sensorless vector control; 3) *I-f* control

B. Transition from EMF Sensorless Control to I-F Control

Transition from emf motion-sensorless vector control to *I-f* control is realized when the estimated rotor speed $\hat{\omega}_r$ is below a certain level (Fig. 6.4b). In that case, the control system automatically generates an angle (θ_{crt1} - feedforward position angle) having the same frequency as the last value of the estimated rotor frequency:

$$\theta_{crt1} = \int \hat{\omega} dt \tag{6.23}$$

The transition to *I-f* control is performed smoothly by employing the first-order lag compensator (2→3) (Fig. 6.5a) having zero input and the error $\hat{\theta}_r - \theta_{crt1}$ as initial condition.

$$\theta_{comp2} = \frac{1}{1+sT_c}(\hat{\theta}_r - \theta_{crt1}); \quad \theta_{comp2}(0) = \hat{\theta}_r - \theta_{crt1}. \tag{6.24}$$

Now the angle used in Park rotator operator becomes:

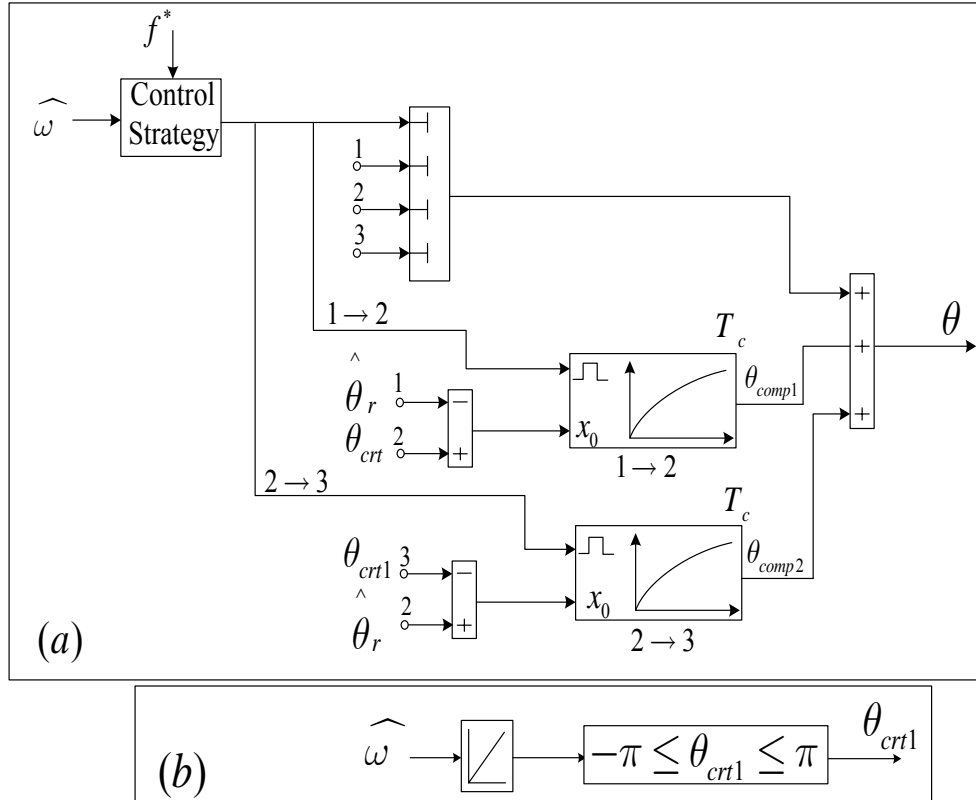$$\theta = \theta_{ctr1} + \theta_{comp2}. \tag{6.25}$$

Fig. 6.5. a) Transition strategy (1→2): *I-f* emf motion-sensorless control; (2→3): emf motion-sensorless control *I-f*; b) θ_{crt1} calculation

6.6 SIMULATION RESULTS

The proposed start-up strategy is simulated using Matlab/ Simulink and is implemented on DSpace 1103 control board. The simulation step was set to 100µs and the solver is Runge –Kutta.

Since the initial position is unknown, the *I-f* control performance is investigated for different initial values of the rotor position with full load. Fig. 6.6a shows the start-up of PMSM with constant full load. Until 0.02s the actual rotor speed is considered zero until the electromagnetic torque is equal with the rated torque.
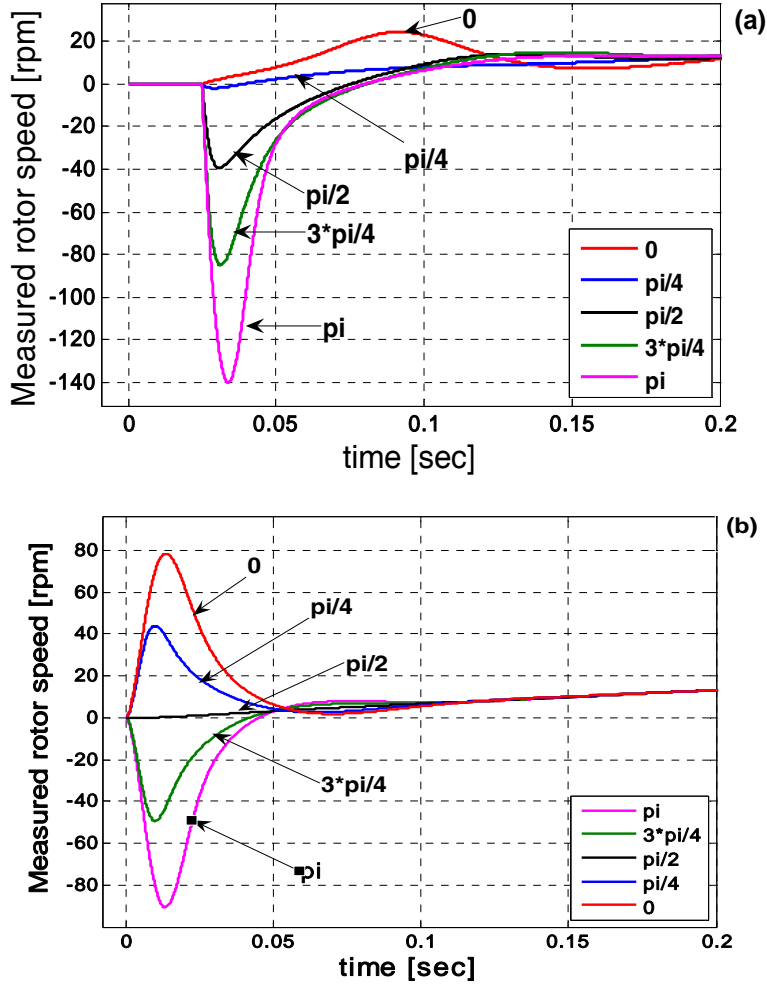
6 Fig. 6.6 Rotor speed: a) Start-up with full load torque; b) Start-up with load torque variable with rotor speed

Note that, for rotor position values higher than *π/4* of the initial rotor position, the PMSM exhibits a brief backward rotation. Better results are obtained for a load torque proportional with the rotor speed (Fig. 6.6b). In this case, backward rotation is recorded only for values higher than *π/2* of the initial rotor position. It seems safe to consider that the machine is able to start from any position at full load torque, after few oscillations around zero speed, provided by the reference current that is large enough.

The transition from *I-f* control to emf based sensorless control is investigated in Fig. 6.7. The reference frequency in Fig. 6.7a has a ramp variation. When it reaches 30

Hz, the first-order lag compensator is triggered (Fig. 6.7b), and the rotator-operator angle $\theta(1)$ has a smooth transition from the current vector angle $\theta_{crt}(2)$ to the estimated rotor position angle $\hat{\theta}_r(3)$ shown in Fig. 6.7c. Fig.6.7d shows the PMSM currents which do not exhibit any transients during transition period from one control strategy to other.

   After the control strategy switches to emf based sensorless control, the machine accelerates until 1400 rpm with load torque proportional with speed. The actual rotor speed, the estimated rotor speed, and the error between them are depicted in Fig. 6.7e,f,g. Note that during the acceleration and deceleration process the proposed motion-sensorless control algorithm shows a very good tracking performance.
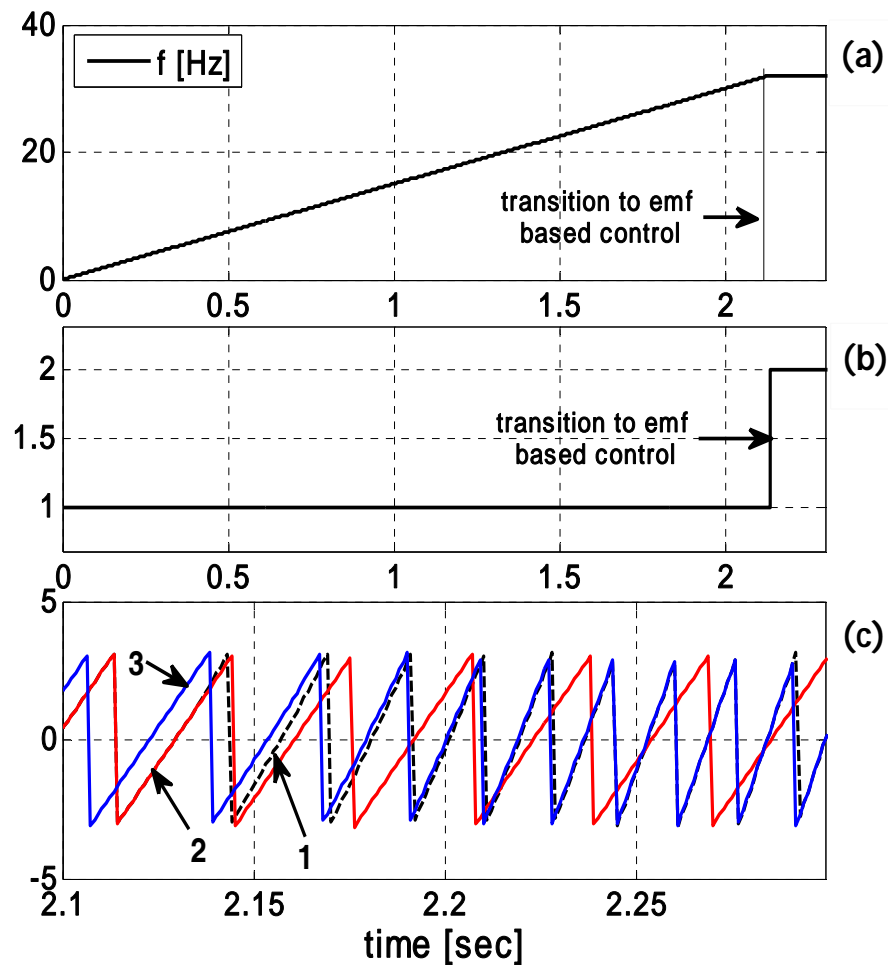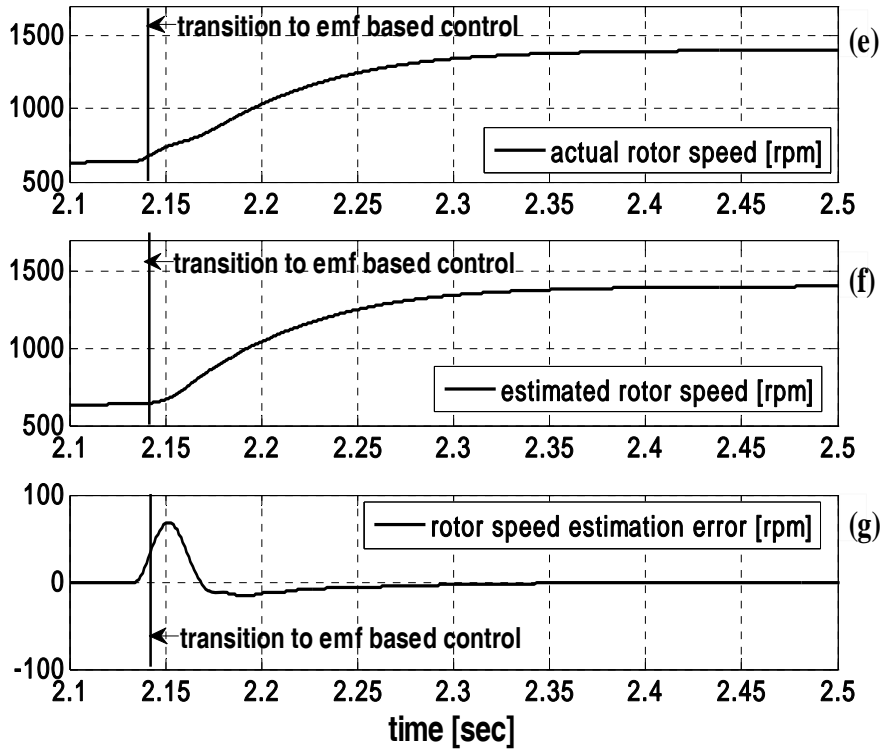
Fig. 6.7 Transition to emf based control
a) Reference frequency
b) Trigger to start emf control
c) zoom to see transition of θ (1): $\theta_{crt}(2) \to \hat{\theta}_r$ (3)
d) PMSM currents [A]
e) Actual rotor speed [rpm]
f) Estimated rotor speed [rpm]
g) Rotor speed estimation error [rpm]

A deceleration is produced by setting the *q*-axis reference current from 4A to 1.2A (Fig. 6.8a). When the estimated rotor frequency (Fig. 6.8b) reaches 20 Hz, the control strategy automatically switches from emf based control to *I-f* control (Fig. 6.8c), with the currents frequency equal with the last value of the estimated rotor frequency. Fig. 6.8d shows the PMSM currents which do not exhibit any transients during transition period from estimated rotor position to current vector control. The actual and estimated rotor speed, as well as the error between those two are illustrated in Fig.8e,f during the transition. Fig. 6.8g shows smooth transition of the rotator-operator angle θ(3) from the estimated rotor position angle $\hat{\theta}_r$ (2) to the current vector angle $\theta_{crt}(1)$.
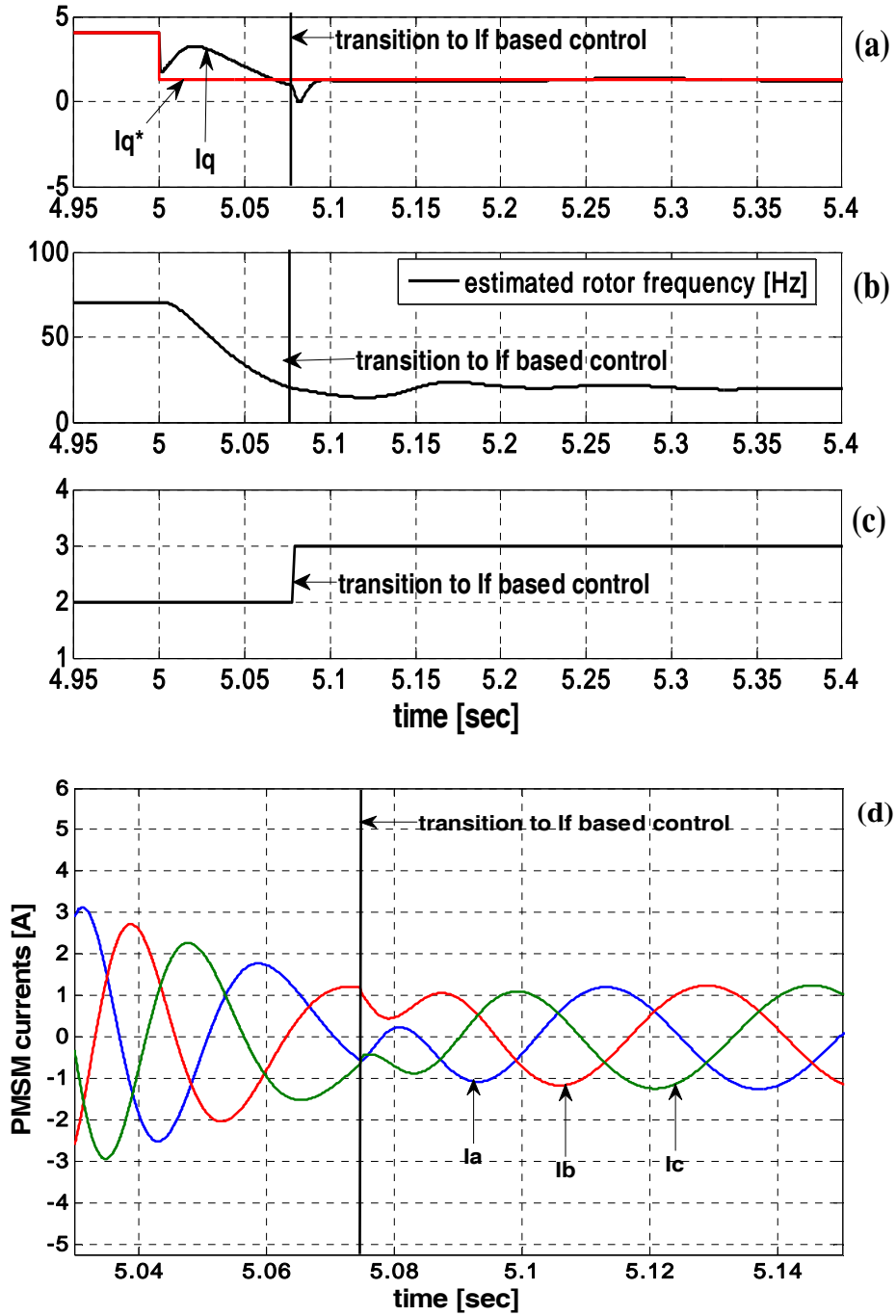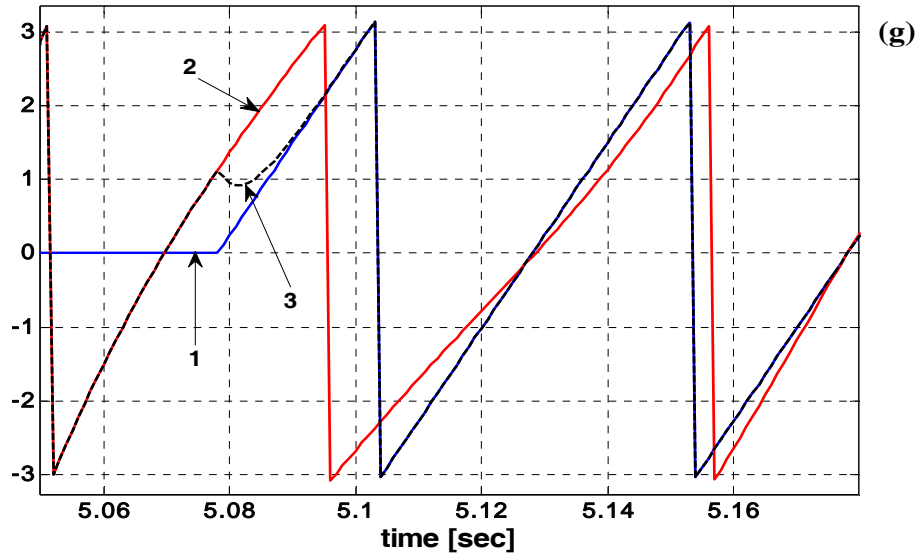
Fig. 6.8 Transition to If based control
a) q-axis reference and measured current [A]; b) estimated rotor frequency [Hz];c) Trigger to start If control; d) PMSM currents [A]; e) actual and estimated rotor speed [rpm]; f) rotor speed estimation error [rpm]; g) Zoom to see angle transition of θ (3): $\hat{\theta}_r$ (2)$\rightarrow \theta_{crt}$(1)

6.6.1 Simulations for Start-Up and Very Low Speed without Load with I-F Control

Low speed reversal was simulated from 0.01Hz to -0.01Hz. The reference frequency is set to 0.01Hz (Fig. 6.9a) and θ_{crt} used for coordinate transformations is shown in Fig. 6.9b. At time $t=150s$ the frequency is reversed at -0.01Hz. The actual rotor speed is depicted in Fig. 9c without any significant transients when the frequency reverses the sign. The PMSM currents are shown in Fig. 6.9d and again there no transients at speed reversal. Q-axis reference and actual current (Fig. 6.9e,f), respectively d-axis reference and actual current (Fig. 6.9g,h) show no transients during the reversal process proving good performance of the current controllers.
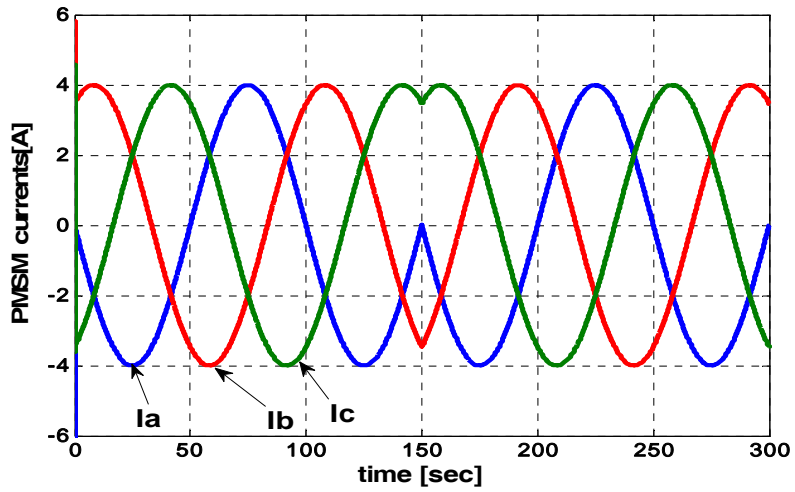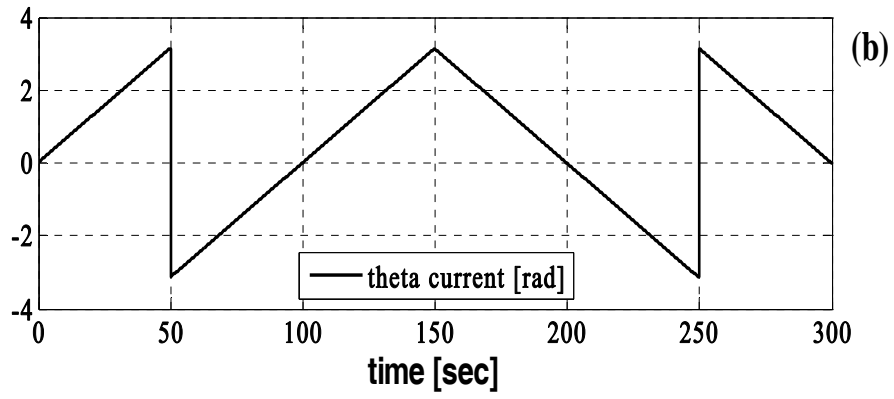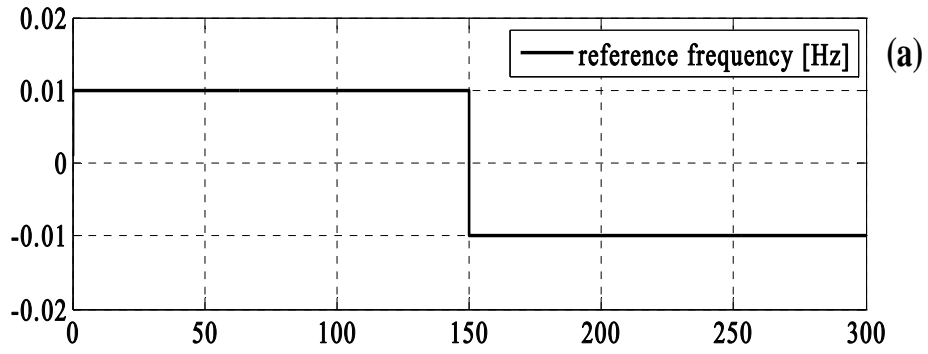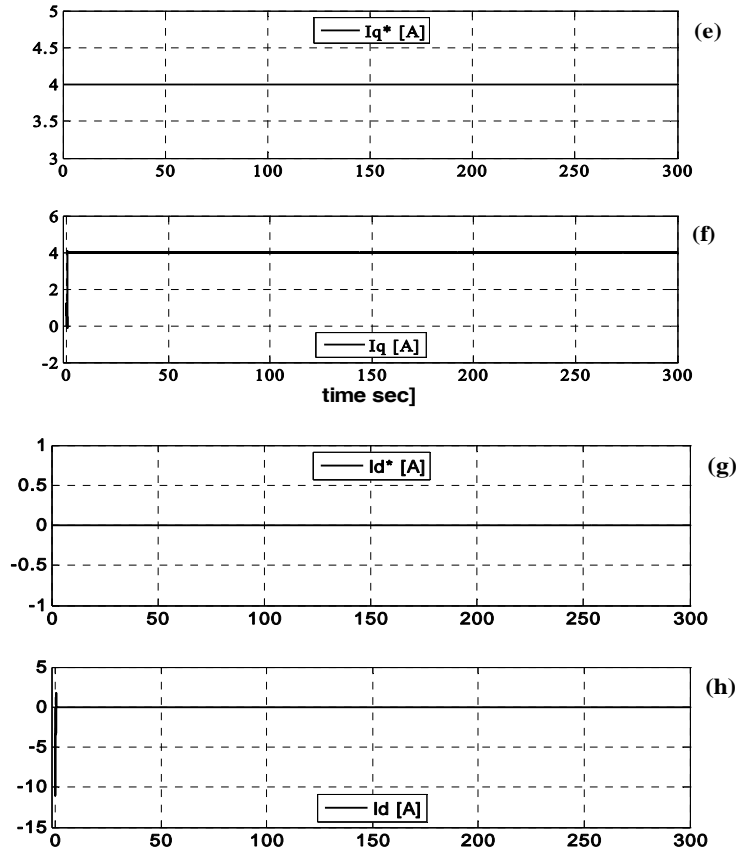
Fig. 6.9 Start up and reversal at 0.01Hz measurements
a)   Reference frequency [Hz];b) Theta current [rad]; c) Actual rotor speed [rpm]
d) PMSM currents; e) q-axis reference current [A]; f) q-axis current [A]; g) d-axis
reference
current [A]; h) d-axis current

A step change was performed in the q-axis current from 1A to 3A under no load
(Fig.6.10) at the same frequency, 0.01Hz. The speed remains constant (0.2 rpm)
even with a notable increase in i_q (see Fig.6.11). A very good dynamic response of
the current controller with no transient in stator currents is shown in Fig.6.12.
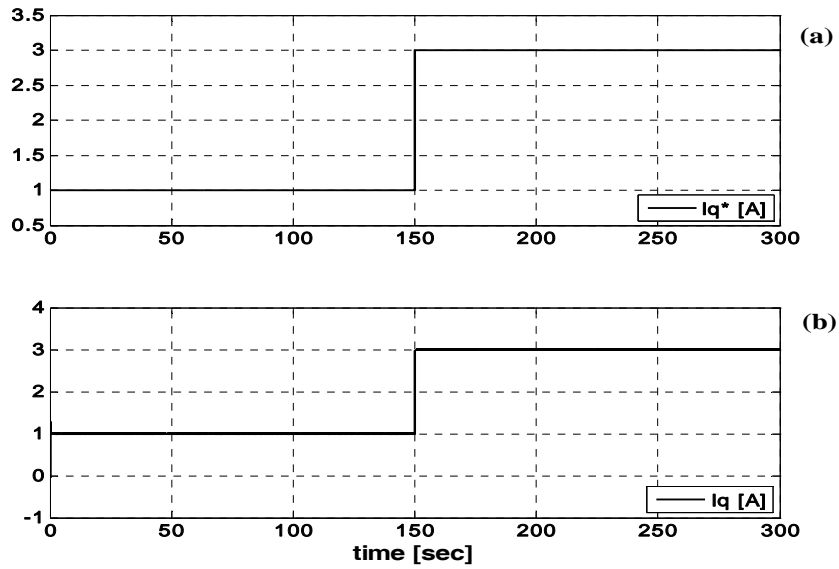
Fig.6.10 Reference and measured q-axis current
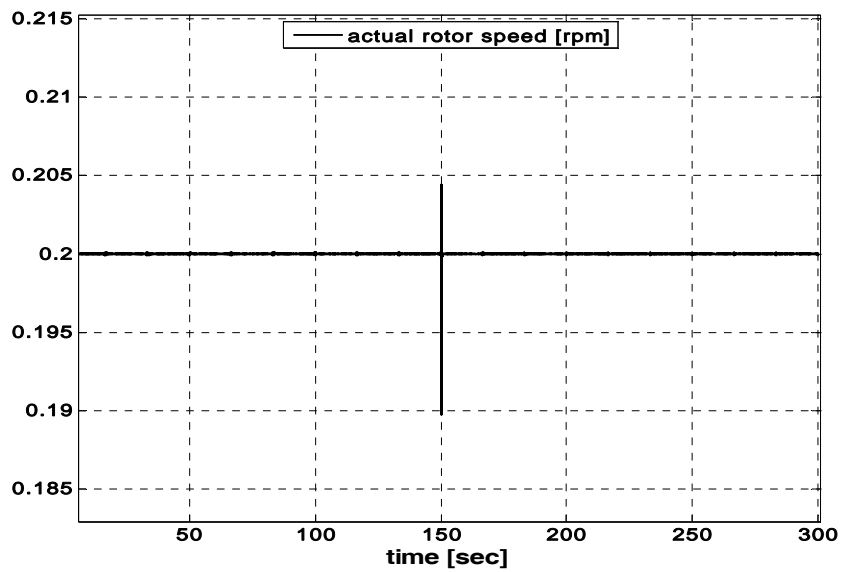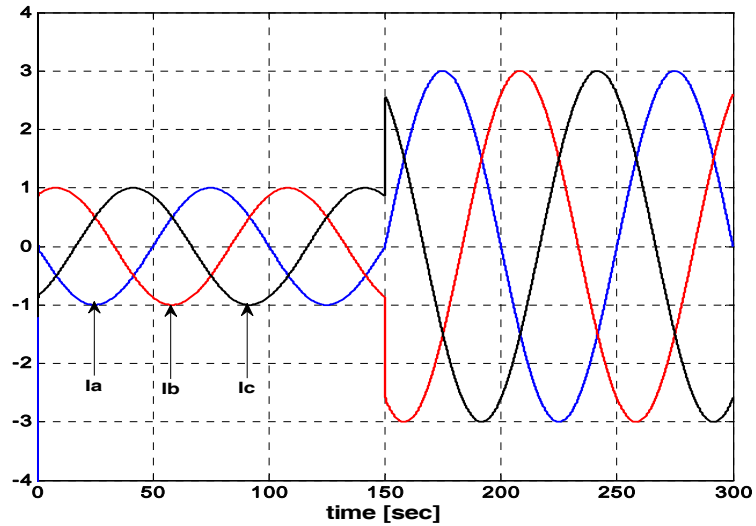

Fig.6.11 Actual rotor speed [rpm]

Fig.6.12 Stator currents

6.7   TEST PLATFORM AND EXPERIMENTAL RESULTS

The experimental test platform is shown in Fig. 6.13. The test setup mainly consists in: motor of 12 Nm PMSM driven by a Danfoss FC-302 voltage source inverter; load of PMSM driven by Simovert Masterdrive; DSpace 1103 platform.
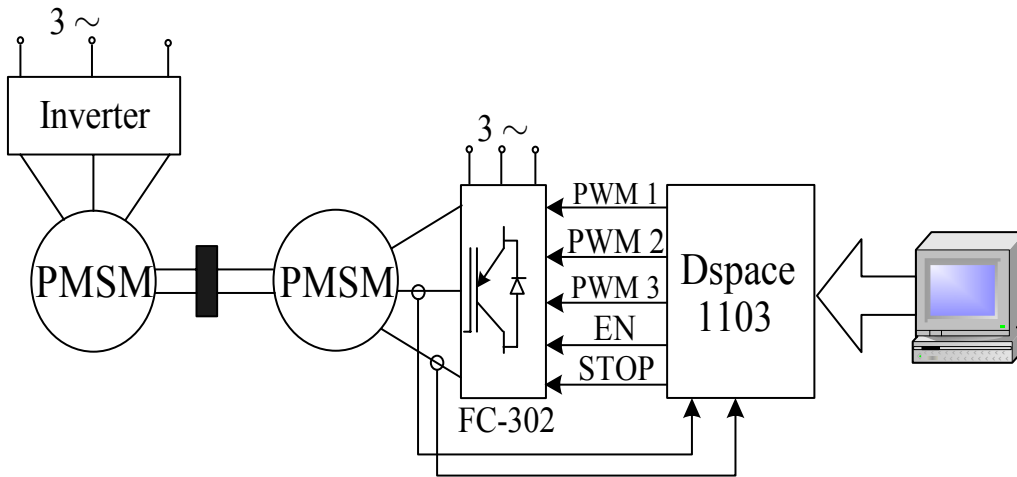
Fig.6.13 Experimental test platform

The sampling and switching frequency is set to 10 kHz.
The PMSM parameters are presented in Table I.

TABLE I
PMSM PARAMETERS

Number of pole pairs (p)	3
Rated power	2.2 kW
Rated speed	1750 rpm
Rated frequency	87.5 Hz
Rated torque	12 Nm
Rated phase to phase voltage	380 V(rms)
Rated phase current	4.1 A(rms)
Stator resistance per phase (R_s)	3.3 Ω
d-axis inductance (L_d)	41.59 mH
q-axis inductance (L_q)	57.06 mH
Rotor permanent–magnet flux λ_{PM})	0.4832 V s rad-1
Inertia of the rotating system (J)	10.07_*10^{-3} kgm^2
Viscous friction coefficient (B)	20.44_*10^{-4} Nms/rad

The performance of the proposed control system is investigated in three cases: start-up and ultra very-low speed with *I-f* control; start-up with *I-f* strategy and transition to emf motion-sensorless vector control, and back (vice-versa) when the estimated speed is below a certain level.

A. Start-Up and Very Low Speed without Load with I-F Control

   Low-speed reversal is performed from 0.01Hz to −0.01Hz. The reference frequency is set to 0.01Hz (Fig. 14a) and the angle θ_{crt}, used in rotator operator, is shown in Fig. 6.14b. At time $t = 133$s, the frequency is reversed at −0.01Hz. The *q*-axis measured and reference current is depicted in Fig. 6.15a, their error - in Fig. 6.15b, and the *d*-axis measured and reference current - in Fig. 6.16. Good performance of the current controllers during entire test is proved. The measured rotor speed is shown in Fig. 6.17, without significant transients at start-up, or when the frequency reverses the sign. The stator currents are shown in Fig. 6.18 and again, there are no transients at start-up or at speed reversal. The estimated stator voltage vector, obtained from the measured dc-link voltage and inverter duty cycles, has the hodograph almost circular (see Fig. 6.19).
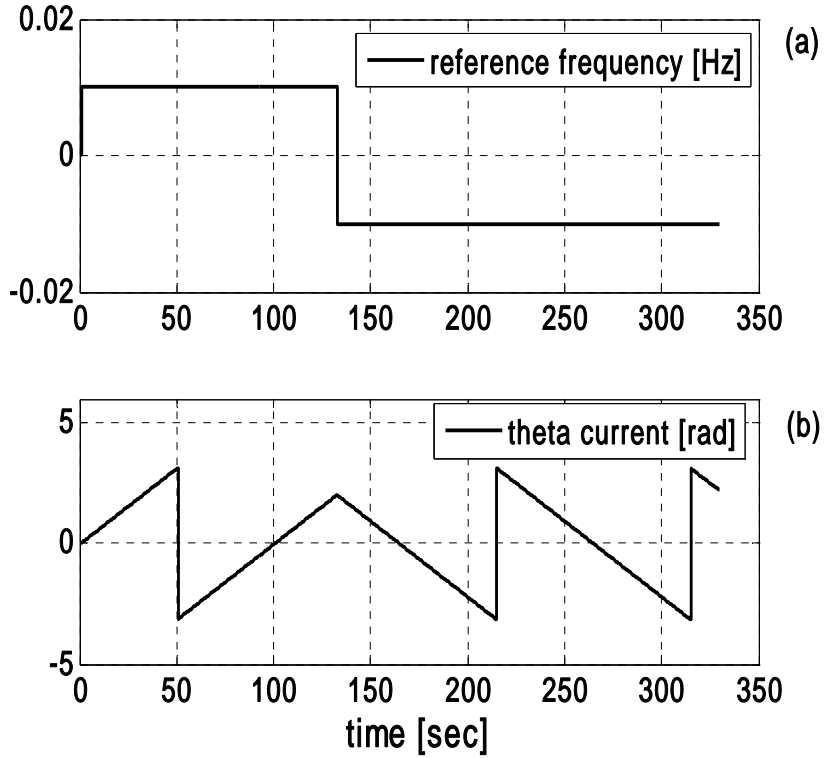
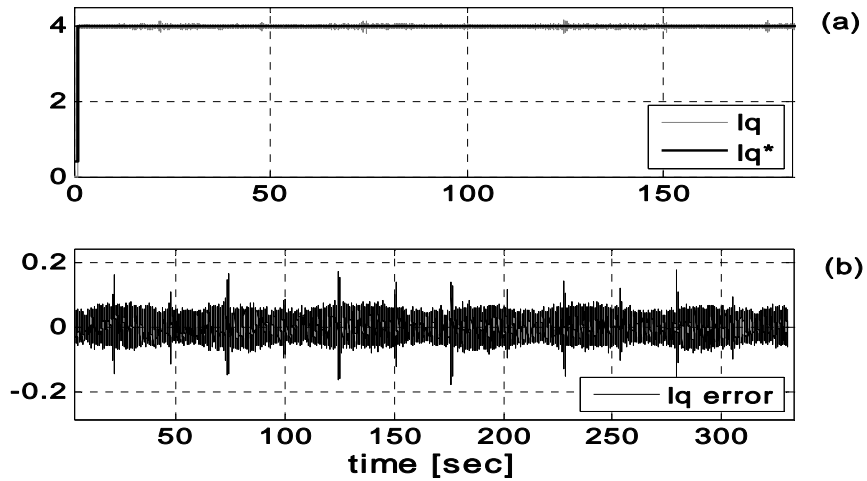Fig.6.14 a) Reference frequency; b) position-angle of current vector

Fig.6.15 a) Measured and reference I_q current; b) I_q error
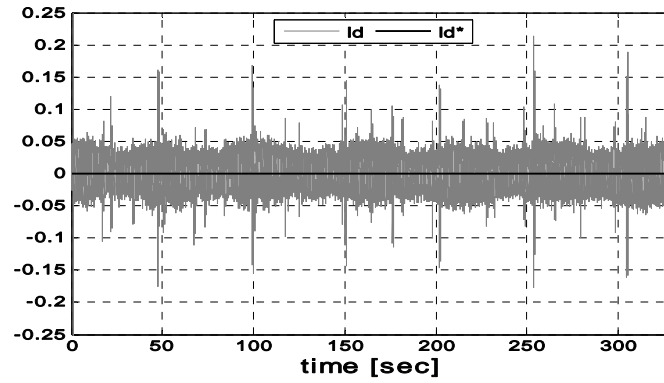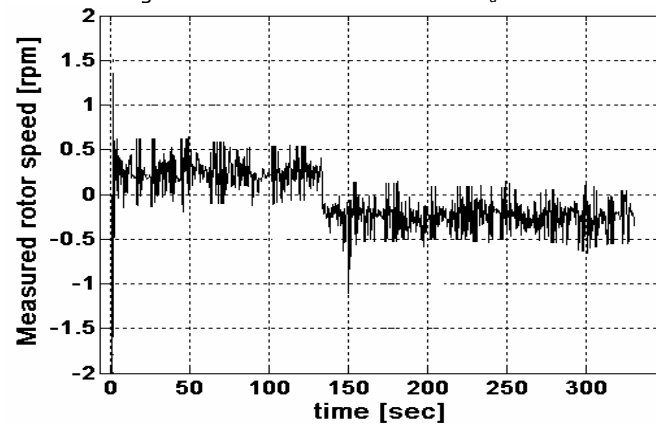
Fig.6.16 Measured and reference i_d current
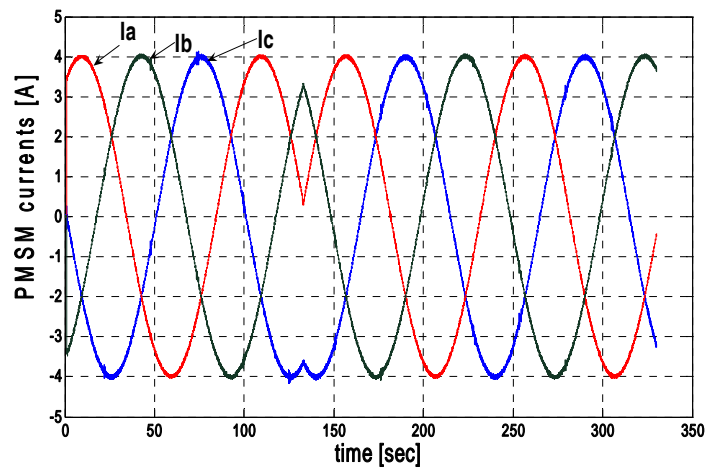

Fig.6.17 Measured rotor speed [rpm]
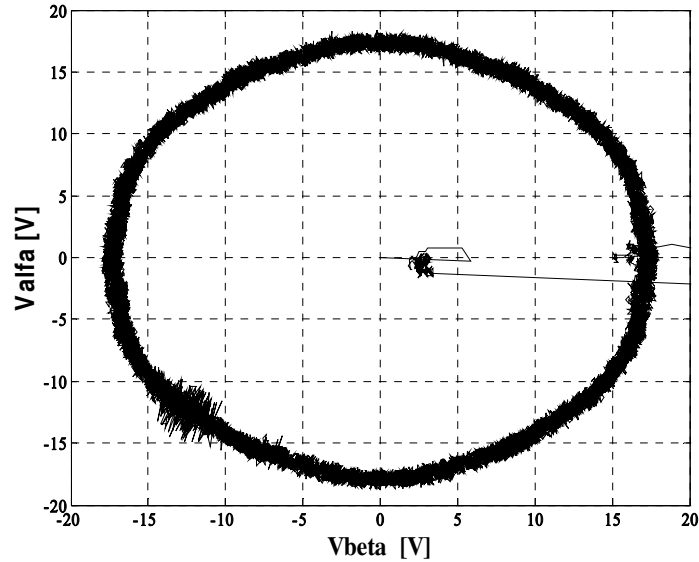

Fig.6.18 Stator currents

Fig.6.19 Estimated stator voltages in $\alpha\beta$-plane

A step change is performed in the q-axis current from 1A to 3A under no load (Fig. 6.20) at the same frequency. The speed (0.2 rpm) remains constant even with i_q notable variation. A very good dynamic response of current controller with no transients in stator currents (see Fig. 6.21) is proved.
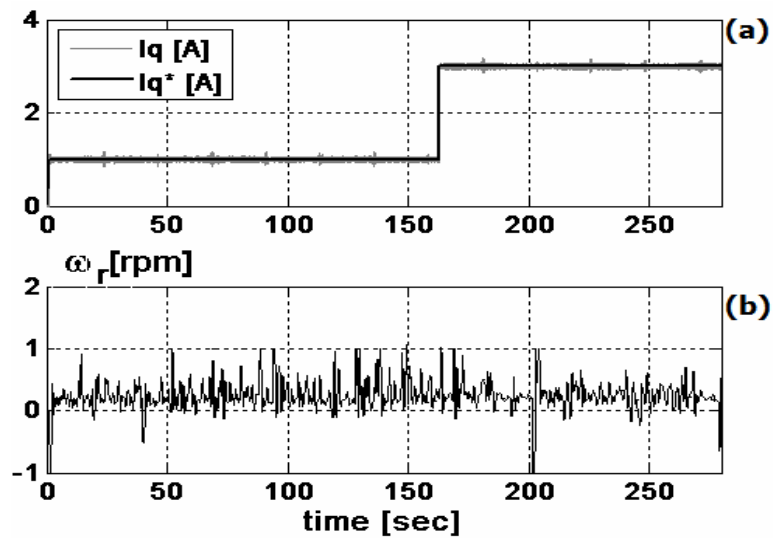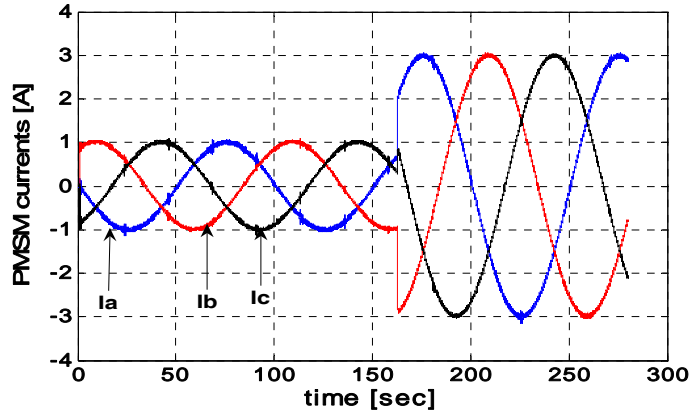

Fig.6.20 a) Measured and reference I_q current, b) measured rotor speed [rpm]

Fig. 6.21 Stator currents for increased i_q* step

B. Transition from I-F to EMF Sensorless Vector Control

To ensure a smooth start-up, a ramp variation up to 30 Hz is imposed to the reference frequency (Fig. 6.22a). The control strategy switches automatically from I-f strategy to emf sensorless vector control when the reference frequency reaches 30 Hz (Fig. 6.22a). To avoid large speed transients, the q-axis reference current is set to 0.3A until the reference frequency reaches 10 Hz, and after that, the current reference is set to 4A.

In Fig. 6.22b, the measured q-axis current is without significant transients at start-up or in the switching moment t = 8.5s when one strategy goes to the other (Fig. 6.23a).
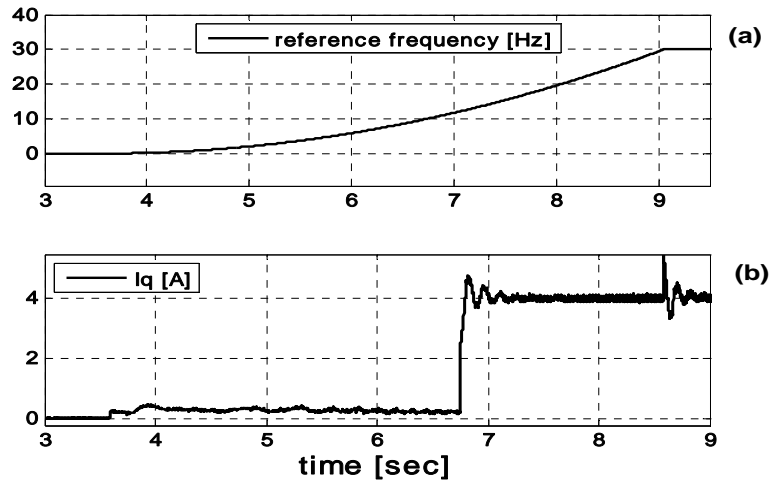
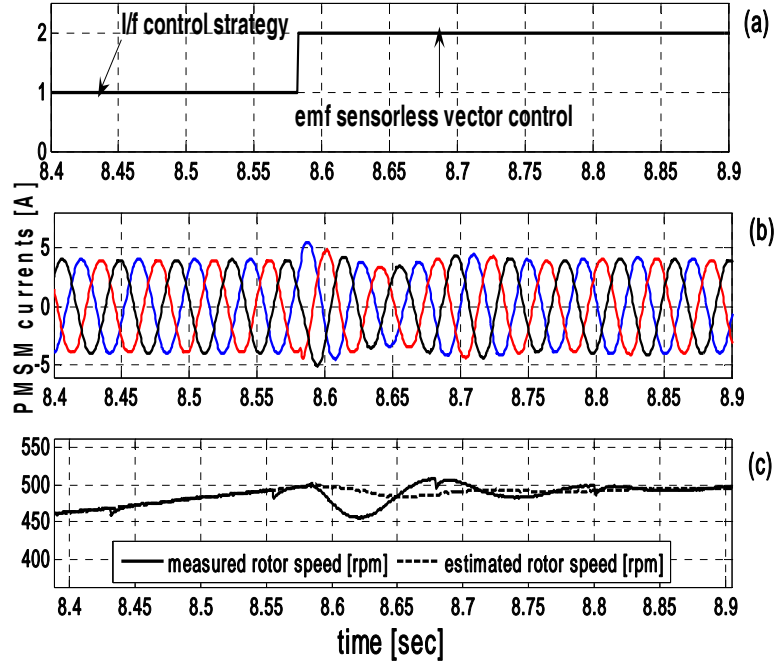Fig. 6.22 a) Reference frequency; b) q-axis current

Fig. 6.23 Transition from *I-f* to emf sensorless control: a) switching signal; b) stator currents; c) estimated and measured rotor speed
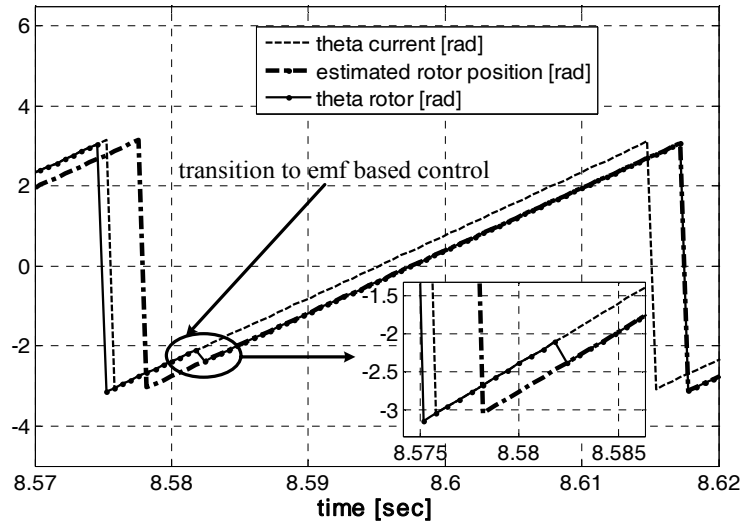

Fig. 6.24 Current vector angle, estimated rotor position angle, and rotator operator angle [rad] in transition to emf sensorless control
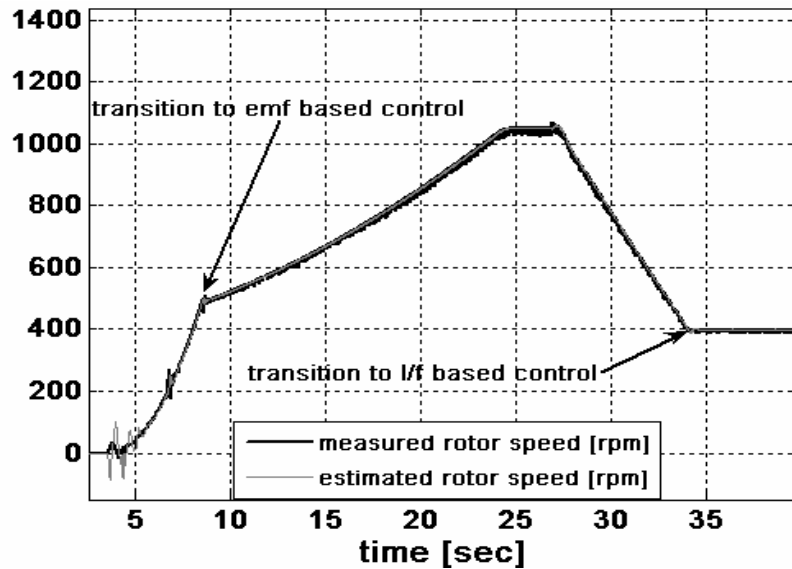
Fig. 6.25 Measured and estimated rotor speed [rpm] in transition strategies
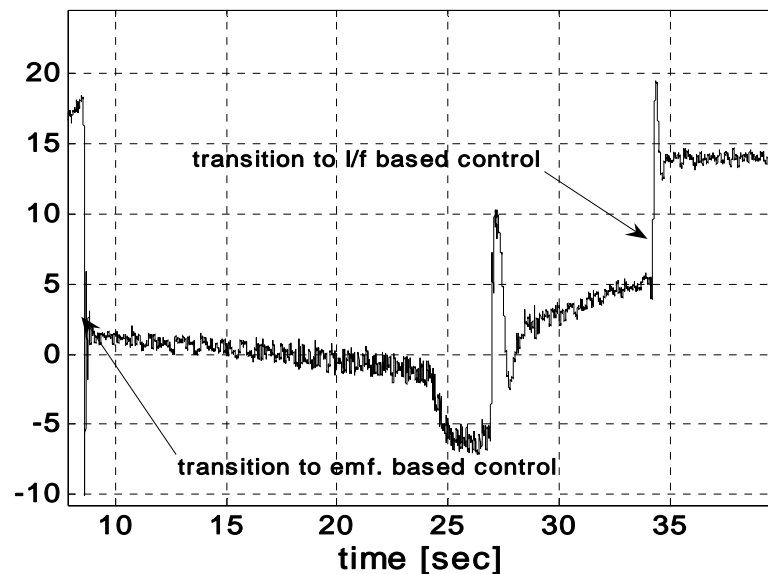
Fig. 6.26 Position estimation error [elec. deg] in transition strategies

The estimated and measured rotor speeds are displayed in Fig. 6.23c with good speed response, with no significant transients when the strategies are switched. In Fig. 6.24 the current vector angle, the estimated rotor angle and the rotator operator angle are shown. When the system automatically switches between the two control-strategies, the rotator operator angle switches smoothly from current

vector angle to estimated rotor angle. After transition, the system accelerates until 1060 rpm, and then it decelerates safely to 400 rpm with emf-based control (Fig. 6.25). During entire transient process, from the switching moment to steady state, there is a very close agreement between the estimated and the measured rotor position, showing a good tracking performance and good estimation results (Fig. 6.26).

C. Transition from EMF Sensorless Control to I-F Control

Initially, the system is running using estimated rotor position with $\theta = \hat{\theta}_r$. A deceleration is produced setting the *q*-axis current from 4A to 1A (see Fig. 6.27a). When the estimated rotor frequency (Fig. 27b) reaches a certain level (20Hz), the control strategy automatically switches from emf motion-sensorless vector control to *I-f* vector control (Fig. 6.28a) with currents frequency equal with last value of the estimated rotor frequency.
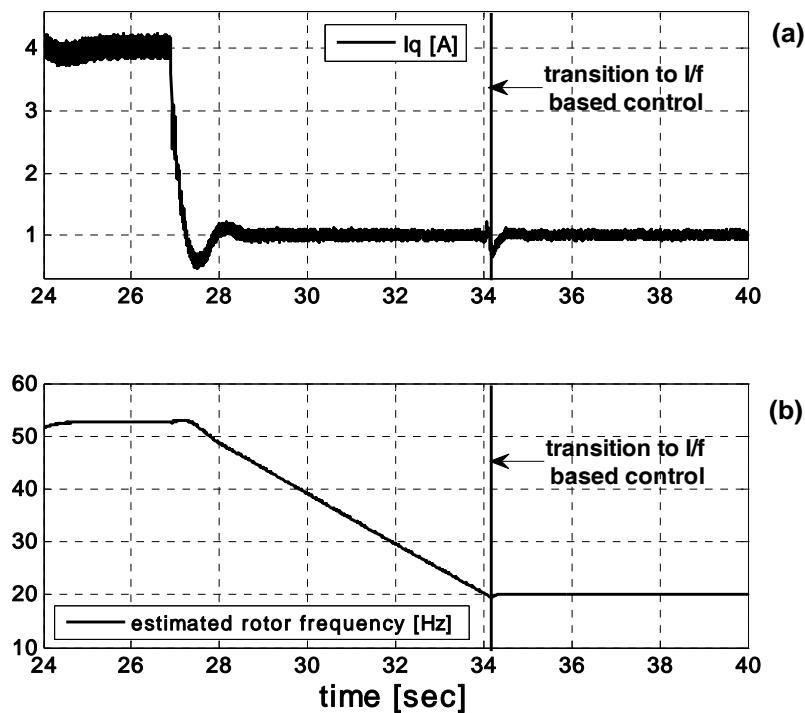
Fig. 6.27 Transition from emf sensorless control to *I-f* control: a) *q*-axis current; b) estimated rotor frequency [Hz]
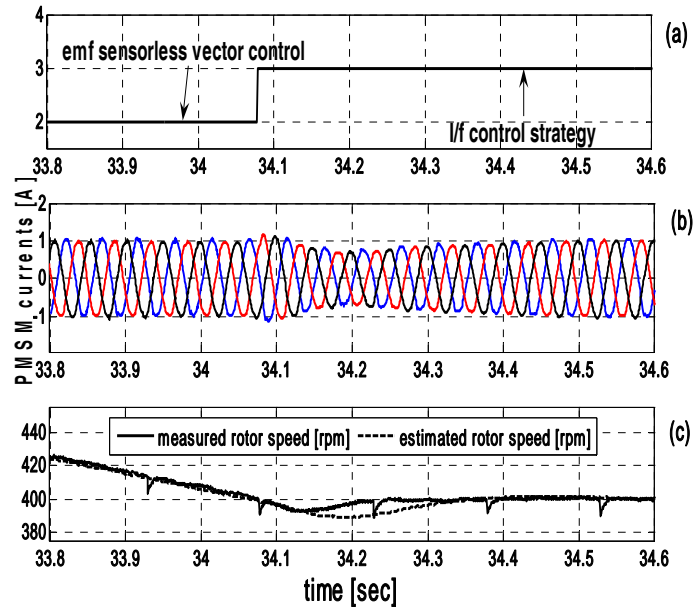
Fig. 6.28 Transition from emf sensorless control to *I-f* control: a) switching signal; b) stator currents; c) Estimated and measured rotor speed
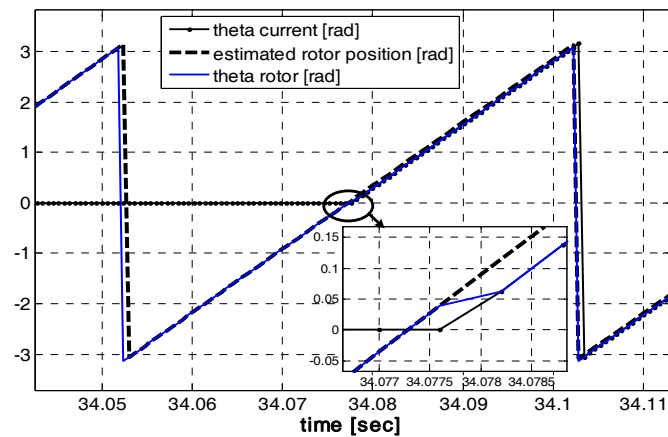
Fig. 6.29 Current vector angle, estimated rotor position angle, and rotator operator angle [rad] in transition to *I-f* control

A smooth transition without significant transients in stator currents is demonstrated in Fig. 6.28b. A closed agreement between estimated and actual rotor position is confirmed in Fig. 6.28c, certifying a good tracking performance and good estimation results. The current vector angle, estimated rotor position angle, and rotator operator angle, as well as the transition from estimated rotor position to current vector angle is shown in Fig. 6.29.

6.8   CONCLUSION

This paper proposes a new hybrid motion-sensorless control system for PMSM drives with smooth transition between *I-f* sensorless control at start-up to emf sensorless vector control. This solution is validated through extensive digital simulation results and experimental test results. The main features are the following:

▪ *I-f* sensorless control strategy for start-up and ultra-low speeds under load, which is independent of machine parameters variation and without initial rotor position detection, has been investigated through tests.

▪ Smooth transitions from *I-f* sensorless control to emf sensorless vector control and vice-versa have been demonstrated in detail, with small current transients.

▪ Good PMSM rotor position and speed estimations have been proved throughout tests.

▪ The proposed method seems quite practical for general industrial applications with

▪ variable-speed PMSM drives in large speed-range and suitable for wind generators safe (faster) self starting when connected to the grid, or moving the rotor a little for inspections/repairs.

References:

[1] A. B. Kulkarni and M. Ehsani, "A novel position sensor elimination technique for the interior permanent-magnet synchronous motor drive,"*IEEE Trans. Ind. Appl.*, vol. 28, no. 1, pp. 144–150, Jan./Feb. 1992.

[2] J. S. Kim and S. K. Sul, "New approach for the low speed operation of PMSM drives without rotational position sensors," *IEEE Trans. Ind.Electron.*, vol. 11, no. 3, pp. 512–519, May 1996.

[3] Z. Chen, M. Tomita, S. Doki, and S. Okuma, "An extended electromotive force model for sensorless control of interior permanent magnet synchronous motors," *IEEE Trans. Ind. Electron.*, vol. 50, no. 2, pp. 288–295, Apr. 2003.

[4] S. Morimoto, K. Kawamato, M. Sanada, andY. Takeda, "Sensorless control strategy for salient pole PMSM based on extended EMF in rotating reference frame," *IEEE Trans. Ind. Appl.*, vol. 38, no. 4, pp. 1054–1061, Jul./Aug. 2002.

[5] S. Östlund and M. Brokemper, "Sensorless rotor position detection from zero to rated speed for an integrated PM synchronous motor drive," *IEEE Trans. Ind. Appl.*, vol. 32, no. 5, pp. 1158–1165, Sep./Oct. 1996.

[6] H. Kim, M. C. Harke, and R. D. Lorenz, "Sensorless control of interior permanent-magnet machine drives with zero phase lag position estimation," *IEEE Trans. Ind. Appl.*, vol. 39, no. 6, pp. 1726–1733, Nov./Dec. 2003.

[7] B. N. Mobarakeh, F. M. Tabar, and F. M. Sargos, "Mechanical sensorless control of PMSM with online estimation of stator resistance," *IEEETrans. Ind. Appl.*, vol. 40, no. 2, pp. 457–471, Mar./Apr. 2004.

[8] R. B. Sepe and J. H. Lang, "Real time observer-based adaptive control of a permanent magnet synchronous motor without mechanical sensors," *IEEE Trans. Ind. Appl.*, vol. 28, no. 6, pp. 1345–1352, Nov./Dec. 1992.

[9] J. A. Solsona and M. I. Valla, "Disturbance and nonlinear Luenberger observers for estimating mechanical variables in permanent magnet synchronous motors under mechanical parameters uncertainties," *IEEE Trans. Ind. Electron.*, vol. 50, no. 4, pp. 717–725, Aug. 2003.

[10] S. Bolognani, R. Oboe, and M. Zigliotto, "Sensorless full-digital PMSM drive with EKF estimation of speed and rotor position," *IEEE Trans. Ind. Electron.*, vol. 46, no. 1, pp. 184–191, Feb. 1999.

[11] H.W. Kim and S. K. Sul, "A new motor speed estimation using Kalman filter in low-speed range," *IEEE Trans. Ind. Electron.*, vol. 43, no. 4, pp. 498–504, Aug. 1996.

[12] G. Henneberger, B. J. Brunsbach, and T. Klepsch, "Field-oriented control of synchronous and asynchronous drives without mechanical sensors using a Kalman filter," in *Proc. EPE'91*, vol. 3, 1991, pp. 664–671.

[13] Y. H. Kim andY. S.Kook, "High performance IPMSM drives without rotational position sensors using reduced-order EKF," *IEEE Trans. Energ.Conv.*, vol. 14, no. 4, pp. 868–873, Dec. 1999.

[14] M. Boussak, "Digital signal processor based sensorless speed control of a permanent magnet synchronous motor drive using extended Kalman filter," *EPE J.*, vol. 11, no. 3, pp. 7–15, Aug. 2001.

[15] P. B. Schmidt, M. L. Gaspery, G. Ray, and A. H. Wijenayake, "Initial rotor angle detection of a nonsalient pole permanent magnet synchronous machine," in *Conf. Rec. IEEE-IAS Annu. Meeting*, vol. 1, 1997, pp. 459–463.

[16] S. Nakashima, Y. Inagaki, and I. Miki, "Sensorless initial rotor position estimation of surface permanent-magnet synchronous motor," *IEEE Trans. Ind. Applicat.*, vol. 36, pp. 1598–1603, Nov./Dec. 2000.

[17] K. Tanaka, T. Yuzawa, R. Moriyama, and I. Miki, "Initial rotor position estimation for surface permanent magnet synchronous motor," in *Conf. Rec. IEEE-IAS Annu. Meeting*, Chicago, IL, Sept./Oct. 2001, pp. 2592–2597.

[18] T. Takeshita and N. Matsui, "Sensorless control and initial position estimation of salient-pole brushless DC motor," in *Proc. Advanced Motion Control Workshop*, 1996, pp.18–23.

[19] M. Schroedl, "Sensorless control of ac machines at low speed and standstill based on the "INFORM" method," in *Conf. Rec. IEEE-IAS Annu. Meeting*, Oct. 6–10, 1996, pp. 270–277.

[20] P. L. Jansen, M. Corley, and R. D. Lorenz, "Flux, position, and velocity estimation in AC machines at zero and low speed via tracking of high frequency saliencies," in *Proc. EPE Conf.*, 1995, pp. 154–160.

[21] S. Kondo, A. Takahashi, and T. Nishida, "Armature current locus-based estimation method of rotor position of permanent magnet synchronous motor without mechanical sensor," in *Conf. Rec. IEEE-IAS Annu.Meeting*, vol. 1, 1995, pp. 55–60.

[22] F. Philippen, "Position estimation in PM synchronous machines using single saliency-tracking, self-sensing methods," M.S. & Diplomarbeit thesis, Univ. Wisconsin, Madison, and Tech. Univ. Aachen, Germany, 1998.

[23] A. Consoli, G. Scarcella, and A. Testa, "Sensorless control of PM synchronous motors at zero speed," in *Conf. Rec. IEEE-IAS Annu. Meeting*, Phoenix, AZ, Oct. 1999, pp. 1033–1040.

[24] M. Corley and R. D. Lorenz, "Rotor position and velocity estimation for a permanent magnet synchronous machine at standstill and high speeds,"*IEEE Trans. Ind. Applicat.*, vol. 34, pp. 784–789, July/Aug. 1998.

[25] T. Noguchi, K. Yamada, S. Kondo, and I. Takahashi, "Initial rotor position estimation method of sensorless PM synchronous motor with no sensitivity to armature resistance," *IEEE Trans. Ind. Electron.*, vol. 45, pp.118–125, Feb. 1998.

[26] D.-W. Chung, J.-K. Kang, and S. Sul, "Initial rotor position detection of PMSM at standstill without rotational transducer," in *Proc. IEEE IEMDC*, May 1999, pp. 785–787.

[27] J.-I. Ha, K. Ide, T. Sawa, and S. Sul, "Sensorless position control and initial position estimation of an interior permanent magnet motor," in *Conf. Rec. IEEE-IAS Annu. Meeting*, Chicago, IL, Sept./Oct. 2001, pp. 2607–2613.

[28] Y. Jeong, R. D. Lorenz, T. M. Jahns, and S. Sul, "Initial rotor position estimation of an interior permanent magnet synchronous machine using carrier-frequency injection methods," in *Proc. IEEE IEMDC*, June 2003, pp. 1218–1223.

[29] S. Shinnaka, "New "mirror-phase vector control" for sensorless drive of permanent-magnet synchronous motor with pole saliency," *IEEE Trans. Ind. Appl.*, vol. 40, no. 2, pp. 599–606, Mar./Apr. 2004.

[30] J. Holtz, "Initial rotor polarity detection and sensorless control of PM synchronous machines", in *Conf. Rec. IEEE-IAS 2006 Annu. Meeting*, Tampa, FL, vol. 4, Oct. 2006, pp. 2040–2047.

[31] I. Boldea, N. Muntean, and E. Hauler, "Distributed anisotropy rotor synchronous motors proving high motor performances and new motion sensorless controller", in *Record of PCIM-1992*, Nurnberg, Germany, April 1992.

[32] M.Fatu, I. Boldea , G.-D. Andreescu, F. Blaabjerg, „I-F Starting Method with Smooth Transition to EMF Based Motion-Sensorless Vector Control of PM Synchronous Motor/Generator", sent pending for, IEEE PESC 2008.

[33] I. Boldea and S.A. Nasar, *Electric Drives*, 2nd Edition, Florida: CRC Press, Taylor & Francis, 2005.

Chapter 7

The experimental test platform

Abstract

This chapter presents an extended description of the laboratory setup used for experiments in chapters 3-6.
It was realized in the Dspace Lab, Institute of Energy Technology, Aalborg Denmark, with the intended purpose to prove and gain new information about the control of permanent magnet synchronous generator with two back-to-back connected inverters to the power grid or in stand alone, as the main part of the thesis.

7.1 Laboratory setup for Chapters 3,4,5

The test setup consists in a 12 Nm PMSG connected to the grid by two back-to-back Danfoss VLT 5005 voltage source inverters, and mechanically driven by a PMSM prime mover with SIMOVERT MASTERDRIVE.

7.1.1 Hardware specifications

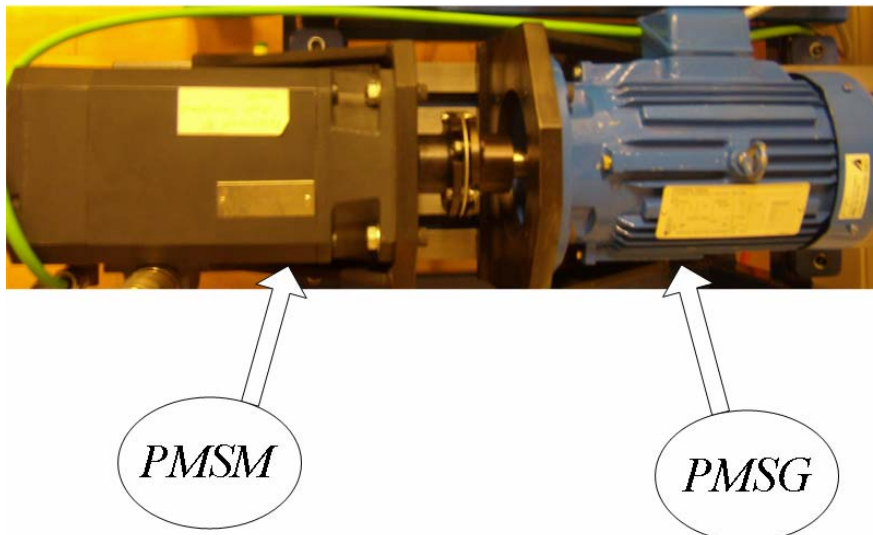The main component in the setup is the permanent synchronous generator(PMSG) manufactured by Yaskawa (see Fig.7.1).

Fig.7.1 PMSG (right) and its driving motor (left)

Parameters of the PMSG are shown in Table I:

Table I
PMSG Parameters

Number of pole pairs (p)	3
Rated power	2.2 kW
Rated speed	1750 rpm
Rated frequency	87.5 Hz
Rated torque	12 Nm
Rated phase to phase voltage	380 V(rms)
Rated phase current	4.1 A(rms)
Stator resistance per phase (R_s)	3.3 Ω
d-axis inductance (L_d)	41.59 mH
q-axis inductance (L_q)	57.06 mH
Rotor permanent–magnet flux λ_{PM})	0.4832 V s rad-1
Inertia of the rotating system (J)	$10.07{*}10^{-3}$ kgm^2
Viscous friction coefficient (B)	$20.44{*}10^{-4}$ Nms/rad

7.1.2 The power inverters VLT 5004 and their interface and protection

The power inverters are commercial VLT 5004, 4.2 kVA manufactured by Danfoss Drives, Denmark (see Fig. 7.2 for a photo of the inverters). The main data for them are given in Table II.
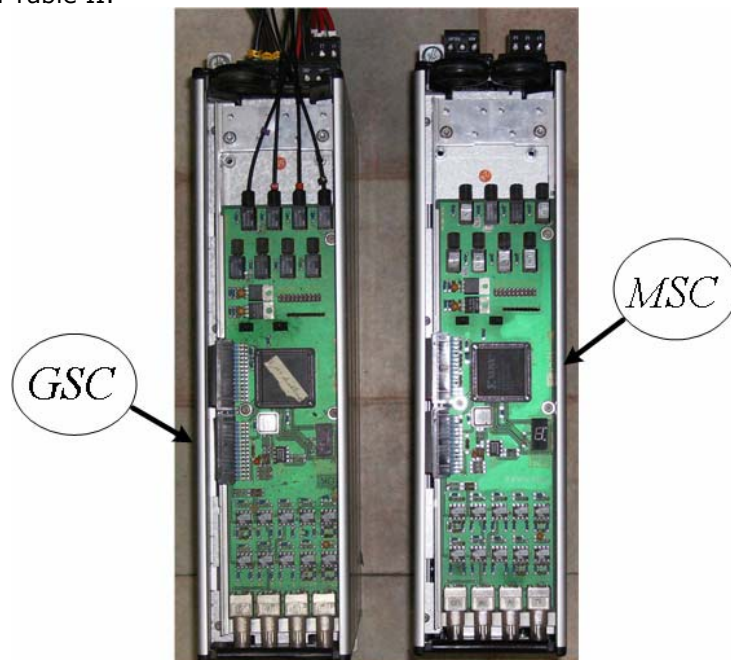

Fig.7.2 The Danfoss power inverters equipped with interface and protection cards (IPC) left – GSC, right – MSC.

Table II
Danfoss inverters specifications

Rated Power	4.2 kVA
Nominal Voltage	380 V
Nominal Current	6.5 A
Maximum DC Link Voltage	1200 VDC
Switching Frequency	10 kHz

Their original interface cards and control panels were replaced with interface and protection cards (IPC – see Fig.7.3), produced by IET, Aalborg University.

Fig. 7.3 Physical layout of the Interface and Protection Card for the power inverters

IPC is a PCB card with the same dimensions and mounting layout as the original VLT5004 control card. It has two flat cables connected to VLT power-card K103 and MK104 sockets and four BNC sockets for output currents **IU-VLT, IVVLT, IW-VLT** and DC-voltage **UD-VLT** signals (not used in our case).

The gate signals can be brought-in via optic fiber using the eight receivers onboard or directly in TTL format, using the J2-socket. Besides the seven IGBT gate signals (**UP, UN, VP, VN, WP, WN** and **BR**), there is an enable signal (**EN)** that inhibits the gate drivers if it is kept low (coasting).

The interface board is featured with two push-buttons: RESET (**RST**) and MANUAL TRIP (**MT**) as they are labeled on the card. Any fault that might occur need to be cleared out by pressing **RST** in order to release the gate signals. **MT** forces a trip when pressed. All faults can be read out the LED digit display, as shown in Table III.

Table III
VLT fault description

	Over Temp. (OT)
	Manual Trip (MT)
	Shoot Through (ST)
	DC Over Voltage (OV)
	Over Current (SC)
	VLOG out of range
	Coast (EN)

IGBT gate signals. The VLT5004 gate drivers require the gate signals to be modulated with 4 MHz. All seven gate signals (**UP, UN, VP, VN, WP, WN** and **BR**) are brought to a CPLD where 4 MHz modulation with edge synchronization is carried out. Because the optic fiber receivers are inverting devices, gate signals are inverted at the input of the CPLD logic block. An asynchronous clear is performed by the active high **INHIBIT** signal, which is signals, OR-ing them for all three phases and negating for turning it in an active high signal. In this design a 2 µs dead-time was implemented in the CPLD. Hence, each

inverter is controlled through 3 signals (UP, VP, WP) – for the upper IGBTs – and an enable signal (EN) – see Fig. 7.4
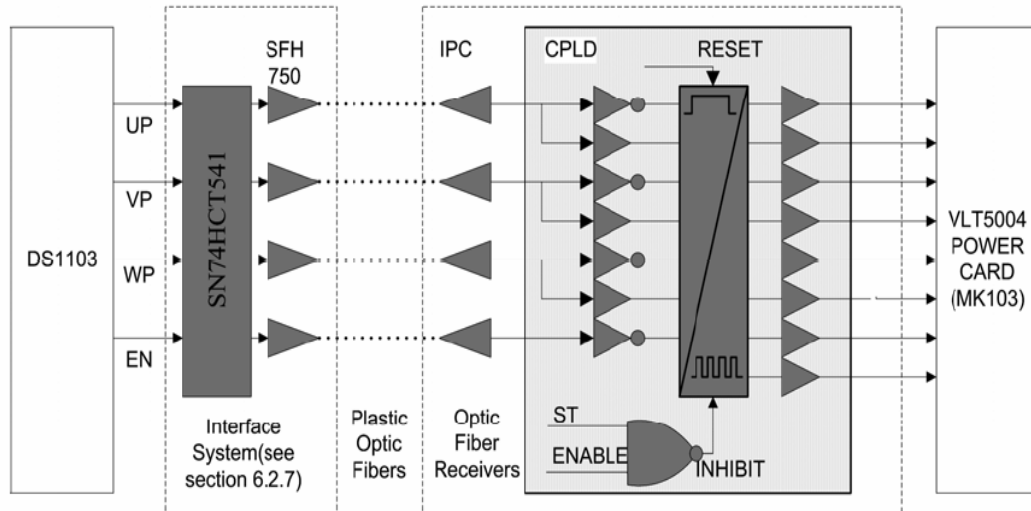
Fig. 7.4 Interface and protection card (for one inverter – for the other is identical)

7.1.3 Grid emulator

The grid is here replaced by a programmable three phase ac power source (California Instruments 5005 from iX Series II), capable to create voltage faults. Each phase was emulated by a programmable AC source.

The *i*X Series II represents a new generation of AC and DC power source that addresses increasing demands on test equipment to perform more functions at a lower cost. By combining a flexible AC/DC power source with a high performance power analyzer, the *i*X Series II systems are capable of handling complex applications that have traditionally required multiple instruments.

The sleek integrated approach of the *i*X Series II avoids the cable clutter that is commonly found in AC test systems. The *i*/*i*X Series II is rack mountable with a 4U chassis design. All connections are made internally and the need for external digital multimeters, power harmonics analyzer and current shunts or clamps is completely eliminated.

Windows® Instrument Control Software is included with the Compact *i*X and *i* Series1 . This software provides easy access to the power source's capabilities without the need to develop any custom code. The following functions are available [1]:

 • Steady state output control (all parameters)
 • Create, run, save, reload & print transient programs
 • Generate & save harmonic waveforms [*i*X only]
 • Generate & save arbitrary waveforms [*i*X only]
 • Measure & log standard measurements
 • Capture & display output voltage & current waveforms [*i*X only]
 • Measure, display, print & log harmonic voltage & current measurements [*i*X only]

 • Display bus traffic to & from the AC Source to help you develop your own test programs.

The *i*X and *i* Series II controllers have a powerful AC and DC transient generation system that allows complex sequences of voltage, frequency and wave shapes to be generated. This further enhances the *i/i*X's capability to simulate AC line conditions or DC disturbances. When combined with the multi phase arbitrary waveform capabilities, the AC and DC output possibilities are truly exceptional. In three phase *i/i*X system configurations, transient generation is controlled independently yet time synchronized on all three phases. Accurate phase angle control and synchronized transient list execution provide unparalleled accuracy in positioning AC output events. Transient programming is easily accomplished from the front panel where clearly laid out menu's guide the user through the transient definition process. The front panel provides a convenient listing of the programmed transient sequence and allows for transient execution, Start, Stop, Abort and Resume operations [1].

Fig.7.5 shows an example Graphical User Interface program supports transient definitions using a spreadsheet-like data entry grid. The programmable three phase source used during experiments is illustrated in Fig.7.6.
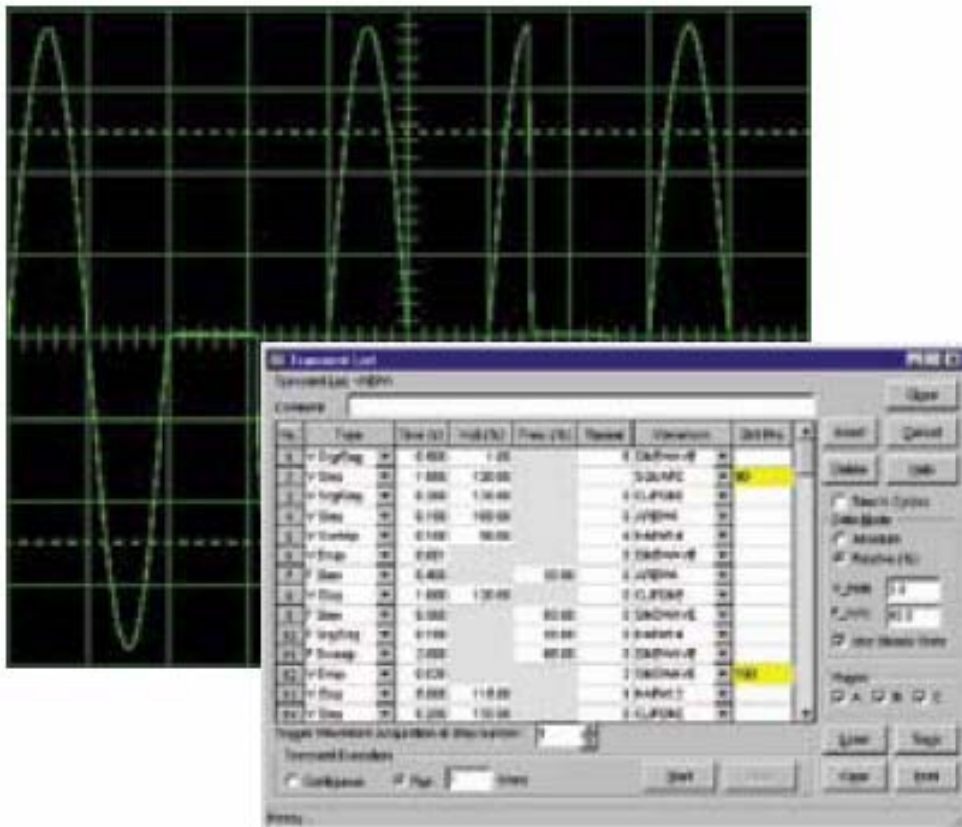

Fig. 7.5 Transient List Data Entry in GUI program. [1]

Fig.7.6 California Instruments 5005 [1]

7.1.4 Wind turbine emulator

The wind turbine mechanical shaft is emulated using a 14.7Nm-3000rpm PMSM driven by a commercial inverter operated in open loop torque control mode (SIMOVERT MASTERDRIVE Fig.7.7).

SIMOVERT MASTERDRIVES are systems-based. They have a uniform operator control philosophy, they can be combined as required, even with units with different control versions and they have a unified design. They always provide the optimum solution as system modules - whether as single drives or as multi-motor drives.

The SIMOVERT MASTER DRIVES product group comprises the following components [2]:

- Converters
- Inverters
- Rectifier units
- Rectifier/regenerative feedback units (RE, AFE)
- Active front end (AFE) incoming units
- Braking units and braking resistors
- DC link bus for cabinet units
- Interference suppression filter
- Line commutating reactor
- Line filters
- Fuses
- Output filters (dv/dt and sine filter)
- Technology modules
- Sensor boards (SBx) for speed and position sensing
- Communication boards (CBx) for field bus interfacing
- SIMOLINK (SLx) for fast transmission of setpoints and actual values

Fig.7.7 SIMODRIVE inverter

The advantages of this system are [2]:
- Can be expanded in a modular fashion: Using operator control panels, terminal expansion modules, braking modules, input and output filters
- High speed and torque accuracy
- Excellent dynamic performance
- Extremely smooth running characteristics at low speeds
- High overload capability
- High power density
- Optimum price-performance ratio
- Can be simply engineered using PATH, in a user-friendly fashion

The PMSM motor was equipped with an incremental encoder which provides a resolution of 2048 lines per revolution. The output is a usual A QUAD B (A+, A-, B+, B-, N+, N-) which can be directly connected to the control system as it provides encoder interfaces.

7.1.5 Voltage and current sensors

As can be seen in Fig.7.1, are 4 currents and 3 voltages are acquired to fulfill the control system requirements. These are:

- 2 stator currents (the third is calculated in the control algorithm taking into account that the sum of them is zero).
- 2 grid currents (the third is calculated in the control algorithm taking into account that the sum of them is zero).

- 2 grid line-to-line voltages which are in fact used to calculate the phase voltages of the grid
- DC voltage

The acquisition system was designed as follows:

- two boxes with 2 current sensors, one for PMSG currents and the other for grid, each type LEM LA 55-P with adequate signal conditioning such that at 10A measured current the sensor output will be 10V, required for the control system's A/D channels.
- one box with 3 voltage transducers type LEM LV 25-P with appropriate signal conditions such as the output of the sensor is 10V, required for acquisition system.

7.1.6 LC filter

Between the grid inverter the grid itself a LC filter was introduced in order to reduce the harmonic content in the line current produced by switching. The filter parameters are: $L_f = 0.01$ H, $R_f = 0.4$ Ω, $C_f = 0.7$ μF.

7.1.7 Control hardware

Dspace 1103 is a very flexible and powerful tool, featuring both high computational capability and comprehensive I/O periphery, built for real-time control system with just one controller board (Fig.7.8). Dspace 1103 has been used in all experiments in this thesis.

Fig.7.8 DS1103 PPC Controller Board [3]

Used with Real-Time Interface (RTI), the controller board is fully programmable from the Simulink® block diagram environment. The user can configure all I/O graphically by dragging RTI blocks from Matlab® libraries. This is a quick and easy way to implement your control functions on the board and also reduces the implementation time to minimum.

For additional I/O tasks, a DSP controller unit built around Texas Instruments TM320F240 DSP is used as a subsystem (Fig. 7.9).

Fig.7.9 DS1104 R&D Controller Board [3]

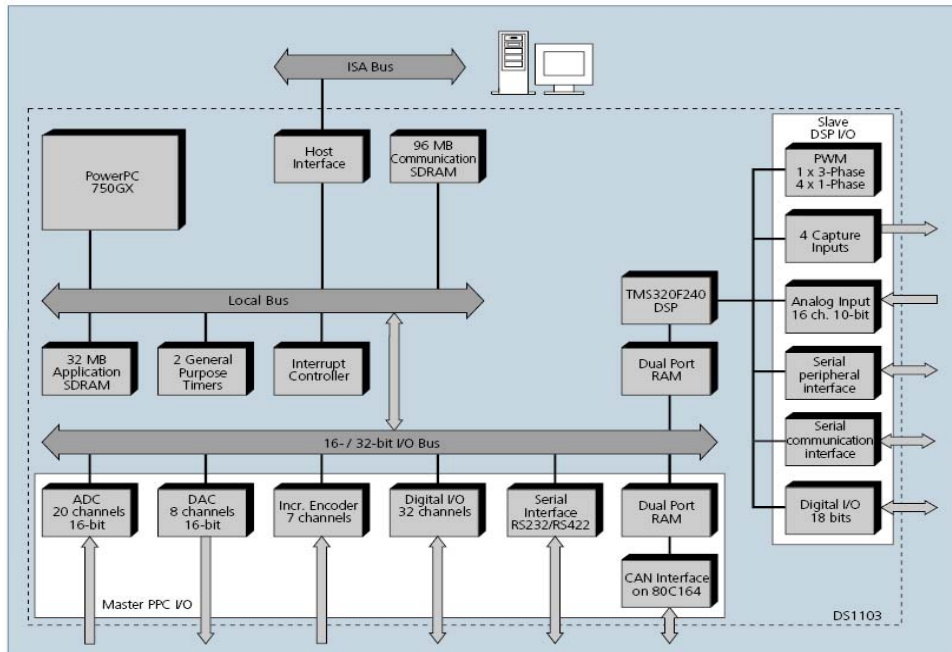An overview of the functional units of Dspace 1103 is shown in Fig.10

Fig.10 Block diagram of Dspace 1103 [3]

7.1.8 The transformer

The PMSG was connected to the local grid through a 1:1 Δ/Y transformer. The short circuit parameters are listed in Table IV.

Table IV

L_t	0.002 H
R_t	0.255 Ω

7.1.9 The static switch

A three-phase static switch (Fig.7.11) is used in Chapter 4 to simulate a fault event on grid side. The static switch used in experiments is a three-phase solid state Crydom® Series 53TP relays capable to switch up to 530 V_{rms} directly to loads such as motors, transformers, heating elements, etc.
The control signal for the static switch is brought via optic fiber from Digital I/O of the Dspace 1103 unit.

Fig.11 Static switch [4]

7.1.10 Power analyzer

In chapter 5 the total harmonic distortion (THD) content of the voltage is measured with a three-phase Voltech PM3000 power meter (Fig.7.12).
The main characteristics of this system are [5]:
   • 0.1% basic accuracy
   • DC to 250kHz bandwidth
   • 1000Vpk/20A RMS direct inputs
   • Graphics display of waveforms and harmonic bar-charts
   • W, V, A, VA, Var, power factor, cosφ, V_{pk}, A_{pk}, crest factors and frequency
   • Channel 1, 2, 3, SUM( ) and neutral quantities on the PM300 three-phase analyzer
   • Harmonics V, A, (incl. phase) and W to the 50th; total harmonic distortion
   • Integrator for W-hr, VA-hr, A-hr, VA-hr, average and target PF
   • Easy-to-use menu structure available in different languages

- Accepts and scales for external current and voltage transducers; external shunt inputs for current transducers with voltage output

Fig.7.12 Three-phase Voltech PM3000 power meter [5]

The results from the power analyzer can be displayed on computer with VPAS Lite Windows software under numerical data and harmonic bar charts.
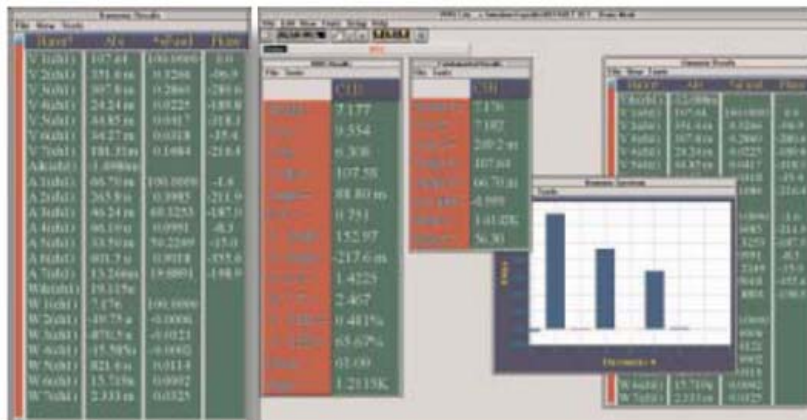

Fig.13 VPAS Lite software [5]

7.2 Laboratory setup for chapter 6

7.2.1 Power inverter FC 302

In chapter 6 the power converter used in experiments is Danfoss FC 302 type (Fig. 7.14a). The original interface card and control panel were replaced with interface and protection cards (IPC2 – see Fig. 7.14), produced by IET, Aalborg University.

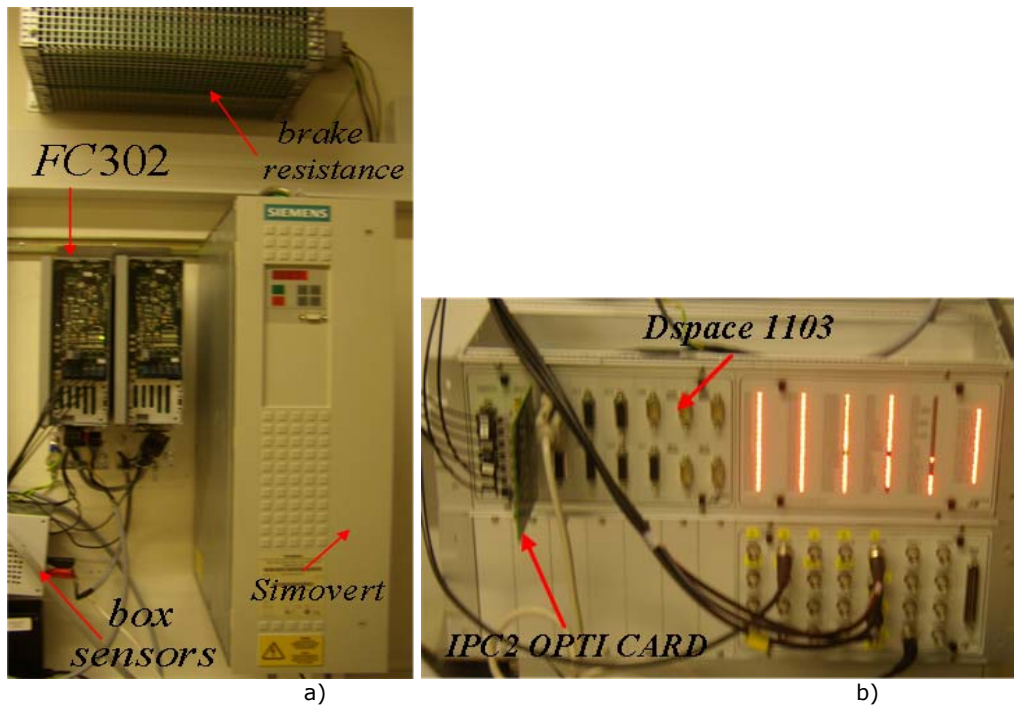a)   b)
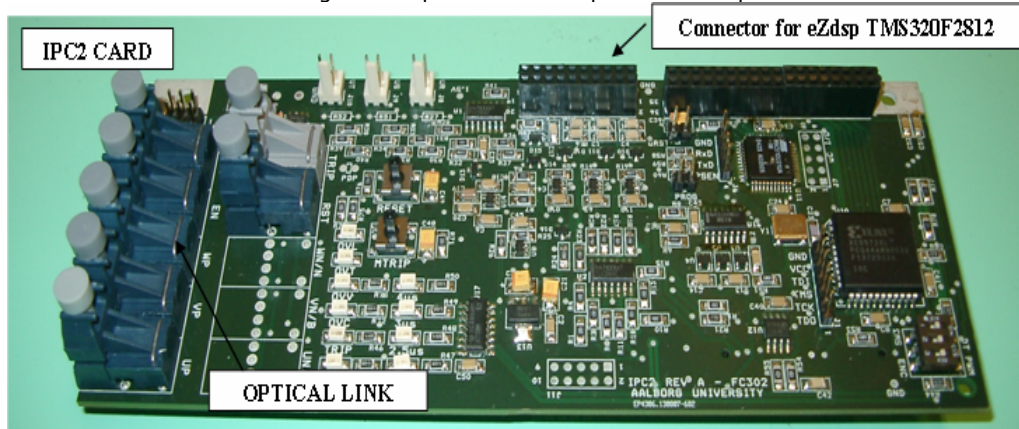
Fig.7.14 Experimental setup used in Chapter 6

Fig.7.15 IPC2 interface card for FC 302

IPC 2 is a PCB card with the same dimensions and mounting layout as the original FC 302 control card. It offers the possibility to be connected with an external digital controller (ex (Zdsp TMS 320F2812). The dead time for switches is hardware implemented on IPC board and the user can choose between 1.5-3µs.

The interface board is featured with two push-buttons: RESET (**RST**) and MANUAL TRIP (**TRIP**) as they are labeled on the card. Any fault that might occur need to be

cleared out by pressing **RST** in order to release the gate signals. **MT** forces a trip when pressed.

IPC 2 card is connected through optical interface IPC2OPTI card with dSPACE DS1103/DS1104. The IPC2OPTI can be featured with 1 or 2 sets of optical cables available for control of back-to-back converters.
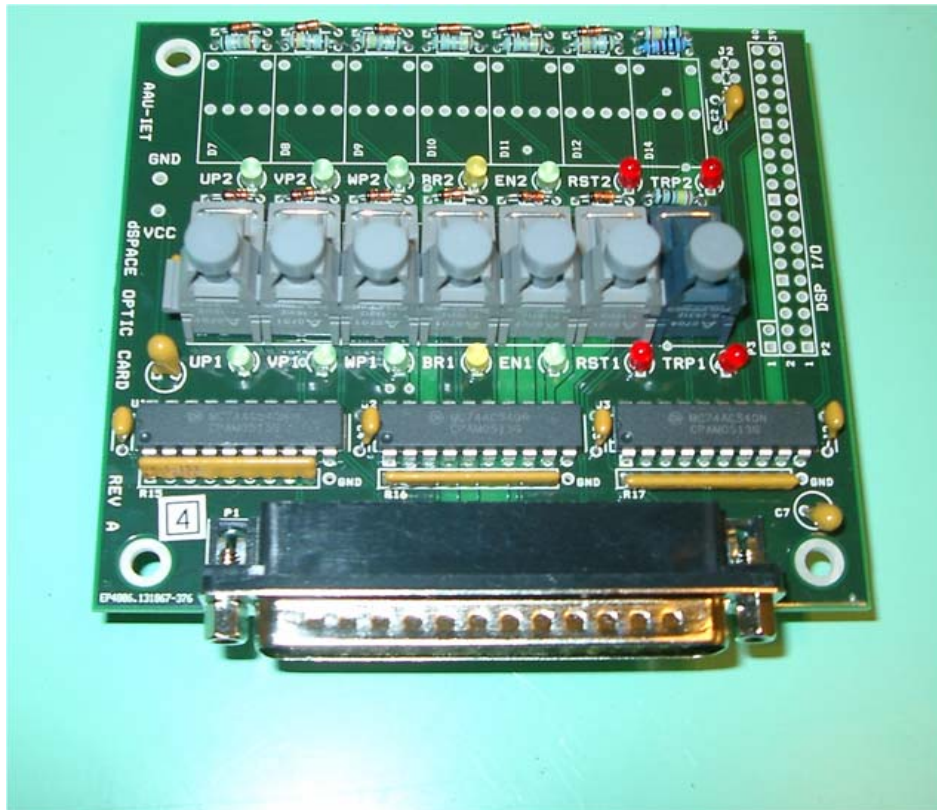

Fig.16 IPC2OPTI card for dSPACE DS1103/DS1104

7.3 Software

The control algorithms were implemented in Simulink environment, compiled automatically using Microtec C compiler for Motorola Power PC and Texas Instruments C compiler and built/downloaded automatically using the dSpace system specialized MLIB/MTRACE mechanism (Fig.7.17).

The software used in Chapters 3,4,5 has two parts:
  - wind turbine emulator triggered by a PWM interrupt at 1ms.
  - control of the machine-side converter respectively grid-side converter triggered by a PWM interrupt at 9KHz.

Fig.17 The Simulink software
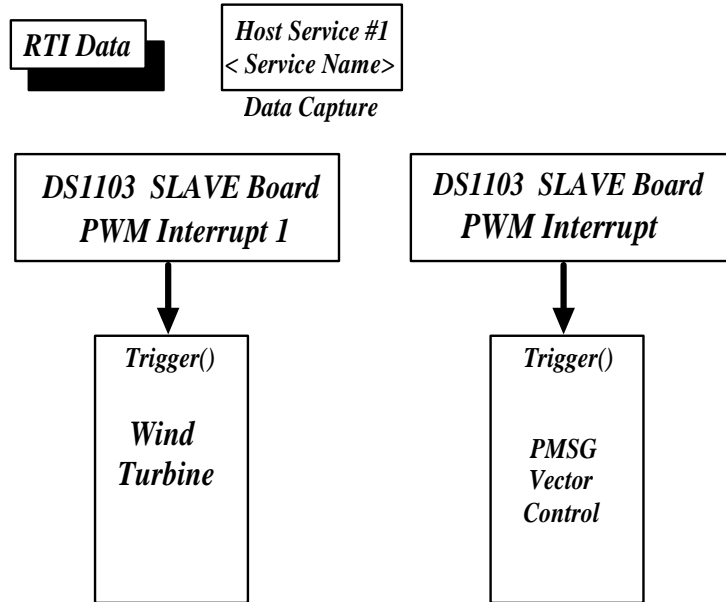
The content of the wind turbine block is shown in Fig.7.18 where *INCLINES* represents the number of lines per revolution and *h* is sample frequency. The torque value for the wind turbine, T_t, is sent from DACch1 of Dspace 1103 interface via a galvanic separation unit ISO-SIMO (see Fig.7.19) to SIMOVERT drive.
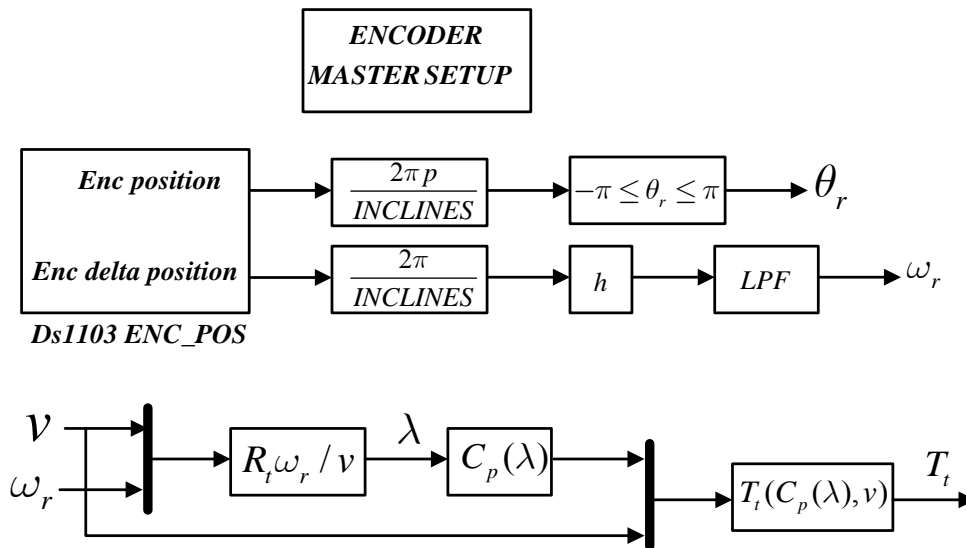

Fig.7.18 Wind turbine emulator implemented with Matlab/Simulink
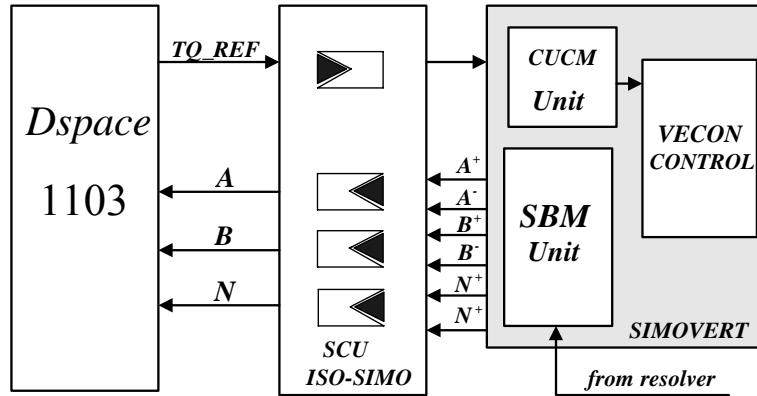
Fig. 7.19 Connections of SIMOVERT drive system to the DS1103 controller card

The PMSG control block contains:
-    acquisition block
-    protection
-    grid-side inverter control
-    machine-side inverter control

The grid and stator currents are acquired on the 4 nonmultiplexed A/D channels with 12-bit resolution, 800 ns sampling time. The rest of the voltages are acquired on the multiplexed channels with 16-bit resolution, 4 μs sampling time.

The mask of the protection block is shown in Fig. 7.20. The block has as inputs the grid and stator currents respectively measured DC link voltage. In order to prevent any damage upon the power converters, four protections have been implemented: overcurrent in the grid, overcurrent in the stator, overvoltage in Dc link, undervoltage in the DC link.
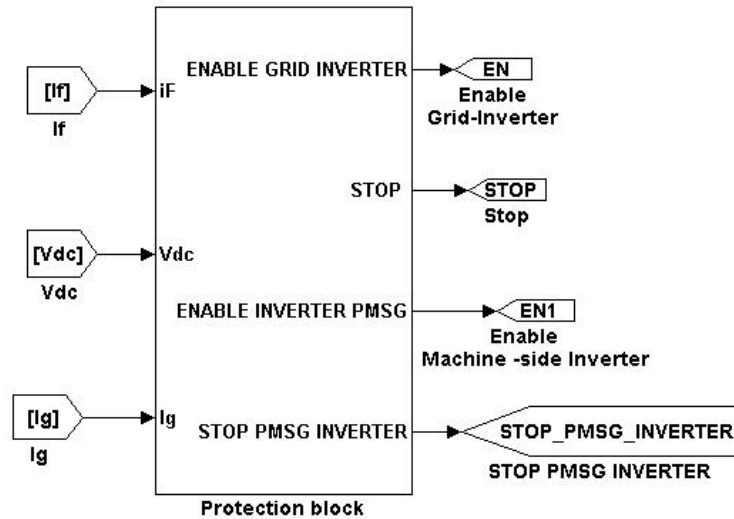
Fig. 7.20 Protection block

The outputs of the protection block are enable and stop signals for the grid –side inverter respectively machine-side inverter.

When the Dc link voltage level exceeds a certain level the damping chopper control is activated and discharges the energy in excess stored in the DC link (see Fig. 7.21).

Fig. 7.21 Chopper control

The grid side control software

Grid-side inverter control consists mainly of two cascade loops (Fig. 7.22). The Dc-link voltage controller is designed for balancing the power flow in the system, while the current control loop is responsible for power quality issues, power factor and current protection.
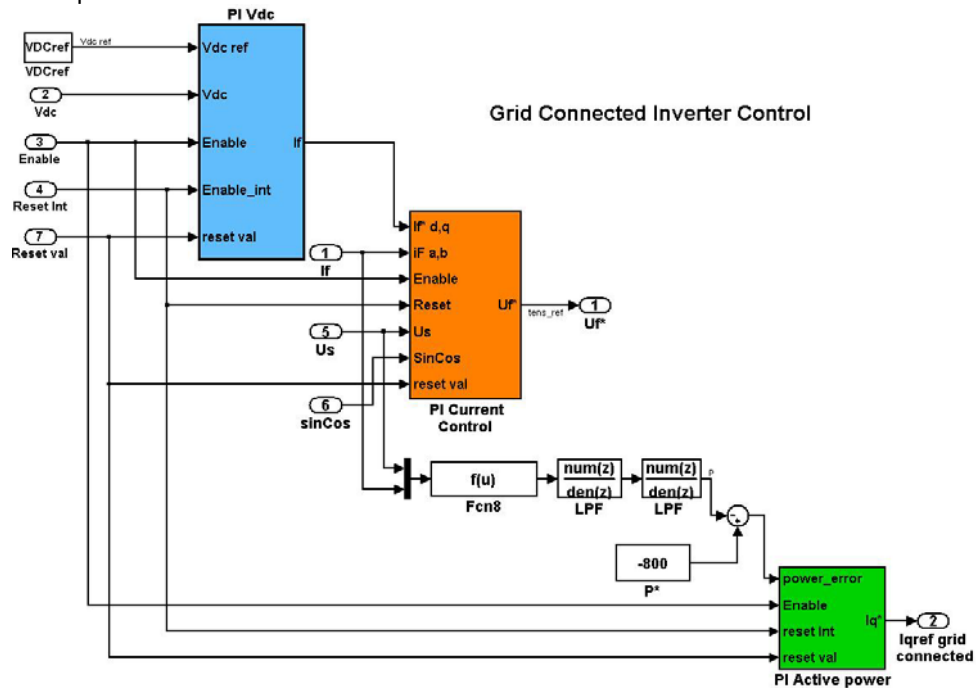
Fig. 7.22 The Simulink Grid-side control

In Fig. 7.22 is depicted the grid –side inverter control implemented in Matlab/Simulink used in chapter 2 and chapter 4 (when the WGS is connected to the local grid).

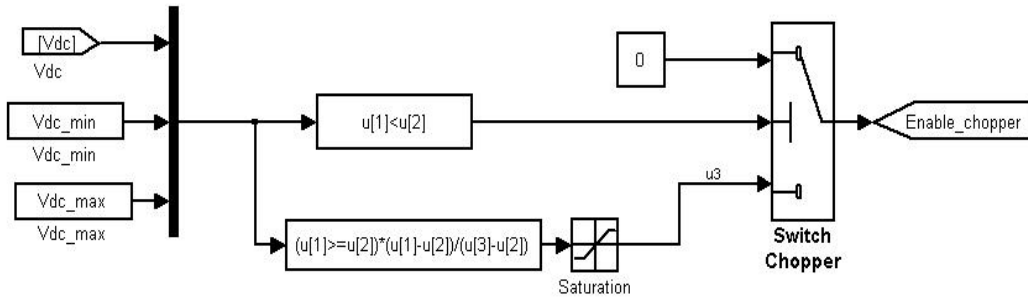Due to large penetration of the WGSs, new requirements have been imposed for interconnecting DPGS to the grid. Among all, the capability of DPGS to ride through short grid voltage and frequency disturbances is one of the most difficult challenges. One of the strategies applied in these situations is to follow the positive sequence of the grid voltages.

A D-module filter is used to identify the positive voltage sequence of the power grid during the asymmetric voltage sags. The software implementation of the proposed method in Simulink is illustrated in Fig. 7.23.

Fig. 7.23 The Simulink grid-side inverter control used in Chapter 3

A detail view of the D-module block is presented in Fig. 7.24 for both positive and negative components.
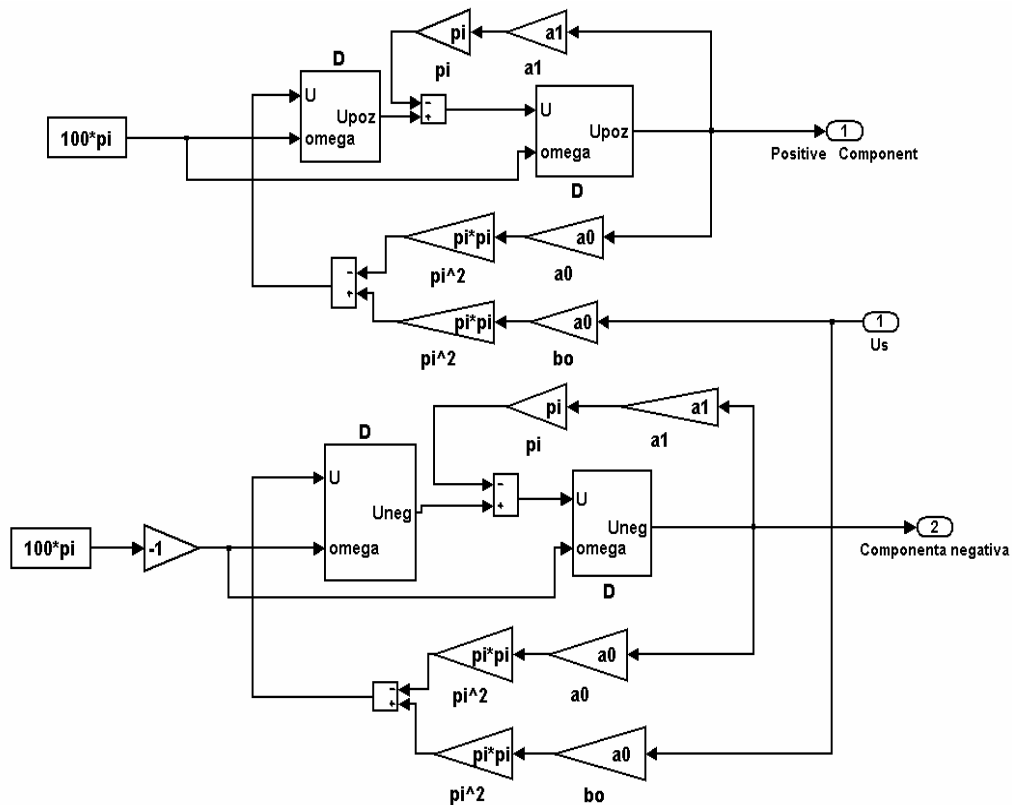
Fig.7.24 D-module filter Simulink implementation

When the DPGS operates in stand-alone mode the voltages are controlled in terms of amplitude and frequency. The voltage control is d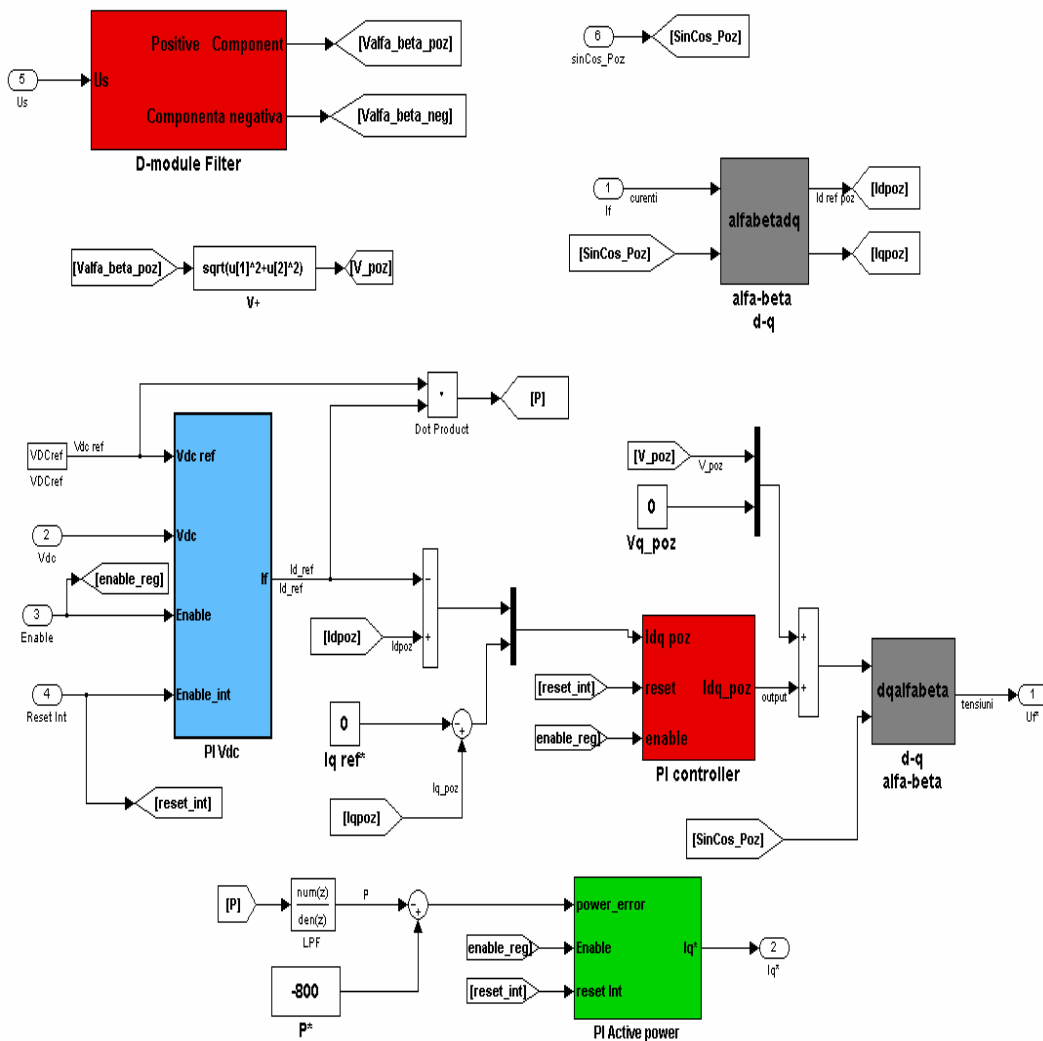ivided in two distinct parts: fundamental voltage control and harmonic voltage control. In the first case the d-axis respectively q-axis voltage controllers are standard PI controllers. The dc link voltage and current controllers lower the reference voltage for the main voltage controller when the dc link voltage is below a designated level; respectively when the load current exceeds a certain level [4]. In a second case the harmonic voltage control uses the line voltage measurements to detect the harmonic voltage to be compensated. The filter acts as a harmonic voltage source, injecting into the load voltages harmonic voltages with the same amplitude and opposite phase to the load voltages.

Due to intense computational effort needed to implement the proposed harmonic compensation algorithm and the sample frequency set during the experiments at 9 KHz, the implementation of the PR controller tuned on 18th harmonic had not the expected

results. So in order to compensate above 12th order PR resonant controllers, implemented in stationary reference frame, have been used for each of the odd 17th, 19th, 23th.
The Simulink implementation is shown in Fig.7.25 below.
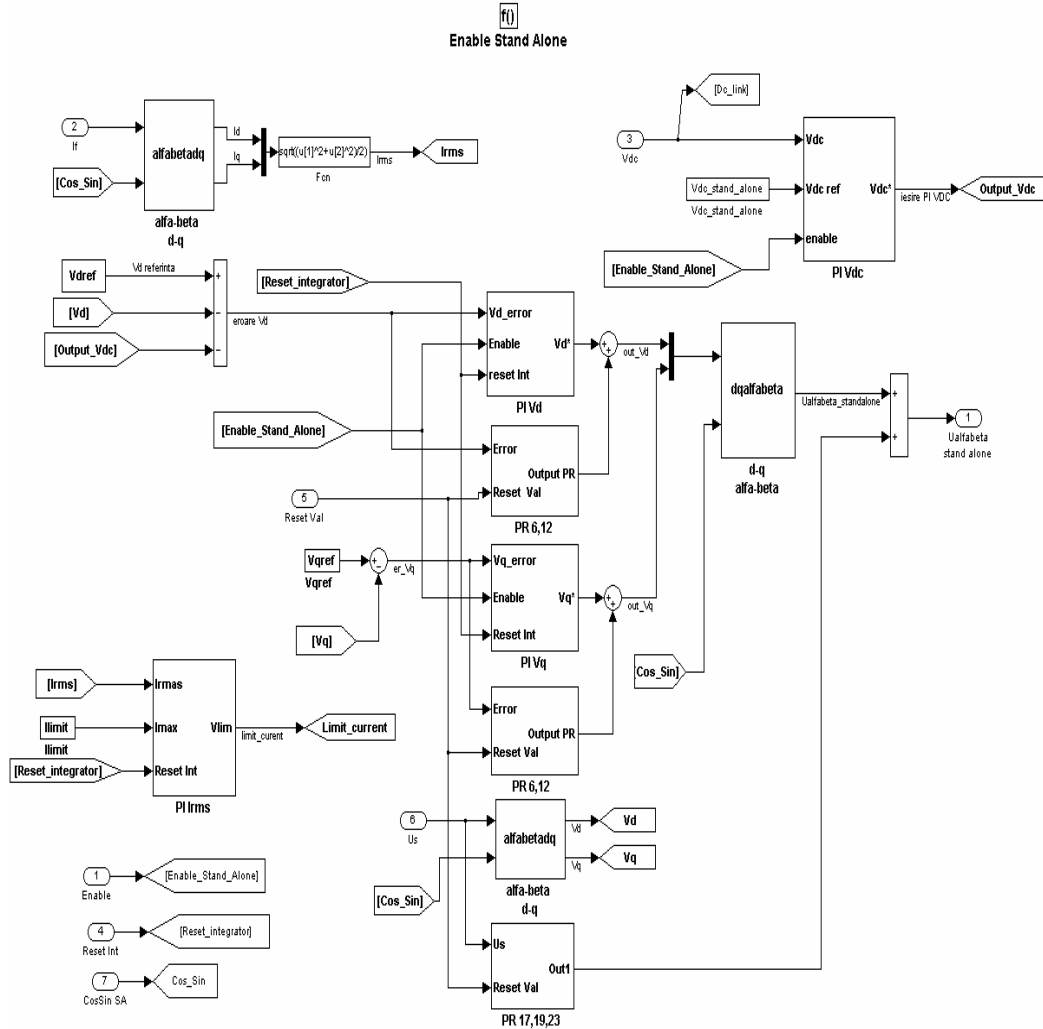
Fig. 7.25 Supply-side inverter control in stand-alone mode

The machine-side converter control software

The machine-side converter (MSC) is power controlled along q-axis when the system works in grid-connected mode and voltage controlled when is in stand alone mode (Fig.7.26).
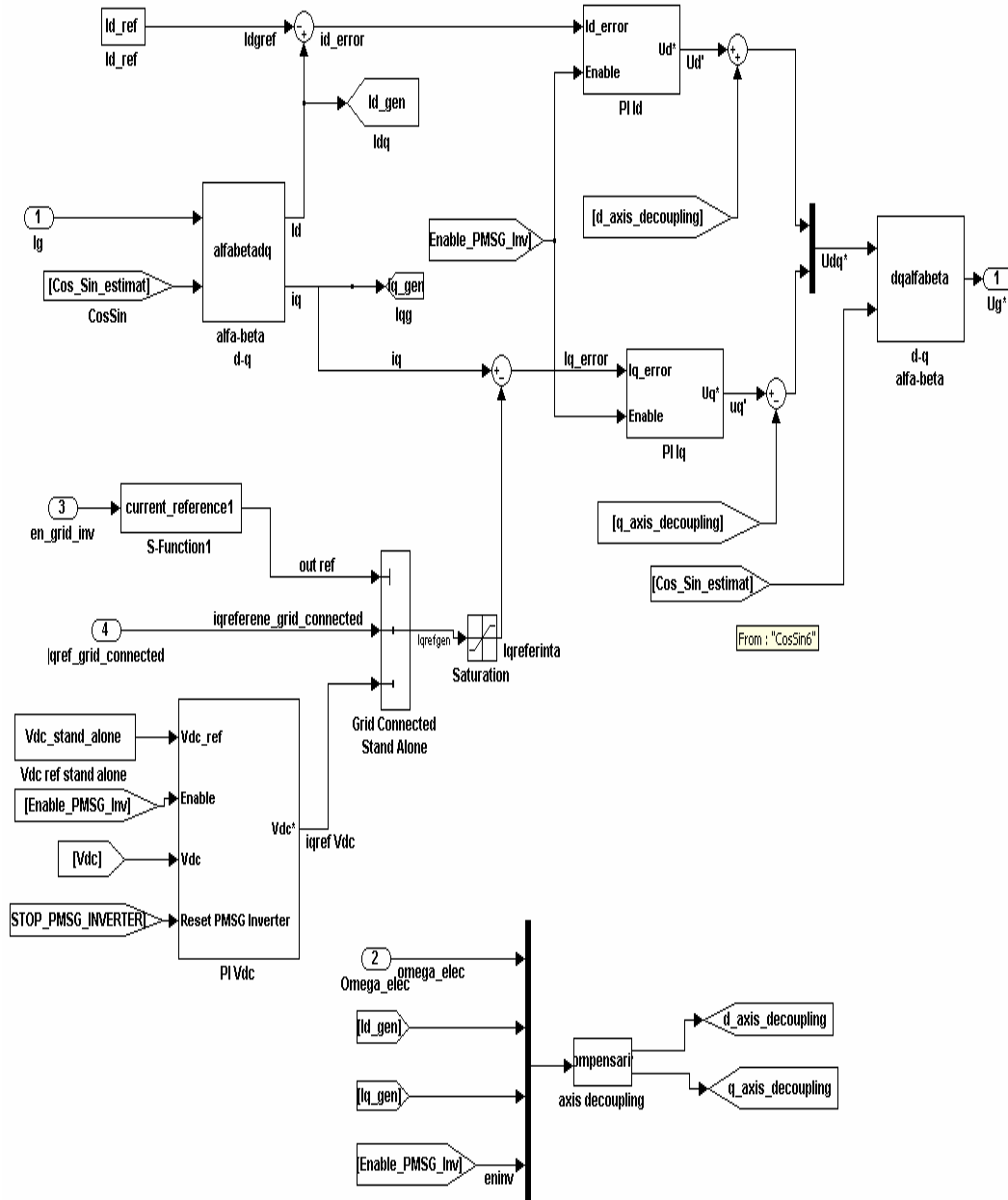
Fig. 7.26 The Simulink machine-side inverter control

The rotor position and speed estimator used, in chapters 3, 4, 5 implemented in Matlab/Simulink, is illustrated in Fig.27.
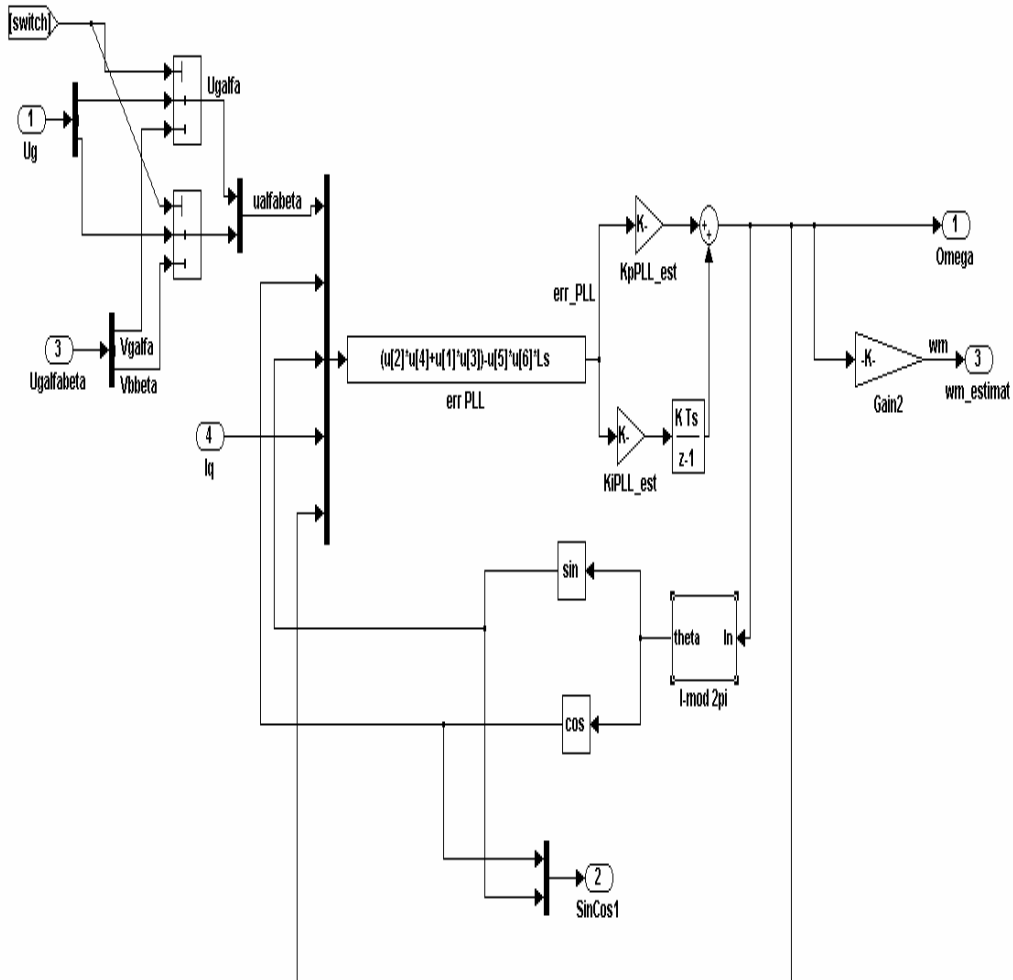
Fig. 7.27 The Simulink rotor position and speed estimator used in chapters 3,4,5

In chapter 6 a new safe, robust sensorless start-up method called "*I-f* control" for PMSM without initial rotor-position detection, with very good performance at low speeds is proposed. The Simulink implementation is shown in Fig.28. The entire algorithm is triggered by a general PWM interrupt at 10 KHz. The Start-up PMSM block contains:
- acquisition block
- protection
- inverter control
- current control
- rotor position and speed estimator

RTI Data

Host Service #1
< Service Name>
Data Capture

DS1103 SLAVE Board
PWM Interrupt

Trigger()

Start-up
PMSM
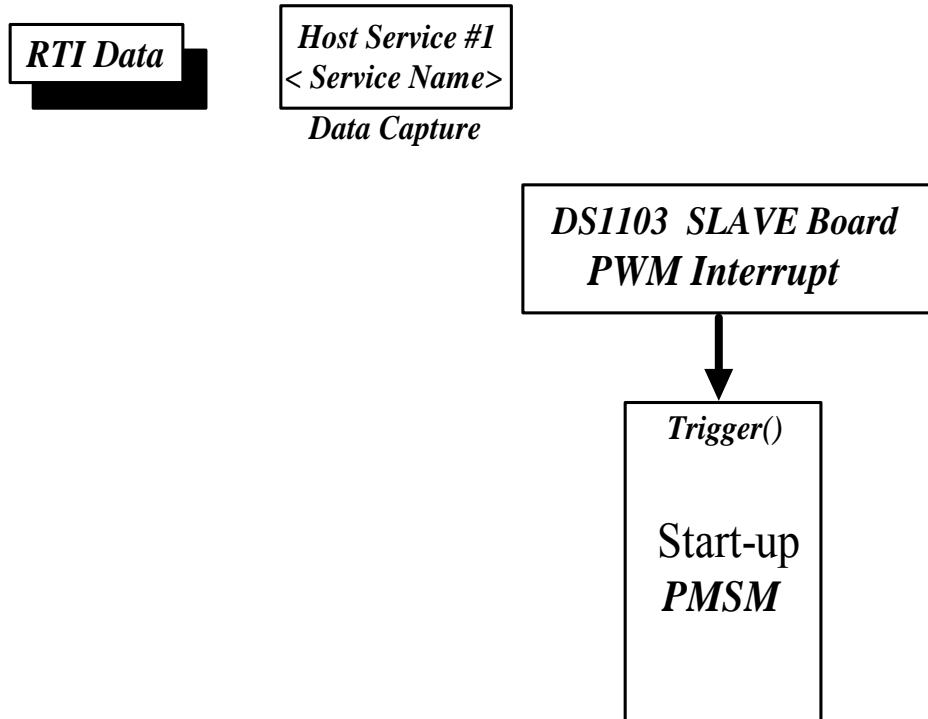
Fig.7.28 Simulink software

I-f control method consists in ramping the stator current frequency while i_q^* and i_d^* references are maintaining constant. The software implementation of the stator frequency variation algorithm under two S-functions in C code is shown in Fig.7.29.
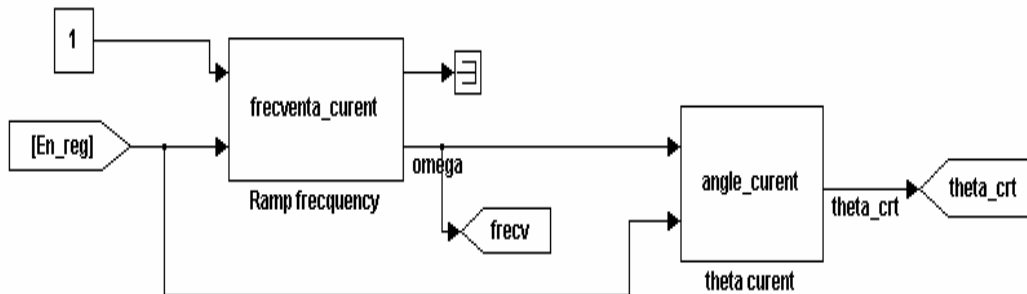
Fig.7.29 Ramp variation of stator frequency in Simulink code

The system uses *I-f* control for start-up and low speeds. When the reference frequency exceeds a certain level (f_{min}), the transition to emf motion-sensorless vector control is automatically initiated.

Transition from emf motion-sensorless vector control to *I-f* control is realized when the estimated rotor speed $\hat{\omega}_r$ is below a certain level (see Fig.7.30).
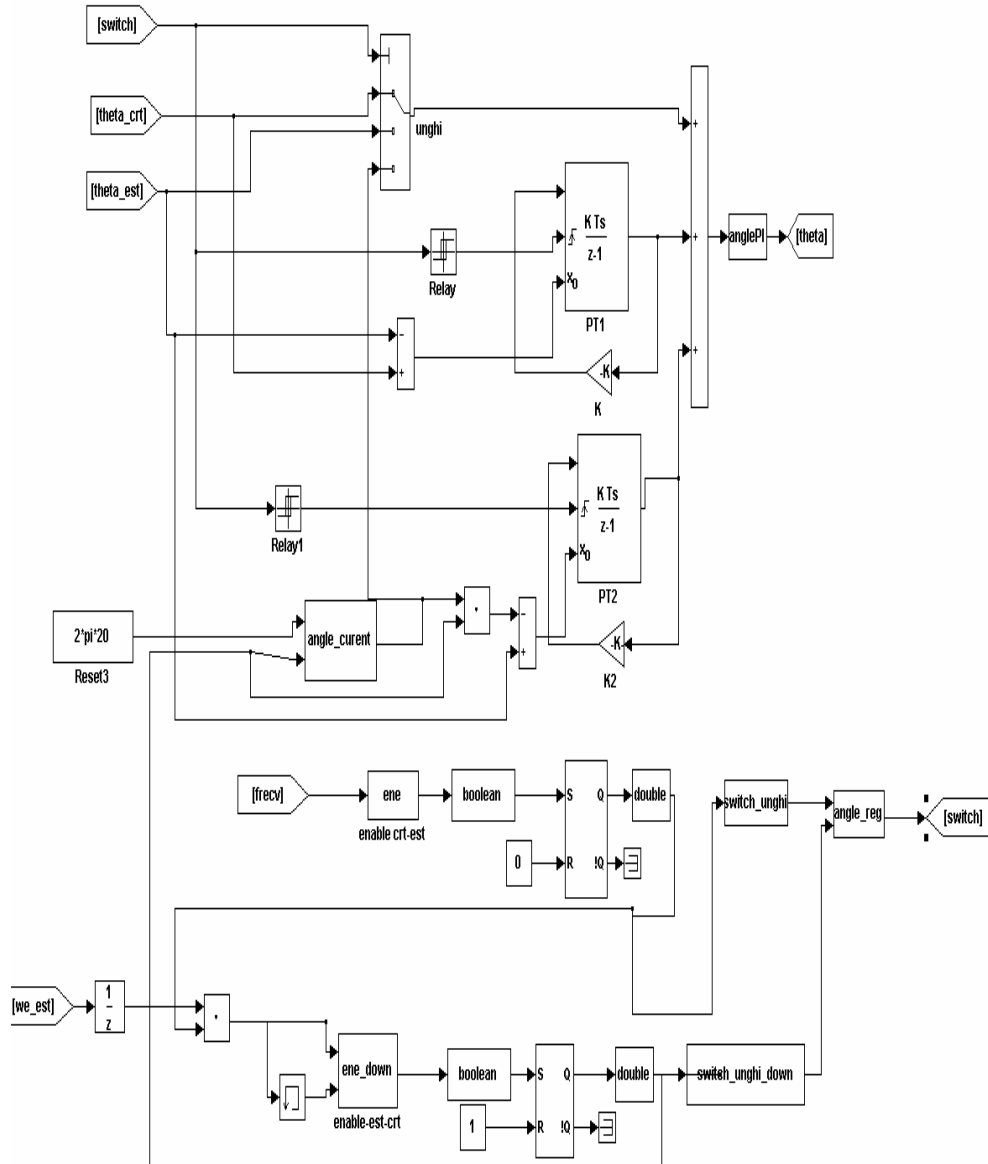
Fig. 7.30 Transition to emf and back to I/f sensorless control algorithm

The stator flux estimator, based on the voltage model in stator reference frame, employs an equivalent integrator (I+API) in close-loop, with a speed-adaptive PI controller to compensate the dc-offset and phase-delay. The Simulink implementation of the proposed algorithm is shown in Fig.7.31.
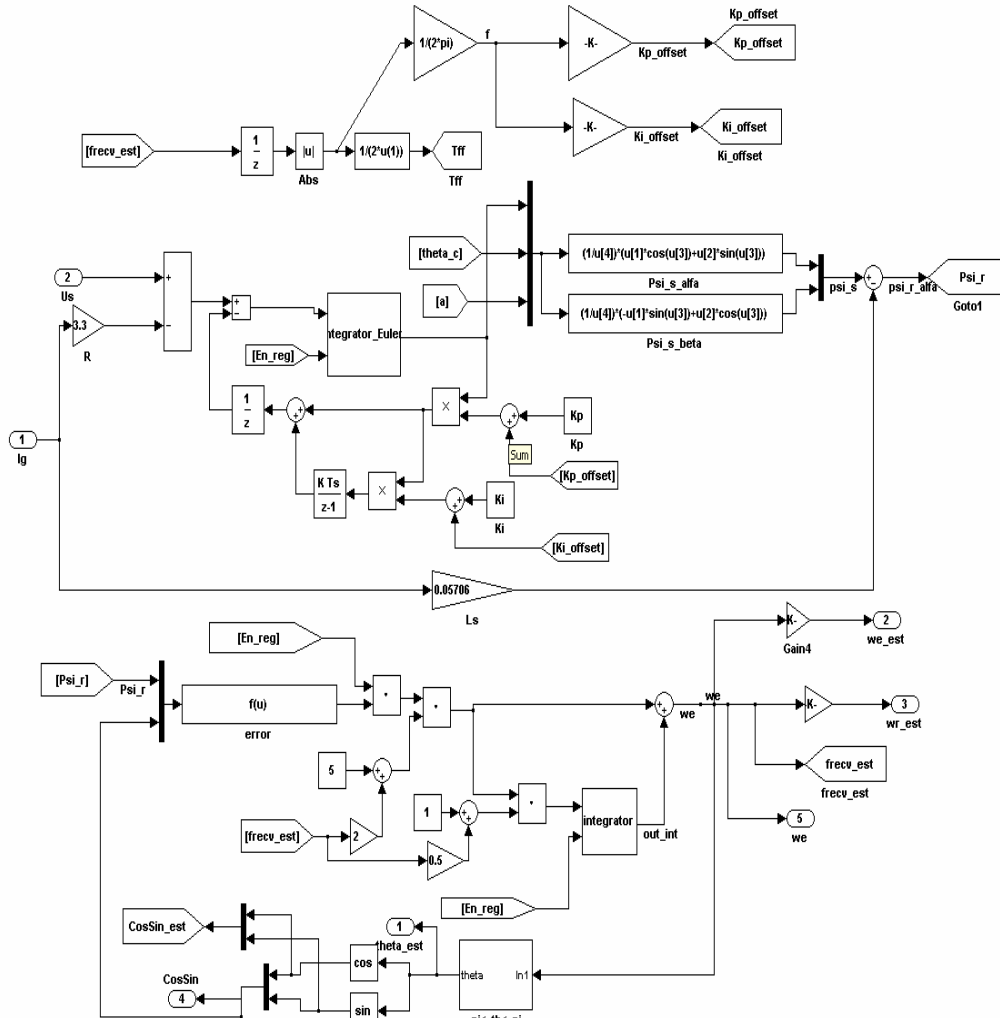
Fig.7.31 Simulink implementation of the proposed algorithm for rotor position and speed estimation

7.4 Conclusion

The experimental test platform used during the tests of state observers and sensorless control of a permanent magnet synchronous generator system was presented in this chapter.
The main application for this test platform is wind power.

All the hardware components of the system were presented, discussed and analyzed. The software used for measurements and protections, signal conditioning, vector control for both inverters is presented.

References
[1] www.california-instruments.com
[2] *** SIEMENS SIMOVERT Compendium CD ROM, 2000
[3]www.dspace.com
[4] http://www.crydom.com
[5] www.voltech.com

Chapter 8

Conclusion and Contributions

The present work was dedicated to advanced motion sensorless control of variable speed permanent magnet synchronous generators for wind power.
The thesis focused on several major topics like:

- Variable speed generators for wind applications.
- Experimental sensorless control of PMSG with two back to back converters under grid faults.
- Experimental seamless transition from grid connected to stand alone and back for sensorless controlled PMSG.
- Experimental selective harmonic and negative sequence compensation for a stand alone wind generation system with PMSG.
- Experimental sensorless motoring control of the system

Based on the presented topics the main conclusions are presented below:

- Variable speed generators are attractive for wind turbines for a number of reasons: it will reduce the mechanical stress in the gearbox, increase the amount of energy captured from the wind and improve the controllability of the active and reactive power, which becomes more and more important in respect to integrate the wind turbines into the grid.
- Permanent magnet synchronous generators (PMSG) with two back-to-back inverters are good candidates for wind power applications for number reasons: four quadrant control at variable speed with ± 100% active and reactive power capabilities, high efficiency reasonable cost and high flexibility.
- Due to large penetration of wind systems in the electrical network, according to the latest regulations, the high power wind turbine must remain connected to the grid during the faults. One method to prevent the damage of the power electronics is to follow the positive sequence of the grid voltages.
- If the grid is not recovered into amount period of time the system should be capable to switch automatically to stand alone control mode and vice versa without major transients.
- When the system is running in stand alone mode the one of the main challenges is to reduce harmonic pollution caused by nonlinear loads which may cause additional losses and heating in the electrical equipment, failures of the sensitive equipments, resonances and interference with electronic equipment, premature ageing.

Original contributions

The present thesis includes, from the author point of view, following major original contributions:

- Simulation under Simulink® environment of the whole PMSG system as solution for wind applications. The simulation includes the mode of the wind
- turbine, PMSG generator itself and the both inverters each of them with their vector control [1].
- Experimental smooth voltage sags ride through of motion sensorless controlled PMSG with two back to back PWM converters for wind turbines [2]:

    - development of a band-pass filter based on D-module filter to extract the positive-sequence voltages of the power grid.
    - Positive-sequence voltage vector control of the grid-side inverter during   asymmetric voltage sags.
    development of rotor position and speed estimator without emf I integration which was successfully tested during one-, two-, three phase voltage sags.

- Experimental motion sensorless bidirectional PWM converter control with seamless switching from power grid to stand alone and back for a PMSG [3].
- Experimental sensorless control of stand alone permanent magnet synchronous generator (PMSG): development and implementation of selective harmonic and negative sequence voltage compensator under nonlinear and non symmetric load [4].
- Digital simulation and experimental validation of a motion-sensorless control system for permanent magnet synchronous motors (PMSM) using a new robust start-up method called *I-f* control, and a smooth transition to emf-based vector control. Their field of application might be in wind generators safe (faster) self starting when connected to the grid, or moving the rotor a little for inspections/repairs and for general industrial variable speed drives where slightly hesitant but full-load self-starting is allowable [5].
- Implementation of 2.2 KW PMSG setup using Dspace 1103 system, to validate the proposed solutions for following situations:
    - voltage sags ride-through.
    - seamless switching from grid connected to stand alone and back.
    - selective voltage harmonic and negative sequence compensation in stand alone mode.
- Implementation of 2.2 KW PMSM setup using Dspace 1103 system to validate the proposed I-f start-up method and smooth transition to emf. based motion sensorless vector control and back.

Summary in Romanian

Sumar

Teza de faţă este dedicată controlului de înaltă performanţă al generatoarelor de turaţie variabilă având ca sursă primară energii regenerabile şi în special pentru aplicaţii cu turbine de vânt. Lucrarea ofera câteva soluţii   moderne pentru controlul generatorului cu magneţi permanenţi conectat la reţea prin intermediul unui invertor bidirecţional cât şi pentru regimul de funcţionare autom.

În ultimii ani energia eoliană a avut una dintre cele mai mari rate de crestere în raport cu celelalte surse de energie regenerabile. Concomitent turbinele de vânt au devenit din ce în ce mai mari, pe piaţă fiind deja disponibile unităţi de 6 MW în 2007. Din punct de vedere al ponderii în sistemul energetic naţional Europa se află pe primul loc, Danemarca şi nordul Germaniei având gradul cel mai înalt de penetrabilitate.

Aceasta situaţie implică noi cerinţe, grupate în aşa numitele coduri de reţea (grid codes), turbinelor de vânt privind capacitatea acestora de a suporta un interval determinat de timp anumite regimuri de avarie a retelei respectiv aspecte privind calitatea puterii.

Obiectivul principal al tezei este de a oferi soluţii performante pentru controlul generatorului sincron cu magneţi permanenţi conectat la reţea prin intermediul unui invertor bidirecţional a cărui cotă de piaţă este în continuare creştere.

Partea experimentală a fost realizată în laboratorul Dspace din cadrul "Institute of Energy Technlogy", Aalborg, Danemarca şi în Laboratorului de Reglaj Inteligent al Miscarii, Facultatea de Electrotehnica, Universitatea "Politehnica", Timisoara, Romania.
.

Organizarea tezei

În primul capitol este prezentată o viziune de ansamblu asupra generatoarelor cu turaţie variabilă utilizate in coversia energiei eoliene în energie electrică cât şi electronica de putere care le deserveşte. Sunt analizate principalele soluţii existente pe piaţă evidenţiindu-se avantajele şi dezavantajele fiecăreia atât din punctul de vedere al generatorului cât si al tipului de invertor folosit.

În capitolul *doi* modele de simulare dezvoltate pentru analiza sistemului cu generator sincron cu magneţi permanenţi conectat la reţea prin intermediul unui invertor bidirecţional sunt prezentate. Un algoritm sensorless este introdus şi testat cu rezultate bune şi discutat pentru diverse regimuri dinamice.

În capitolul *trei, experimental,* este investigată comportarea sistemului în condiţiile unor regimuri nesimetrice ale reţelei. Un algoritm sensorless pentru controlul generatorului sincron cu magneţi permanenti fara a integrara tensiunii electromotoare indusa este dezvoltat şi testat. Rezultatele sunt ilustrate şi discutate. Estimarea pozitiei este dovedită în toate situaţiile. Un estimator pentru secvenţa pozitivă a tensinii reţelei bazat pe un filtru în modul D este propus iar performanţele sale dinamice au fost investigate

pentru cele trei regimuri considerate. Rezultatele experimentale au dovedit capacitatea estimatorului, din momentul declanşării regimurile nesimetrice si pe durata acestora, de a extrage foarte rapid secvenţa pozitiva din tensiunile reţelei protejând astfel invertorul. Trecerea sistemului prin toate aceste regimuri nespecifice reţelei cu mici variaţii ale tensiunii din intermediar este amplu detaliat cu rezultate experimentale.

În capitolul *patru, experimental*, este investigată capacitatea sistemului de a trece rapid, fără regimuri tranzitorii din starea de conectat la reţea (grid connected) la aceea de a furniza energie unui consumator local (stand alone) în cazul unei avarii. Un sistem de monitorizare al parametrilor reţelei (frecvenţă , amplitudine) este propus şi implementat. În momentul în care se constată funcţionarea în afara limitelor admise, sistemul de control decide în mod automat schimbarea strategiei de control pentru invertorul legat la reţea: de la controlul în curent (grid connected) la cel în tensiune (stand alone). Un algoritm de trecere între cele două strategii este propus si implementat. Rezultatele sunt ilustrate şi evidenţiaza trecerea lină fără variaţii semnificative ale curenţilor sau ale tensiunii din intermediar. Când sistemul de monitorizare detecteaza revenirea parametriilor reţelei în limitele admise, se declansează automat procedura de sincronizare între cele doua sisteme de tensiuni. Cand eroarea de unghi este foarte mică sistemul de control comandă invertorul dinspre reţea în tensiune. Rezultatele evidenţiază o trecere lină fără şocuri de curent. Soluţia sensorless este cea folosită în capitolul trei, iar rezultatele experimentale confirmă performanţele dinamice excelente.

În capitolul *cinci, experimental,* este investigată funcţionarea senorless a generatorului cu magneti permanenţi in cazul alimentării unui consumator local nesimetric (în acest caz, un redresor trifazat cu diode). Aspectele considerate sunt:
-   compensarea armonicilor din tensiune
-   compensarea secventei inverse a tensiunii în cazul connectării unui consumator local nesimetric

Performanţele algoritmului de a compensa armonici în tensiune până la ordinul 23 cât si reducerea nesimetriei de *zece* ori sunt evidenţiate şi discutate.

În capitolul *şase, experimental,* este investigată autopornirea şi funcţionarea sistemului în regim de motor. O noua metoda de pornire sensorless, independentă de parametrii maşinii, este propusă si investigată prin ample simulări numerice şi validată experimental. În momentul în care viteza estimată atinge un anumit prag, sistemul trece automat la estimarea vitezei şi poziţiei rotorului pe baza unui algoritm sensorless cu rezultate foarte bune în domeniul vitezelor medii şi mari . Structura de control este capabilă să comute automat, fără regimuri tranzitorii, de la algoritmul sensorless la algoritmul folosit pentru autopornire şi funcţionare la viteze mici. Rezultatele sunt ilustrate şi discutate.

Capitolul *şapte* este dedicat standurilor experimentale folosite pentru toate testele.

Capitolul *opt* este unul de sinteză unde sunt prezentate concluziile şi contribuţiile tezei.

Contribuţiile tezei

După părerea autorului teza conţine următoarele contribuţii originale:

- Simularea în mediul Similink® a sistemului cu generator sincron cu magneţi permanenţi. Simularea conţine include modelele turbinei de vant, generatorul propriu-zis si ambele invertoare conectate spate in spate, fiecare având propriul control vectorial [1].
- Dezvoltarea unei metode fara traductori de poziţie (sensorless) pentru sistemul cu PMSG cu estimarea precisă a vitezei şi poziţiei rotorului inclusiv în următoarele condiţiile: regimuri nesimetrice ale reţelei, trecerea de la regimul de funcţionarea conectat la reţea (grid connected) la cel autonom (stand alone)[2,3,4].
SDezvoltarea unui control vectorial pentru invertorul conectat la reţea bazat pe un estimator de secvenţa pozitivă a reţelei. Acesta conferă sistemului capacitatea de a rămâne conectat în timpul diverselor regimuri nesimetrice ale reţelei [2].
- Dezvoltarea unei noi metode de trecere automată, lină, fără întreruperea curentului, a sistemului din regimul de conectat la reţea la cel autonom şi invers când se detectează revenirea parametrilor reţelei la cei nominali [3].
- Dezvoltarea unei scheme de control pentru compensarea selectivă a armonicilor din tensiune, precum şi compensarea nesimetriei tensiunilor în cazul connectării unei sarcine nesimetrice pentru regimul de funcţionare autonom [4].
- Dezvoltarea unei strategii hibride de autopornire, funcţionare, la viteze foarte mici independentă de variaţia parametrilor MSMP şi trecerea lină la o metoda de control fără traductori de poziţie pentru domeniul de viteza mediu şi mare şi invers [5].
- Implementarea unui stand cu MSMP de 2.2 KW pentru studiul regimurilor de generator şi motor. Este efectuată analiza algoritmilor de control în cazul apariţiei unor regimuri nesimetrice, trecerii de la regimul de funcţionare la reţea la cel autonom şi înapoi, respectiv funcţionarea în regim autom.

Curriculum vitae

Marius Fatu

Office
Politehnica University of Timisoara, Romania
Bd. Vasile Parvan no.2 , room 108
Tel: +40 256403463
Email: fatu_marius@yahoo.com
Home
Micea Eliade no.36, Fagaras, Romania
Tel: +40 268217454
Education
2004 Dipl. degree in Electrical Engineering
1999-2004 University „Politehnica" of Timisoara, Timisoara, Romania
Department of Electrical Engineering
1995-1999 National College "Radu Negru", Fagaras, Romania
Professional Experience
3 month in 2006 Guest Researcher in Institute of Energy Technology, Aalborg
University Denmark
2 month in 2007 Guest Researcher in Institute of Energy Technology, Aalborg
University Denmark
1 month in 2007   Guest Researcher in Ebm-Papst St. Georgen GmbH / R&D
Laboratory for Electric Drives, Germany

Personal Information
Born: February 4th, 1981
Family: Unmarried

Author's papers related to the Ph. D. thesis

[1] M.Fatu, I.Boldea, C.Lascu, L.Tutelea, G.D.Andreescu, „Motion sensorless variable speed PMSG control at power grid", Proceedings of OPTIM 2006, Braşov, Romania.

[2] M.Fatu, C.Lascu, G.-D. Andreescu, F. Blaabjerg, R.Teodorescu, I. Boldea ," Voltage Sags Ride-Through of Motion Sensorless Controlled PMSG for Wind Turbines", Record of IAS -2007, New Orleans, USA.

[3] M. Fatu , L. Tutelea, R.Teodorescu, F. Blaabjerg, I. Boldea "Motion sensorless bidirectional PWM converter control with seamless switching from power grid to stand alone and back ",PESC'07, Orlando, Florida, USA, June 2007.

[4] M.Fatu, L.Tutelea, I. Boldea, R.Teodorescu "Novel motion sensorless control of stand alone PMSG: harmonics and negative component sequence voltage compensation under nonlinear load", *Record of EPE*-2007, Aalborg, Denmark.

[5] M.Fatu, I. Boldea , G.-D. Andreescu, F. Blaabjerg, „I-F Starting Method with Smooth Transition to EMF Based Motion-Sensorless Vector Control of PM Synchronous Motor/Generator", accepted at IEEE PESC 2008.